Technologies for single chip integrated optical gyroscopes

Muhammad Hassan Iqbal

October 2021

A thesis submitted for the degree of Doctor of Philosophy of
The Australian National University

Research School of Physics

Australian National University

Declaration

I **Muhammad Hassan Iqbal,** University ID **U5906401** authenticate that the material reported in this dissertation does not include any intellectual property which has previously been used to obtain a degree or published in any journal without due acknowledgement. The contents of this dissertation are purely based on original research and entirely my own work.

Muhammad Hassan Iqbal

Date: 8-10-2021

Acknowledgement

Thanks to Allah almighty who enabled me to complete this milestone.

There are so many people who helped and supported me during the tenure of my PhD and I thank them all from the core of my heart. I want to mention all of them here by names and if someone is missed mistakenly, I sincerely apologize for that in advance.

I will start with my primary supervisor Dr. Steve Madden for whom I don't have words to express my deepest gratitude. I am obliged for his extraordinary support and guidance from the day I arrived in Australia, for always making himself available for discussions, for showing the correct direction and his enthusiastic approach to research. Without his supervision, there would not have a smooth progress in my project. I also express my gratitude to secondary supervisors Dr. Duk-Yong Choi, Dr Khu Vu and Dr. Kunlun Yan for taking part in my supervisory panel and having many fruitful discussions.

I am also grateful to the members of my research group at Laser Physics Centre (Dr. Pan Ma, Mr Sukhanta Debbarma, Dr. Harry-Dean Kenchington Goldsmith, Mr Choon Lai Kong, Ms Huma Latif and Mr Yile Zhong) who always helped with simulation and experimentation. It would be unfair not to mention the help with the fabrication facilities (PECVD, Barrel etcher and SEM) I got from the staff of ANFF ACT node. Therefore, I acknowledge the support of the ANFF ACT node in carrying out part of this research. I am also thankful to my friend Dr. Usama Elahi for his help with the MATLAB and Dr. Teng Choon Kho for helping me with the deposition of LPCVD Si_3N_4 films.

Throughout this work, the enormous support I got from my wife (Dr. Faiza Naseem), the prayers of my parents (Muhammad Iqbal and Iffat Iqbal) and Continuous encouragement from siblings (Capt. Muhammad Hussain Iqbal and Dr. Ayesha Iqbal), I must say Thank is just not enough.

Abstract

Optical gyroscopes are being employed for navigational purposes for decades now and have achieved comparable or better reliability and performance than rotor-based gyroscopes. Mechanical gyros are however generally bulky, heavy and consume more power which make them unsuitable for miniaturized applications such as cube satellites and drones etc. Therefore, much effort is being expended worldwide to fabricate optical gyros having tactical grade robustness and reliability, small size, weight, cost and power consumption with minimal sacrifice of sensitivity. Integrated optics is an obvious approach to achieving this.

This work comprises detailed comparative analysis of different types and structures of integrated optical gyroscopes to find out the suitable option for applications which require a resolution of <10 ^{o}/h. Based on the numerical analysis, Add-drop ring resonator-based gyro is found to be a suitable structure for integration which has a predicted shot noise limited resolution of 27 ^{o}/h and 2.71 ^{o}/h for propagation losses of 0.1 dB/cm and 0.01 dB/cm respectively.

An integrated gyro is composed of several optical components which include a laser, 3dB couplers, phase/frequency modulators, sensing cavity and photodetectors. This requires hybrid integration of multiple materials technologies and so choices about which component should be implemented in which technology. This project also undertakes theoretical optimization of few of the above-mentioned optical components in materials systems that might offer the most convenient/tolerant option, this including 3dB coupler, thermo-optic phase modulator and sensing cavity (resonator and waveguide loop). In particular, the sensing element requires very low propagation loss waveguides which can best be realised from Si_3N_4 or Ta_2O_5. The optimised Si_3N_4 or Ta_2O_5 waveguides however are not optimal for other functions and this is shown and alternatives explored where the Si_3N_4 or Ta_2O_5 can easily be co-integrated.

The fabrication process of low loss Si_3N_4 and Ta_2O_5 waveguides are also reported in this thesis. Si_3N_4 films were grown by using low pressure chemical vapor deposition (LPCVD) technique. Dry etching of Si_3N_4 films have been optimized to produce smooth and vertical sidewalls. Experimental results predicted that the propagation loss of 0.009 dB/cm is achievable by using optimum waveguide dimensions and silica cladding with the relatively standard processes available within the Laser Physics Centre at the

Australian National University. A CMOS back end of line compatible method was developed to deposit good quality Ta_2O_5 films and silica claddings through ion beam sputtering (IBS) method.

Plasma etching of Ta_2O_5 waveguides has been demonstrated by using a gas combination of $CHF_3/SF_6/Ar/O_2$. Oxygen was introduced into the chamber to produce non-vertical sidewalls, so the waveguides could be cladded without voids with IBS silica. Average propagation losses of 0.17 dB/cm were achieved from Ta_2O_5 waveguides which appeared after extensive investigation to be limited by the spatial inhomogeneity of the processing. Lastly, a detailed theoretical and experimental analysis was performed to find out the possible causes of the higher average propagation loss in Ta_2O_5 waveguides, some sections being observed with 0.02 dB/cm or lower losses.

Table of contents

Chapter 1
Introduction

1.1 Gyroscope

Inertial navigation systems (INS) are being extensively employed to measure acceleration and rotation rate in a wide range of applications including the rapidly growing and increasingly important autonomous vehicle sector. An INS is a combination of two functional units, an Inertial Measurement Unit (IMU) and a navigation computer. The IMU provides the measurement of the rotation rate and acceleration respectively, whereas the navigation computer uses these measurements to calculate the relative position, orientation and velocity. Gyroscopes are used to measure the rotation rate of an object, whereas accelerometers measure the change in the velocity in one linear direction. Improvement in the performance of these sensors along with size reduction is increasingly important for modern applications (e.g. fabrication of high performance gyros for mini-satellites) [1].

The first gyroscope was essentially a rotating wheel. In early times, spinning top was used as a toy due to its unique ability of balancing itself while rotating. At the start of the 19th century, scientists and sailors began attempting to use spinning gyros for scientific purposes.

Prior to the commercial use of spinning gyros, sextants were the default navigational instrument, these measuring the angle between specific stars and horizon and observational star charts to derive latitude. Once the latitude is determined, the longitude was measured by comparing the time with Greenwich time. However, this method was entirely dependent on the weather as clouds could cover the stars and fog could obscure the horizon.

By the mid 19th century, a French scientist Foucacult used the gyroscopic effect (conservation of angular momentum) to measure the earth's rotation and named the instrument as a "gyroscope". The name originated from two Greek words; gyro meaning "revolution" and skopein meaning "to see". With the invention of the laser and new microfabrication techniques, a number of highly sensitive non-rotational gyroscopes based on different working principles were fabricated to meet the modern era applications. These are discussed in the coming sections. A gyro is specified by a number of key performance parameters:

Resolution: It determines the ability of a gyro to detect the minimum angular velocity and is described in units of deg/h.

Angular random walk: Sometimes gyro output is obtained as the absolute change in the angle rather than the angular rate which is done by simply integrating the output over time. Angular random walk (ARW) represents/specifies the rms noise (broadband and random noise) in the output with a unit of deg/$h^{1/2}$. The variation in the output due to this noise element is described by the ARW and can be measured by the Allan Variance [2]. The smaller the ARW, the better the quality of a gyro.

Constant bias: Constant bias is defined as the nonzero reading per unit time for a non-rotating gyro. This error is estimated by taking the mean of the output over a long duration measurement of a non-rotating gyro. Once the constant bias is known, it can be offset from the measurement.

Bias stability: Bias stability is the determination of gyros output stability over a time period. It is thus the AC equivalent of the Constant bias. It describes the drift in the output over time and is reported in units of deg/sec or deg/h. It is one of the most important performance metrics and is obtained through Allan Variance plot [2]. The smaller the value of bias stability, the better the quality of a gyro.

In-run bias stability: This is defined as minimum drift in the output during the operation. The minima of the Allan Variance curve is the in-run bias stability.

Bias repeatability: It indicates the average change in the bias while turning on and off the gyro multiple times. It is also described in units of deg/h.

Environmental sensitivity: Variations in the temperature can greatly degrade the gyro performance. Therefore, it is necessary to characterize the gyros parameters over temperature variation to confirm their compatibility with the intended application. Vibration, humidity and shock can also degrade gyro performance and are especially important in military applications where gyros routinely encounter harsh operating environments.

Today, gyros are being employed for numerous applications starting from general electronic products through to the aerospace & defence industry. In 2018, the estimated market size for gyros used in mobile phones was USD 1.5 billion to 1.7 billion that is projected to go up with a compound annual growth rate of four to five percent during 2019–2025 and will reach around a record value of USD 2.4 billion [3]. The main growth drivers for this industry include high military spending, increase in the number of vehicles worldwide and sharp rise in demand for consumer electronics.

As per the data reported by Global System for Mobile communication (GSM), there are currently 5 billion mobile users in the world and this number will grow to 6 billion in 2025. Almost all smart phones now manufactured have built-in gyros that measure the angular rate of the device [3].

Gyros are also used in vehicles to maintain their orientation and angular velocity. Gyro is the part of electronic stability program (ESP) of a vehicle and help avoiding the roll of the body during cornering and travelling uneven paths. The rapid increase in the demand of the automobiles around the world has positively impacted the gyro market. According to the numbers reported by the Organisation Internationale des Constructeurs d'Automobiles (OICA), 97 million vehicles were manufactured in 2017 with an expected growth in the future [3].

The emergence of cube satellites, small drones, and unmanned aerial vehicles (UVAs) attracted a lot of attention and funds recently. Increasing investments and technological innovation are paving the way for the lower cost high performance gyros [4].

All applications require different sensitivity as can be seen in figure 1.1. For example, the automotive industry needs a sensitivity of around 60–1000 °/h whereas space and defence applications require 0.01–10 °/h [5-7]. For this work a readout rate of 1 Hz will be assumed.

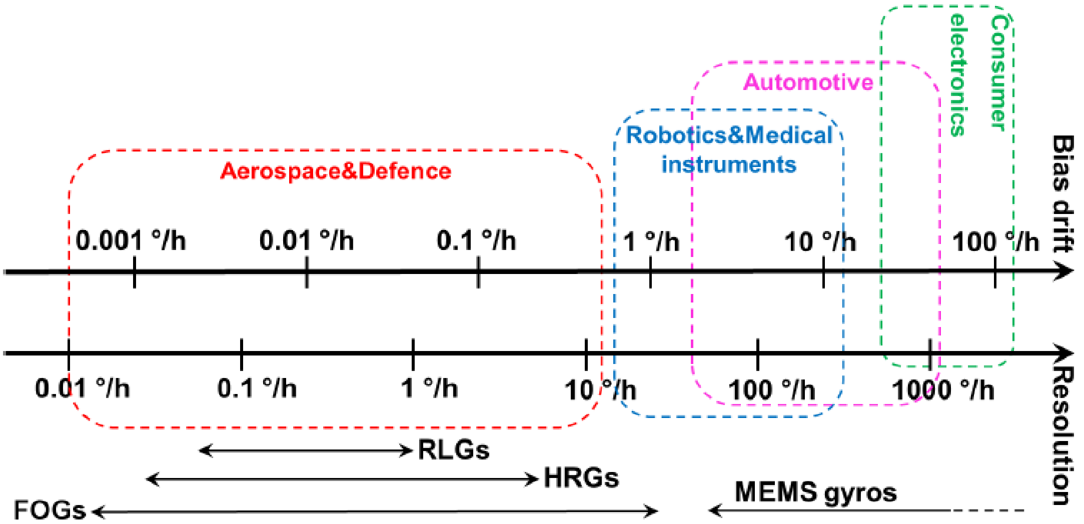

Figure 1.1: Showing the performance comparison between different types of gyros and their applications [5].

The stringent sensitivity requirements in space and defence applications are extremely important to reduce the chances of any disastrous incidents. For instance, NASA sent an exploration craft to MARS on 30th July 2020, which landed on the red planet on 18th February

2021 [8]. Considering the amount of flight time, these craft could potentially diverge from their original path by unacceptable margins even with an error of 0.05 ^{o}/h. Therefore, keeping the consequences in mind, the highest performance gyros are required for these applications.

Since the turn of the century, the world has moved rapidly towards the miniaturization of instrumentation anticipating the increasing demands of smart devices and rapidly developing space technology as well as recognizing the intensity of the energy resources being consumed. All these factors demand the development of small footprint, reliable, robust and low power consuming devices. With the progress in integrated optics (a technology used to fabricate various photonic devices on the same chip to perform different functions), the fabrication/development of such types of optical instruments and devices is becoming reality.

1.1.1 Types of gyroscopes

There are number of different types of gyros based on various operating principles that have been reported to date. These gyros include mechanical gyros, vibrating gyros, nuclear magnetic resonance gyros, cold atom gyros and superfluid gyros. Optical gyros, cold atom gyros and superfluid gyros work on the principle of Sagnac effect [9]. The nuclear Magnetic resonance gyros determine the angular rate by determining the shift in the Larmor precession frequency of the nuclear spin [10], whereas mechanical and vibrating gyros working mechanism is conservation of angular momentum (COAM) [11] and Coriolis effect [12] respectively. These will now be examined briefly.

1.1.2 Mechanical gyroscope

The first mechanical gyroscope was built by a physicist from Germany named G. C. Bohnenberger [13] at the start of the 19th century (1817). Thirty-five years after its invention (1851), a French scientist (Leon Foucault) took a step forward and showed that this sensor could detect the rotation of the earth [14, 15]. Mechanical gyros work on the principle of COAM in a spinning disc (rotor). A driving motor is used to rotate the disc continuously around its axis. The basic structure of a mechanical gyro is shown in figure 1.2.

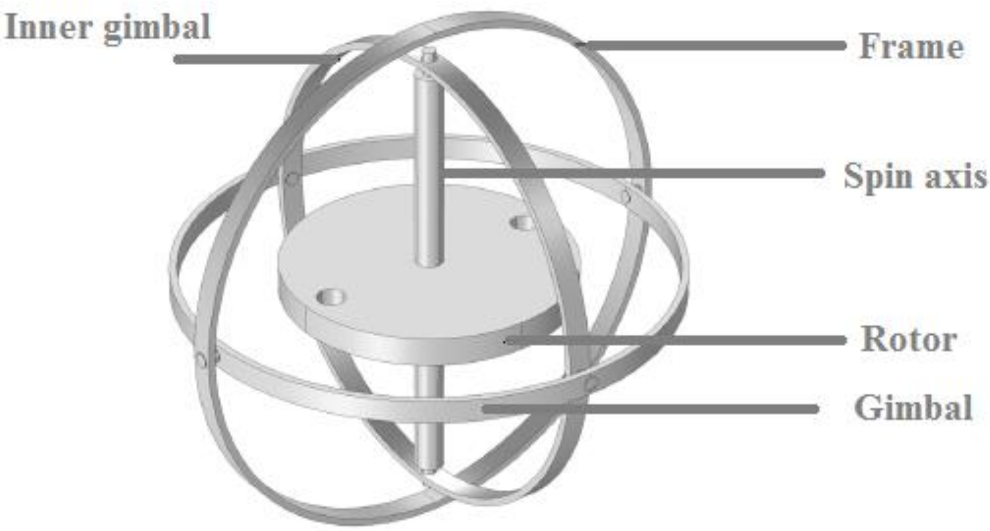

Figure 1.2: Illustrating the structure of a mechanical gyro [16].

A disc that can be rotated around an axis is the fundamental part of a mechanical gyro. Angular momentum generated by this spinning disc resists any change in the orientation of its spin axis. If the gyro is mounted into a 3 axis gimble (as shown in figure 1.2) using low friction bearings which allow the spinning disc to move freely in all three directions, the orientation of the spin axis will remain unchanged, this property is called gyro inertia. When the rotor is spinning and torque is applied perpendicular to the spin axis, the rotor experiences a precession motion which is normal to the input torque. The rotation rate of a gyro is measured using this effect. The precession rate corresponds to the input torque and written as:

$$\mathbf{T = I\omega\Omega} \qquad (1.1)$$

Here, T is the applied torque, I is rotational inertia of the spinning disc, ω is rotor angular frequency and Ω is the precession rate.

For angular position measurement, the gimbaled structure is mounted on the vehicle and allowed to move freely, whereas the rotor’s spin axis holds its angular position throughout the vehicle’s movement. Total change in the angular position is correlated to the relative change of the angle between the fixed direction on the gyro frame and spin axis of the disc [17] and measured by an angle pick-off device mounted on the gimbals.

Since their discovery, mechanical gyros were the only rotation rate sensors used in civilian and military applications until the inception of optical gyros. The rapidly evolving and stringent requirements of military systems have pushed spinning disc based gyros to the limits, as their sensitivity to gravitational fields become an issue in the increasingly high-g environment of the modern military applications. These gyros are also sensitive to external shocks as well which sometimes act as an applied torque to the rotating disc causing the deviation in the spin axis direction and inducing precession error [18]. A small imbalance in the spinning disc due to fabrication tolerance inaccuracies can also act as an external torque and cause a gyro to drift with time even when the vehicle is not having high transient acceleration. Due to the gimbaled structure requirement, they are quite large in size, costly and have high mechanical complexity [19].

Despite the issues mentioned above, mechanical gyros are still employed for high performance applications. Mechanical gyros used in commercial aircraft are quite sensitive and drift only 0.1^{o} in 6 hours of flight [20].

1.1.3 Vibrating gyroscope

All vibrating gyros work on the principle of Coriolis effect in which two resonant modes of the vibrating mass exchange energy due to Coriolis acceleration. Coriolis effect is defined as "a moving proof mass in a rotating frame of reference experiences a force acting orthogonal to the rotation axis as well as the direction of motion" [21]. Vibrating gyros use this effect to measure the angular velocity. This can be better understood by a mass spring system (see figure 1.3). The proof mass (m) can move along the two axes, say sense axis (x) and drive axis (y). By using an electrostatic comb driver for example, the proof mass is driven into linear oscillations along the drive axis. If the system rotates around an axis which is orthogonal to the drive axis, a Coriolis acceleration is induced and results in a periodic displacement at a particular amplitude along the sense axis in proportion to the angular velocity [22]. Rotation induced displacement in the sense axis is mostly detected by using a capacitive sensor which is integrated with the gyro. The displacement induced by the rotation is extremely small for practical applications which results in a capacitance change of the order of 10^{-21} F. Due to this, it is important to minimise the sensitivity to noise sources such as environmental variations, package stress and electronics noise which is partially achieved by integrating the electronics on the same chip as the sensor.

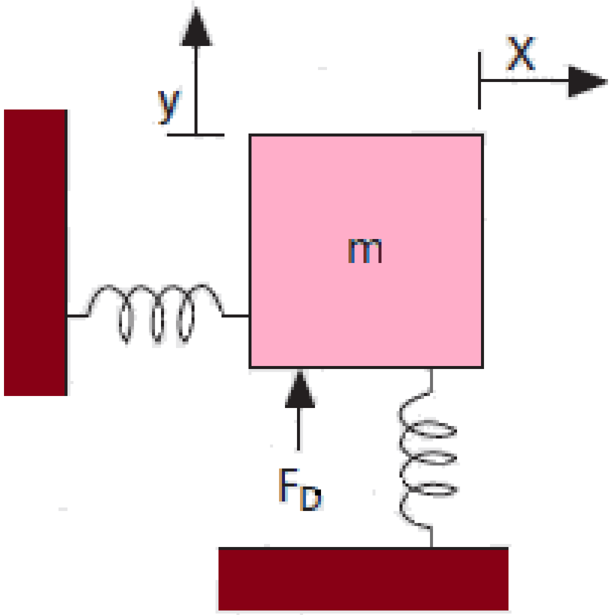

Figure 1.3: Showing a mass spring system having dual movement axis.

The amplitude of the displacement along the sense axis is represented by equation (1.2) [17]:

$$\Delta x = \frac{2\Omega F_{cx} Q_y}{m\omega_y} \frac{1}{\sqrt{\left(\omega^2{}_y + \omega^2{}_x\right)^2 + \left(\frac{\omega_y \omega_x}{Q_x}\right)^2}} \tag{1.2}$$

Here, m is the proof mass, F_{cx} is the Coriolis force along the sense axis, Ω is the rotation rate, $Q_{y/x}$ and $\omega_{y/x}$ represent the quality factor and resonant frequency of the driving (y) and sensing mode (x) respectively.

Passaro et al. [17] reported that the sensitivity of the vibratory gyro can be enhanced by improving the mechanical quality factor as well as by matching the resonant frequencies of both the modes. It is important to note that resonant frequencies of both the modes cannot remain matched over long periods due to temperature variations and structure fatigue. Therefore, electrostatic tunning is employed to match the resonant frequencies [23].

As far as Q factor is concerned, the limiting effects in mechanical Q in vibrating gyros include: energy dissipation due to the surrounding environment, surface loss, clamping loss and thermoelastic dissipation [24]. Environment related loss is caused by the resistive force of the ambient air or gas and is usually reduced by operating the gyro in vacuum. Surface loss is related to the loss of mechanical energy due to surface defects such as crystal termination defects and dangling bonds. Surface loss is most influential in nano scale devices and almost negligible for micro scale structures. Clamping loss is related to the energy lost through the substrate which is reduced by isolating the beam vibrations from the bulk substrate. However, thermoelastic dissipation is a fundamental limit on the Q factor of a vibrating structure. It arises due to the temperature variation of the vibrating springs/beams. When a beam is flexed, it induces compression and tension at one and the other side, respectively. The compressed side experiences a tiny increase in the temperature which is related to its thermal expansion coefficient and vice versa. This tiny thermal gradient results in a heat flow to attain thermal equilibrium which causes irreversible energy loss [25]. The maximum achievable Q factor is limited by the current microfabrication technologies because they are restricted to only a few materials. The currently used materials such as silicon have relatively high thermoelastic damping. The value of the thermoelastic dissipation is maximum when the vibrating frequency of the structure is close to thermal relaxation frequency.

The proof mass/vibrating element can have number of shapes such as a hemi-spherical dome, hollow cylinder, tuning fork and rod. These gyros do not require a rotating body and bearings to operate, therefore can easily be miniaturized. Several gyros have been fabricated and tested based on the Coriolis effect such as the hemispherical resonator gyro [26], tuning-fork gyros [27] and cylindrical resonator gyros [28].

Furthermore, microfabrication techniques (electron beam lithography and photo lithography) allowed the co-integration of electronic circuits and micromechanical elements for high-volume fabrication of miniaturised, and low-cost versions of these gyros, leading to the now well-known terminology of Micro Electro-Mechanical systems (MEMS) gyros. However, the miniaturisation of the sensing elements has its own drawbacks in terms of getting good performance and high resolution. The sensitivity of the MEMS sensors is affected by thermally induced noise which is usually negligible for macro systems but cannot be ignored for micro devices. As the size of the sensor goes down, signal from the device weakens, and noise goes up which limits the sensitivity. In addition, these gyros are known to have high bias drifts due to their sensitivity to thermal variations and external vibrations. As mentioned above, the rotation detection depends on the vibration of an element and any external vibration could induce undesired drift in the output. Another source of drift is the unwanted coupling between both axes due to asymmetries in the mechanical transducer [29]. A lot of efforts are being made to reduce the noise level in MEMS gyro by employing different structures. Recently, Li et al. [30] reported a disk resonator based MEMS gyro which gave a bias stability of only 0.04 ^{o}/h at room temperature. However, it still needs to be tested in the harsh operating environments. MEMS gyros have certain advantages over conventional spinning gyros which include low power consumption, small size and weight and relatively low cost due to batch fabrication ability. These sensors are well suited for applications requiring low performance such as in automotive industry and mobile devices (smartphones and smartwatches) due to their compact size and low cost fabrication [31]. These gyros are still at the development stage for high performance applications.

1.1.4 Nuclear magnetic resonance gyros

Nuclear magnetic resonance gyros (NMRGs) detect the angular rate by measuring the shift in the frequency of Larmor precession of the nuclear spin. It is well established now that nuclear spin is exhibited by many elements and it represents the total angular momentum of an atomic nucleus. Nuclear spin originates from the net quantum spin of the nucleons (protons and neutrons). Both constituents of the nucleus have a spin quantum number of 1/2. Nuclear spin is not exhibited by elements with even mass number because the quantum spin of both protons and neutrons pairs up and cancel each other. However, atoms with an odd mass number exhibit nuclear spin due to the incomplete coupling/pairing of the nucleon quantum spins**.** All such atoms can experience nuclear magnetic resonance (NMR) [32].

To understand the process of how nuclear spin is used to measure the rotation rate, starting with a cell that contains atoms with certain magnetic moments is useful. The atomic magnetic moments have no alignment in the absence of an external magnetic field (see figure 1.4(a)). However, in the presence of a constant magnetic field B_0, the atomic magnetic moments become more ordered and align themselves along the magnetic field lines, but their spin states are still misaligned as seen in figure 1.4(b). Atoms with spin states along the direction of applied magnetic field (up in the given diagram) have low ground state energy and vice versa. The difference in the ground state energies contributes to this misalignment.

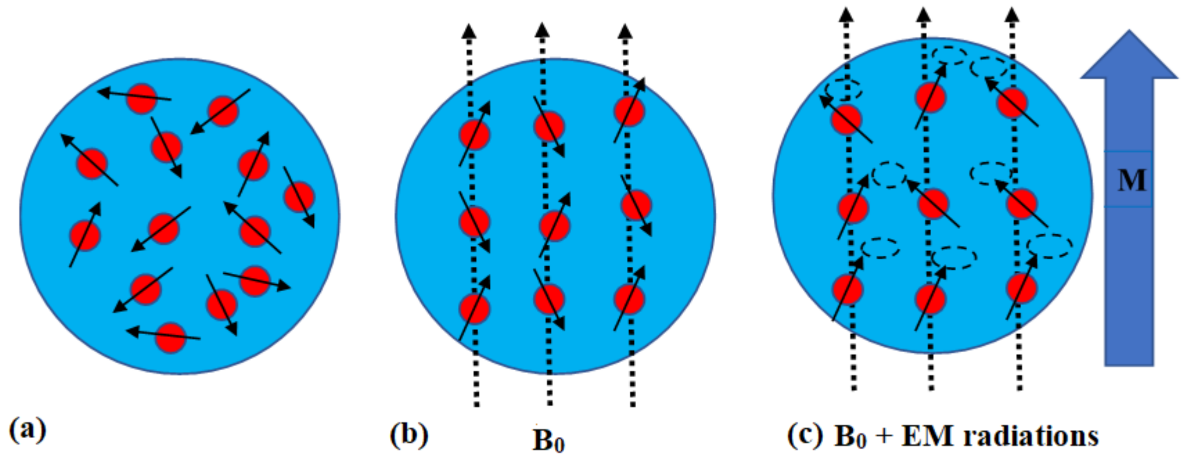

Figure 1.4: Showing the step-by-step process of NMR gyro working principle. Arrows in the figure represent the spin states. When the atoms as well as their spin states are aligned along the direction of magnetic field lines, the gas cell has higher degree of magnetic moment.

The undesired nuclear spin states are switched through optical pumping. This phenomenon can be understood by defining the spin states; setting the spin states for the ground state energies as $L = -\frac{1}{2}$ & $+\frac{1}{2}$, then upon irradiation with circularly polarized light that has a quantum spin number of +1, only atoms that have -1/2 state will absorb photons and thus switch to the other state. The L = +1/2 state cannot absorb photons as it will not conserve energy and angular momentum of the system [33]. The atoms that are absorbing photons will undergo spontaneous emission and end up in either of the spin states. This process will keep going on until the atom attain the L = +1/2 state. This is how an atomic system is polarized via optical pumping and the net magnetic moment is aligned as shown in figure 1.4(c). Even after the optical irradiation, the magnetic moments of the atoms are not perfectly aligned to the field lines due to the nuclear spin associated with them. This tiny misalignment causes the atoms to keep rotating around the magnetic field lines. Therefore, it can be concluded that the spin polarized atoms undergo precession at a certain frequency in the presence of the magnetic field. This is called the Larmor precession frequency and is represented by the following equation [34]:

$$\omega_L = yB_0 \tag{1.3}$$

Here, $\omega_L$represents the Larmor frequency, B_0 is the strength of applied magnetic field sand y is the gyromagnetic ratio.

The rotation of a cell containing spin polarized atoms causes a shift in the frequency of Larmor precession which is proportional to the rotation rate. The method used to sense the rotation rate employs a circularly polarized beam for optical pumping and a linearly polarized beam for probing. The vapor cell contains a mixture of an alkali metal atom and two noble gas isotopes.

Alkali metal atoms help to enhance the spin polarisation of the whole system by transferring their electronic spin polarisation to the noble gas isotopes through collision. The precession rate of the noble gas isotopes relative to the fluctuation in the magnetic field is deduced from the precession frequency of the alkali metal atom as its precession rate is 1000 times greater. Noble gas isotopes are selected in a way that their gyromagnetic ratios are opposite to each other and consequently precess in opposite directions. Upon gyro rotation, the precession frequency of both isotopes is combined and the resultant precession rate is independent of the rotation of the gyro due to the opposite gyromagnetic ratios and depends only on the net magnetic field. The combined frequency signal is phase locked to an external stable frequency source through feedback to the coils generating the main magnetic field. With the main magnetic field held constant relative to the external frequency source, signal from any of the noble gas isotopes is employed to measure the gyro rotation by comparing it with a second stable frequency signal from the same external frequency source. The relative phase angle between the measured noble gas isotope signal and reference signal change with a 1 to 1 correspondence as the gyro is rotated. As a result, the NMR gyro provides the absolute angle instead of rotation rate. [35].

The lack of moving parts means these gyros can be miniaturized as well as show no sensitivity to shock and vibrations. However, their performance is highly sensitive to external magnetic fields and is limited by the attainable frequency shifts due to the magnetic dipolar interactions between the spins. A lot of work has been done in the past two decades to improve their performance and an ARW of 0.002 $^{o}/h^{1/2}$ and bias stability of 0.04 ^{o}/h has been achieved [36].

1.1.5 Cold atom interferometer gyro

As suggested by the name, this type of gyro relies on the cooling of the atoms induced by monochromatic laser light. Laser cooling has been a studied phenomenon for more than two decades now. If the frequency of the laser is close to an electronic resonance of the interacting material, the atoms of the material can get trapped and loose their kinetic energy which results in the reduction of their temperatures down to the micro kelvin level [37]. The state of the trapped atoms can be modified through controlling laser pulses and allowing the atomic wavefunctions travel on an identified spatial path (path 1 & 2. See figure 1.5). These gyros are also based on the Sagnac effect and the counter propagating atomic wavefunctions accumulate phase difference under rotation. Figure 1.5 shows the basic setup of a cold atom interferometer gyro.

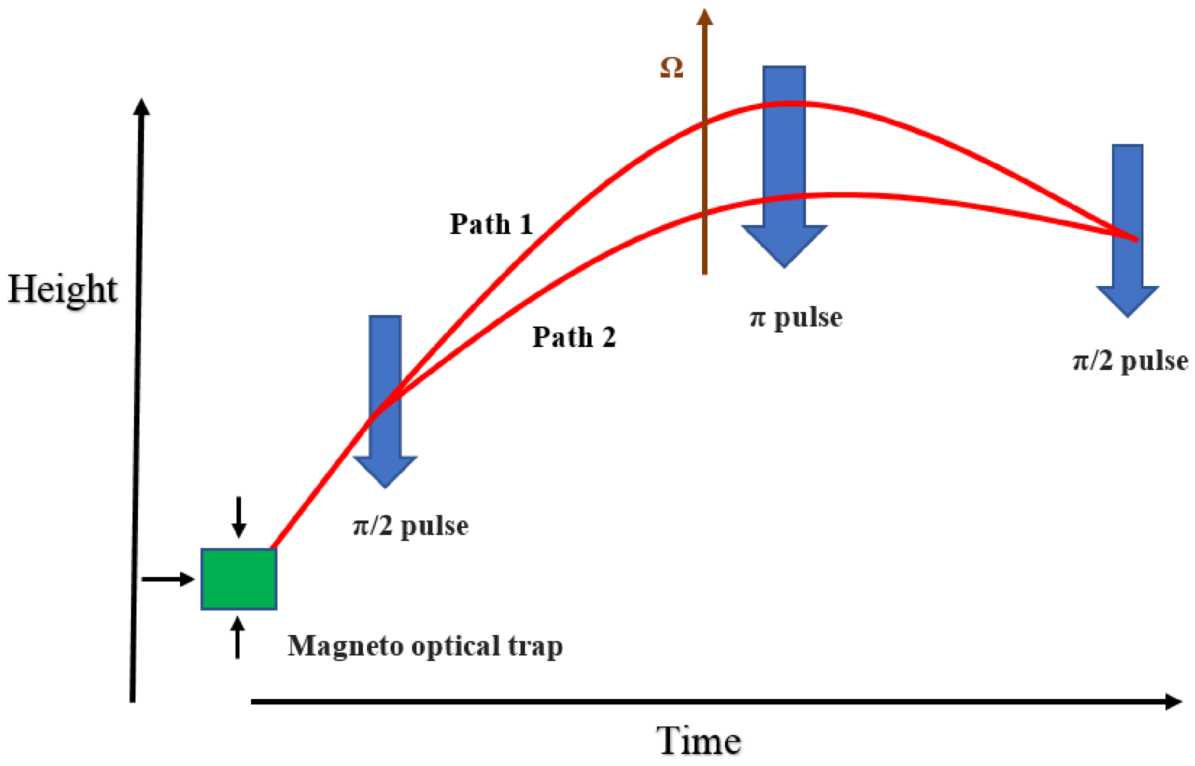

Figure 1.5: General description of a cold atom interferometer gyro setup. The cold atoms are launched to a parabolic trajectory and manipulated with the laser pulses for the gyroscopic purposes.

Before launching, the atoms are cooled down to micro kelvin level in order to reduce the interference error that could originate from the atom position error and velocity distribution. Secondly, the cooled atoms are easy to manipulate. Like an optical signal, the atomic wavefunctions can also split and interfere to form a fringe pattern. Therefore, during the travelling trajectory, atomic wavefunctions are altered with the laser pulses equivalent to beam splitters ($\pi/2$ pulses) and reflectors (π pulses) to realise an atomic interferometer [38]. When an atom having a certain quantum state interacts with the photons of a counter-propagating laser pulse, it goes to an excited state by absorbing the momentum from the pulse. The interaction with a second laser pulse results in stimulated emission and the atom comes down to the hyperfine ground state. With the change in the quantum state, the initial trajectory of the atom is changed. It is well known that the transition probability of atoms depends on the laser intensity and interaction duration. With an appropriate selection of laser intensity and duration, optical beam splitters and reflector/mirrors can be formed.

The working of an atomic interferometer for rotation sensing is shown in figure 1.6. The atoms having $|0\rangle$ quantum state enter the interferometer from the left side where they interact with an optical beam splitter formed by the counter propagating laser pulses. The beam splitter interaction with the atoms results in a quantum superposition state for each atom in a way that it can be in any of the two states ($|0\rangle$ and $|1\rangle$). Laser pulses also transfer some momentum to the wavefunction in state $|1\rangle$.

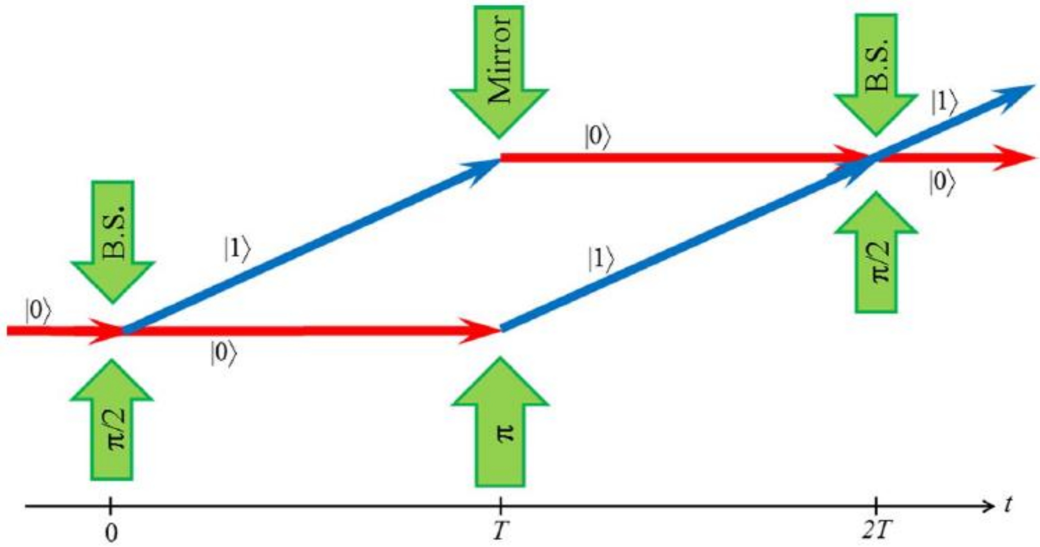

Figure 1.6: Showing the atomic interferometer which can be used for rotation sensing [39].

After a certain time interval T, the wavefunctions interact with the optical mirrors, again formed by counterpropagating laser pulses that simultaneously transfer momentum to both the wavefunctions which cause the change in their quantum states. Both the wavefunctions interfere at the second beam splitter after another time interval T. The number of atoms coming out of the interferometer in state $|0\rangle$ and $|1\rangle$ depends on their phase difference which is a function of rotation rate as well as laser phases during the interaction time [39].

In terms of theoretical sensitivity, cold atom gyros have a fundamental edge over optical gyros which arises from the fact that de Broglie wavelength is much smaller than the optical wavelength. An identical area atomic interferometer will induce a much larger phase shift for a given rotation rate as compared to an optical interferometer. However, atomic interferometers are sensitive to gravitational acceleration as well. The phase difference induced by gravitational acceleration is around 6 orders of magnitude larger than that from typical angular rate signals which results in a low signal to noise (SNR) ratio for rotation rate measurements [40]. Due to these technological limitations, these sensors are mostly used for constant/very low frequency measurements such as local gravity [41].

1.1.6 Superfluid gyro

Superfluid gyros also work on the principle of Sagnac effect and use superfluids as suggested by the name to measure the rotation rate. Superfluids are characterized as “fluids having extremely low viscosity and flow without dissipation below transition temperatures" [42] . ^{3}He (Helium 3) whose transition temperature is 10^{-3} K was used initially and later replaced by ^{4}He due to its relatively high transition temperature of 2 K and lower cost.

A quantum mechanical wavefunction $\psi = \psi_0 e^{i\Phi}$ is used to characterize a superfluid system, whose amplitude ψ_0 describes the superfluid density and complex phase Φ describes the kinematic behaviour of the system. The change in the phase is related to the fluid velocity field and is expressed by equation [43]:

$$\text{phase gradient} = \left[\frac{2\pi m}{h}\right] v \tag{1.4}$$

Here, v is the superfluid velocity field, m is the He atomic mass and h is Plank's constant.

For the rotation rate measurement, the superfluid is injected into a ring which is separated by a flow restrictor as shown in figure 1.7:

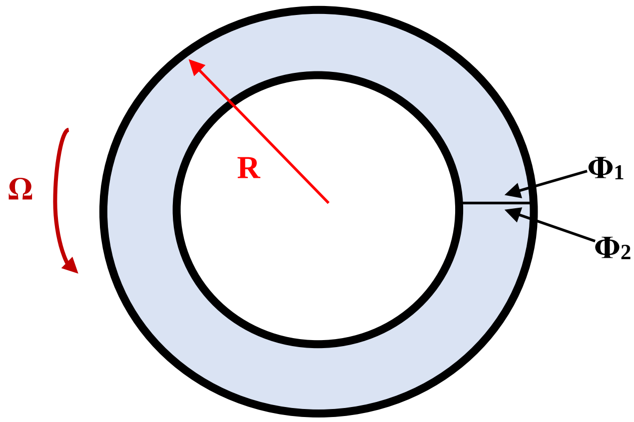

Figure 1.7: Illustrating superfluid cavity use to measure the rotation. The flow restrictor in the cavity has an orifice.

Where, R is the radius of the cavity.

In the absence of rotation, the velocity of the superfluid ground state must be zero and the phase is constant throughout the liquid as per the equation. However, when the cavity rotates, the velocity state of the superfluid is non-zero and a phase difference ($\Delta\Phi = \Phi_2 - \Phi_1$) is induced across the flow restrictor. This phase difference implies a very large fluid velocity across the flow restrictor and by measuring that velocity, rotation rate can be estimated [43]. The velocity of the fluid around the orifice is significantly higher relative to the rest of the cavity. It depends on the size of the orifice.

A diaphragm pump (shown in figure 1.8) is added to the apparatus to measure the increased velocity of the flow through the flow restrictor. The function of this pump is to provide an additional flow on top of the rotation induced flow. The magnitude of the additional flow is monitored by an extremely sensitive displacement sensor in the diaphragm. The property of superfluids to flow without friction exists up to a certain critical velocity. For example, for ^{4}He, the critical velocity through an orifice is around few a meters per second [44]. When a superfluid passing through an orifice attains critical velocity, a vortex line may be created that will cross all the streamlines of the flow while passing through the orifice causes a reduction in the flow energy and the phase difference across the orifice changes by 2л. This concept is known as phase slip and was proposed by Anderson et al. [45].

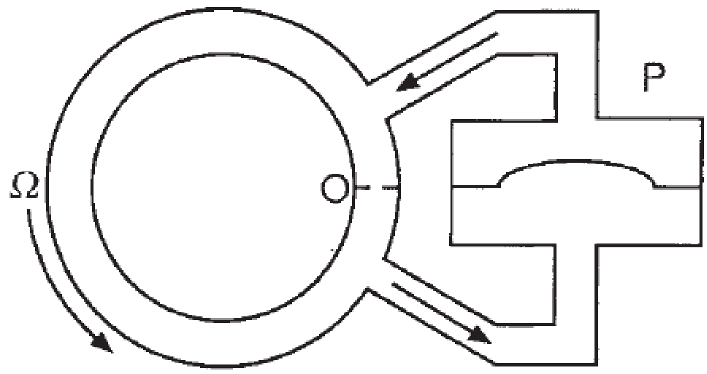

Figure 1.8: Illustrating a schematic of superfluid gyro [44].

Upon rotation of the gyro, the flow in the orifice changes and pump flow modulation is required to reach the critical velocity. This makes it possible to determine the rotation via superfluids.

Hoskinson et al. [46] achieved a resolution of 0.04 ^{o}/h from a ^{4}He superfluid gyro operating at near 2K temperature. Despite demonstrating good sensitivity, maintaining such a low operating temperature for long operations becomes a limit for most applications. Mechanical vibrations of the apparatus also degrade the gyro sensitivity by acting as another rotation input to the sensor which cannot be distinguished.

1.1.7 Optical gyroscopes

In comparison with other gyros, optical rotation rate sensors are insensitive to high-g environments, vibration and external magnetic fields, highly linear over a wide dynamic range, and do not need gimbaled mountings or vibrating elements. On top of that, they are almost maintenance free due to lack of moving parts and so have a longer lifetime. Rotation of the light beams instead of metal wheel circulation or vibrating elements results in a fast response rate in optical gyros.

The operating principle of optical gyros is the Sagnac effect discovered by a French scientist George Sagnac in 1913 [47]. He stated that when an interferometer, confining two counter propagating beams, is rotated around an axis perpendicular to the plane of the interferometer it induces a phase shift between the two counter-rotating beams which is proportional to the angular velocity. By using a partially reflective mirror and a prism; a fraction of both beams is extracted for the readout system from the interferometer, these being interfered in the prism to form a fringe pattern on a photodetector array [48]. By counting the intensity maxima in the fringe pattern the angular velocity can be calculated. The sign of the angular rate is determined by observing the movement of the fringe pattern on the surface of photodetector array which moves with the direction of the rotation [49].

Optical gyros can be classified as active or passive depending on whether the gain medium generating the light is inside or outside of the rotation sensing element, respectively. In active gyros, a ring cavity generates counter-rotating laser modes by pumping the gain medium. He-Ne ring laser gyros are the most widely used angular velocity sensor in applications requiring very high performance [17]. In passive gyroscopes an external laser source is split by a beam splitter before being coupled/injected into the sensing element (resonant ring or spiral) in both directions. For rotation rate measurement, more detection components are needed in the passive gyros as compared to the active ones. A Resonant Micro Optic Gyro and an loop gyro are examples of passive systems [50, 51] and are discussed in greater detail in chapter 2.

1.1.7.1 Sagnac Effect

The Sagnac effect induces a path length difference between the counter propagating (clockwise and counter-clockwise) beams inside the rotating element. The schematic diagram of the Sagnac effect is shown in figure 1.9.

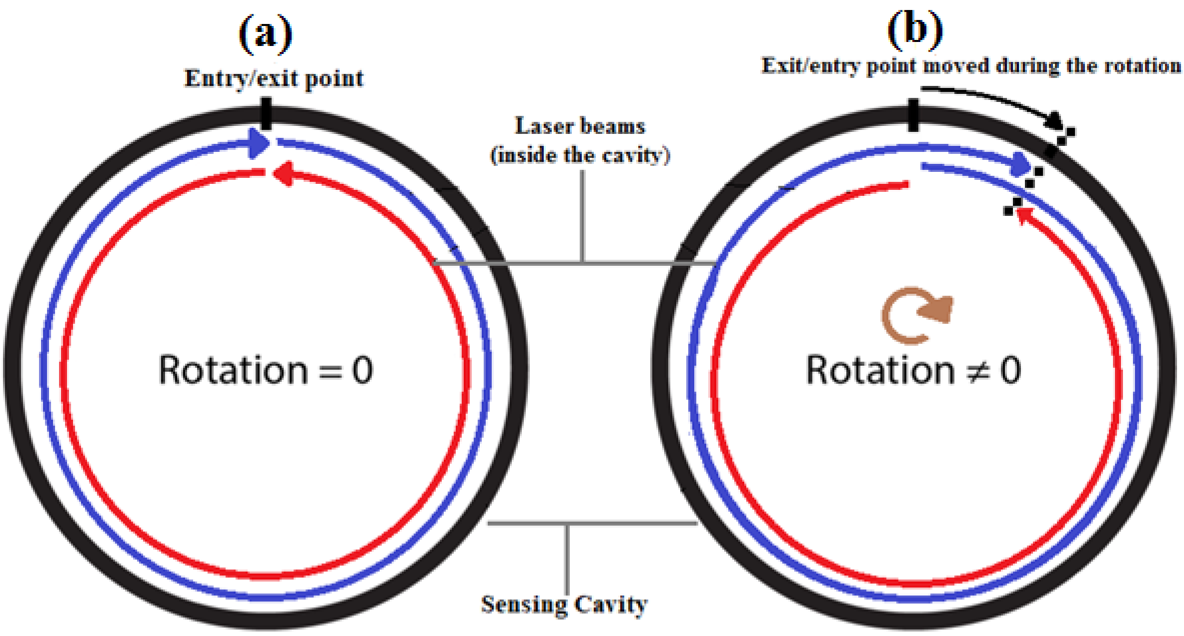

Figure 1.9: Showing optical cavities with and without rotation. When the rotation is zero, both the beams travel the same path as seen in figure 1.9(a). Whereas beams experience path length difference due to the rotation as seen in figure 1.9(b).

As mentioned earlier, the beams can be generated inside the element or can be coupled into the element. In the absence of rotation, both oppositely travelling beams cover equal distance to reach the entry/exit point as shown by figure 1.9(a). After one round trip their time (t) is represented by equation (1.5):

$$\mathbf{t} = \frac{\mathbf{2\pi R}}{\mathbf{c}} \tag{1.5}$$

where, R is the element radius and c is the speed of light in vacuum. When the element is rotating at a certain angular velocity, the beam which is travelling along the direction of rotation covers a longer path to arrive at the entry/exit point as compared to oppositely travelling beam as shown by figure 1.9(b). Therefore, the beam in the direction of rotation takes a time to reach the output given by:

$$\mathbf{t_+ \times c = 2\pi R + \Delta s} \tag{1.6}$$

Here Δs represents the optical path length change due to the rotation along the direction of the rotation and calculated by using the arc-length formula:

$$\mathbf{\Delta s = R\Omega t_+} \tag{1.7}$$

By putting Δs into equation (1.6) it becomes:

$$\mathbf{t_+ \times c = 2\pi R + R\Omega t_+} \tag{1.8}$$

Likewise, the beam propagating against the rotation takes relatively less time to reach its starting point which is described as:

$$\mathbf{t_- \times c = 2\pi R - R\Omega t_-} \qquad (1.9)$$

Thus, the time difference between the counter propagating beams to reach their starting point upon rotation can be derived as:

$$\boldsymbol{\Delta t = t_+ - t_- = \frac{4\pi R^2\ \Omega}{c^2 - R^2\Omega^2} \approx \frac{4\pi R^2}{c^2}\Omega = \frac{4A}{c^2}\Omega} \qquad (1.10)$$

where $c^2 - R^2\Omega^2 \approx c^2$ as $c^2 \gg R^2\Omega^2$ for any reasonable values of R and Ω. A represents the area enclosed by the sensing element presuming it is circular. The path length difference can thus be calculated as:

$$\mathbf{\Delta L = c\Delta t = \frac{4A}{c}\Omega} \qquad (1.11)$$

It can be seen in equation (1.11), the path length difference between the CW and CCW beams inside the rotating element is proportional to the angular velocity. However, the magnitude of the differential path length/time delays are extremely small for devices compatible with chip scale integration. For instance, with a circular cavity of 15mm diameter, an angular velocity of 1 °/h results in a path length difference of 4.5×10^{-17} m (about one tenth the diameter of a proton) and corresponding time difference of 2×10^{-23} sec. These values are small enough that a direct measurement of the delay cannot realistically be used for practical measurements. However, their relative shift in phase (in the case of interferometer/loop) or frequency (in case of a resonator) is significantly larger. Therefore, the frequency shift or phase shift between the CW and CCW beams is generally used to measure the rotation rate. For an interferometric optical gyro, the Sagnac phase shift is calculated as:

$$\mathbf{\Delta\Phi = \omega\Delta t} \qquad (1.12)$$

ω is the angular frequency of the beams. Inserting equation (1.10) into (1.12) gives:

$$\mathbf{\Delta\Phi = \frac{8\pi A}{\lambda c}\Omega = \frac{4\pi NLR}{\lambda c}\Omega} \qquad (1.13)$$

Here, λ is the wavelength of the probe light, L is the cavity length and N represents the number of turns in the loop.

As can be seen in equation (1.13), the scale factor of an interferometric/loop gyro, which relates the input rotation to the output phase shift, mainly depends on the length and radius of the loop. In other words, the phase shift is dependent on the size and number of turns in the loop. For an angular velocity of 1 °/h, a cavity having a radius of 15mm induces a phase shift of 1.83×10^{-10}

degrees. To measure the frequency shift between the oppositely travelling beams, resonant cavities are used in passive gyros, and the ring laser gyro is a successful type of active gyro.

1.1.7.2 Ring Laser Gyro

A bulk optic ring laser gyro (RLG) was the first optical sensor to measure angular velocity. It is an active frequency sensitive device, where the oppositely travelling beams are generated by pumping a gain medium contained inside a ring cavity [52]. Figure 1.10 illustrates the schematic of a RLG.

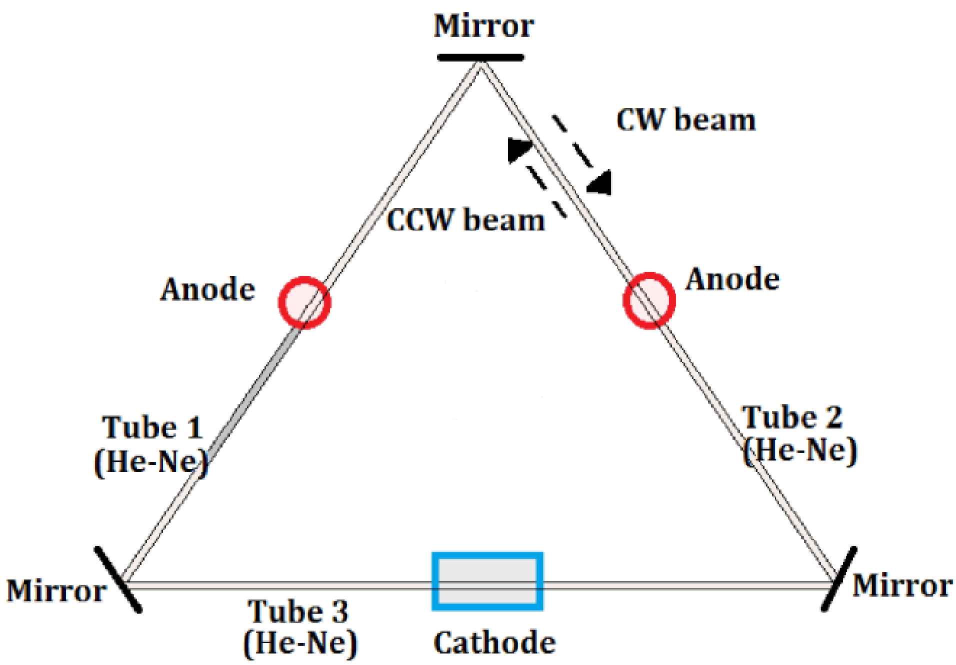

Figure 1.10: Conventional triangular symmetry of RLG [17].

Two conditions need to be satisfied for lasing: (1) the total optical loss of the cavity must be compensated by the gain of the active medium and (2) the length of the cavity must be an integer multiple of the wavelength. Condition (1) can be met by ensuring a low loss cavity and choosing an appropriate active medium and then pumping it effectively to get a sufficient gain. Condition (2) is written as [53]:

$$\mathbf{L} = \mathbf{n}\boldsymbol{\lambda} = \frac{\mathbf{nc}}{\mathbf{f}} \tag{1.14}$$

Here, n is an integer (1, 2, 3….). When the cavity is at rest, both the beams have same resonant frequency and cover identical paths. When rotating, the resonant frequencies of the two counter propagating beams change due to the unequal paths covered by them induced by the Sagnac effect. Therefore equation (1.14) is written as:

$$\mathbf{f_+} = \frac{\mathbf{nc}}{\mathbf{L_+}} \tag{1.15}$$

$$\mathbf{f_-} = \frac{\mathbf{nc}}{\mathbf{L_-}} \tag{1.16}$$

The relative shift in the resonant frequencies between the two beams is written as:

$$\mathbf{\Delta f} = \mathbf{f_+} - \mathbf{f_-} = \frac{\mathbf{\Delta L}}{\mathbf{L}}\mathbf{f} \tag{1.17}$$

Putting the value of ΔL from Eq. (1.11):

$$\mathbf{\Delta f} = \frac{\mathbf{4A}}{\boldsymbol{\lambda}\mathbf{L}}\boldsymbol{\Omega} = \frac{\mathbf{2R}}{\boldsymbol{\lambda}}\boldsymbol{\Omega} \tag{1.18}$$

This is called the beat frequency. Due to resonant nature of the cavity, the beat frequency only depends on the radius/size of the cavity and is independent of the length of the cavity. With the same cavity radius (15mm) and rotation rate (1 ^{o}/h) mentioned above, a beat frequency of 0.093 Hz is induced. Whilst low, this is feasible to measure directly, though this is not the usual readout method. This shows that the beat frequency measurement is relatively more sensitive than the phase shift measurement. Based on the gain medium used inside the cavity, RLGs are divided into two categories: (1) Gaseous RLG and (2) Solid state RLG.

1.1.7.2.1 Gaseous RLG

After the invention of the laser in the 1960's, gaseous RLGs were the first to be developed commercially and used for high-tech applications e.g. aeroplanes. The gain medium of these RLGs is a mixture of Helium and Neon gases, hence they are called He-Ne RLGs [54]. This type of gyro has two geometries (square and triangular) and the resonator cavity is usually made of a material called Zerodur [55, 56]. This material has a low diffusion coefficient for He and Ne gases as well as a very low thermal expansion coefficient. At each corner of the tube, a highly polished and reflective mirror (to minimize the backscattering from the surface) is used for directing the beams along the closed cavity path. The RLG is a very sensitive device and capable of measuring the rotation rate with a resolution of less than 1 ^{o}/h [57] and a bias drift of 0.01 ^{o}/h [58].

At a rotation rate lower than a certain critical value, the beat frequency between the CW and CCW beams is suppressed due to mutual coupling between them. This coupling arises from backscatter effects that injection-lock the laser modes due to the gain in the cavity, this being termed the Lock-in effect [59] and it severely limits the sensitivity of the gyro. The Lock-in effect occurs primarily due to the backscattering of the light from the mirrors inside the cavity. This is the dominant mechanism in He-Ne gyros. Backscattering can only be reduced by improving the mirror fabrication (both surface roughness and coating quality), this however makes them much more expensive and the devices are already close to the state of the art. The most widely used method to get rid of the Lock-in effect is mechanical dithering [60, 61]. In this method, the gyroscope is mounted on a dither motor which rotates back and forth at an accurately known rate. It acts to keep the gyro beyond the dead band zone and the dither signal can be removed from the output electronically. Dithering makes the whole packing heavier, larger and produces higher power consumption.

A lifetime limiting issue in RLGs is helium out-diffusion from the tube. Helium, being a small atom, diffuses out of the lasing cavity through the seals or glass body and needs to be refilled after a certain amount of time. Despite of having limitations such as Lock-in effect, lifetime, high power requirements, large cavity size and high cost, RLGs have emerged as suitable angular velocity sensors for high grade applications [17] and have attained a published resolution of 0.15×10^{-3} ^{o}/h [48]. Due to the military applications for high precision gyros, it is extremely difficult to determine the highest sensitivity ever attained.

Because of the gaseous gain medium and the size, this type of gyro cannot be used for integrated applications. However, the gaseous gain medium can be replaced with a semiconductor or rare earth gain medium to achieve longer lifetime and minimize the overall size, cost and power consumption.

1.1.7.2.2 Solid state RLG

Semiconductor RLGs (SRLGs) have been proposed in different geometries such as circular, racetrack, square and triangular. However, circular and racetrack geometries have been used extensively for their ease of fabrication and lower bending losses. Generally, AlGaAs or InGaAsP are used as semiconductor gain medium due to their superior lattice matching properties and operation in the most widely used 1550nm wavelength range.

As mentioned earlier, coupling between the counter propagating beams severely limits the gyro sensitivity. In SRL gyros, the presence of counterpropagating beams of different resonant frequencies inside the semiconductor gain medium (i.e. rotation) results in the formation of a spatial population inversion grating due to the increased carrier depletion from higher intensity nodes in the summed intensity. This also leads to the formation of a refractive index grating as index depends on the charge carrier density. This index grating reflects/backscatters the counterpropagating beams which results in a non-linear coupling between them. This type of coupling is totally different compared to the one that occurs due to the back reflection from the mirrors or scattering from the sidewall roughness, and rather more serious. As a consequence of this non-linear coupling, the phase and field distribution of the beams inside the ring laser get spatially and temporally modulated. If the modulation frequency is less than the inter-band carrier relaxation time (typically ~1ns), gain medium parameters also get modulated. Sidebands are produced as a result of this modulation and exchange energies causing the suppression of the beat signal [62].

The replacement of the gaseous gain medium with a solid state one allows the fabrication of a complete single chip gyro system, but the performance is badly degraded by the numerous nonlinearities (homogeneous gain saturation, spatial hole burning effect and carrier induced index change) present in semiconductor gain media. Arpit et al. [63] calculated the sensitivity SRLGs and found them to be no better than 120 °/h and with a lock-in threshold of 10^8 °/h [62], which overshadows the beat frequency detection issues. Their analysis is consistent with experimental values (10^9 °/h) observed by Peter et al. [64]. Therefore, the viability of the semiconductor gain media is yet to be proven.

Cao et al. [65] reported a novel way of measuring the beat frequency without having lock-in issues for SRLG. An optoelectronic Integrated Circuit (OEIC) containing two optically independent SRLs, directional couplers, waveguides, and Y-junction couplers are fabricated as seen in figure 1.11. Both the lasers are coupled with spirals inside and outside for R1 and R2 respectively. These asymmetric spirals supposedly made lasing in one direction (counter-clockwise for R1 and clockwise for R2) more favourable under certain drive conditions.

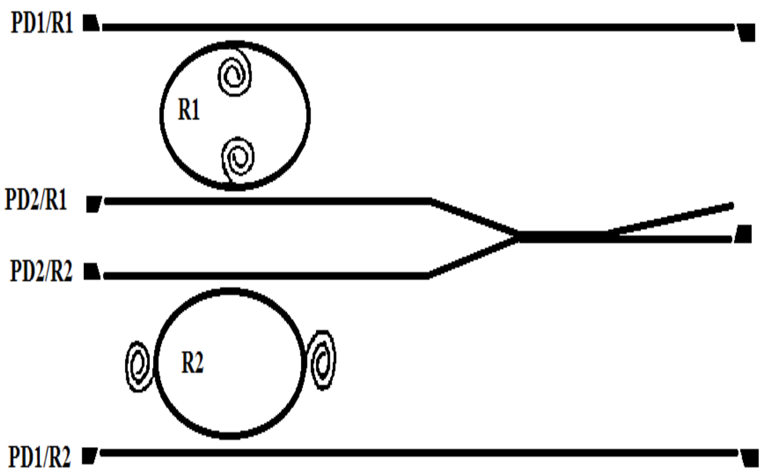

Figure 1.11: Showing redrawn block diagram of two semiconductor ring lasers which can potentially avoid lock-in effect [65].

From figure 1.11, PD1 and PD2 are the detectors for CW and CCW travelling beams in the rings. The output of the counter propagating lasers was combined in a directional coupler prior to detection. A resistive heater was incorporated to thermally control the laser wavelengths to enable the zero rotation rate beat frequency to be tuned for heterodyne detection or nulled for baseband detection. The frequency difference between the counter propagating beams was measured as a function of the tuning current and data from Cao et al. is replotted in figure 1.12.

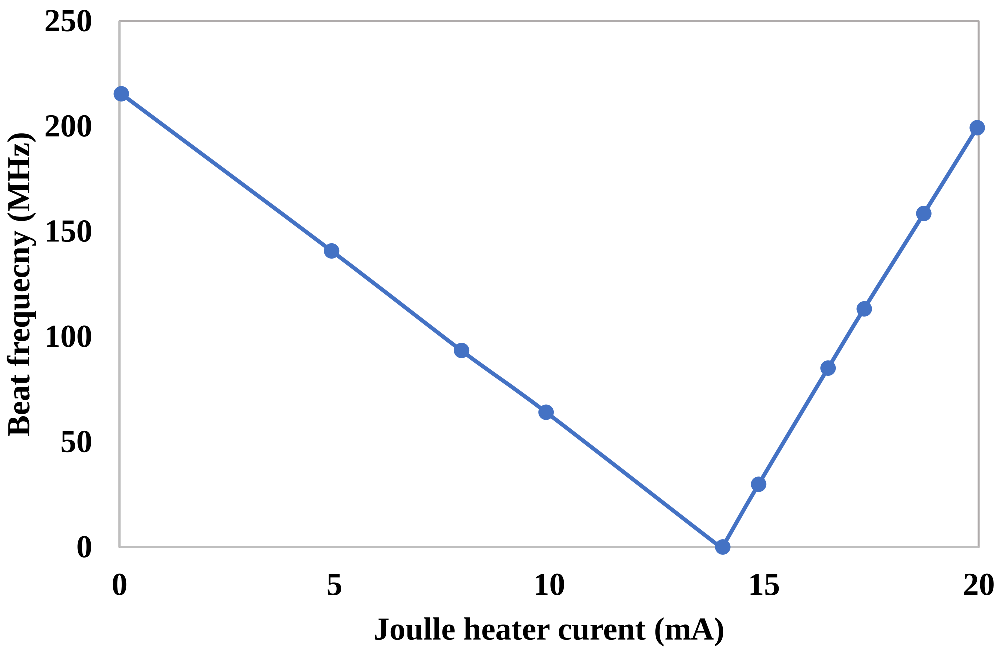

Figure 1.12: Exhibiting the redrawn graph of the beat frequency dependence on heating current [65].

As can be seen in figure 1.12, at 14 mA of heating current, the beat frequency passed through zero and showed no sign of lock-in effects which makes this configuration a suitable option for RLGs. However, the tuning slope is approximately 15 MHz/mA, so very small amounts of current noise leads to large frequency deviations. The beat frequency vs rotation rate for a ring resonator having diameter of 30mm was calculated by using equation (1.18) and can be seen in figure 1.13:

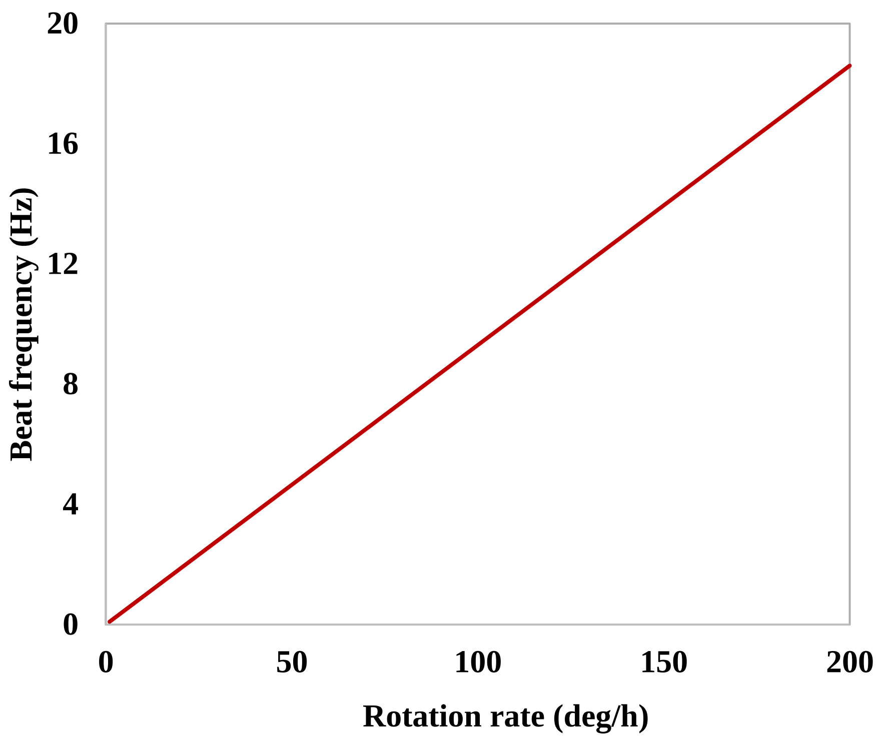

Figure 1.13: Depicting beat frequency vs rotation rate theoretically calculated for ring resonator of 30mm in diameter.

For a rotation rate of 1 ^{o}/h, beat frequency of 0.093 Hz is found, so the frequency tuning sensitivity in this device is a major challenge as femto amp current stability/noise is required.

Replacing the semiconductor gain medium with rare earth doped materials was another option to materialize integrated RLG's. However, it also doesn't help to realize a sensor which can be used for high performance applications, again due to a large lock-in effect. Nonlinearities associated with solid state gain media restrict this realization. Ideal operation of an Er doped RLG depends on single longitudinal modal propagation in both directions with equal intensities. But practically, it is affected by the spatial hole burning present in the gain media which results the formation of multiple longitudinal modes and strong coupling between CW and CCW beams due to the scattering from the gain grating. This coupling leads to strong mode competition and lock-in phenomena [66, 67]

Therefore, it can be concluded that active RLGs are not suitable for integration because whilst gaseous RLGs are very effective, they are not solid-state devices. On the other hand, solid state RLGs gyros meet the requirements of an integratable device, but their sensitivity is badly affected by the lock-in effect. Passive optical gyros seem to be the only choice which can be realized/used as an integrated option. Fibre optic gyros are the most successful type of passive optical gyros.

1.1.7.3 Fibre Optic Gyroscope

A Fibre Optic Gyro (FOG) is a passive optical gyro meaning an external laser source is used to measure the angular velocity and has two implementations: (1) Interferometric Fibre Optic Gyro and (2) Resonant Fibre Optic Gyro.

1.1.7.3.1 Interferometric Fibre Optic Gyro

In Interferometric Fibre Optic Gyros (IFOGs), the phase difference between the oppositely travelling beams inside a fibre loop is used to measure the angular velocity (phase-sensitive sensor) [68]. The basic architecture of an IFOG is shown in figure 1.14:

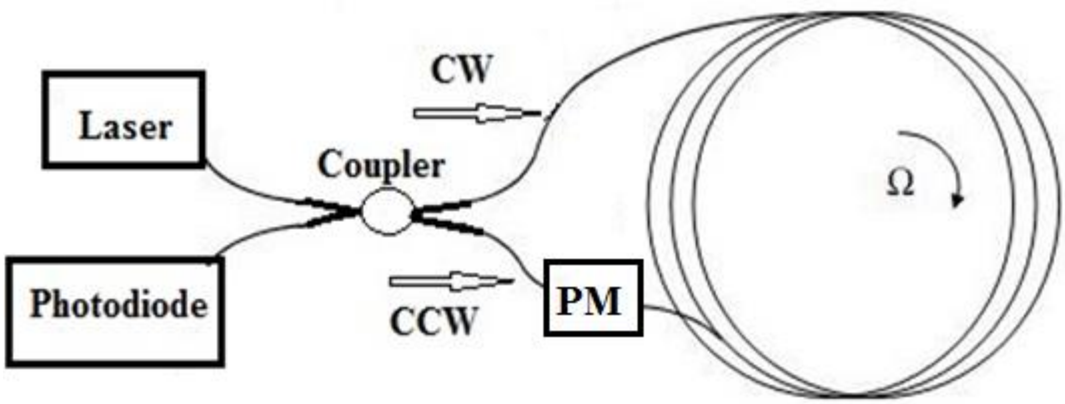

Figure 1.14: Typical configuration of an open loop IFOG.

Here, PM represents phase modulator.

A fibre coupler is used to couple the light in and out of the fibre coil. A photodetector captures the output light and converts it into a measurable electrical signal (the detection scheme/mechanism of a loop gyro is explained in the next chapter). As seen in equation (1.13), sensitivity of this device strongly depends on the length and radius of the fibre loop because the phase shift keeps accumulating as beams travel further through the fibre. Therefore, Kilometres of fibre is typically used to increase the length and diameter of the loop.

The performance of IFOG has been significantly improved with the development of ultra-low loss and speciality fibres (polarisation maintaining fibres) as well as sophisticated integrated optical components (phase modulator and coupler) [69]. A resolution of less than 0.1 ^{o}/h and bias stability of less than 0.01 ^{o}/h has been achieved by IFOG and reported in the literature [57, 70].

On the other side, IFOG sensitivity is limited by a number of undesired error sources [71-73]. Fibre cable encounters time dependent variations in reciprocity due to temperature, stress, shock or vibration. Thermally induced non-reciprocity arises due to the presence of time varying thermal gradients in the fibre loop. When counter-propagating beams traverse a loop having a time dependent thermal gradient, a non-reciprocal phase shift is induced because the beams experience different propagation constant along the loop [74].

Shock and vibration can also mechanically degrade the fibre with time [75]. However, these non-linear noise sources can be minimised by isolating the fibre loop from disturbances with the help of special coil winding methods and cautious thermal design [76-79]. This type of gyro cannot be used in compact applications due to the use of kilometre long fibres as the sensing element which cannot be integrated or miniaturised to a similar degree.

1.1.7.3.2 Resonant Fibre Optic Gyro

The Resonant Fibre Optic Gyro (RFOG) is also a passive sensor, in which rotation induced shifts in the resonant frequencies of an optical cavity between the counter propagating beams is used to measure the rotation rate [80]. A typical configuration of RFOG is seen in figure 1.15.

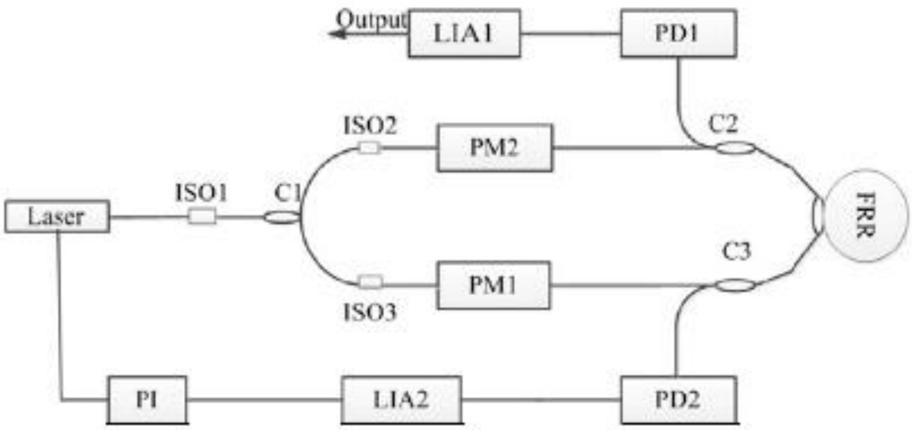

Figure 1.15: Schematic diagram of fibre resonator based optical gyro [81].

The abbreviations shown in the figure 1.15 are:

ISO = Isolator, C = Coupler, PM = Phase modulator, FRR = Fibre ring resonator, PD = Photodiode, LIA = Lock-in amplifier, PI = Proportional integrator

To measure the shift in the resonant frequencies, light from an external laser source is split and launched into the fibre resonator in CW and CCW directions. The laser source should be linearly polarized, highly coherent and thermally stable. To avoid the lock-in effect, each beam is phase modulated at a different frequency before entering the resonator. Two photo detectors are used to detect the CW and CCW beams coming out of the resonator. A feedback loop is used to lock the laser frequency in one propagation direction meaning the laser frequency is locked to the resonant frequency of one direction. The synchronous demodulation of the detected signal of the other direction then gives the resonant frequency difference (Sagnac frequency).

The fundamental edge of this device over an IFOG is the significant reduction in the fibre length which results in a much smaller device. Rather more signal processing components are however required to measure the angular rate and all of these components add extra noise in the output. Despite having a shorter length cavity, this type of gyros also cannot be used for miniaturized application due to their large cavity radius to avoid bending loss. However, waveguide resonators can be fabricated with relatively smaller radii and seem a viable option for integrated gyros.

1.2 Gyro Comparison for Modern Applications

The first gyro employed for the navigation purposes was a mechanical gyro which was found to be a reliable rotation rate sensor and served for number of years in civil and military applications. However, due to their bulky gimbled structure and rotating parts, these gyros do not match the requirements of size, weight and power consumption imposed by rapidly evolving modern applications. Their sensitivity to high-g environments as well as external vibration were other factors which encouraged the search for alternatives.

With advancements in microfabrication technology, compact mechanical Coriolis effect gyros using Micro-Electro Mechanical Systems (MEMS) came into the market and became known as MEMS gyros. These sensors meet the size, weight and power consumption demands for many current applications and are widely used in low performance requirement applications. Due to their mechanical structures, these gyros are sensitive to harsh environmental fluctuations and are still under development for advanced applications.

After the invention of the laser, RLGs and FOGs emerged and were found to be suitable sensors for applications requiring high performance. In comparison with mechanical gyros, optical gyros are insensitive to high-g environments and vibrations, highly linear over a wide dynamic range and eliminate the need for gimbaled mounting or vibrating elements. On top of that, they are almost maintenance free due to no moving parts. Rotation of the light beams instead of metal wheel circulation results a fast response rate in optical gyros At the same time, current RLGs and FOGs are quite large in size and expensive to manufacture. Therefore, multiple optical gyro configurations are studied to find an integrateable option that meets the performance demands as well as size, weight and power consumption requirements. Waveguide type passive optical gyro and stimulated Brillouin ring laser gyro are found to meet the requirements of miniaturized applications. Both options also offer the monolithic integration of different gyros components which makes them more compact, robust and reliable (Whilst both options address the problem under study, SBS gyros emerged recently after the decision was made to pursue resonant devices).

The achievable performance from the above mentioned gyro types are summarized in table 1.1. The best reported performance of waveguide type passive optical gyro [82] is significantly below the other options and needs to be improved in order to be used in any application.

Table 1.1: Showing different type of gyros along with their state of the art performances [20, 34, 36, 43, 46, 57, 58, 83-91].

Gyroscope	Resolution (°/h)	Bias stability (°/h)	ARW (°/h$^{1/2}$)	Fundamental limit
Mechanical gyro	—	0.016	—	—
MEMS gyro	20	0.8	0.09	Thermal noise
NMR gyro	0.01–0.1	0.01	0.001	Shot noise
Cold atom gyro	0.0001	0.00006	—	Shot noise
Superfluid gyro	0.04	—	—	Thermal and mechanical noise
He-Ne RLG	0.15	0.01	0.001	Shot noise
FOG	< 0.1	< 0.01	0.0001	Shot noise
SBS gyro	22	3.6	0.068	—
Waveguide type passive optical gyro	900	38	8.52	Shot noise

The motivation of this thesis is to review gyro architecture to find the best option for miniaturised and high-performance applications and progress hybrid integrateable realisation of this such that a true single chip gyro can be realised. Waveguide type passive optical gyros meet the demand of cost, size, weight and power consumption but their below par performance can be improved by choosing the right type and structure (explained in detail in the next chapter) as well as improving the optical loss of the sensing cavity. Furthermore, the progress on fabrication of a low loss CMOS compatible cavity is also reported in chapter 3 and 4.

1.3 Integrated Optics

In 1960, the development of a stable coherent light source (laser) enabled the possibility of transmission and processing of signals optically instead of electrically. Early experimentation used bulk optical components that are sensitive to vibration and temperature changes, require precision mechanical alignment, and occupy significant space. The emergence of the electronic integrated circuit and the limitations described above led to the first proposals for integrated optics in the mid-1960s. Advances in materials and microfabrication techniques over the next 30 years enabled integrated optics to move out of the laboratory and it is now being employed in number of fields such as telecommunications, IT, astronomy, medical science and consumer electronics etc [92].

Optical integrated circuits employ thin film waveguides to confine and transmit the light. Waveguides work on the same principle as optical fibres do. Light is confined and transmitted by a high refractive index material surrounded by low index material called core and cladding, respectively. The propagation loss mainly depends on the waveguide material and its dimensions as well as side sidewall roughness. Waveguides are used to fabricate and connect active (laser sources, amplifiers, modulators etc..) and passive (couplers, beam splitters and filters etc..) optical components fabricated on the chip [93]. Active optical components need external fields such as optical, electric or thermal to perform their functionalities. Whereas passive components are defined as which have fixed input/output characteristics.

The integration of different optical components on the same chip makes the optical system much more compact and stable. There are numerous special features of an integrated optical device and the more important are discussed briefly below [94]:

Faster operation: Low capacitance due to small size electrodes used in integrated photonic devices allows fast switching speed, high modulation bandwidth, and fast detection.

Miniaturized and lightweight: The small dimensions of the waveguides (typically in the micron range and below) and tight bending capability allow the integration of numerous optical components with an area of few centimetres square make the optical device compact and lightweight.

Low cost: The fabrication techniques used in the semiconductor industry are employed to manufacture integrated optical devices at the wafer scale and such parallel manufacture allows low cost mass production.

Stable alignment: Typical optical components in a system need to be precision aligned and this alignment often drifts over the long term. However, this problem can be completely avoided with the integrated optical device as once the device is fabricated, it is completely aligned and stable.

Environmental stability: Integrated photonics decreases the sensitivity to environmental conditions as circuits are built on a robust solid-state platform which minimizes the deviations between the adjacent optical components.

Multifunctional system on a chip capability: With the advancement in the fabrication technology, a large number of optical devices such as couplers, beam splitters, resonators, interferometers etc can be realized on the same chip and they provide stable phase relationships between input/output because all the functions are being performed on the same platform.

For decades now, gyroscopes have been used in a wide range of applications which include civil and military aeroplanes, missiles, satellites, drones, space shuttles etc. As many of these applications move to more compact platforms (e.g. cube sats, drones, etc), interest in improving robustness, reliability, overall size, weight, cost and power consumption with minimal sacrifice of sensitivity has accelerated.

MEMS technology has been developed to a level where miniaturized gyros are being fabricated but their performance is still not compatible with the given applications. Whereas optical gyros (He-Ne RLG and FOG) provide excellent performance, they are bulky in size which makes them unsuitable. A gyro which is small in size weight, cost and power consumption as well as provides moderate performance can be realized by scaling down the conventional optical gyros through integrated optical technology [95]. Integrated gyros can be fabricated by two methods, (1) monolithic integration where all the components of the gyro are fabricated on the same substrate/platform and (2) hybrid integration where multiple substrates/platforms are used to obtain optimized performance of each required component.

To realise a fully integrated optical gyro, several active and passive optical components need to be fabricated on a chip including:

- Narrow linewidth laser source (< 100 kHz)
- Couplers (Minimal imbalance)
- Phase modulators and/or frequency shifters (10 kHz – 10 MHz)
- Ultra low loss ring resonator or spiral (< 0.05 dB/cm)
- Photodetection system (1 GHz)
- Electronic readout system

Monolithic integration approach can provide more compact and robust optical devices. However, using a single material system, the fabrication as well as integration of multiple optical functionalities with optimized performances is still underdeveloped. For example, indium phosphide (InP) is a material which has demonstrated impressive level of monolithic device fabrication. However, its high propagation loss is unsuitable to fabricate monolithically integrated gyro for high tech applications. On the other hand, in passive platforms which generally provide ultra low propagation loss, it is extremely difficult to directly obtain electrically pumped laser sources. Silicon based photonic devices for example are still powered by external lasers or by adding other laser technology.

For realising multifunction photonic integrated circuits, hybrid integration has become a preferred option. The advantage of this approach is that the optimised performance of the active and passive components is obtained by using different materials systems. For example, for hybrid integrated external cavity diode lasers, the gain medium and resonator are separately fabricated which allows independent optimisation of both the components and ultimately better reliability. Multiple options exist for coupling between technologies. Diodes can be integrated by flip chip based butt coupling or evanescent integration. Different material layers can be connected through compact and low loss vertical tapers [96]. In this technique, the effective index of the propagating mode is gradually varied, so that high coupling efficiency can be achieved [97].

A large number of materials (semiconductors and dielectrics) have been and are being used to realise optical devices and those materials include silicon, silica, indium phosphide, gallium arsenide, silicon oxynitride, silicon nitride, tantalum pentoxide, and Germanium doped silica etc [98]. All of them have their own pros and cons.

For the fabrication of narrow linewidth lasers, III-V semiconductors (InP & GaAs) and their alloys are usually employed because of their tiny sizes, high efficiency and direct electrical pumping. Since laser diodes can be made on InP substrate directly, it would be extremely beneficial to fabricate other photonic devices on the same platform. However, the challenge is how to make InP based passive devices (optical waveguides, couplers and interferometers) matching the demanding requirements for gyros. A lot of work has been reported on the integration of active and passive components on the InP platform through different methods which include offset quantum-well waveguides, butt-joint regrowth and selective area growth [99]. In 2012, Infinera reported the first photonic integrated chip based on InP substrate where more than 450 devices were integrated [100]. However, due to low optical isolation, photonic circuits on a chip cannot scale down to the level of electronic circuits. On top of that the processes to fabricate integrated photonic circuits on InP platform are relatively complex requiring multiple epitaxial growth steps. Because of this monolithically integrated InP chips are relatively expensive. To tackle this issue, hybrid integration approach is widely being employed where the active devices are fabricated on the InP platform and passive components are fabricated on other materials such as silica and silicon nitride etc. A number of narrow linewidth laser's and efficient photodetectors and other functionalities have been manufactured through hybrid integration of InP and passive materials and reported in the literature. e.g. [101-105]. InP cannot be used for the fabrication of low loss sensing cavity because of its relatively high propagation loss, a best reported result of 0.45 dB/cm [106] meanings other low loss materials need to be considered. However all other elements of the gyro could be integrated in InP and the sensing element hybridised on potentially making InP a leading contender for the base platform. Cost is a serious issue however as InP is typically processed on 100mm or less diameter wafers and if 30mm diameter sensing elements are required that is very few chips from a very expensive wafer. CMOS on InP is also not possible meaning a multichip module approach would be required to add the electronic read out circuitry.

Within dielectric platforms, silicon substrate based waveguides (such as silica on silicon (SOS), silicon nitride (Si_3N_4)) as well as Ta_2O_5 waveguides are the most widely used in ultra low loss applications. The use of a silicon substrate means large wafers are possible at low cost (up to 300mm diameter) thus offering some mitigation of processing cost. All these platforms have certain advantages and disadvantages over the others.

Silicon on insulator (SOI) waveguide technology fulfils the demand of high density optical component integration. Due to the high index contrast (core = 3.48 & cladding = 1.444 at

1550nm), waveguides can be bent to extremely small radii (depending on waveguide dimensions, these waveguide can support as small as 2μm bends) enable dense integration [107]. The main edge of this material is the existing fabrication infrastructure and its compatibility with active optical components like phase modulators and detectors even though free carrier absorption leads to higher than desired optical losses. SOI is transparent in the near IR region ranging from 1.1μm to 3.7μm and exhibits typical optical losses of 0.1 to 2 dB/cm [108, 109]. Despite offering high density integration, high propagation loss hinders its usage in applications requiring extremely low losses such as gyros. Further, its optical nonlinearity and very small mode area could also be a hindrance in cavity based devices. One other factor that has to be considered in a single chip implementation is back reflection into the laser source as there are no suitable on chip isolators. The high refractive index of SOI is a potential issue here that will require special attention. Lastly, it is important to point out that this platform is fully compatible with co-integration of the read out electronics as these can also be integrated in the SOI layer. Whilst the sensing element and laser source present issues, SOI is clearly a strong contender for the base platform in a hybrid architecture where the laser and sensing cavity are added using other materials.

The LPCVD Si_3N_4 platform has also been widely studied for integrated optics. The index contrast of Si_3N_4 (core = 1.994 & and silica = 1.444 at 1550nm) is smaller than SOI and therefore, minimum bending radius is relatively larger but fits within requirements for moderately dense integration [110]. However, lower index contrast relative to crystalline Si result in a low scattering loss. Another advantage of this platform is that the loosely confined mode field is less sensitive to fabrication imperfections of the waveguide which results in a higher probability of reproducing the circuit as compared to with SOI. Si_3N_4 has a wide transmission window ranging from UV to mid IR. Despite its moderately high index contrast relative to SOS; extremely low loss waveguides can be achieved. A progation loss of 0.001 dB/cm at 1550nm from thin Si_3N_4 waveguides is predicted by a loss model proposed by Bauters et al. [110] and losses in the sub dB/m region observed experimentally [111]. This platform appears to be excellent choice to realise the passive components of the gyro which include low loss sensing cavity and couplers, but its deposition temperature is around 800 ^{o}C and it also requires a high temperature (1100 ^{o}C) anneal to completely remove the hydrogen content which makes it CMOS BEOL incompatible. Thin Si_3N_4 waveguides where the mode field is loosely confined also cannot make useful phase modulators as is explained in chapter 5.

Tantalum pentoxide (Ta_2O_5) is another suitable candidate for integration with silicon based photonic devices due to the potential to deposit low loss films at <400 ^{o}C making it CMOS BEOL compatible. Another advantage of Ta_2O_5 over Si_3N_4 is the low annealing temperature required to remove the OH content from the film. Low temperature annealing processes are always desired, so materials (such as polymers) which cannot withstand high temperature can also be integrated. A propagation loss of 0.03 ± 0.01 dB/cm has been reported from thin Ta_2O_5 waveguides by Belt et al. [112]. This material is a perfect candidate for the given application due to its ultra low loss capability and CMOS compatibility. Because of the thin waveguide geometry reported by Belt et al., it also cannot be employed for modulation purposes.

Germanium doped silica (Ge:SiO_2), also known as silica on silicon (SOS) is another extensively used optical material due to its low propagation loss in the visible and infrared range, highly efficient coupling to optical fibre, and high photosensitivity to ultra-violet (UV) light enabling photo tuning of devices or the inscription of Bragg gratings. A key point here is the index contrast. SOS waveguides have been fabricated with contrasts from ~0.5% up to 5%. As the contrast increases, so to do the sidewall scattering loss. However the radiative loss in waveguide bends decreases meaning higher contrast can be bent more sharply increasing integration density. Thus there is a trade off between propagation loss and integration density. Dumais et al. [113] and Bellman et al. [114] extensively studied Ge:SiO_2 waveguides with a range of index contrast. Dumais reported a propagation loss of 0.02-0.04 dB/cm from 3.8% index contrast Ge:SiO_2 waveguide for a bend radius of 1mm. Whereas Bellman achieved a propagation loss of 0.086 dB/cm from 3.5% Δ waveguide for a bend radius of 0.57mm. Bellman reported the insertion loss vs bend radius from 0.75% to 4% index contrast.

Whilst very good losses are possible with acceptable bend radii and SOS offers excellent passive functionality, active devices are an issue. Even though waveguide lasers can be realised by rare earth doping, a Flip Chip pump laser diode is still required (has been demonstrated), and there are currently no commercially viable high speed modulation or detection methods for SOS, though the potential for poling and 2-D materials in these areas is a future possibility. Finally, the most common implementation of this platform needs to be annealed at high temperature (>1000 ^{o}C) to remove the hydrogen content and consolidate the glass in some cases which makes it CMOS BEOL incompatible. Other less common approaches can however avoid this.

Given the brief description of all the platforms, fully integrated optical gyros absolutely require hybrid integration. There are several potential ways forward.

1) The fabrication of laser, couplers, modulators and photodetectors on an InP substrate, with the ultra low loss sensing cavity and electronic readout system hybrid integrated using perhaps Ta_2O_5 and silicon, respectively. The drawback of this approach is high cost, especially for larger sensor diameters as previously noted.

2) Use SOI for the modulators, couplers, and detectors and hybridise the low loss ring with Si_3N_4 or Ta_2O_5 and the laser via direct flip chip, or use a rare earth doped glass with flipped chip pump diode [115]. This scheme offers integration of the electronics on chip butt mandates the use of CMOS BEOL compatible processing. Large wafer sizes are however possible, and cost will be moderate with industry benchmarks for wafer processed SOI material being around the 5-10 c/mm^2 level meaning raw SOI chip cost for a 30mm sensor is around US$100 before hybrid elements.

3) Further development of hybridisation onto the SOS platform should make a fully integrated approach possible. Deposition techniques for low loss germanosilicate that are CMOS BEOL compatible have been demonstrated but are not mainstream, Flip chip mounting of semiconductor laser diodes is an established technology for SOS, and adding modulators and detectors on chip should be feasible at a suitable price point. The most straightforward approach is to flip chip mount InP photodiodes which is possible with currently available methods though a wafer scale approach would be preferable. Modulators based on thermo-optic approaches are analysed later in this thesis, and other options include poling (can accept high operating voltages as frequencies do not exceed a few MHz), hybridising on electro-optic polymers or thin film Lithium Niobate technology. The low refractive index of the germanosilicate is a significant advantage here in terms of easily implementing vertical coupling architectures, which for example, makes adding an ultra-low loss Ta_2O_5 sensor element straightforward.

Consequently, this thesis is mostly focussed on identifying a single chip gyro architecture that can be integrated with good performance taking into account the specific needs of a single chip platform. The sensing element is clearly a key need, and a suitable CMOS BEOL compatible approach that delivers the very low losses is a major theme of the research here.

1.4 Conclusion

In order to find a suitable angular velocity sensor for miniaturized applications such as cube satellites and drones, number of gyros based on different operating principles are studied. Optical gyros based on the Sagnac effect seem to be the most reasonable option. For active systems, gaseous RLGs are limited by the lock-in effect and mechanical dithering is needed to use them which makes the whole system bigger, heavier and more power consuming. Solid state RLGs (especially semiconductor) are even more severely limited by the lock-in effect due to numerous non-linearities present in the gain medium. Therefore, passive optical gyros appear to be the most viable option for high tech applications. The performance comparison of different types and structures of Passive Integrated Optical Gyro (PIOG) is studied in a great detail and presented in the next chapter.

1.5 Outline of this Thesis

This work reveals the study of different types and structures of gyros in order to find out the best option for minituarized applications which provides moderate performance and suitbale for single chip planar interation. It also includes the modelling of major optical gyro components such as sensing cavity, thermo-optic phase modulator and 3dB coupler. Futhermore, the progress on the fabrication of low loss Si_3N_4 and Ta_2O_5 waveguides is also reported along with the challenges faced during the process. The rest of the thesis is arranged as follows,

Chapter 2 Comprehensivley studies the different types and structures of passive integratable optical gyros (PIOG) and proposes an optimum type and structure. The proposed device is based on the results obtained by extensive theoretical modelling and numerical calculations. The recent development on Brillouin ring laser gyro is also reported where a record best bias drift of 3.6 ^{o}/h is achieved. Commonly known peroformance limmiting effects of an optical gyro and their mitigation strategies are also discussed.

Chapter 3 starts with the introdcution of propagation of light in waveguides, Si_3N_4 waveguide design and simulation. Performace of these waveguides is also simulated by using a commerical software named R-Soft and single-mode, single-polarisation, low loss waveguides are modelled. This chapter also covers the fabrication process of Si_3N_4 waveguides which starts from LPCVD Si_3N_4 film deposition, photolithography, etching optimization and deposition of silica cladding. A high quality etching of Si_3N_4 is achieved by using a gas mixture of CHF_3 and O_2 in Inductively Coupled Plasma (ICP) machine. Lastly, the mothods to meausre the waveguide loss and experimental results are also reported. Ultra-low loss can be achieved from LPCVD Si_3N_4 but its high deposition temperature and annealing requirement restrict its usage where the hybrid integration is required. Therefore, it was decieded to use Ta_2O_5 which has similar optical properties as Si_3N_4 and can be deposited at room temperature.

Chapter 4 covers the deposition of Ta_2O_5 films and waveguide dimensions optimization. It also includes the simulation of different gyro components (3dB coupler, coupler for bus waveguide ring resonator gyro and low loss waveguides intersections to realise a waveguide loop for interferometric optical gyro) from optimized waveguide dimensions. The fabrication process of Ta_2O_5 waveguides is also reported in detail along with the loss measurement.

In chapter 5, thermo optic phase modulator, one of the important components of an optical gyroscope is modelled by using R-Soft. 3µm thick Ge:SiO_2 waveguides with a polymer cladding is used to get the large change in effective index with temperature. Different cladding indices were used to optimize the best cladding as phase shifter can be designed in different ways (i) lowest loss, (ii) shortest length or (iii) compromise between loss and length for higher phase shift. For this work, a phase modulator is designed with an insertion loss and total length of $\leq$ 0.47dB and $\leq$ 2mm respectively. By keeping the loss and length of the device constant for all cladding indices, the cladding index of 1.460 incuded highest phase shift of 8.63 radians.

Chapter 2 Comparative study of integrated optics gyroscope implementations

After exploring and realizing the drawbacks of active routes, Passive Integrated Optical Gyro (PIOG) is still a platform which could offer a fully integrated gyro. Passive IOG's can meet the demands of size, cost and power reduction and they have many advantages over active ones. Their sensitivity is not governed by the lock-in effect and hybridization of all optical components will make it a robust and reliable device. There are three types of Passive IOG's, (1) Interferometric Integrated Optical Gyro (IIOG), (ii) Resonant Integrated Optical Gyro (RIOG) and (iii) Brillouin Ring Laser Gyro (BRLG).

2.1 Interferometric Integrated Optical Gyro

Like a FOG, IIOG is a phase sensitive device in which a fiber loop is replaced with waveguide loop or spiral and the phase difference between the counterpropagating beams is used to measure the angular velocity [116]. The schematic diagram of an IIOG is shown in figure 2.1,

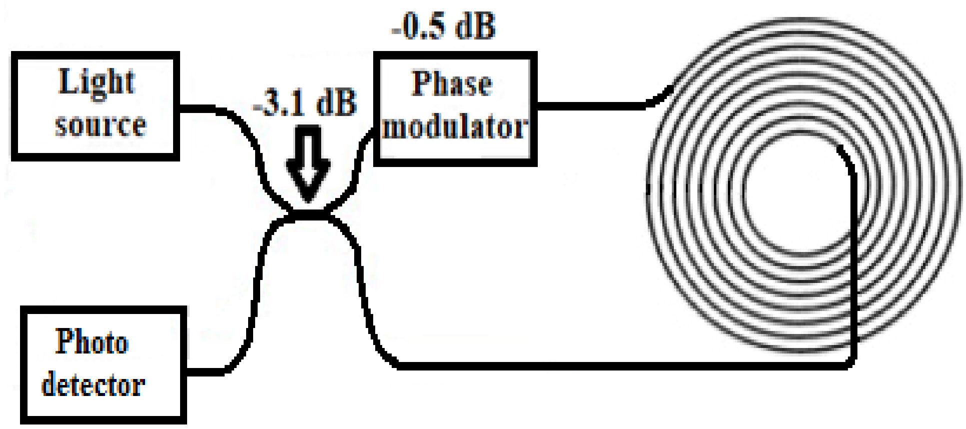

Figure 2.1: Showing open loop configuration of Interferometric integrated optical gyro.

The phase shift between CW and CCW beams is not large enough for direct measurement in practical applications even if for several turns of loops as the length is orders of magnitude smaller than FOG's. Phase difference vs rotation rate was calculated by using equation (1.13) and plotted for 13 different lengths of loop (up to 50 turns) at a diameter of 30mm and shown in figure 2.2,

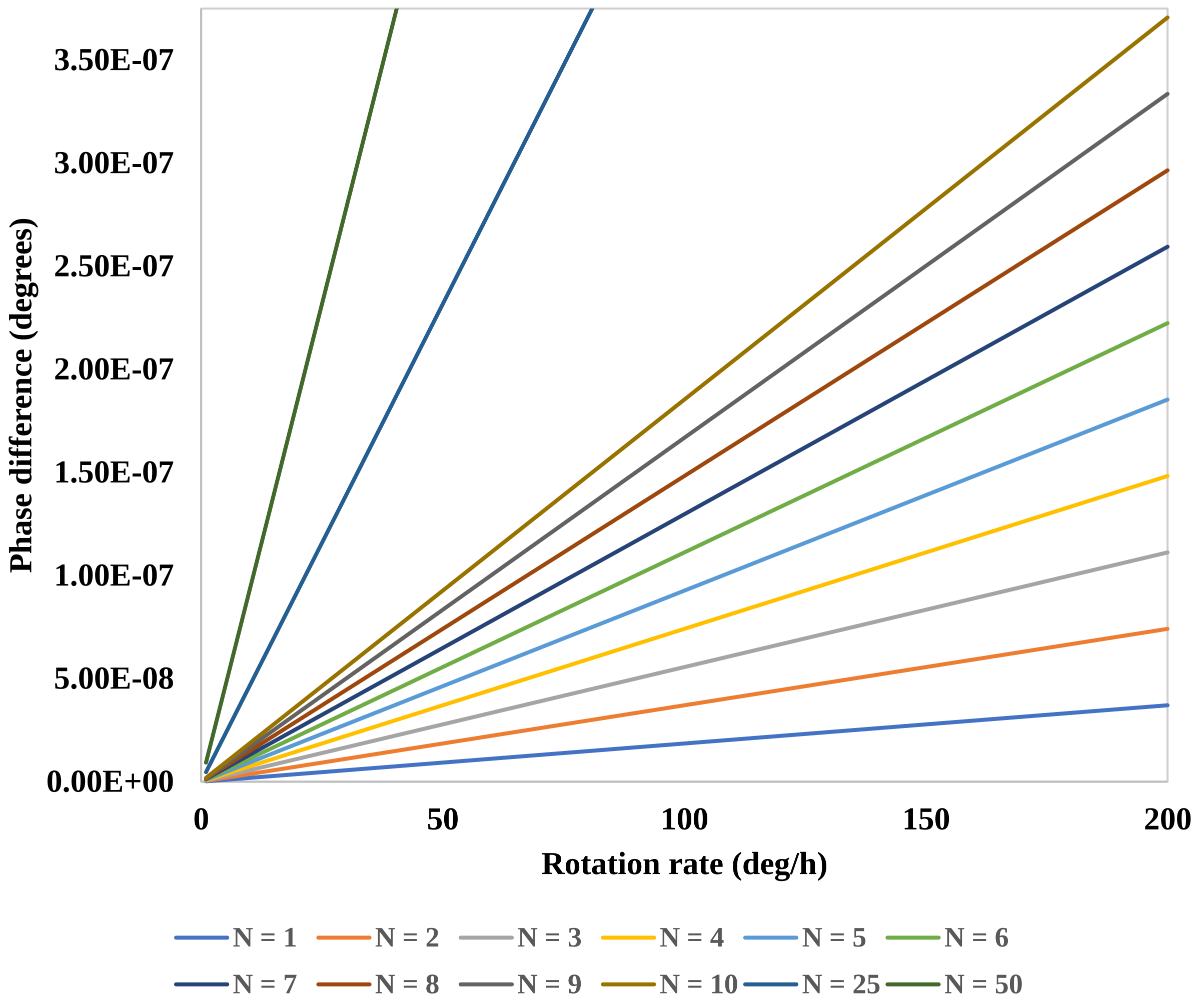

Figure 2.2: Depicting the phase difference vs rotation rate for IIOG vs number of turns for 30 mm diameter.

It is evident from figure 2.2 that for all lengths, the phase difference is very small even for a rotation rate of 200 °/h. Therefore, a phase modulator in one arm of the device is used to overcome the near zero sensitivity.

Without a phase modulator, the light intensity at the photodetector is written as [117, 118]:

$$I = \frac{I_0}{2}[1 + \cos \Delta\phi_r] \tag{2.1}$$

Here, $\Delta\phi_r$ = Saganc induced phase shift, I_0 = Intensity of light before sagnac shift

However, by having phase modulator in the loop, the CCW beam reaches the phase modulator at time T later than the CW beam where T = L/c (beam transit time around the loop of length L). If Φ(t) is the applied phase modulation, the phase difference between counter propagating beams due to the applied modulation can be written as:

$$\boldsymbol{\phi_m(t) = \Phi(t) - \Phi(t - T)} \tag{2.2}$$

Therefore, the current intensity at the photodetector would become:

$$\boldsymbol{I = \frac{I_0}{2}[1 + \{\cos\Delta\phi_r + \phi_m(t)\}]} \tag{2.3}$$

In order to retrieve $\Delta\phi_r$ accurately, sinusoidal modulation can simply be applied:

$$\boldsymbol{\Phi(t) = A\,sin\,\omega_m t} \tag{2.4}$$

Substituting into equation (2.2):

$$\boldsymbol{\phi_m(t) = 2A\sin[\omega_m T/2]cos\,[\omega_m(t - \frac{T}{2})]} \tag{2.5}$$

For simplification, write:

$$\boldsymbol{\phi_m = 2A\sin[\omega_m T/2]} \tag{2.6}$$

$$\boldsymbol{t^/ = \left(t - \frac{T}{2}\right)} \tag{2.7}$$

Then equation (2.3) becomes:

$$\boldsymbol{I = \frac{I_0}{2}[1 + \cos\{\Delta\phi_r + \phi_m cos\omega_m t^/\}]} \tag{2.8}$$

To get rotation information ($\Delta\phi_r$), equation (2.8) is expanded into its Fourier components [117]:

$$\boldsymbol{I = \frac{I_0}{2}[1 + J_0(\phi_m)\cos\Delta\phi_r - 2J_1(\phi_m)\sin\Delta\phi_r\,cos\omega_m t^/ - 2J_2(\phi_m)\cos\Delta\phi_r\,cos2\omega_m t^/ + \cdots]} \tag{2.9}$$

Where, $J_n(.)$ is the nth order Bessel function of first kind.

The intensity variation at the even-order harmonics has a dependence on cos $\Delta\phi_r$ and odd-order harmonics depend on sin $\Delta\phi_r$. For example, output [I_0 $J_1(\phi_m)$ sin $\Delta\phi_r$] can be obtained by synchronously demodulating the first harmonic with the modulation frequency giving maximum sensitivity around zero rotation rate due to the discrimination function provided by synchronous demodulation.

For rotation rate detection, the light/beams coming out of the coil from both the directions is combined at the beam splitter which then measured by a photodetector. Upon zero rotation, the beams from both the directions interfere constructively or destructively depending on the beam splitter used for the measurement. However, in the presence of the rotation at a certain angular speed, both the beams travel un identical path due to Sagnac effect and consequently a phase difference is induced between them which can be represented by equation (1.13).

Figure 2.3 depicts the intensity of the current coming out of the detector as a function of non-reciprocal phase shift. In the absence of the rotation, the intensity peaks as both the beams interfere constructively at ΔΦ = 0. Upon rotation, phase shift is induced means ΔΦ moves slightly away from the zero position in any side depending upon the rotation direction and the intensity changes. For an infinitesimal phase shift, the biggest change in the intensity of the detected current appears at ΔΦ = ± π/2 where the intensity has the maximum slope.

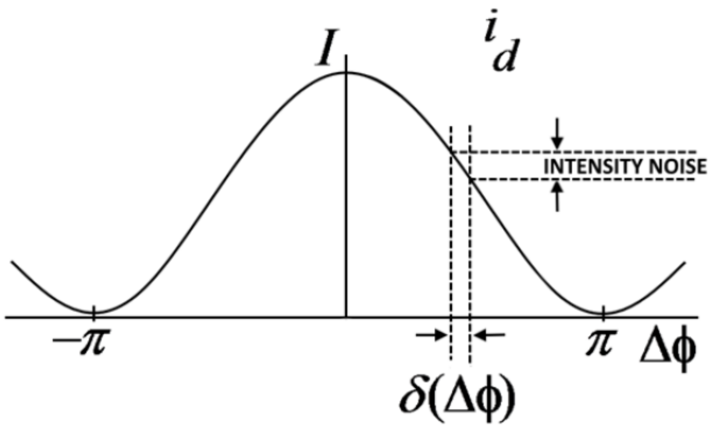

Figure 2.3: Revealing the variation in the detected current intensity as a function of the phase shift [17].

Therefore, by applying a non-reciprocal phase shift of ± π/2, the gyro can be operated in the maximum sensitivity region. Moreover, in this way, phase shift induced by an applied rotation causes/generates a linear variation in the detected intensity.

It is important to note that variations in the light source intensity also cause fluctuations/variations in the detected current intensity and induces an uncertainty in the measurement of the rotation rate. These fluctuations are indistinguishable from variations of the phase shift but can be compensated by reducing the uncertainty in the measurement. In an ideal case, the rotation rate measurement is only shot noise limited and can be written as:

$$\boldsymbol{\delta}(\Delta\Phi) = \frac{\textbf{Shot noise}}{\mathbf{i_D}\ \textbf{slope}} \tag{2.10}$$

As you can see, the uncertainty in the measurement is minimum when the slope of the detected current intensity is maximum. This condition leads to [17]:

$$\boldsymbol{\delta}(\Delta\Phi) = \frac{\sqrt{\boldsymbol{2ei_D B}}}{\frac{\boldsymbol{i_D}}{\boldsymbol{\pi}}} \cong \frac{\sqrt{\boldsymbol{N_{ph}\eta\tau}}}{\frac{\boldsymbol{N_{ph}\eta\tau}}{\boldsymbol{\pi}}} = \frac{\boldsymbol{\pi}}{\sqrt{\boldsymbol{N_{ph}\eta\tau}}} \tag{2.11}$$

N_{ph} = Number of photon’s per second arriving at photodetector, τ = Integration time

η = Quantum efficiency of the detector, e = electron charge, B = Measurement bandwidth

By putting δ(ΔΦ), equation (1.13) becomes [119, 120]:

$$\delta\Omega = \frac{\lambda c}{2NLd}\sqrt{\frac{Bh\nu}{\eta_{pd}P_{pd}}} \quad [rad/s] \tag{2.12}$$

c = Speed of light in vacuum, d = Diameter of the loop coil, λ = Laser Wavelength, P_{PD} = Optical power reaching at the photodetector, η_{pd} = Quantum efficiency of the photodetector, L = Length of the loop, N = Number of loops, B = Gyro bandwidth, h = plank's constant, v = Operating frequency

As can be seen in equation 2.12, resolution mainly depends on the diameter, length of the loop and optical power reaching the photodetector. The main advantage of the IIOG is that the structure of the device requires only one 3dB coupler and one phase modulator. Therefore, a significant amount of input light power can reach the photodetector. Diameter of the loop and optical power reaching at the photodetector can be fixed by exactly knowing the loss induced by the optical components. Therefore, the resolution of an IIOG is calculated vs number of loops for a loop diameter of 30mm and a representative maximum input laser power of 10 mW. Loss induced by the optical components is also considered as -3.1dB for 3dB coupler and -0.5dB for a phase modulator. Resolution vs number of loops plotted in figure 2.4 for three propagation losses 0.1 dB/cm, 0.01dB/cm and 0.003 dB/cm. For the practical estimation of resolution vs number of loops, an average loss of 0.027dB per crossing is also included in the calculation. The total crossing loss keeps accumulating with the number of loops means low loss waveguide loops have higher crossing loss effect.

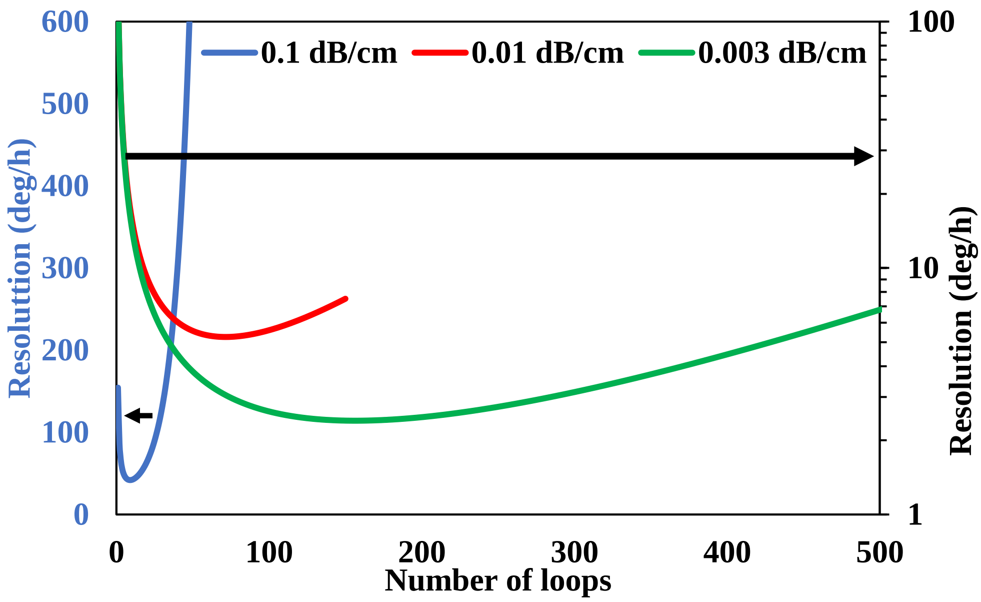

Figure 2.4: Illustrating the resolution of loop gyro vs number of loops for propagation loss of 0.1 dB/cm, 0.01 dB/cm and 0.003 dB/cm.

The trade-off between the length of the loop vs the optical power at the photodiode determines the sensitivity of a loop gyro. The best sensitivity for 0.1 dB/cm is 41.89 ^{o}/h when the length is 84.78 cm and for 0.01 dB/cm is 5.25 ^{o}/h when length is 668.82 cm. The sensitivity possible from the lowest ever achieved propagation loss (0.003 dB/cm) is 2.40 ^{o}/h When the length is 1469.52 cm. For all three propagation losses (0.1 dB/cm, 0.01 dB/cm & 0.003 dB/cm), the optimum lengths correspond to 9, 71 and 156 loops respectively. The diameter used for all the loops was 30mm. In case of 0.01 dB/cm and 0.003 dB/cm, the sensitivity does not improve significantly after certain number of loops which offers a trade-off between size of the coil vs sensitivity. For example, 30% degradation in the sensitivity (from 5.25 ^{o}/h to 6.87 ^{o}/h) helps reducing the size of the coil (71 loops to 31 loops) significantly for 0.01 dB/cm. This trade-off has even bigger effect for 0.003 dB/cm, the size of the coil reduced (from 156 loops to 69 loops only) immensely for 30% degradation in the sensitivity (from 2.40 ^{o}/h to 3.12 ^{o}/h). Therefore, size of the device can be reduced by sacrificing small percentage of the sensitivity.

The propagation loss of planar waveguides is inherently much higher than optical fibre, therefore waveguide loops cannot be made nearly as long as fibre loops, consequently sensitivity relative to FOG is reduced.

In 2016, Gundavarapu et al. [121] demonstrated a Sagnac sensor using a 3m long Si_3N_4/SiO_2 waveguide loop and compared its output with fiber loop gyro. The relatively higher propagation loss associated with waveguide technology was compensated by using additional attenuators in the fiber gyro setup. The scale factor of waveguide loop based gyros came out to be nearly half of the fiber loop gyro and this could be related to the difference in the length of the sensing coil. The authors didn’t measure the detection limit in this paper.

The same author [88] measured Angle Random Walk (ARW) and bias instability of an IIOG in 2018 and came to be 8.52 °/h$^{1/2}$ and 58.7 °/h respectively which are comparable to commercial grade gyros.

Wu et al. [9] theoretically calculated the rotation rate of Silicon on Insulator (SOI) based IIOG. The small footprint (600µm x 700µm) was deliberately chosen to make it a suitable device for compact application but this led to an extremely low sensitivity of 184680 ^{o}/h.

2.2 Resonant Integrated Optical Gyro

The resonant integrated optical gyro (RIOG) is a frequency sensitive device in which the frequency difference between CW and CCW resonant frequencies is used to detect the rotation rate which can be represented by equation (1.18).

For rotation rate detection, the Pound-Drever Hall technique [122] is widely used to lock the input laser frequency to the resonant frequency of the resonator [123] in one propagation direction. The synchronous demodulation of the detected signal of the other direction then gives the resonant frequency difference (Sagnac frequency) [89].

The key element of a RIOG is the waveguide resonator which defines the fundamental limit on its sensitivity. In other words, the precision with which Δf can be measured depends on the quality factor of the resonator and signal to noise ratio in the measurement. For a bus coupled ring resonator, assuming shot noise limited detection, equation (1.18) can be written as [80, 81, 124-128]:

$$\boldsymbol{\delta\Omega = \frac{\lambda L}{4A}\frac{\sqrt{2}\,FWHM}{SNR}} \quad \left[\frac{\mathbf{rad}}{\mathbf{s}}\right] \tag{2.13}$$

Here, FWHM = Full width half maximum of the resonance, SNR = Detected signal to noise ratio

SNR = $(N_{ph}\eta\tau)^{1/2}$, FWHM = Operating frequency/Quality factor

N_{ph} = Number of photon's per second arriving at photodetector, τ = Integration time

η = Quantum efficiency of the detector

Substituting FWHM and SNR in equation (2.13) gives [106, 129]:

$$\boldsymbol{\delta\Omega = \frac{\sqrt{2}c}{dQ}\sqrt{\frac{Bh\nu}{\eta_{pd}P_{pd}}}} \quad \left[\frac{\mathbf{rad}}{\mathbf{s}}\right] \tag{2.14}$$

Where, c = Speed of light in vacuum, d = Diameter of the resonator, Q = Quality factor of the micro-ring resonator, P_{PD} = Average optical power at the photodetector, η_{pd} = Quantum efficiency of the photodetector, B = Gyro bandwidth, h = plank's constant, v = Operating frequency

The shot noise limited sensitivity of a waveguide resonator is determined by the quality factor, size of the ring and optical power reaching at the photodetector as can be seen in equation (2.14). Quality factor mainly depends on the propagation loss of the waveguide and coupling coefficient. In terms of optical device parameters, sensitivity is maximized by obtaining the highest possible Q and the largest feasible diameter of the resonator. The sensitivity of a RIOG is plotted vs Q in figure 2.5 for representative values of ring diameter (d) of 30mm and input laser power of 10 mW. The laser power reaching at the photodetector used for this calculation was 2.5 mW to plot a reasonably realistic graph. To calculate the quality factor required for a certain resolution, all the other parameters in equation 2.14 need to kept constant. That is why same amount of laser power at the photodetector is used in the calculation.

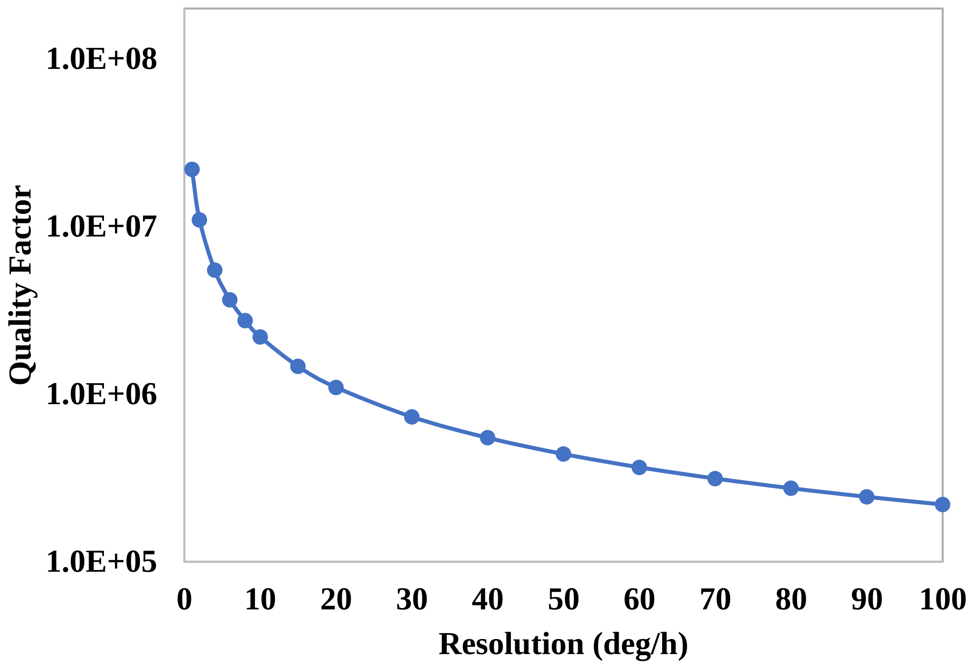

Figure 2.5: Quality factor vs resolution theoretically calculated for a ring resonator 30mm in diameter.

Figure 2.5 roughly illustrates how much quality factor is needed for a certain resolution. However, for a precise value of Q vs resolution in a RIOG, loss induced by the optical components and coupling loss need to be considered. For this graph, calculations were made at 25 % of drop transmission in order to get the best sensitivity as has been reported previously [130]. Other than optical parameters, sensitivity also depends on how accurately laser can be locked to the resonant frequency of the resonator and at 75 % resonant depth, slope of the demodulator curve is maximum (as can be seen in figure 2.6) meaning frequency noise which can be induced in the measurement will be minimum. Drop transmission vs slope of the demodulator curve was computed for propagation losses of 0.1 dB/cm and 0.01 dB/cm by using a ring resonator having 30mm in diameter.

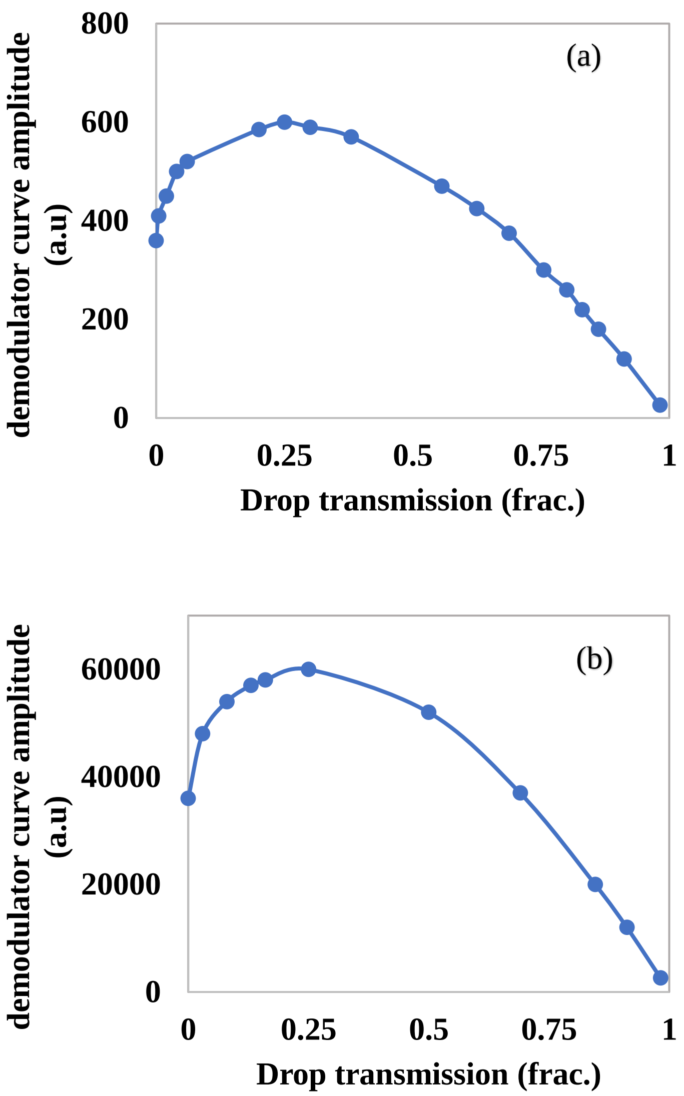

Figure 2.6: illustrating the graphs between slope of the demodulator curve amplitude vs drop transmission, (a) 0.1 dB/cm and (b) 0.01 dB/cm.

Figure 2.6 is showing the graphs between drop transmission vs slop of the demodulator curve from critical coupling to under-coupling. As can been seen, the maximum slope is found at 25% of drop transmission in both cases. Therefore, this can be referred to as optimum coupling state for this kind of optical gyro.

Translating figure 2.6 to resolution vs propagation loss was accompanied by computing quality factor for a bus waveguide ring simulator with 11 different propagation losses all also at 75 % resonant depth. The actual propagation loss for a given resolution will be high as loss induced by optical components is neglected and this calculation will only give a rough estimation of loss vs resolution. The result is shown in figure 2.7,

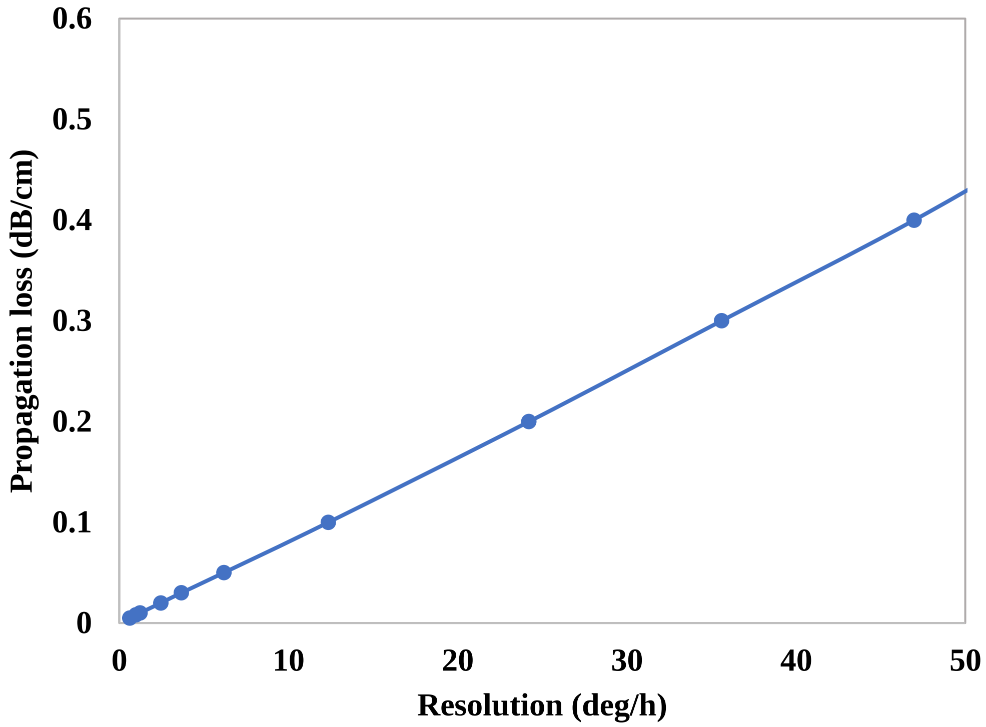

Figure 2.7: Propagation loss v resolution for bus waveguide ring of 30mm in diameter.

As can be seen in figure 2.7, for a resolution of around 10 ^{o}/h, a propagation loss of < 0.1 dB/cm is required which is achievable and reported in the literature for many waveguide technologies. Kominato et al. [131] achieved an average propagation loss of 0.003 dB/cm from germanium doped silica waveguides deposited with flame hydrolysis. A progation loss of 0.001 dB/cm from thin Si_3N_4 waveguides is predicted by a loss model proposed by Bauters et al. [110]. Therefore 1 ^{o}/h is achievable.

As resolution depends mainly on the quality factor and optical power reaching the photodiode for a given ring diameter, therefore optimum couping into/out of the ring was computed for add-drop and bus waveguide ring resonatosr in order to find the best combination of quality factor and optical power reaching the photodiode, whilst using realistic component inserion losses.

In case of the add-drop ring resonator (block diagram is shown in figure 2.8), quality factor and drop transmission are obtained by simulating various input and output coupling states and calculating resolution by using equation (2.14) for the values of d = 30mm, t_0 = 1s, f_0 = 193 THz, η = 90 %, input power of the laser = 10 mW. The loss induced by the required additional optical components such as 3dB coupler (-3.1dB = -0.1dB excess loss + -3.0dB for splitting light into 50:50) and Phase modulator (-0.5dB), etc was also included.

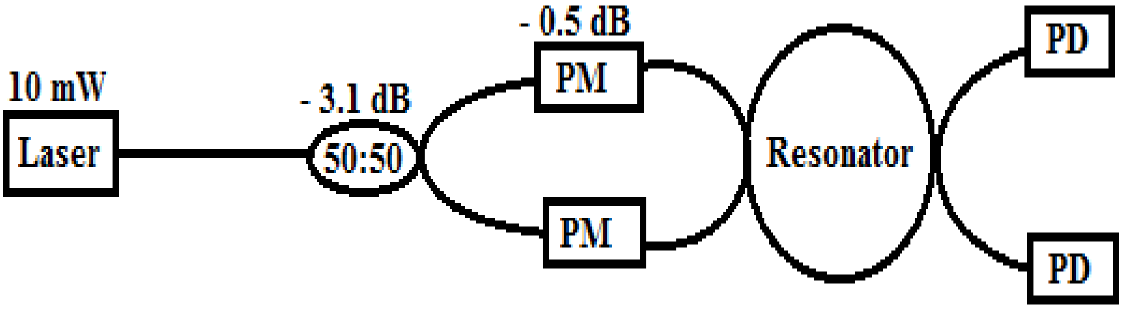

Figure 2.8: Block diagram of add-drop ring resonaotr with laser power and optical loss induced by the components (PM = phase modulator & PD = photodetector).

Laser power attenuated by optical components was 5.64 mW. Optical power reaching the photodiode is the product of drop transmission and input laser power left after passing thorugh different optical comonents. Finally, sensitivities contours are plotted for varying input and ouput coupling to find the optimum operating point for add-drop ring resonator gyroscopes with waveguide losses of 0.1 dB/cm and 0.01 dB/cm as shown in figure 2.9.

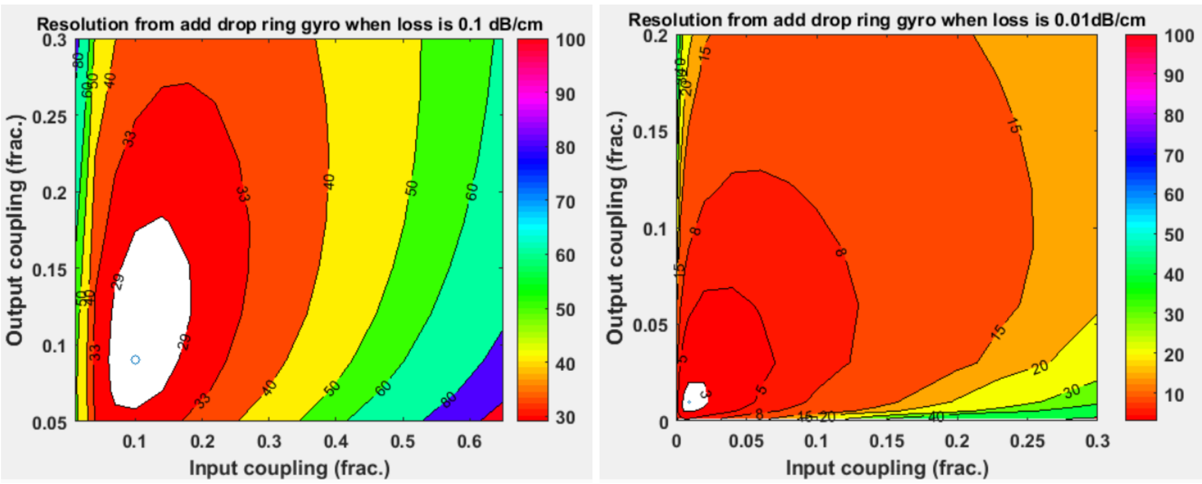

Figure 2.9: Exhibiting optimum operating point for add drop ring resonator gyroscope (a) 0.1 dB/cm, (b) 0.01 dB/cm.

For both propagation losses (0.1 dB/cm and 0.01 dB/cm), the highest sensitivites is found to occur when input to drop transmission was around 75 %. Best resolution was found to be 27.24 ^{o}/h for 0.1 dB/cm and 2.61 ^{o}/h for 0.01 dB/cm for a 10 mW source laser.

For the bus waveguide ring resonator gyroscope (block diagram seen in figure 2.10), Quality factor, mimimum and maximum transmissions were obtained by computing using 21 different bus coupling states (from under coupling to over coupling) and is shown in figure 2.11 (a & b) for 0.1 dB/cm and 0.01 dB/cm respectively.

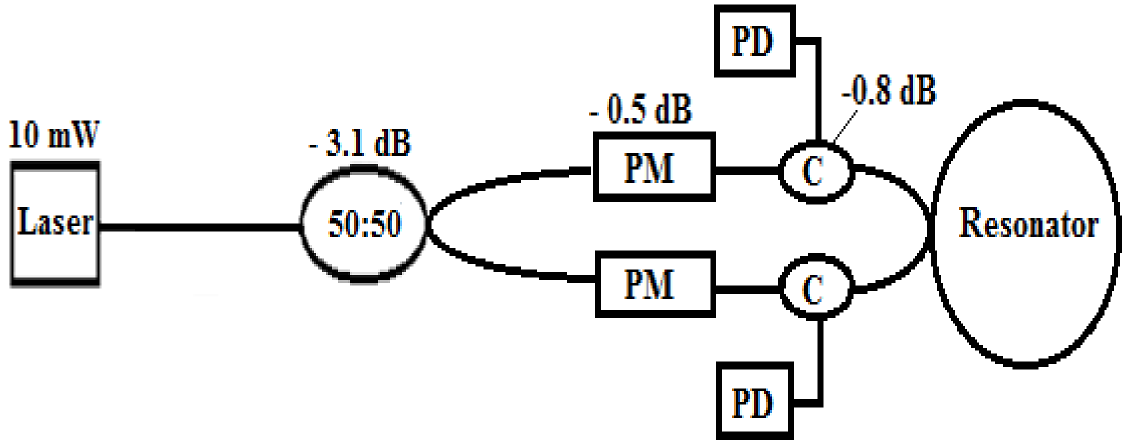

Figure 2.10: Block diagram of bus waveguide ring resonator with laser power and optical loss induced by the components (PM = phase modulator, PD = photodetector & C = circulator).

The most important difference in structure is the circulator or 3dB coupler to receive light from the resonator. Bulk circulators induce an insertion loss of about -0.8dB from input back to photodiode but no such circulator yet exists in planar form. The excess insertion loss for a 3dB coupler is -0.1dB but it also splits the light 50:50, therefore the total loss induced by a 3dB coupler is -3.1dB per pass. The integration of a circulator is still a challenge; therefore calculations have been made to draw a comparison with a 3 dB coupler which can be integrated.

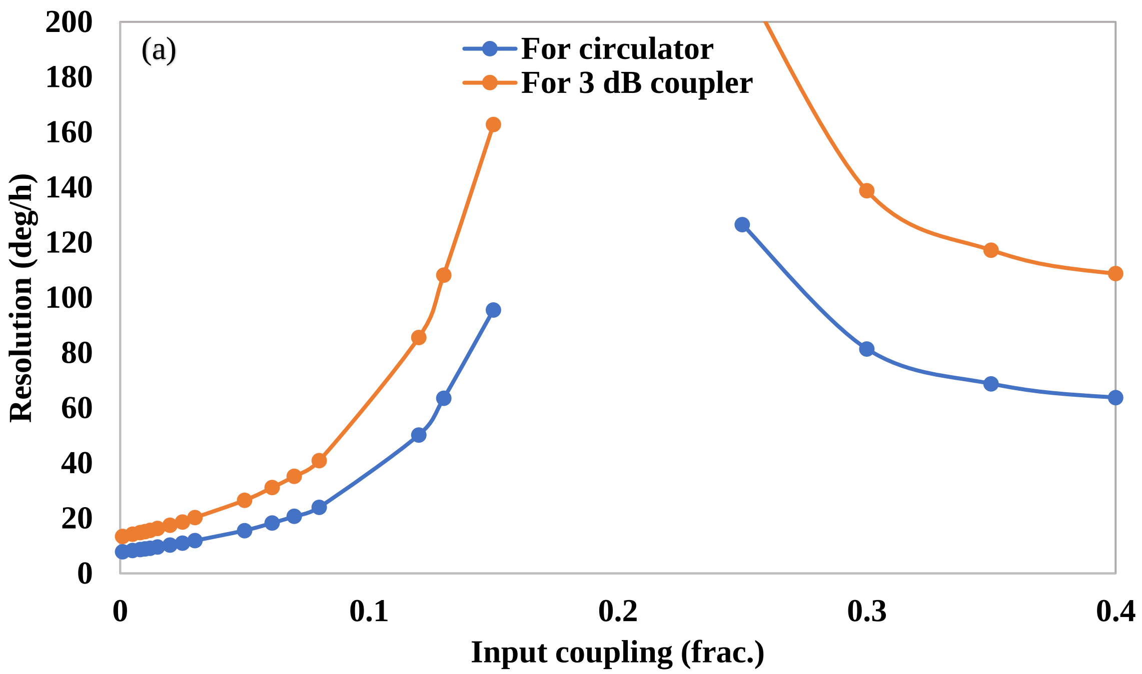

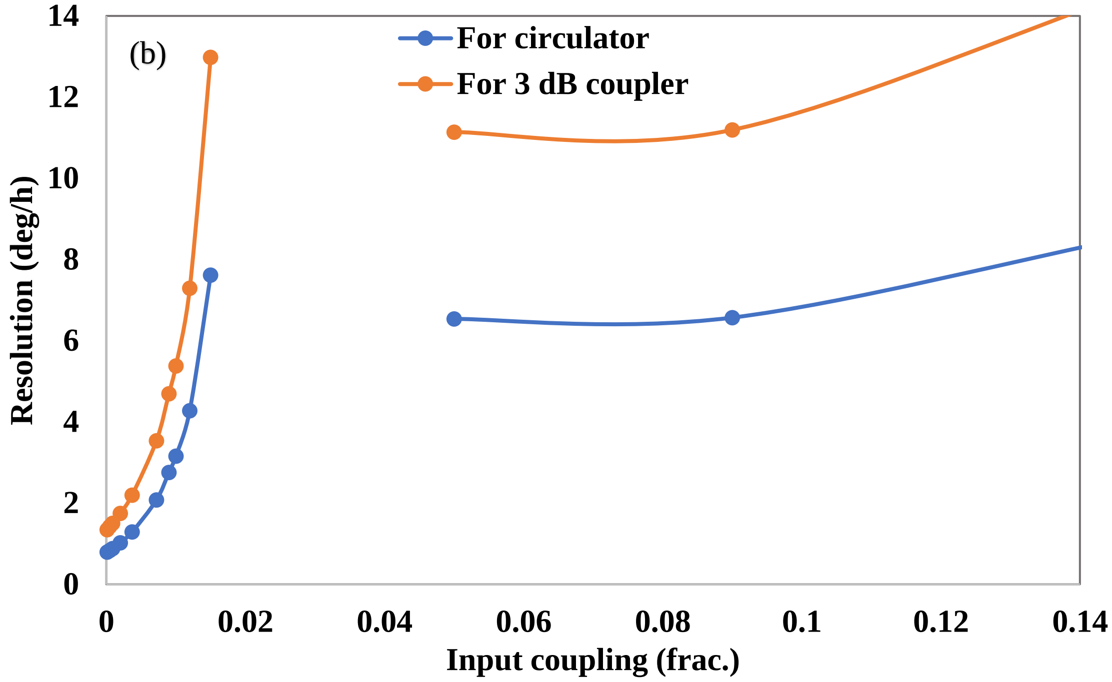

Figure 2.11: **Resoluton vs input coupling for bus waveguide ring resonator, (a) 0.1 dB/cm, (b) 0.01 dB/cm propagation loss.**

For 0.1 dB/cm, the best computed sensitivity for a circulator and a 3dB coupler were 7.87 ^{o}/h and 13.41 ^{o}/h respectively. For 0.01 dB/cm, sensitivity was 0.79 ^{o}/h and 1.34 ^{o}/h for circulator and 3dB coupler respectively. It can be clearly seen that bus coupled ring resonator gyros give the best sensitivity when working in the under-coupling state because in that state both quality factor and transmission are maximised. However, the resonance dip in the under coupled region is relatively small compared to critical or over coupling and even a small parasitic reflection in the system could lock the laser off resonance which consequently leads to an incorrect measurement. Whereas, in case of circulator, the best sensitivity at the optimized coupling state (75 % resonant depth) found to be 20.68 ^{o}/h and 2.07 ^{o}/h for 0.1 dB/cm and 0.01 dB/cm respectively. Even at 75 % resonant depth, the sensitivity is significantly better in case of bus waveguide ring gyro for circulator but by having add-drop ring structure, circulators can be avoided.

Much research has been made on RIOG in recent years [132-136]. In 1989, Iwatsuki et al. [137] reported the first experimental demonstration of a waveguide type ring resonator gyroscope. The sensitivity was found to be 1846800 ^{o}/h. The reason behind this extremely poor sensitivity is unknown as the dimension and loss of the resonator was not reported.

Suznki et al. [138] reported an improved resolution of 432000 ^{o}/h from a resonator integrated on a silica planar lightwave circuit. The propagation loss and length of the resonator was 0.024

dB/cm and 14.8cm respectively. The improved resolution can be correlated to applied countermeasures for backscattering and polarisation induced noise.

A bias stability of 360 ^{o}/h has been reported by Ma et al. from a resonant optical gyro. A 7.9cm long polarisation maintaining silica waveguide-based resonator was used to measure the rotation rate. The backscatter induced noise was significantly reduced by using a double phase modulation technique which resulted a better sensitivity as elaborated in the paper. The potential lower sensitivity limit for a bus waveguide and add-drop ring resonator gyro is currently (1.05 ^{o}/h) and (2.62 ^{o}/h) respectively for the record low planar waveguide loss of (0.003 dB/cm) [131].

2.3 Brillouin Ring Laser Gyro

Brillouin Ring laser gyroscope (BRLG) is an interesting option which avoids the shortcomings of both active and passive ring laser gyros. i.e. lock-in effect (in active RLGs) and small phase difference (in case of interferometer) respectively. Stimulated Brillouin Scattering (SBS) originates from spontaneous scattering process in which a pump wave scatters from thermally excited acoustic waves in the material. The backscattered wave then interacts with the pump wave and excite acoustic waves through electrostriction. However, below a certain threshold, laser power is not strong enough to modify/alter the optical properties of the cavity medium and stimulate Brillouin scattering. At a certain laser power, the interaction between the backscattered and pump waves generates a periodic change in the refractive index of the medium which acts as an optical grating and scatters the pump wave even stronger through Bragg diffraction. The frequency of the backscattered wave is downshifted due to the Doppler shift associated with the grating travelling with the speed of sound and shift in the Brillouin frequency is represented by equation (2.15):

$$\mathbf{v_B = 2\frac{nV_A}{\lambda_0}} \tag{2.15}$$

Here, v_B is the Brillouin frequency shift, V_A is the acoustic velocity, λ_0 is the pump wavelength and n is the refractive index.

By definition, the scattered wave which is downshifted in frequency to pump wave is called stoke. First stoke acts as a pumping source for the second stoke which also propagate in the opposite direction to its source and downshifted in optical frequency. This process goes on depending on the laser power [139]. Neighboring stokes produced in this process can be used to measure the Sagnac shift and are well suited for gyro application due to the inherent difference in their optical frequencies avoids lock-in effect automatically [86]. Secondly, in most of the solid state amplifiers, gain competition perverts the simultaneous resonance of the counter propagating beams which can be avoided in the Brillouin ring laser gyro because of the directionality of the gain [140].

Li et al. [86] reported a SBS based ring laser gyro and measured a rotation rate of 22 ^{o}/h. For the detection, the laser (pump wave) is locked to the resonant frequency of the resonator by using a well-known Pound-Drever-Hall method. The threshold pump power for the generation of 1st stoke was found to 250µw and it was adjusted to generate stokes of up to the third order. The pump wave and 2nd order stoke coupled out of the resonator in the clockwise direction. Whereas 1st and 3rd order stokes were following counter clockwise symmetry. Both these stokes were directed towards the detector by using fibre circulator. 2nd and 3rd order stokes were selected with the help of a band pass filter and beat frequency at 10.87 GHz was detected by a fast photodetector. Recently, the same group achieved a bias stability of only 3.6 deg/h from a BRL gyro with a disc resonator having 18mm in radius [85].

For designing a Brillouin ring laser gyro, it is worth noting that shift in the Brillouin frequency is a temperature dependent quantity as both the refractive index and acoustic velocity vary with temperature and is expressed as:

$$\mathbf{v_B(T) = v_{B0} + \frac{dv_B}{dT}\,(T - T_0)} \tag{2.16}$$

v_{B0} is the shift in the Brillouin frequency at a reference temperature T_0. It has been reported in the literature that v_B increases linearly with temperature [141] which allows to rewrite equation (2.16) as:

$$\mathbf{v_B(T) = v_{B0} + C_T\,(T - T_0)} \tag{2.17}$$

C_T is a frequency temperature coefficient which depends on the pump wavelength and fiber/waveguide material. Thermal induced shift in the Brillouin frequency should be carefully calculated and compensated in gyro applications. A limited amount of work has been done and reported on BRL gyros so far, but it shows that this can be used as fully integratable option in the future.

2.4 Performance Limiting Effects

The three commonly known performance limiting effects in optical gyro’s are (1) Backscattering Induced noise, (2) Kerr effect and (3) polarisation induced noise.

2.4.1 Backscattering induced noise

Rayleigh backscattering is one of the major noise sources in optical gyros [142-145] and affects in two ways,

(1) Backscattered intensity itself

(2) Interference between the backscattered wave and primary counter propagating wave

Backscattered intensity doesn't make random noise but induces non-linearity in the output [138, 142]. Whereas, the error induced by the interference term is a dominant nosie source and can be written as [146]:

$$\mathbf{Error} = \frac{\mathbf{c\lambda_0\sigma_R}}{(\mathbf{2\pi})^2\mathbf{DL}}\left(\frac{\mathbf{\Delta V}}{\mathbf{V}}\right)^{\mathbf{N}} \tag{2.18}$$

σ_R = Backscatter coefficient, L = Length of the resonator, D = Diameter of the resonator

N = Number of the suppressed carrier (0, 1, 2), $(\Delta V/V_{sc})$ = Suppressed carrier voltage error

V_{sc} = Voltage for perfect suppression

Variation in the interference intensity due to phase difference between backscattered and counter propagating wave makes a severe random noise source. This error can be greatly reduced by minimizing interference intensity between backscattered and primary wave by suppressing the carriers of both the beams [147-149] and carriers can be suppressed by applying phase modulation. High carrier suppression is crucial to completely removing this noise. The possible interference between the oppositely travelling sidebands can be moved outside the gyro bandwidth. The amplitude of the modulation should be optimized in a way that carrier is suppressed close to zero. However, carrier suppression level is sensitive to accuracy of modulation amplitude and temperature stability of the phase modulator. These conditions can be relaxed by using more than one phase modulator on each arm. Ma et al. [89] used four Phase Modulators to modulate the beams at both arms to enhance the suppression of the carriers as well as relax the conditions mentioned above. The addition of two extra PM's helped to reduce the carrier suppression level to 120dB. Consequently, an improved bias stability of 38 ^{o}/h though for a short time (50 second) was observed. In informetric gyro's, this error can be removed by using broadband light source [150].

2.4.2 Kerr effect

One of the main sources of error in optical gyro's is optical Kerr effect [151-155]. Mismatch between the input light intensities between the counter rotating modes in the waveguide resonator is responsible for this effect. It is a non-reciprocal error. When a light passes through a narrow waveguide core, the density of light increases in the core causes the change in refractive index resulted a non-linear propagation of the light. A constant intensity mismatch does not induce random bias in the output and is removed electronically. However, bias stability is badly affected by the fluctuation in the mode intensities. The error caused by this effect can be represented by equation (2.19) [156]:

$$\mathbf{\Omega} = \frac{\boldsymbol{\lambda}\mathbf{Fc}\boldsymbol{\zeta}\boldsymbol{\Delta}\mathbf{P_i}}{\mathbf{4}\boldsymbol{\pi}^{\mathbf{2}}\mathbf{DA}} \tag{2.19}$$

F = finesse, D = diameter of the resonator, ζ = Waveguide nonlinear susceptibility, ΔP_i = Intensity mismatch between the counter propagating beams, A = Waveguide cross-sectional area.

By using values close to our designed device (D =30 mm, A = 0.25 μm^2, λ = 1550 nm, F = 6 and $\zeta = 2 \times 10^{-13}$ m/W), rotation rate error was calculated by using equation 2.19 and found to be 0.49 ^{o}/s/µW.

Ma et al. [151] indicated a linear relationship between the 2nd harmonic of the demodulated signal and input light intensity to the sensing cavity and verified experimentally. The intensity fluctuation was measured by inserting a 50% tap coupler prior to light launched into the resonator, that's how input light intensity to resonator was controlled and splitted equally into the resonator. Photodetector output signal was collected with digital multi-meter to observe intensity fluctuation and second harmonic of the demodulated signal was obtained through FPGA. Both signals showed almost similar intensity fluctuations (coupler = 5.44%, second harmonic signal = 5.86%). By using second order harmonic as feedback error signal, light intensity fluctuation reduced to 0.0027% from 5.86% which reduced the rotation rate error to 4.1×10^{-5} °/s. Optical kerr effect can be reduced even more by applying this technique on both arms of the gyroscope.

2.4.3 Polarisation induced noise

This noise originates due to change of birefringence in the waveguide [157-160]. During the operation of Polarisation Maintaining (PM) waveguide ring resonators, two states of polarisation are simultaneously excited and if they return to their original state of polarisation after one round trip are known as Eigen States of Polarisation (ESOP) but even PM waveguides cannot remove the unwanted component of ESOP's which appear in the resonant curve as shown in figure 2.12. These peaks are observed by sweeping the optical frequency around the free spectral range. State 1 and 2 are desired and undesired ESOP's respectively. When the optical frequency is carefully tuned just to excite the desired ESOP, the light from that state will fall on the detector. However, even the frequency is significantly detuned away from the resonant frequencies of the undesired ESOP's, off resonance light (exaggerated in the figure 2.12) from that state will also fall on the detector. This undesirable light leads to both intensity and interference error. Bias error due to Interference can be minimized by making sure the orthogonality of the two ESOP's. Even in ideal case when both polarisation states are orthogonal to each other, the shape and position of resonant frequency peaks is the result of superposition of wanted and unwanted light intensities. If the resonant peaks have a frequency separation of exactly half of FSR, the resultant line shape at the wanted resonance is symmetric. However, a slight deviation from the centre of the FSR results the asymmetric line shape (as can be seen in figure 2.12) and the position of the desired resonant peak will depend on the amount of deviation. Resonators with one polarisation mode (TE or TM) are not affected by this polarisation fluctuation induced noise [138].

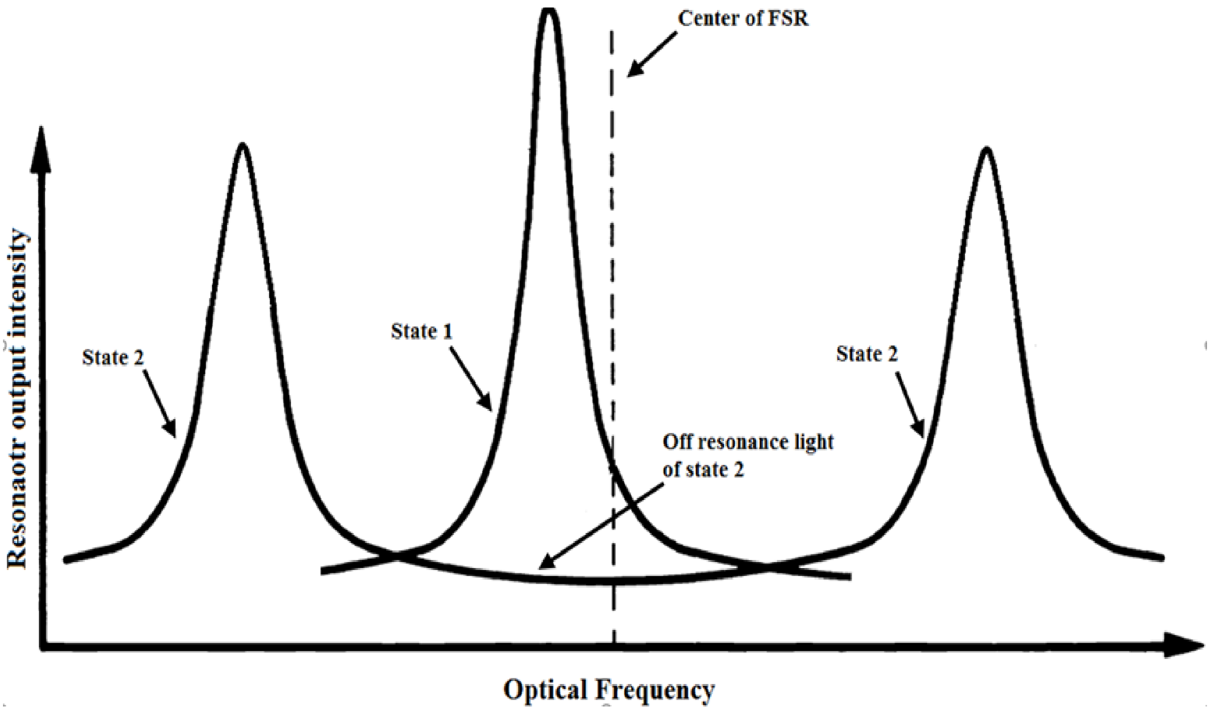

Figure 2.12: Illustrating the resonance curve without any countermeasures to control the unwanted ESOP [161]**.**

Investigation shows that undesired ESOP component originates due to temperature variations as ESOP is birefringence dependent which is strongly temperature dependent. Ma et al. [162] investigated the bias stability due to temperature variation of silica WRR (Waveguide Ring Resonator) based resonant micro optical gyroscope and shown below in figure 2.13. Frequency separation of the two ESOP's varies significantly with the change in temperature. The resonant frequencies of both the ESOP's move towards each other around 25 ^{o}C and their interference causes a large error in the output. At the same time, a tiny fluctuation in that temperature results a significant instability in the bias as seen in figure 2.13(b). Therefore, the operating temperature should be optimized to maximally separate the ESOP resonance frequencies to help minimise the bias error due to thermally driven polarisation fluctuation.

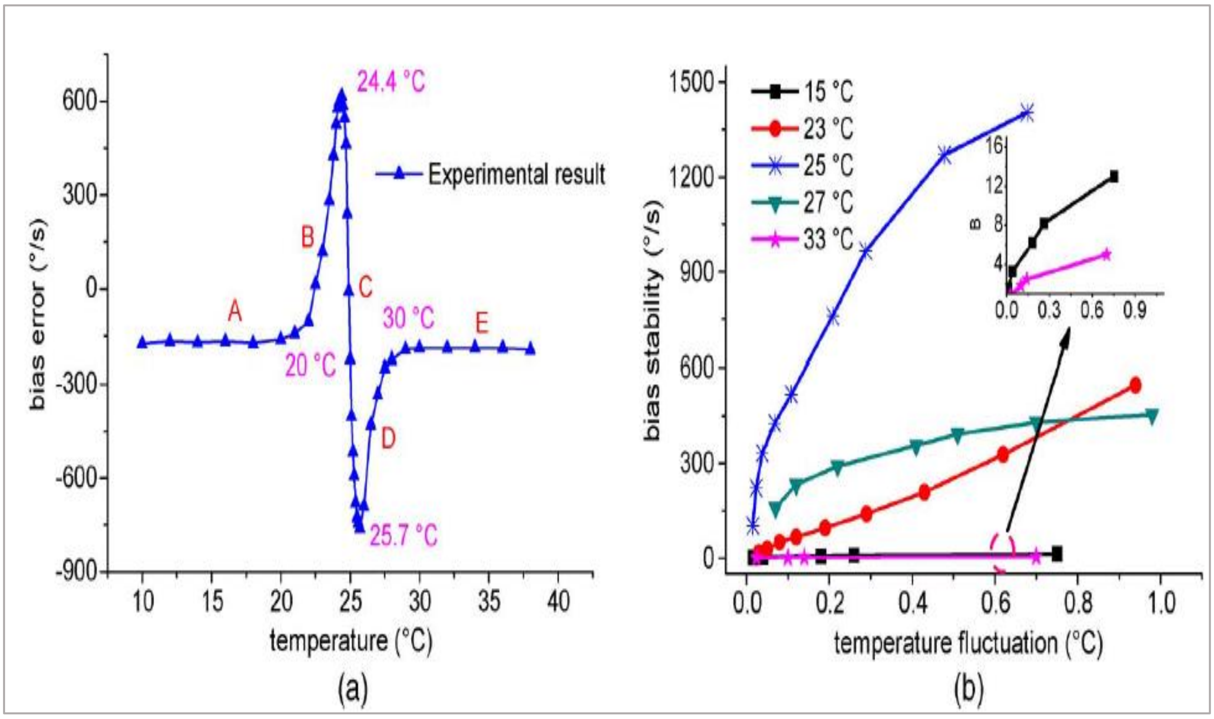

Figure 2.13: (a) exhibiting a significant variation in bias error as temperature varies from 20 ^{o}C to 30 ^{o}C. (b) Gyro stability reacts differently by small temperature fluctuation at different temperatures [162]**.**

By setting the temperature of the silica waveguide at below 20 ^{o}C or above 30 ^{o}C, long-term stability could be achieved as demonstrated in figure 2.14. A large bias error results from other non-reciprocal noise sources (backscattering induced noise and optical kerr effect). A careful attention to these noise sources could significantly improve the bias error.

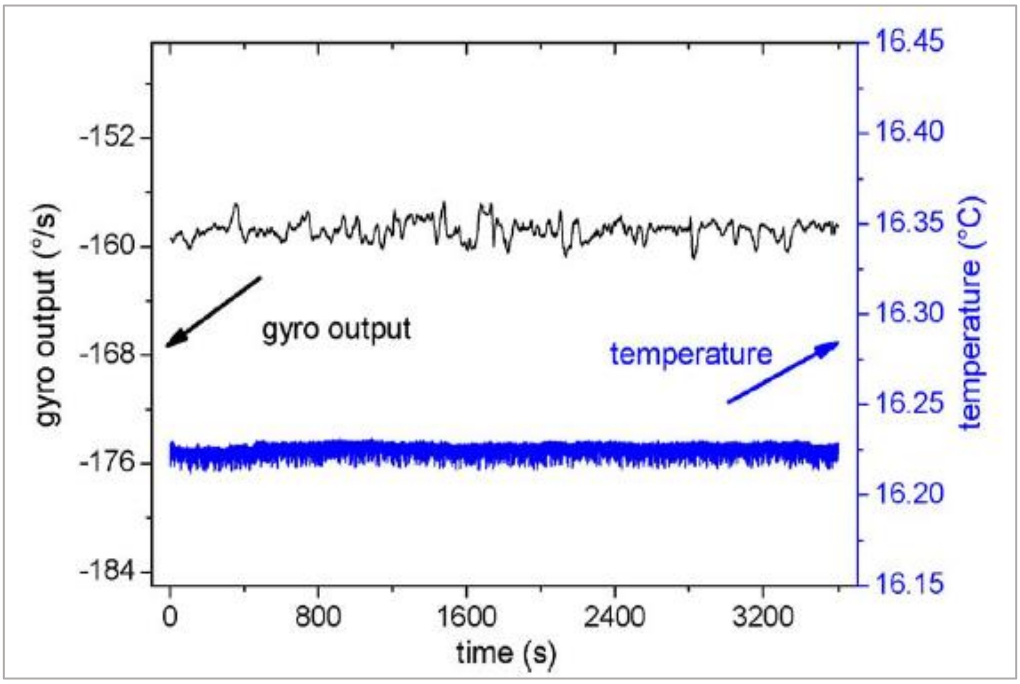

Figure 2.14: showing the stable output of a gyroscope at 16.22 ^{0}C [162]**.**

A bias stability of 0.67 ^{o}/s was achieved by operating the device at 16.22 ^{o}C. This noise can further be reduced by operating a gyro in a highly thermally stable environment.

2.5 Conclusion

Different passive optical gyros are discussed in detail and their performance is compared to find out the best possible structure which can be easily integrated and used for compact applications. Add- drop ring resonator based optical gyro came out to be an optimum structure which fulfils both the requirements. According to best of our knowledge, this kind of simulation and numerical calculation based performance comparison for integratable gyro has never been done before. Lastly, three commonly known noise sources in optical gyros and their solution are also reviewed.

Chapter 3 Design and fabrication of Low Loss Si_3N_4 waveguides

This chapter records the optimization of Si_3N_4 waveguides for ultra-low propagation loss dimensions and their fabrication. Firstly, the theory behind light propagation in optical waveguides is discussed briefly. Secondly, simulations are performed to optimise the waveguide design in order to obtain low loss, single-mode, single-polarisation waveguides. Lastly, waveguide fabrication using photolithography and Reactive Ion Etching (RIE) as well as cladding deposition is discussed in detail.

3.1 Theory Behind the Waveguide

The propagation of electromagnetic waves in a vacuum are described by the four Maxwell's equations which are given below [163]:

$$\nabla . B = 0 \tag{3.1}$$

$$\nabla . E = \frac{\rho}{\varepsilon_0} \tag{3.2}$$

$$\nabla \times \mathrm{B} = \mu_0 \left(\mathrm{J} + \varepsilon_0 \frac{\partial E}{\partial t} \right) \tag{3.3}$$

$$\nabla \times \mathrm{E} = -\frac{\partial B}{\partial t} \tag{3.4}$$

Where, B and E are the magnetic and electric fields respectively, ρ and J are the electric charge density and electric current density and ε_0 and μ_0 are the free space permittivity and permeability respectively. For the case of dielectric propagation media (linear and isotropic, no conductivity and magnetic effects), Maxwell equations can be rewritten as:

$$\nabla \times \mathrm{H} = \varepsilon_0 n^2 \frac{\partial E}{\partial t} \tag{3.5}$$

$$\nabla \times \mathrm{E} = -\mu_0 \frac{\partial H}{\partial t} \tag{3.6}$$

n is the refractive index of the propagation medium and H represents the magnetic field. The refractive index distribution for amorphous materials is generally position-dependent $[n = n(r)]$. The wave equations for E and H can then be derived as [94]:

$$\nabla^2 H + \frac{1}{n^2} \nabla n^2 \times (\nabla \times \mathrm{H}) - \varepsilon_0 \mu_0 n^2 \frac{\partial^2 H}{\partial t^2} = 0 \tag{3.7}$$

$$\nabla^2 E + \nabla \left(\frac{1}{n^2} \nabla n^2 E \right) - \varepsilon_0 \mu_0 n^2 \frac{\partial^2 E}{\partial t^2} = 0 \tag{3.8}$$

Generally, all electric and magnetic field components are described by these two vectorial equations which cannot be reduced to a scalar representation except for very low refractive index contrasts. Moreover, the optical modes of waveguides having non-cylindrical or non-slab geometries cannot be solved analytically, therefore the eigenvalues of the above eigenmode equations can only be accurately solved by using numerical techniques.

3.2 Waveguide Simulation and Geometry Optimisation

Simulation of optical waveguide-based devices is an essential part of integrated photonics. It plays a huge role in optimising the design, size, fabrication cycle, performance and tolerance of any optical device [164]. For this thesis, photonic devices of various geometries are designed before fabrication using components of the Synopsys, Inc. RSoft Component Design [165]. Inbuilt modules within RSoft allow users to compute various optical parameters, such as number of modes, propagation constants and modal field/intensity distributions in essentially arbitrary geometry devices.

The software allows simulation modules to work with others, such as output of one module can be input of the other. e.g. waveguide modes are usually computed by using the finite element simulation (FemSIM) module and these computed modes can be launched into the same or another photonic structure in a following simulation for propagative studies using the beam propagation method (BeamPROP module). In this module, the evolution of field distributions can be tracked during propagation through a longitudinally varying device. For this work, these two modules (FemSIM and BeamPROP) were extensively used to compute waveguide modes and their propagation in numerous photonic device geometries.

In FemSIM, the finite element method is used to compute modes in a 2-D cross section [166]. This method can calculate pure guided modes and also leaky modes such as substrate radiation modes and modes in bent structures which helps to optimize optical structure. For optical devices having sub-wavelength features, non-uniform meshing needs to be used to obtain accurate results whilst maintaining usable model sizes. The solver is a full vector mode engine that can deal with complex inhomogeneous refractive indices and anisotropic materials and is therefore quite a general solver.

BeamPROP is a finite difference 3-D beam propagation (BPM) software module [167]. It can also operate in full vector mode making it useful for the types of refractive index contrasts used in many planar devices, though there is a restriction that it can only do so with a uniformly spaced solution grid. It is extremely useful in investigating and visualising the mode coupling effects in longitudinally varying components and looking at sidewall roughness and structure induced mode coupling effects.

Multiphysics is another important module of R-soft which enables users to incorporate electro and thermo-optic effects in the model. It is useful to calculate waveguide phase shifts induced inhomogeneous refractive index variations induced by thermally or electrically driven refractive index changes and very useful for those applications requiring on chip phase modulation.

The Integrated photonics industry relies on optical waveguides to fabricate and integrate many photonic components on chip scale devices. Waveguides can be fabricated with different configurations such as buried channel waveguides and ridge/rib waveguides etc [168]. However, high quality very low loss ridge waveguides are required for this thesis as previously discussed and these will be fabricated through a top down approach (as can be seen in figure 3.1) using film deposition, photolithograph (patterning) and dry and wet etching followed by overcladding deposition [169].

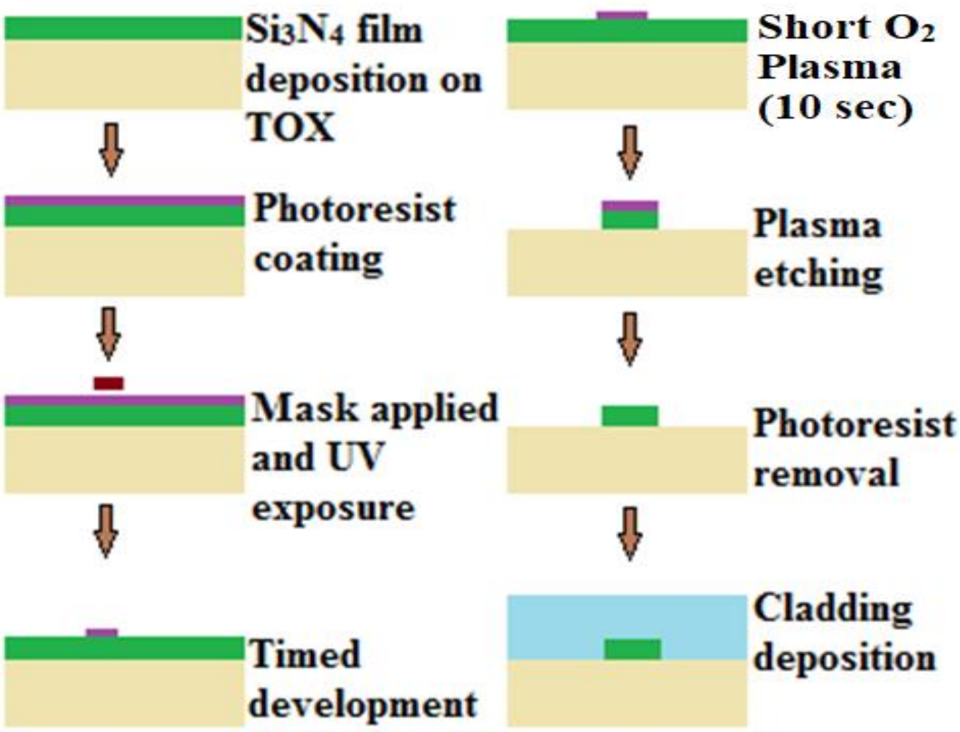

Figure 3.1: Illustrating the step by step Si_3N_4 waveguide fabrication process.

Ridge waveguides are made up of three materials typically deposited onto a silicon wafer and are a widely used geometry in integrated optics. The high index core (1.994 at 1550nm) is defined by two parameters, width (w) and thickness (t) which is surrounded by low index material (1.444 at 1550nm) from all the sides for the strong confinement of the light. The core of the ridge waveguide is mostly fabricated in rectangular or square shape. The structure of the squared shape ridge waveguide is shown in figure 3.2:

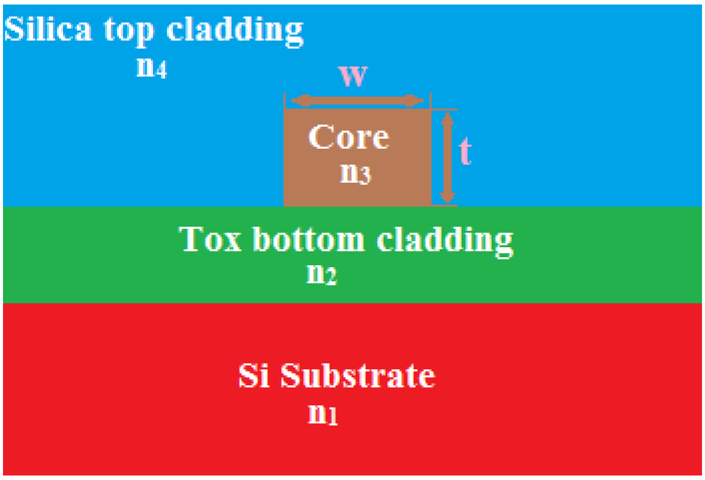

Figure 3.2: Depicting the structure of ridge waveguide. Here t represents the thickness and w is width of the waveguide.

Extremely low loss, single-mode and single-polarisation ridge waveguides can be designed and materialised by varying the core refractive index, width and thickness. Scattering due to interaction with roughness on the etched sidewalls is the main contributor of loss in high index contrast waveguides which can be reduced significantly by decreasing core thickness [110, 170, 171] where less optical field interaction with the sidewalls results in low scattering loss.

3.2.1 Waveguide width and thickness

Waveguide index contrast, width and thickness are critical parameters while designing any integrated optical device. The core dimensions play a vital role in the scattering loss. As previously discussed, obtaining a waveguide that has only a single polarisation mode is highly desirable for gyroscope sensors. It has been reported in the literature that the confinement of the TM mode is much lower than the TE mode [107] in thin high index contrast waveguides and at a certain thickness, the TM mode can preferentially leak into the silicon substrate and becomes extremely lossy [172] whilst the TE mode remains low loss. Under appropriate circumstances it is possible to cut off the TM mode altogether. Simulations were run using RSoft FemSIM to determine the single-mode and single-polarisation Si_3N_4 waveguide design boundaries.

Due to high temperature deposition of LPCVD Si_3N_4 and low deposition rate, the growth of intrinsic stress during the deposition limits the maximum film thickness and around 200nm thick films can be grown in one step. To find out the single-mode and single-polarisation Si_3N_4 waveguide dimensions, a number of simulations were performed to plot a map showing single-mode and single-polarisation boundaries as a function of waveguide width and thickness. In the simulation, the refractive index used for upper cladding was 1.448 at 1550nm with thickness of 10µm. Bulk silica refractive index of 1.444 at 1550nm could not be achieved by PECVD and therefore did not use for the simulation as well (see section 3.8). The plot showing single-mode and single-polarisation dimensions is presented in figure 3.3:

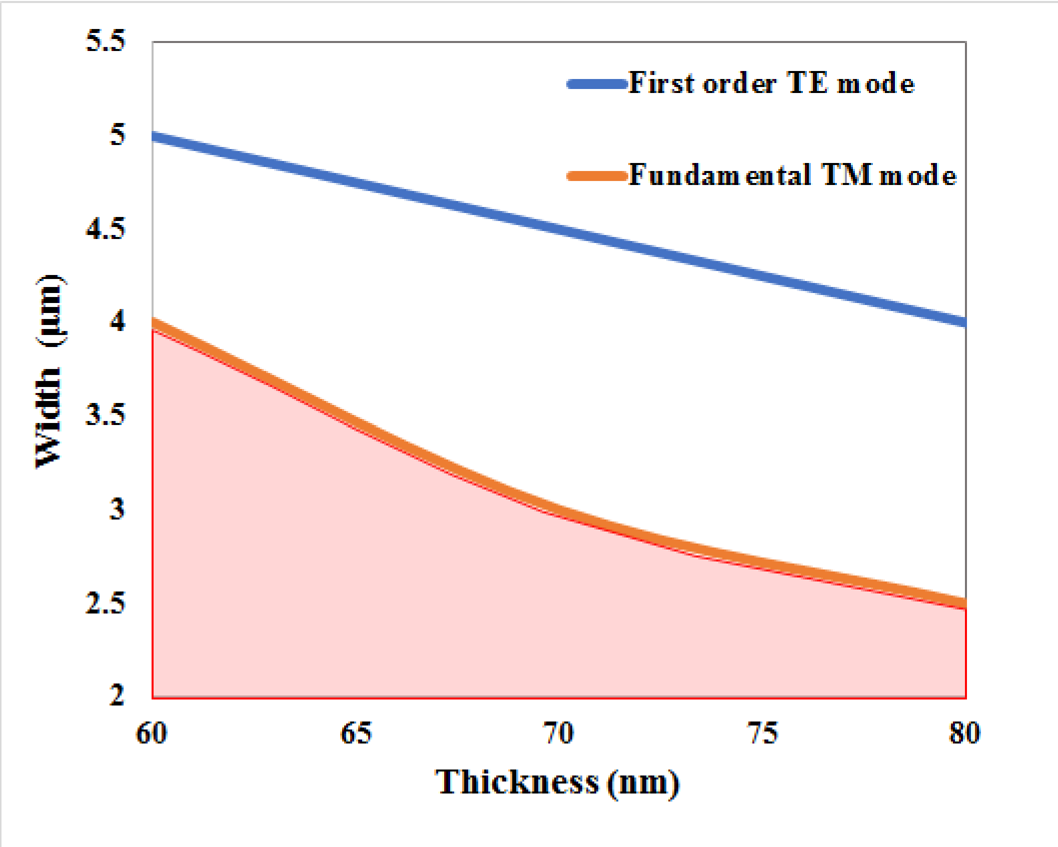

Figure 3.3: Illustrating the dependence of TE and TM modes excided by a Si_3N_4 waveguide on its width and thickness.

The red shaded part in figure 3.3 showing the single-mode and single-polarisation waveguide dimensions. The wanted region keeps shrinking with the increase in the waveguide thickness. 80nm thick and 2µm wide waveguide was chosen for this work for two reasons. 1) Thinner waveguide (60nm) requires thicker bottom cladding which are quite expensive as compared to 5µm thermal oxide wafers. 2) At 80nm thickness, 2.5µm width could also have been chosen/used but it was decided not to work exactly at the limit to keep the room for the fabrication tolerance. The mode field profile of 80nm thick and 2µm wide Si_3N_4 waveguide is shown in figure 3.4.

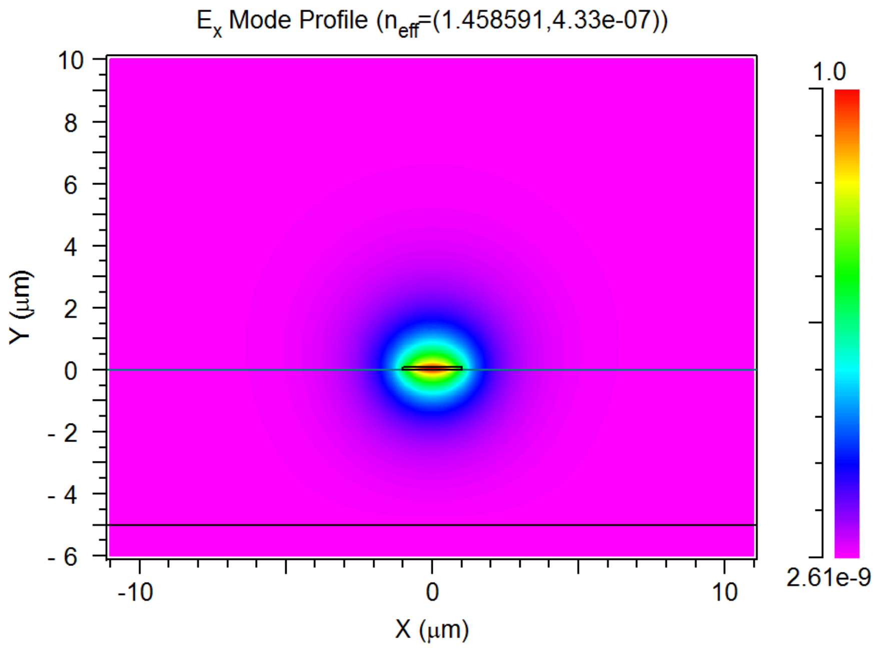

Figure 3.4: Showing the field of fundamental TE mode of a thin Si_3N_4 waveguide (t = 80 nm and w = 2 µm).

Due to the high aspect ratio design of the waveguide, 93 % of the field is in the top and bottom claddings. If the bottom cladding is not thick enough, light leaks into the silicon substrate and induces high radiation loss. Therefore, in the following section, attention is paid to minimise the overall loss of the waveguide. Lastly, it is important to mention that a non-uniform grid was employed because very thin structures were being simulated. The gridding scheme used for thin Si_3N_4 waveguides is shown in figure 3.5:

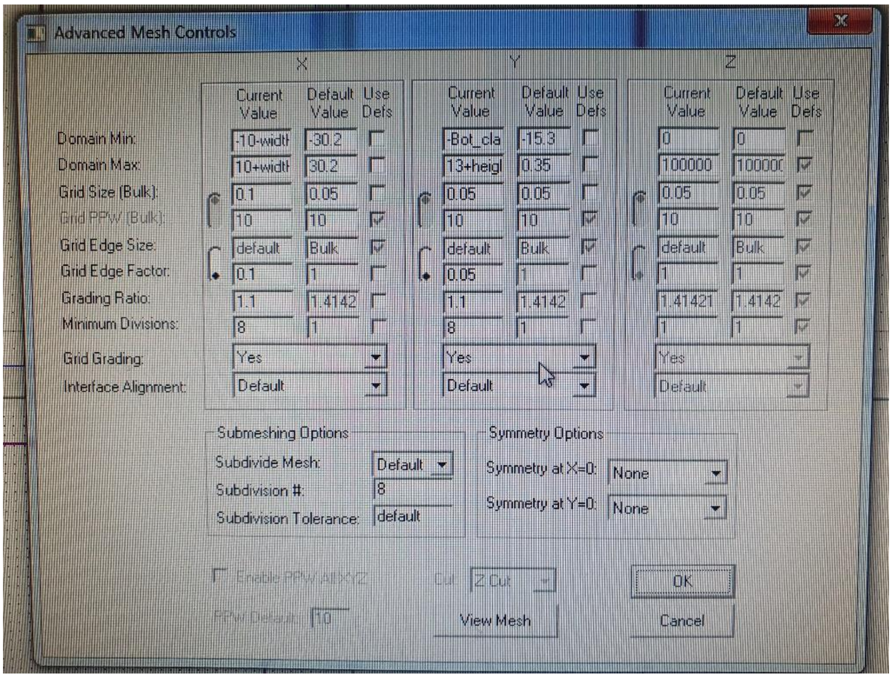

Figure 3.5: Exhibiting the gridding scheme employed for the thin Si_3N_4 waveguides simulation.

3.2.2 Loss optimisation

Optical loss is a critical parameter for resonant gyro sensors. In planar waveguides, total propagation loss in a ring based device is the sum of the substrate radiation loss, scattering losses (volume and surfaces), bending and junction losses, and material absorption loss. Substrate radiation and bent waveguide losses can be modelled in FemSIM. The imaginary component of the computed modal effective index can be used to calculate the loss of a waveguide by employing the following equation [173]:

$$\alpha\left(\frac{\mathrm{dB}}{\mathrm{cm}}\right) = \frac{4\pi K * 4.3429}{\lambda} \tag{3.9}$$

α = optical loss, K = imaginary part of effective index, λ = wavelength

As can be seen in figure 3.4, the k of a straight waveguide of 80nm thickness, 2µm width, deposited on a 5 micron undercladding at 1550 nm is 4.33 x 10^{-7} which corresponds to a loss of 0.15 dB/cm, not low enough for a gyro based device. However, with a thicker bottom cladding, substrate radiation losses improve enormously as can be seen in figure 3.6:

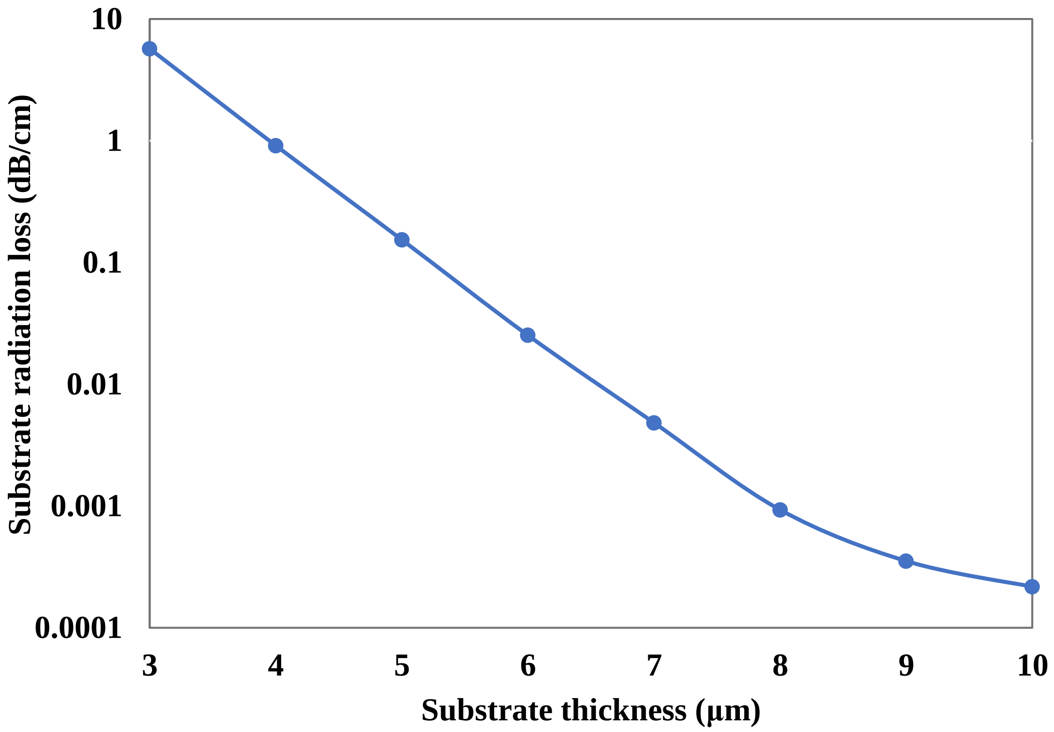

Figure 3.6: Showing the substrate radiation loss vs substrate thickness of Silicon Nitride waveguide 80nm thick and 2µm wide.

Bending a waveguide will also in general induce loss. The main sources of the bending loss are light shedding into radiation modes where the extremity of the optical field would have to exceed light speed to remain bound and the junction loss – mode field mismatch between the straight and bent waveguide modes. Bending radiation loss varies almost exponentially with the bending radius [174]. Therefore, the design of any optical device should be carefully optimised to ensure the high loss zone is not closely approached. FemSIM was employed to compute the bend radiation loss dependence on the bending radius by using conformal transformation methodology [175]. This technique replaces the curved geometry with an equivalent straight waveguide by means of conformal mapping. In simulations, leaky modes were enabled and a perfect matching layer (PML) of 1 μm was set at the edges of the domain. A PML boundary comprises of numerous mesh points which are added to the edge of the simulation window/domain. It acts as an absorbing material and absorb all the optical field reaching at the simulation window. It is employed to eliminate reflections from the simulation domain and consequently ensure accurate results.

Bend radiation propagation loss for the single polarisation waveguide discussed above was calculated by using equation (3.9). Bending loss in dB/turn was then calculated by the following equation.

$$\beta\left(\frac{\mathrm{dB}}{\mathrm{turn}}\right) = 2\pi\mathrm{R} * \alpha\left(\frac{\mathrm{dB}}{\mathrm{cm}}\right) \tag{3.10}$$

R = Bending radius

The modal overlap integral between the guided mode in the straight waveguide and the guided mode of the bent waveguide was used to calculate the junction loss. Overlap integral is defined as how much the mode filed of the straight waveguide overlaps the mode field of bent waveguide. The junction loss is measured in dB per junction, whereas bend radiation loss is measured in dB per turn.

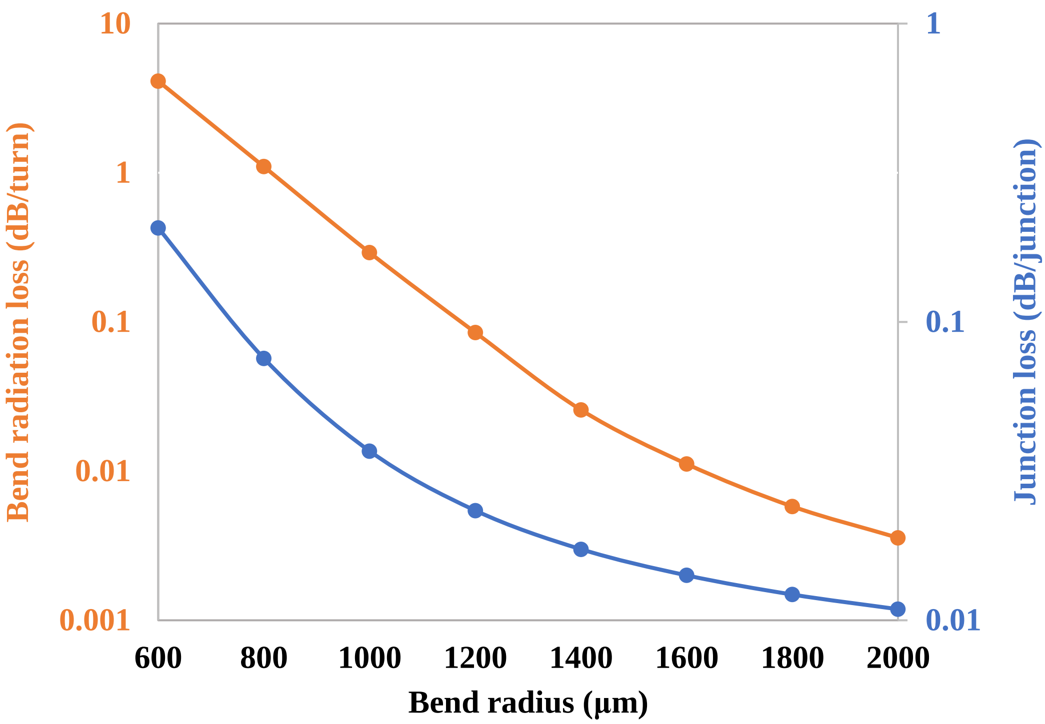

Figure 3.7: Junction and bending radiation loss dependence on the bend radius of single polarisation Silicon Nitride waveguide 80nm thick and 2 µm wide.

Figure 3.7 illustrates the bend radiation and junction loss for bend radii ranging from 600µm to 2000µm and both the losses decrease almost exponentially. The bend radius in the designed gyroscope sensor is 15000µm so radiation losses in the sensor loop are negligible and a circular loop has no junctions. At 1400µm bend radius as might be used in say a directional coupler, the total loss from 2 junctions and a bend would be 0.059 dB (almost equal contribution from both losses). Furthermore, junction loss can be eliminated by having bends that adiabatically decrease bend radius from a large radius at the ends to the desired radius in the centre of the bend [176]. Doing so will increase the length of the bends though this can be managed.

3.3 Waveguide Fabrication Process

3.3.1 Silicon Nitride deposition

For waveguide fabrication, Si_3N_4 films are generally grown by chemical vapour deposition (CVD) techniques like plasma enhanced CVD (PECVD) and low-pressure CVD (LPCVD). Both processes have their own pro’s and con’s in terms of thermal budget and film quality.

PECVD offers Si_3N_4 films deposited at lower temperature which enables the possibility of monolithic integration of photonic circuits with CMOS based read-out electronics. Low residual stress films is another advantage of low temperature processes which allows the growth of thicker films because highly stressed films can delaminate or crack beyond a critical thickness. On the other hand, higher hydrogen content (20-25 at.%) present in PECVD Si_3N_4 films causes the formation of Si-H and N-H stretching bonds which give rise to strong absorbance peaks at around 2200 cm^{-1} and 3300 cm^{-1} wavenumbers respectively [177-179]. Overtones of the latter also cause a strong absorption feature at 1520nm with a tail that extends beyond 1550nm. Therefore PECVD is unsuitable for those applications requiring very low propagation loss unless deuterated source materials are used to move the absorption peak to longer wavelengths. This however requires very expensive gas feed stock and whilst possible is therefore not common practice. Loss can also be improved by high temperature annealing which significantly reduces the concentration of the above-mentioned bonds [180] but still extremely low loss numbers in the range of dB/m has not been reported for PECVD materials.

LPCVD relies on thermal decomposition of the reactants (usually ammonia and dichlorosilane) [181]. A surface temperature in the range of 600 °C to 800 °C is usually required for these reactions. Due to the high processing temperature, hydrogen content in LPCVD Si_3N_4 films is relatively small (2-10 at.%) which can further be reduced by annealing the films at even higher temperatures for longer times. A very low propagation loss of 0.7 dB/m has been reported in the literature [110] which led to fabricate high Q resonators. Therefore, the Si_3N_4 films studied in this thesis were deposited by LPCVD in the Research School of Engineering at ANU. A schematic of the LPCVD setup is shown in figure 3.8. For the deposition, wafers are placed in a quartz carrier inside the furnace. The deposition was carried out by reacting ammonia and dichlorosilane to form Si_3N_4 by the reaction shown in equation 3.11 below [182]:

$$3\,\mathrm{SiH_2Cl_2} \quad + \quad 4\,\mathrm{NH_3} \quad \rightarrow \quad \mathrm{Si_3N_4} \quad + \quad 6\,\mathrm{HCl} \quad + \quad 6\,\mathrm{H_2} \tag{3.11}$$

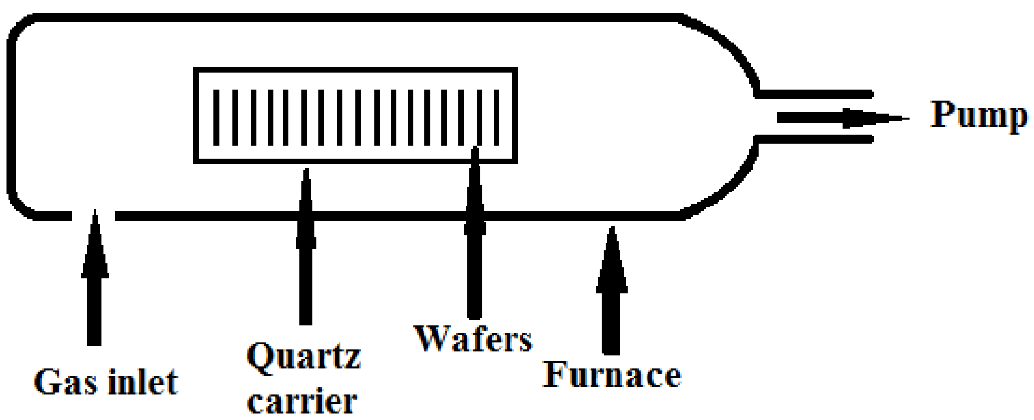

Figure 3.8: Schematic of the LPCVD employed to grow/fabricate silicon nitride films.

The Si_3N_4 deposition process used for this work is described as follows:

1. Wafers were placed inside the furnace and allowed to thermally equilibrate at a temperature of 775 °C in N_2 for 10 minutes
2. Furnace was pumped down to a pressure of 0.5 torr
3. Deposition started with turning on the gasses. Flow rate used was 30 sccm for dichlorosilane and 120 sccm for amonia. Deposition rate was typically 5 nm/min.
4. Gas supply turned off and tube pumped out
5. System is then allowed to cool down to room temperature
6. N_2 gas purged into the chamber to break the vacuum

3.3.2 Techniques used for the measurement of refractive index and thickness of films

The refractive indices and film thickness were measured by using a variable angle spectroscopic ellipsometer (J. A, Woollam) and dual angle spectroscopic reflectometer (SCI FilmTek 4000) for thin and thick films respectively. In the Filmtek system, the range of the wavelength spectrum is from 450nm to 1650nm. At two incidence angles (70^o and 0^o), spectroscopic reflection data are acquired to determine the properties of the films being measured. The film thickness and Lorentz oscillator parameters and the Tauc bandgap were varied in a nonlinear fitting procedure to fit to the obtained reflection data and so obtain the thickness and dispersion data, and fine tuning of the modal parameters and thickness was performed using an iterative least square root error minimization process. It has been reported that this system can measure the index/thickness with an accuracy of $2x10^{-5}$ for thick silica films [183].

An ellipsometer measures the change in the polarisation state of incident light upon reflection from the substrate and compares it to a model to extract index and thickness. An ellipsometer uses phase information in the polarisation states and can reach a resolution in the sub-nanometres range. Therefore, it is a suitable technique for very thin films (even for around few nanometers thick). It is important to note that most of the models in the ellipsometer assume that the sample is made of well-defined optically homogeneous layers. For this project, a J. A. Woollam M-2000D ellipsometer was employed. In this ellipsometer, the wavelength range was from 193nm to 1690nm. The system had the capability to scan the samples from 45^o to 90^o and measure the thickness with an accuracy of 0.1–0.2nm [184].

3.4 Photolithography

After measuring the refractive index and thickness (1.994 at 1550nm and 80nm respectively), 1.3μm thick photoresist (Clariant AZ 701 MiR) was coated onto the as-deposited Si_3N_4 films by using an SVG 8600 series track. The photoresist was soft baked at 90 ^oC for 1 minute in vacuum contact mode on the track hot plate to remove any solvent and enhance the adhesion to the Si_3N_4 film. The photoresist was then patterned using a Canon MPA 500 1:1 scanning projection mask aligner operating in broadband exposure mode (254-430nm). A Post exposure bake at 110 ^oC for 60 seconds was employed, followed by single puddle development in AZ MIF developer at room temperature for 60 seconds. Lastly, the wafer was hard baked at 120 ^oC for 1 minute to enhance the resistance of the resist during etching [185]. Photoresist deposition, development and baking was undertaken on the SVG 8600 series track to ensure run to run consistency. The outcome of this whole process is shown in figure 3.9.

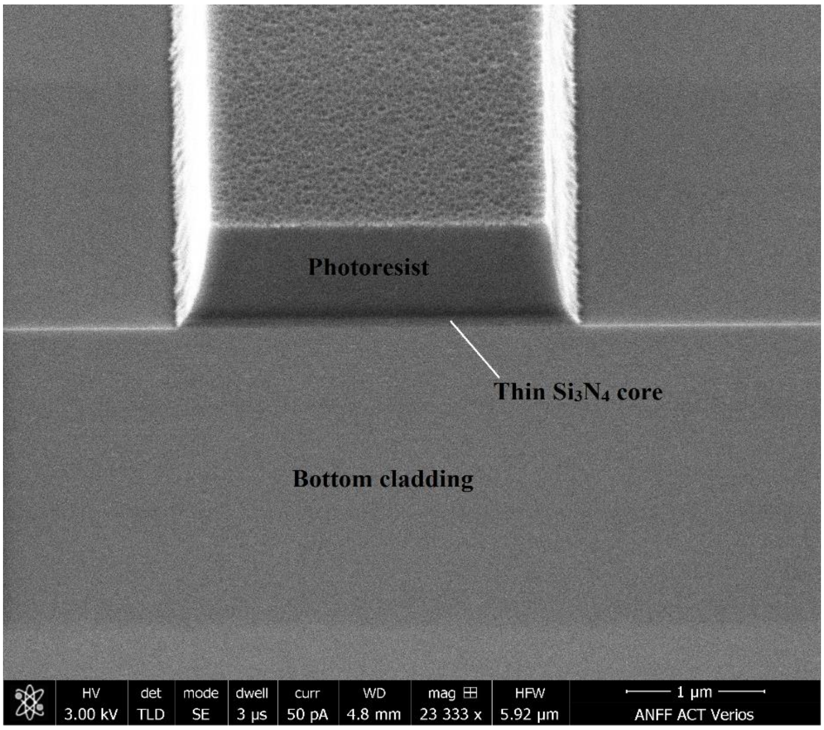

Figure 3.9: Showing the SEM image of a lithographed photoresist mask on thin Silicon Nitride core.

3.5 Plasma Etching:

Plasma etching is a widely used method in semiconductor electronic and optoelectronic processing for pattern transfer during the fabrication of devices. It is also known as dry etching as etching is carried out in gaseous phase with zero liquid used. It has numerous advantages over wet etching. For example, problems like undercutting, isotropy and reduction in polymer adhesion during wet chemical etching can overcome by highly anisotropic plasma etching plus it offers precise etching control and real time monitoring, cleanliness and compatibility with vacuum processing [186, 187]. Dry etching is most commonly of two types:

1) Physical sputtering
2) Reactive Ion etching (RIE)

In the first type of dry etching, the bombardment of highly energetic ions physically sputters the film. One advantage of this technique is that any material can be etched. However, it is not an extensively used method as there are a number of drawbacks associated with it. The sputtered material can be redeposited on the wafer which results an increase in the surface roughness, the etch rate is often quite slow and erosion of mask's corner often results in non-vertical etch profiles.

In 1974, Hosokawa et al. [188] introduced Reactive Ion etching which is now a widely used etching method. In this system, a wafer is placed on an electrode which is capacitively coupled to an RF source and forms the cathode of the plasma generator inside the vacuum chamber. The etching reaction can be initiated upon the introduction of gases and the RF field which breaks down the gas feed stock. One of the main advantages is that fairly safe gases can often be used as feed stock to the system, these being dissociated into highly reactive species by the plasma. For example, under normal conditions, CF_4 is an inert gas but generates many free radicals in the plasma state which react with silicon and form SiF_4 (by-product) which then is pumped out of the chamber. At the same time, positively charged ions in the plasma accelerate towards the cathode and physically sputter the film. This action enhances the vertical etch rate because ions are being accelerated normal to the substrate surface. This will result in an etch profile that has minimal undercut and is strongly anisotropic [189].

In RIE, another important factor is volatility of the by-products. Any non-volatile by-products in the chamber will remain on the wafer surface and create problems in the form of roughness and micro-masking which often results in reduction in the etch rate. Therefore, gases should be chosen carefully and their chemistry has to be matched with the films being etched in order to produce volatile by-products. Chemical reaction and by-products can also be controlled by wafer temperature, plasma generation power and pressure inside the chamber in addition to choosing suitable gases [190].

Dry etching has produced extremely smooth and flat sidewalls in silicon nitride and many other materials for photonics based devices. In optical waveguide technology, sidewall roughness induced by the lithography and etching process reflects the process quality and determines the waveguide propagation loss. The sidewall roughness loss is approximately dependent on the product of the interface root mean square roughness squared and the index contrast squared [191, 192]. Sidewall roughness is the main parameter which determines the propagation loss in high index contrast waveguides as most of the mode field resides inside the core and consequently interacts with the sidewalls. Therefore, fabrication process quality becomes more significant in such cases.

Fabrication of waveguides for this work used a combination of dry and wet etching processes. Photoresist patterns were transferred by using dry etching for all the processes. However, photoresist removal is carried out by wet etching with pre and post removal O_2 plasma treatment. A sidewall roughness of 6nm rms was achieved which can further be reduced by optimizing the etching process.

3.5.1 Available gases and their selection for etching

In RIE, the selection of gases is extremely important for etching. The gases need to/(should) be reactive with the materials being etched to form chemical species that are volatile at the processing temperature and also ideally produce polymerizing species which passivate the sidewalls and help to obtain the highly anisotropic etching profile. The process parameters and the gas mixture are chosen in a way that the sidewall polymer is not etched in the process whilst concurrently etching it from the horizontal surfaces. Halogen containing gases such as CHF_3, CH_3F, CF_4, Cl_2 and HBr are commonly used to etch glass and semiconductor materials [193, 194].

Fluorine and Chlorine are mostly used to etch silicon compounds and Ga, Al and As containing III-V compounds respectively. Other gases such as Hydrogen and Methane are also used to etch various compounds such as (II-VI, III-V and IV-VI). Methane dually aids the etching process by:

(1) producing volatile metallo-organic compounds

(2) forming C_nH_m (active radicals) and $C_nH_m^+$ (ions) which act as a precursor and produce polymer for sidewall passivation.

Plasma etching process can also be aided by dilutants such as Nitrogen or Argon. It helps to stabilise the plasma and restrict over polymerization by providing additional ions. Therefore, to achieve the required etch rate and selectivity, gas mixture must be carefully selected. Several gases (SF_6, O_2, C_4F_8, CHF_3, H_2, CH_4 and Ar) were available in the ICP used in this thesis to optimize the recipe.

3.5.2 Etching system

An inductively coupled plasma (ICP) system, PlasmaLab 100 from Oxford instruments, was used to perform the Si_3N_4 etching work for this thesis. The block diagram of the system can be seen in figure 3.10.

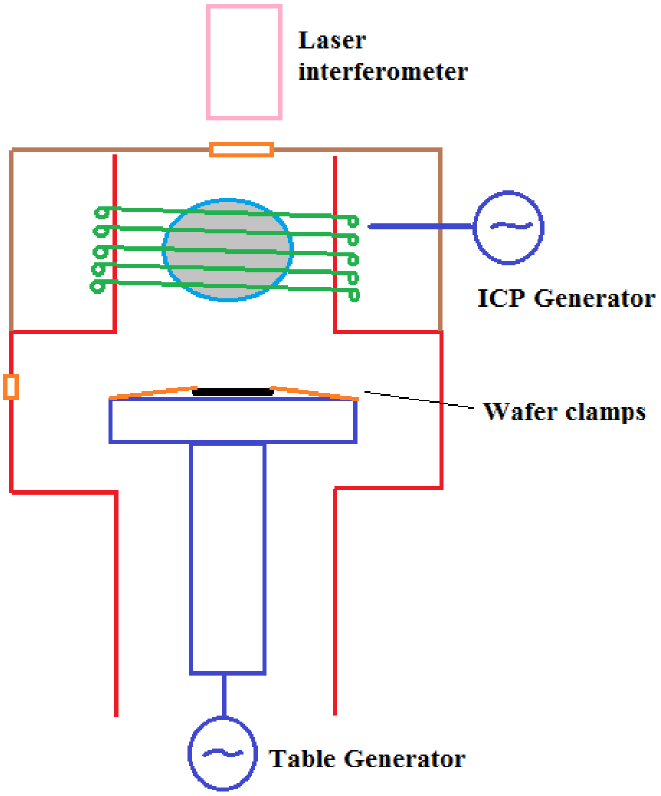

Figure 3.10: Schematic diagram of the inductively coupled plasma (ICP) etching system.

The ICP system had two chambers (loading and sample chamber) and both are pumped down separately. A high capacity Turbomolecular pump is used to maintain the pressure of the main chamber along with a position-controlled gate valve acting as an automatic pressure controller. Initially, the etching chamber pumped down to around ~$2x10^{-6}$ torr and then gases can be introduced up to 100 sccm flow rate. The system maintains a pressure of ~8 mTorr at 100 sccm flow. The operating pressure can be increased up to 100 mtorr with the APC but practically the machine had tolerance issues at that high a pressure. Mass flow controllers (MFCs) are used to control the flow of etch gases. A 3KW RF power source is used to drive the induction coil at 13.56 MHz. The wafer was placed in the loading chamber, transferred into the main chamber and held in place by a 3 point mechanical clamp. The temperature of the lower electrode is controlled by water cooling which can be set between 10 ^{o}C and 90 ^{o}C. Helium gas is available to be used as heat transfer medium between lower electrode and wafer but never used as all the etching work was performed at 20 ^{o}C. An in-situ laser interferometer operating at 677nm was used to monitor the etch rate and end point etching of transparent thin films.

3.6 Sample Imaging by Scanning Electron Microscopy (SEM)

The waveguide surface morphology and etched profile were studied using a scanning electron microscope. In SEM, a focused electron beam is scanned over the sample surface to produce an image by detecting the emitted electrons. As can be seen in figure 3.11, the sample interaction with the electron beam generates various signals, each possessing specific sample information.

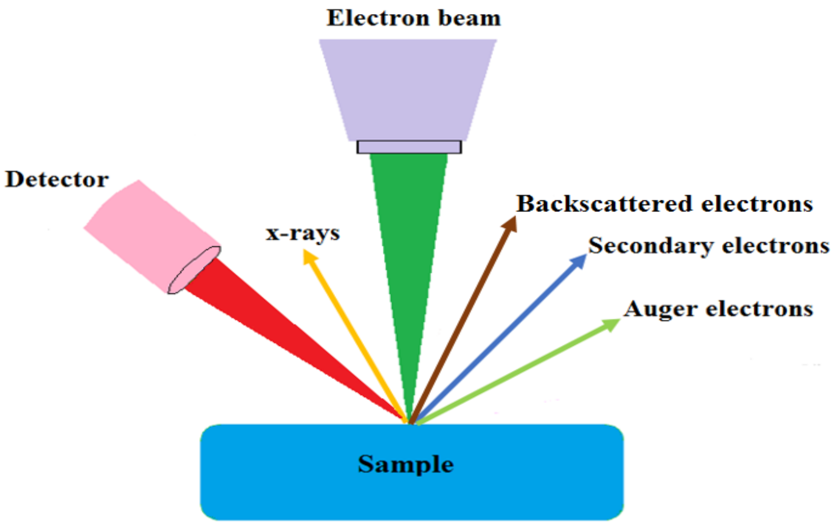

Figure 3.11: Showing the different types of signals generated when electron beam interacts with the material being scanned.

Among the different signals, information related to surface morphology is carried/retained primarily by secondary electrons and in greater topological contrast and atomic number contrast by backscattered electrons. Nanoscale resolution can be obtained in both these modes by capturing them with appropriate detectors. Secondary electrons are referred to as electrons ejected from the outer shells of the surface atoms due to the inelastic interaction between the electron beam and sample and they possess a very low energy of less than 50 ev. Electrons knocked out from the inner atoms of the sample are trapped by the surrounding material because of their low energies and cannot escape the sample surface. Therefore, electrons ejected from the top few nano-meters of the sample surface only contribute to the image.

On the other hand, backscattered electrons are generated by the elastic interaction between the electron beam and sample. The yield of backscattered electrons is proportional to the atomic number of the surface atoms. They are useful in determining the chemical composition of a sample made of different atomic compositions depending on the fluctuations in the intensity of the backscattered electrons with the atomic size.

For this project, an FEI Helios 600 NanoLab SEM was used to investigate the waveguide etched profile in order to optimize the etching process. This system can capture an image with a resolution of around 1nm.

3.7 Si_3N_4 Etching:

Different Si_3N_4 etching recipes have been reported in the literature, e.g. [195, 196], but results do not directly translate between different etch tools, and recipes mostly need to be optimised on every other system type. The following section discusses optimisation the Oxford Instruments ICP-100 system which also behaved differently upon changing the turbo pump after a failure.

3.7.1 CHF_3 and SF_6 based plasma etching:

Halogen containing gases like CHF_3 and SF_6 are extensively employed for etching different materials [197, 198] and have produced smooth sidewalls in waveguides. The mixture of these gases form plasma which contains fluorine (F) and Fluorocarbon (CF_x) radicals. The role of both these radicals has been reported in numerous studies [199]. The CF_x (x = 1, 2, 3) radicals, specially CF_2, are responsible for the formation of polymer which is deposited on the sidewalls during etching to protect the waveguide profile to achieve anisotropic etching [200]. The F radicals act as a chemical etching agent and form volatile products by reacting with compounds [201]. Therefore, Si_3N_4 films may be etched by using a standard silicon etch recipe for the ICP system and gas flow's as well as etching conditions can be seen in table 3.1. The etching rate for Si_3N_4 was 32 nm/minute.

Table 3.1: Showing the gas flows and etching parameters used to etch Si_3N_4 before changing the vacuum pump.

Parameters	Values
CHF_3	50 sccm
SF_6	2.5 sccm
ICP power	200 W
Pressure	15 mtorr
Table power	15 W
Temperature	20 ^oC

This recipe served pretty well and produced smooth sidewalls with an estimated roughness of around 6nm rms. The line edge roughness was measured from a SEM image similar to that shown in figure 3.12 for a film 170nm thick. Unfortunately, the cross-section images of the waveguide were not taken during SEM imaging of this sample.

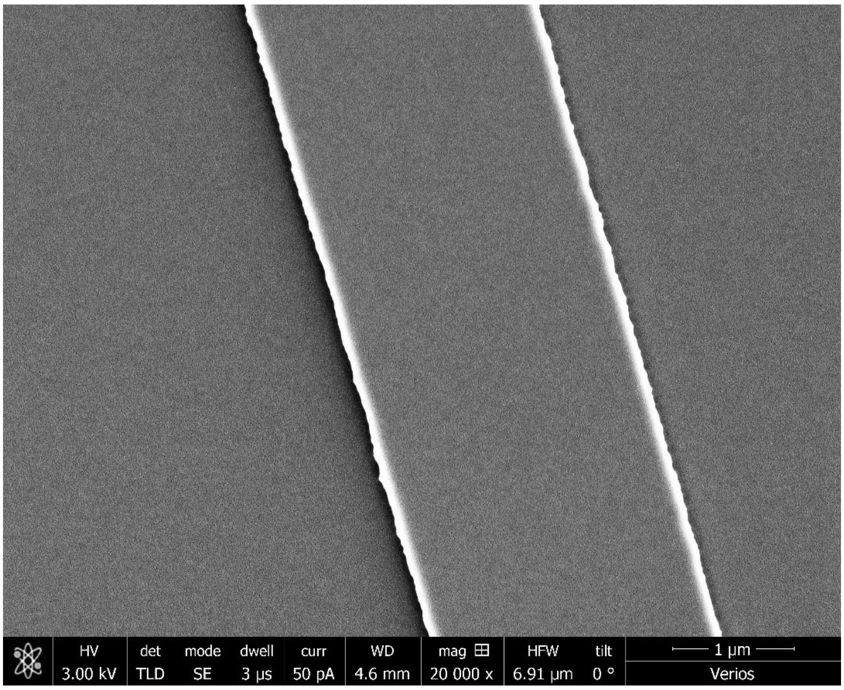

Figure 3.12: Top view of a Si_3N_4 waveguide etched with CHF_3 and SF_6.

At this point the etcher's turbo pump suffered a catastrophic failure and was replaced with another brand with the same notional specifications. After changing the turbo pump, Si_3N_4 films were etched again with the same recipe but the same level of sidewall roughness could not be attained. Despite much effort in process refinements, the same level of sidewall roughness (around 6nm) could not be recovered for reasons that are not clear at this time.

3.7.2 CHF_3/Ar based etching of Si_3N_4

Before the pump replacement, Si_3N_4 films were also etched by a standard oxide etch recipe for the ICP system to investigate if this process improves the sidewall roughness as compare to those waveguides etched with a silicon etch recipe. The gas flow's and etching parameters for this process are tabulated in table 3.2.

Table 3.2: Showing the gas flows and etching parameters used to etch Si_3N_4 before changing the vacuum pump.

Parameters	Values
CHF_3	50 sccm
Ar	50 sccm
ICP power	0 W
Pressure	30 mtorr
Table power	250 W
Temperature	20 ^oC

Ar addition helps the etching process in two ways, (i) Physical sputtering results in a reduction in the etch by products formed during chemical etching, (ii) it also enhances the chemical etching by breaking bonds, making the film more accessible and the surface more reactive to the etchant species [202, 203]. Therefore, Ar flow was optimized by doing number of experiments. The SEM image of an etched waveguide 170nm thick is shown in figure 3.13.

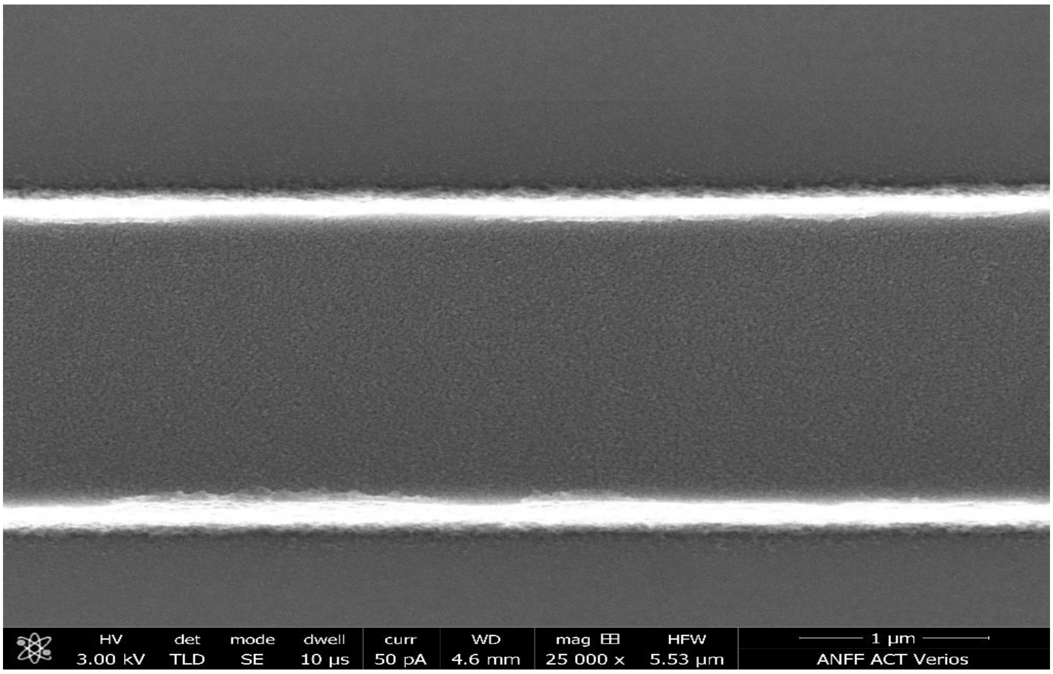

Figure 3.13: Exhibiting the top view of a Si_3N_4 waveguide etched with CHF_3 and Ar before changing the vacuum pump.

The sidewall roughness could not be estimated due to the bright line edges but the result looks fairly smooth. Si_3N_4 waveguides were also etched by using the same gas flow's and etching parameters after the pump replacement but the same level of sidewall roughness could not be attained due to unknown reasons. After investing significant amount of time, it was concluded to optimise etching with another recipe.

3.7.3 CHF_3/O_2 based etching of Si_3N_4

The etching of Si_3N_4 by using CHF_3 and O_2 gases has also been reported in the literature [204]. Therefore, a recipe containing CHF_3 and O_2 gases was optimized to achieve smooth sidewalls and optimized etching parameters are tabulated in table 3.3.

Table 3.3: Illustrating the gas flows and etching parameters used to etch Si_3N_4.

Parameters	Values
CHF_3	30 sccm
O_2	1.5 sccm
ICP power	0 W
Pressure	20 mtorr
Table power	150 W
Temperature	20 ^oC

Figure 3.14 shows the sidewalls of the waveguide etched with the optimized recipe tabulated above. This is the best line edge roughness we could achieve by CHF_3/O_2 plasma chemistry.

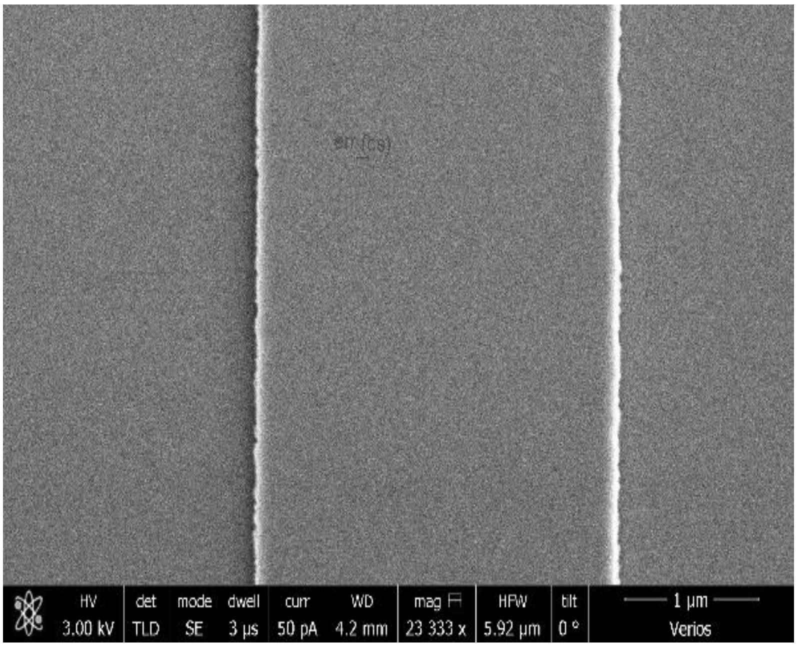

Figure 3.14: Showing the top view of a Si_3N_4 waveguide etched with CHF_3 and O_2.

After analysing the results obtained through all the recipes, it was decided to etch Si_3N_4 by

CHF_3/O_2 plasma chemistry to achieve smooth sidewalls and consequently low loss waveguides.

3.8 Silica Cladding Optimization:

For high index contrast thin waveguides, most of the mode field is in the upper and lower cladding, therefore cladding material and thickness must be chosen carefully. Silicon dioxide (SiO_2 or silica) is the most widely used material as cladding because the optical loss of silica is extremely low from visible to near IR which makes it a suitable option [205]. Silica can be deposited by various techniques but the Plasma Enhanced Chemical Vapour Deposition (PECVD) technique was available locally to deposit silica for this work. The biggest advantage of using PECVD is that silica can be deposited at temperatures below 400 ^{o}C making it compatible with CMOS back end of line processing in principle, and aiding compatibility with other more exotic materials for hybrid integration. However, silica films deposited by PECVD at lower temperatures typically have high Si-H and Si-OH concentrations and are more porous than those deposited at higher temperature. To remove these impurities and improve the film quality, PECVD processes can be optimised by changing various deposition parameters including gas flow rate, pressure, substrate temperature, RF power and post deposition processing like temperature and environment of the annealing process. The schematic of a typical PECVD chamber is shown in figure 3.15.

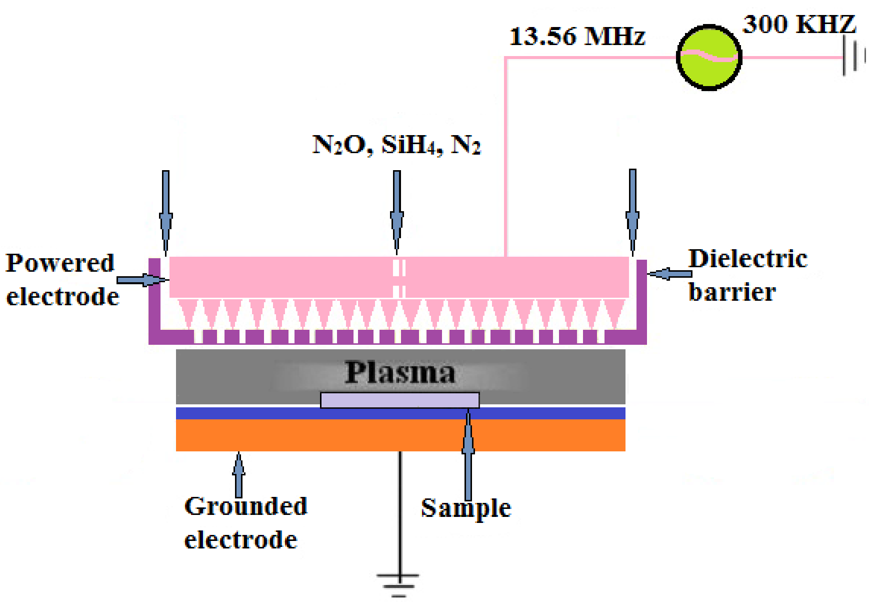

Figure 3.15: Schematic representation of a PECVD system.

The refractive index of the silica can also be tuned over a significant range (1.48 to 1.444 at 1550nm) by modifying the deposition parameters. At a given substrate temperature, the influence of the N_2O/ SiH_4 flow ratio was investigated to achieve the target refractive index of 1.444 which is the refractive index of the thermal oxide (undercladding).

Annealing was then performed to completely remove the Si-H and Si-OH impurities. The refractive index of the films and strength of the hydrogen bonds was characterized using the Filmtek and Fourier Transform Infrared Spectroscopy (FTIR) respectively. The constant parameters used to deposit all the silica films can be seen in the table 3.4,

Table 3.4: deposition parameters for PECVD silica films.

Temperature (°C)	Pressure (mtorr)	N_2 Gas flow (sccm)	HF (W)
300	150	161	20

N_2O/ SiH_4 gas flow ratio was significantly modified to greatly reduce the refractive index from 1.482 to 1.451 as shown in figure 3.16.

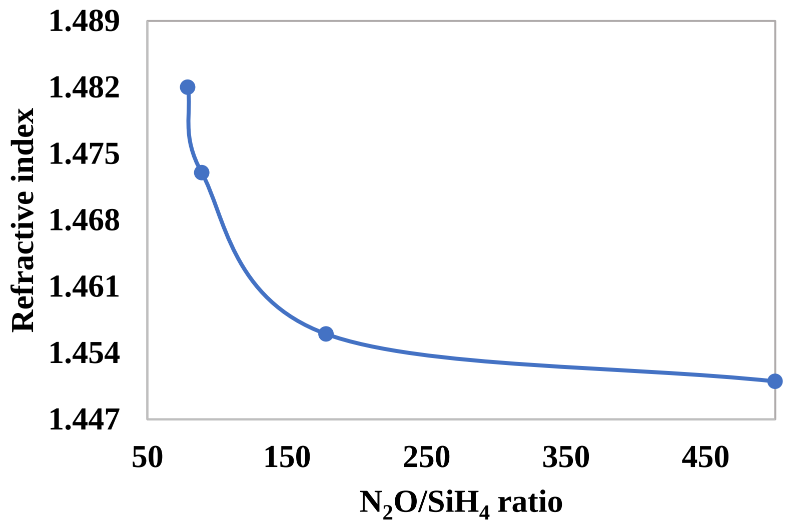

Figure 3.16: Illustrating the influence of N2O/SiH4 flow on silica refractive index.

The refractive index when flowing large amounts of the oxidiser N_2O would intuitively be expected to be lower than when flowing larger amounts of the silicon source material SiH_4 due to a larger O:Si ratio in the plasma. Therefore increases in the N_2O/ SiH_4 gas flow ratio should be correlated with a reduction in the refractive index. This was indeed what the data of fig. 3.16 shows. As can be seen, to reach the target value of refractive index would require a very much higher N_2O/ SiH_4 gas flow ratio than could be accommodated with the mass flow controllers installed in the machine. For further reduction in the refractive index, the chamber pressure was increased from 150 mtorr to 300 mtorr. It has been reported that higher chamber pressure increases the deposition rate [206] due to an increase in the residence time that occurs for the precursor gases. More Si radicals are created/formed and contributed to the growth of the film due to higher disassociation efficiency of SiH_4 when the residence time is longer. Higher deposition rate leads to an increase in the Si-H and Si-OH concentration/impurities and a reduction in the film density due to the inclusion of these species into the SiO_2 lattice [207] which ultimately reduces the refractive index. A refractive index as lower as 1.448 was achieved at the end.

3.9 Thermal Annealing

For this project, thermal annealing was investigated to determine the effects on the reduction of the S-H and N-H impurities in LPCVD silicon nitride and the Si-H and Si-OH species in PECVD silica films. Annealing environment, temperature and time were optimised for both materials. A conventional horizontal tube furnace (Lindberg 1500 °C) was employed to carry out the thermal annealing in different ambient conditions (Air, N_2 and Ar gases). Before being injected into the furnace, the gas was filtered/treated with a moisture absorbing filter. Samples were initially placed in a quartz boat which was then slowly pushed towards the heated zone of the furnace tube with the help of quartz rod. This process usually took around 1-2 minutes. After annealing, the furnace cooled down according to the rate set at the start of the process and samples can be pulled out of the tube in the same way as they were placed into the tube. The samples were annealed from 400 ^{o}C to 1100 ^{o}C for different times. The temperature ramped up/down rate was 5 ^{o}C/minute. The slow ramping rate was chosen to avoid any crack or delamination issue which could arise due to the rapid change in the thermal environment. The annealing temperature and time analysis of silica films is given in the next section.

3.10 Fourier Transform Infrared Spectroscopy (FTIR)

After achieving the desired refractive index during PECVD deposition, the next target was to remove the hydrogen from the film by annealing it at a suitable temperature. Initially, the film was annealed at 500 ^{o}C for different times to optimize the annealing time where hydrogen is almost completely removed. The FTIR spectra of the as deposited and annealed films are shown in figure 3.17.

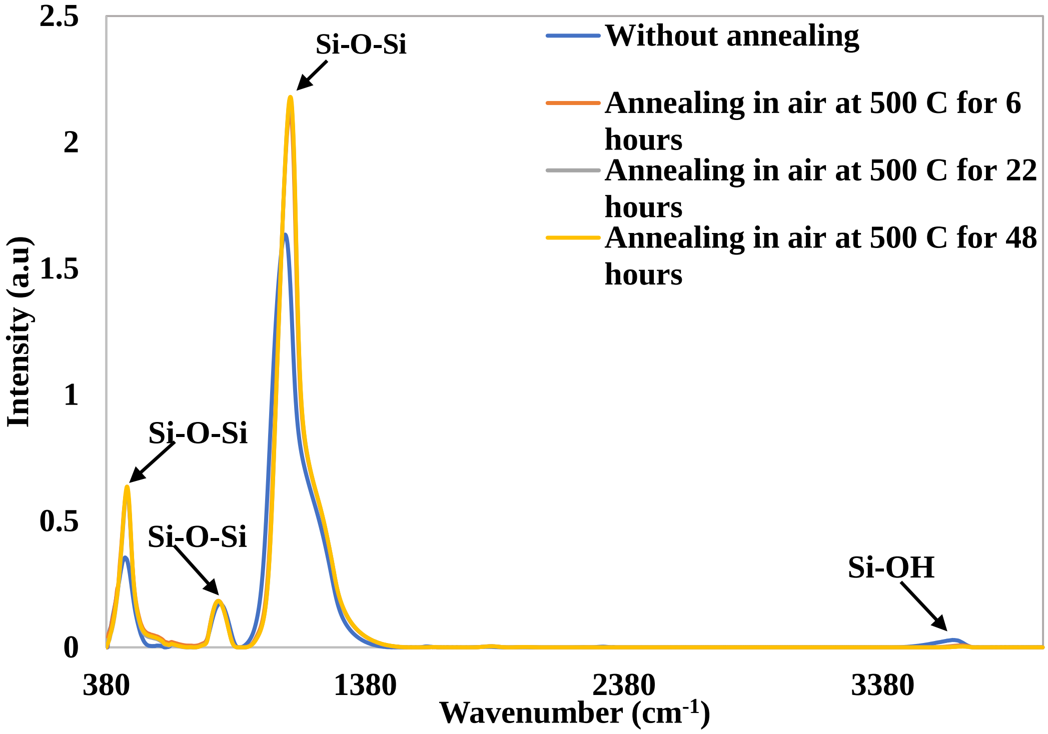

Figure 3.17: FTIR spectra of PECVD silica film annealed at 500 C for different times.

Figure 3.17 shows the absorbance spectra of PECVD as deposited and annealed silica films at 500 ^{o}C for three different times. Three peaks around 1100 cm^{-1}, 817 cm^{-1} and 466 cm^{-1} correspond to stretching, bending and rocking of normal Si-O-Si bonds present in amorphous silica respectively [208-210]. After annealing the concentration of these normal bonds is seen to increase. A band around 3660 cm^{-1} can also be seen which correlates to stretching mode of the Si-OH bond [211]. Due to the scaling of the vertical axis, the reduction in hydrogen content after the annealing is not clearly visible. Therefore, the same graph is rescaled and shown in figure 3.18,

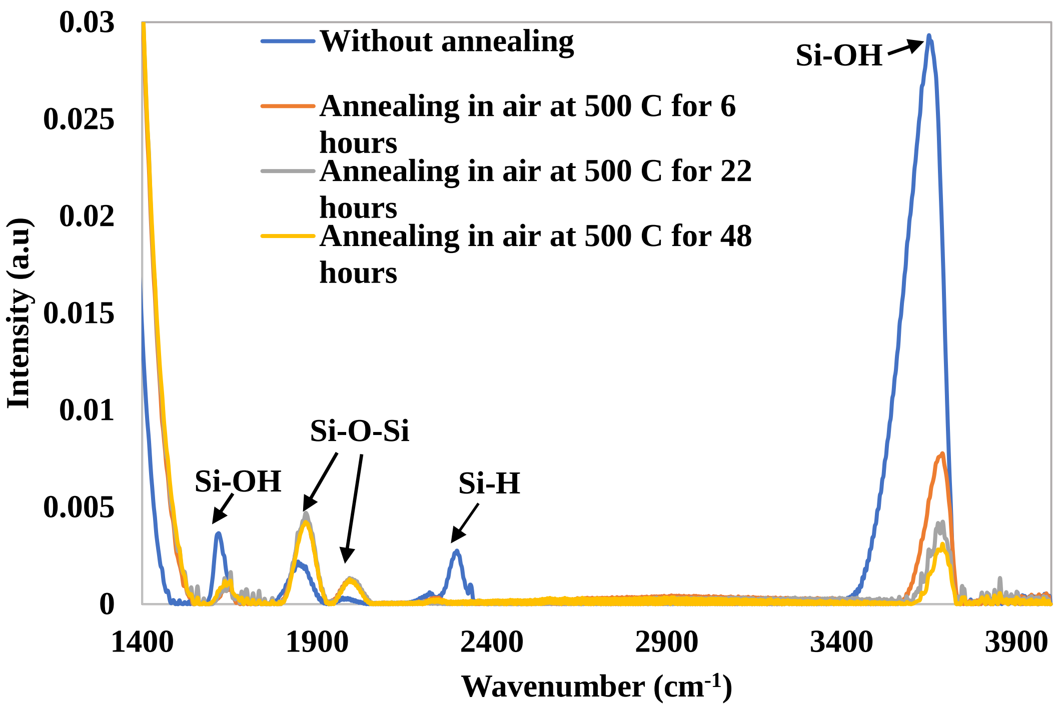

Figure 3.18: Showing the rescaled version of figure 3.17.

Figure 3.18 reveals two more Si-O-Si peaks around 1850 and 2000 cm^{-1} [211], these again increasing after annealing indicating normalisation of the silica film. The Si-OH and Si-H bond peaks at 1630 and 2304 cm^{-1} respectively are also visible in the as deposited film [212-214] but are almost completely removed upon annealing. The intensity of the Si-OH bond at 3660 cm^{-1} is significantly reduced after the annealing and suggests longer annealing time or higher temperature annealing is required to completely remove it. Therefore, SiO_2 films were annealed at 800 ^{o}C for three different times and the rescaled image is shown in figure 3.19,

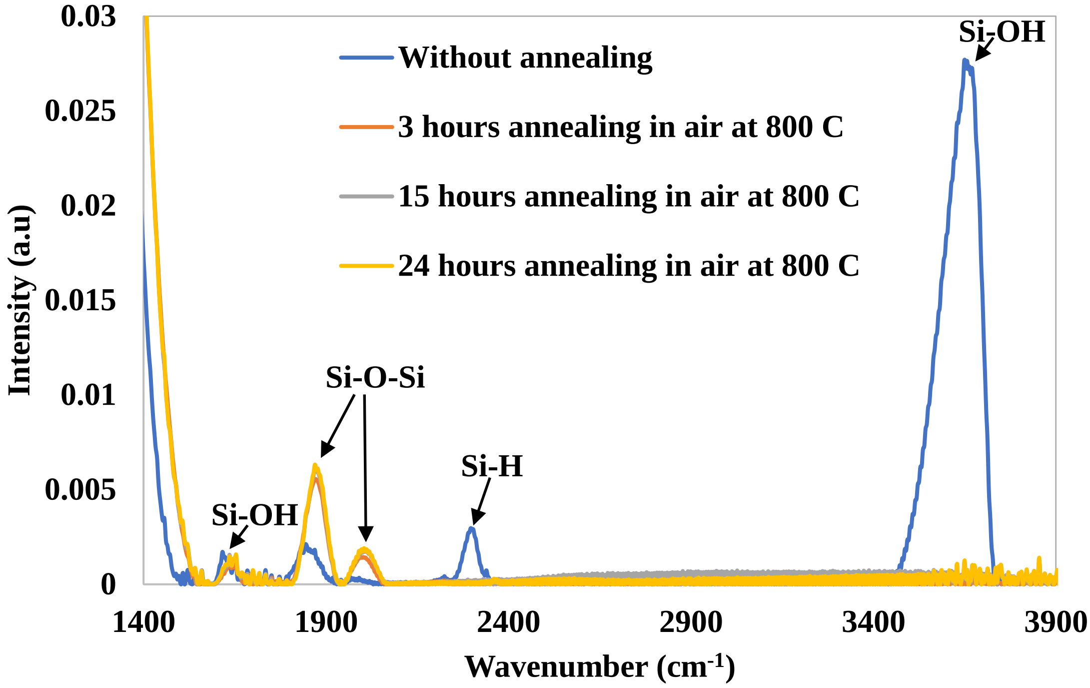

Figure 3.19: FTIR spectra of silica film annealed at 800 ^{o}C for three different times.

The main Si-OH band was completely removed after annealing at 800 ^{o}C even for three hours. Based on the results presented in figure 3.19. it can be concluded that the waveguides cladded with silica can be annealed at 800 ^{o}C for the maximum of 3 hours to completely remove the hydrogen concentration from the silica cladding. However, it is important to note that more work needs to be done to find out the minimum temperature and time required to remove OH band from the PECVD silica films. The optimum annealing temperature would at least be more than 500 ^{o}C which is already above the backend-of-the-line (BEOL) tolerance. This makes the PECVD silica cladding unsuitable for the integrated optics applications.

3.11 Diced End Facets

The basic function of a dicing saw is to separate the processed silicon or glass wafers into individual chips using resin or nickel bonded diamond blades rotating at up to 30000 rpm. The sample is placed on dicing taper held to the translation stage by a vacuum chuck, and its speed under the blade can be optimised according to the requirements. All the dicing is done under water to control the blade and sample temperature and its flow rate is optimised beforehand. Before slicing the sample, the blade is dressed in a 100mm silicon wafer to remove any contamination and to expose fresh new diamonds for a clean cut. For this work, a DISCO DAD 321 dicing saw was used to develop a process to obtain smooth waveguide facets in order to perfectly butt couple them with fibre to minimize the insertion loss. Besides translation and rotational speed, dicing also largely depends on the grit size of the blade. It has been reported that a small diamond size (large grit size) provides a better quality cut for brittle materials. However, if the diamonds are too small then the blade will wear quickly and affect the cut quality as dicing proceeds. Nickel bonded blades comes in greater range of smaller grit sizes as compared to resin bonded blades. Therefore, nickel blades were used to cut the wafer from the top around 100µm and then the underlying silicon was diced with a resin blade by flipping the wafer. All the dicing parameters were optimized and an rms roughness of around 6nm was achieved for both Ge:SiO_2 and Si_3N_4 diced surfaces. With the use of index matching fluid this was certainly good enough to have negligible impact on the coupling losses.

3.12 Waveguide Loss Measurement

Propagation loss is one of the most important parameters to characterize an optical waveguide. It essentially determines the quality of the whole fabrication process starting from film deposition to etching and upper cladding deposition. Waveguide loss is usually measured by launching light from one end of the waveguide and receiving the transmitted light at the other as shown in figure 3.20. The light was coupled into/out of the waveguide by using lensed tip or Ultra-High Numerical Aperture (UHNA) fibre and the loss spectrum was recorded by employing an Optical Spectrum Analyzer (OSA) and “white light” source (either a phtonic crystal fibre based supercontinuum source or an erbium doped fibre amplifier). Total loss is the sum of input/output coupling loss of the waveguide, propagation loss of the waveguide and Fabry-Perrot cavity loss within the chip. The latter loss source originated due to relatively high reflectivity facets.

$$L_{total} = L_{coupling} + L_{cavity}$$

Here, $L_{coupling}$ represents the overlap loss due to mode field mismatch between fibre lens and waveguide at both ends of the waveguide. Whereas L_{cavity} manifests the propagation loss of the waveguide and Fabry-Perrot induced loss.

There are number of methods to measure or estimate the propagation loss of a waveguide; coupling loss removal by calculation, scattering streak measurement, the Fabry-Perot method and the most widely used conventional cut back method.

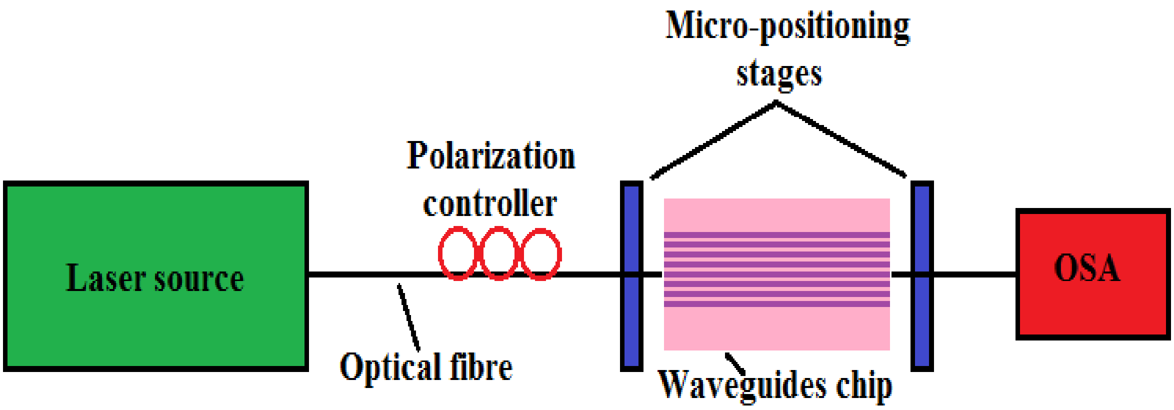

Figure 3.20: Schematic of the experimental setup used to measure the propagation loss of a waveguide.

In the cut back method, waveguide insertion loss is measured at different lengths, often by cutting back the chip length or by using serpentine or spiralled waveguides of different lengths on the same chip. For all lengths, the coupling losses are considered to be constant and the only loss component that changes with length is the propagation loss. Therefore, propagation loss can be obtained by plotting a graph between total insertion loss and waveguide length. The accuracy of this method totally depends on the consistency of the waveguide coupling losses (i.e. cleave/facet quality and fibre to waveguide alignment at both ends).

Apart from cutback, the other loss measurement techniques noted above are non-destructive. In the scattering streak method, the light scattered out of the waveguide during propagation is imaged/captured and its intensity is plotted against distance to evaluate the loss of the waveguide. However, this method is limited by a number of effects (scattering of the un-coupled light, waveguide inhomogeneities, induced noise in the signal and digital noise, etc) and this results in a lower limit of measurable attenuation somewhere around the 0.2 dB/cm level under ideal circumstances.

The coupling loss calculation technique involves the experimental loss measurement of a waveguide from which the calculated input and output coupling losses are subtracted and the remaining loss is divided by the waveguide length to yield average propagation loss. Coupling losses are the sum of the mode field mismatch between fibre and waveguide at both ends and any reflection losses.

In the Fabry-Perot method, the finesse of a cavity which is formed as a result of the reflections between the two facets of the waveguide is measured and the propagation loss is extracted by calculation for the presumed facet reflectivities. It is therefore highly sensitive to the actual facet reflectivity which can vary significantly from the expected value due to contamination, non-perpendicularity, roughness, etc. Also, the method does not work well for waveguides with relatively low end reflections including those made in this work.

Although both the Fabry-Perot and coupling loss calculation methods are non-destructive and convenient, at the same time they are potentially not as accurate as the conventional cutback. In case of coupling loss calculation, the coupling loss is usually underestimated due to imperfect cleaving which thereby means the calculated loss is usually an upper limit to the waveguide propagation loss. Beam launch efficiency actually depends on two factors, facet angle as well as the direction of the beam with respect to the waveguide [215]. As chips are often hand cleaved with a diamond scriber, it is extremely difficult to precisely control the cleaving angle. Also, the amount of light reflected by the waveguide facets depends on the roughness of the facets [216].

The cut back method was chosen as the method to measure waveguide propagation loss in this case by employing three spiral lengths on the same die with all waveguides being closely co-located to minimise facet effects. The picture of the chip layout is shown in figure 3.21:

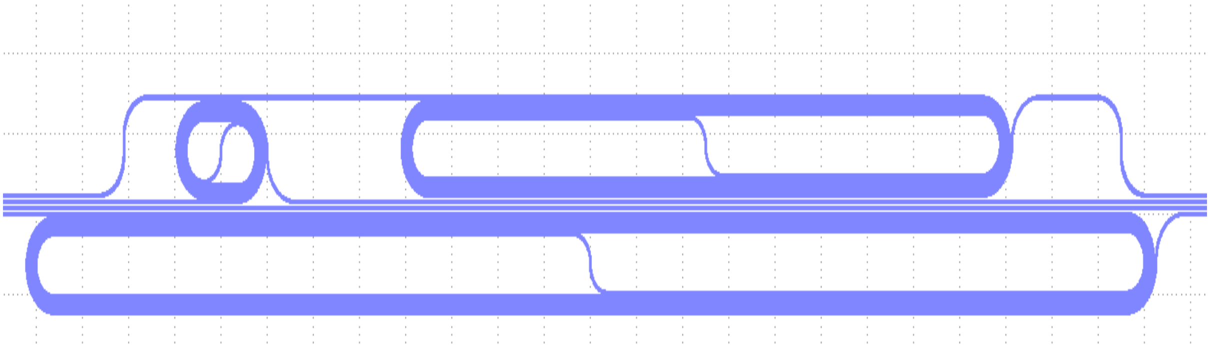

Figure 3.21: Illustrating the layout of a chip used in waveguide fabrication.

The chip is comprised of three set of spirals and one set of straight waveguides. Each set have 5 waveguides, All the spirals have same number of bends with a minimum bending radius of 650µm which is way less than used to optimise optical gyro performance. The spirals have a length of 11cm, 34.5cm and 57cm for smaller, medium and longest spirals respectively. Whereas the straight waveguides are 7cm long.

3.12.1 Theoretical estimation of the loss

The propagation loss of the Si_3N_4 waveguide was estimated by computing and adding scattering loss, substrate radiation loss and bending loss from 800nm to 1600nm. Instead of using the optimized single-mode single-polarisation waveguide dimensions mentioned in section 3.2.1, a bit thicker (170nm) and wider (2.8μm) waveguide dimensions were used. At the time of computing the loss of Si_3N_4 waveguides, it was found that the optimized PECVD silica cladding is giving some contamination issues. A lot of shower head patterns comprising areas of high particle density in arrangements identical to those of the PECVD upper electrode were found on the substrates. Due to the unavailability of the upper silica cladding, it was decided to design and fabricate air cladded Si_3N_4 waveguide to estimate and measure the propagation loss, respectively. Single-mode single-polarisation waveguide dimensions (80nm & 2μm) with air cladding are too thin to support any modes at longer wavelengths and cannot be used to estimate or measure the propagation loss. Therefore, thicker and wider (170nm & 2.8μm) waveguide dimensions were employed to design and fabricate air cladded Si_3N_4 waveguides. This route was chosen to compare the theoretical and experimental loss results of air cladded Si_3N_4 waveguides.

Scattering loss was computed approximately using the effective index method to reduce the 2-D waveguide cross section to an equivalent slab waveguide, whereupon the Payne-Lacey [192] sidewall roughness model can be applied. This requires the effective index be applied in the vertical direction so that the waveguide sidewalls become the slab cladding with the same roughness parameters as the waveguide sidewalls. This type of 2-D approximation is good to about a factor of 2 compared to experimental data for silicon nanowires for example [217]. The sidewall roughness and correlation length used in the modal was 6nm rms and 100nm respectively corresponding to the sidewall roughness measured on a waveguide as noted earlier. For bending loss, the minimum bending radius used was 650μm. The computed loss spectrum for a 170nm thick and 2.8μm wide Si_3N_4 waveguide with air cladding is shown in figure 3.22.

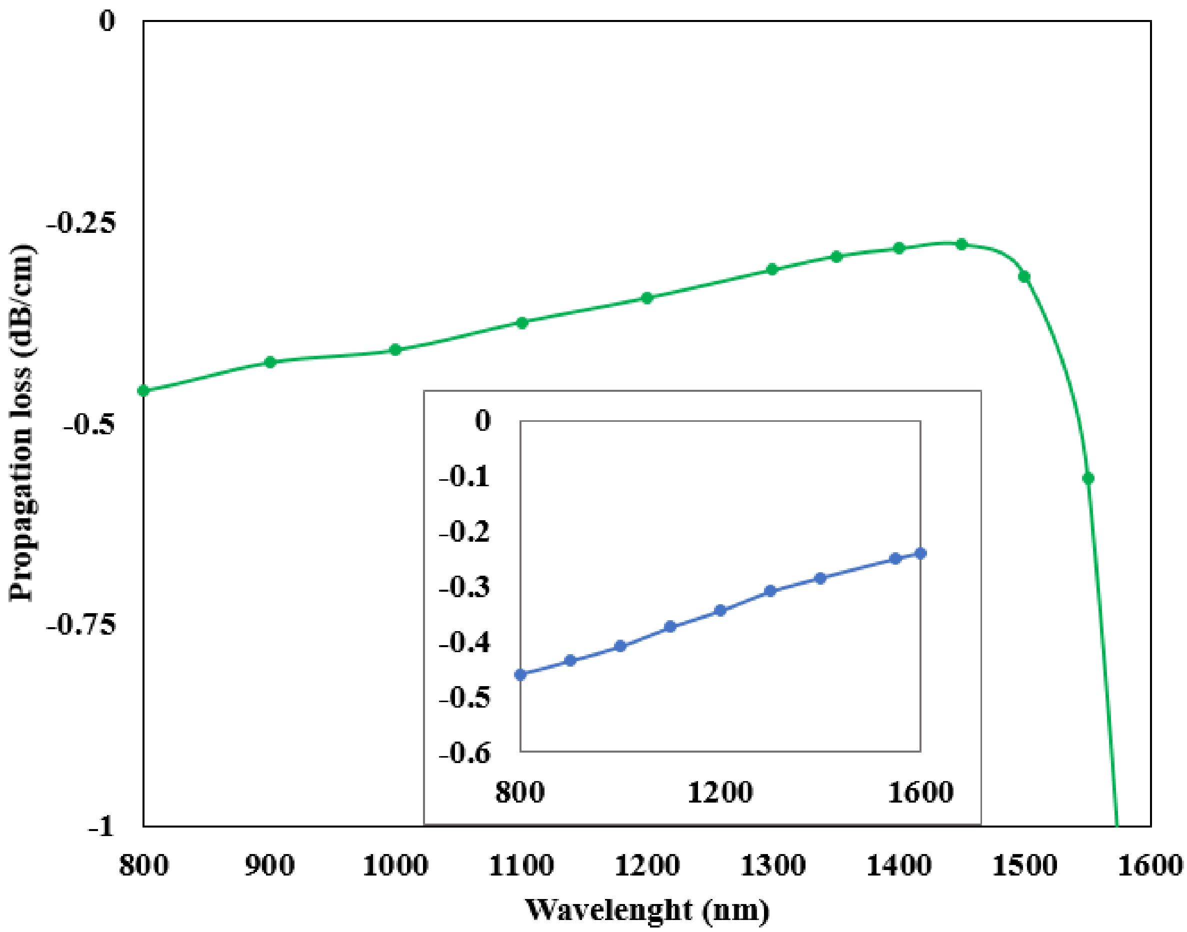

Figure 3.22: Computed spectral loss curve comprising the sum of sidewall scattering loss, substrate radiation loss and bending loss for air clad Silicon Nitride waveguide 170nm thick and 2.8 microns wide. Inset shows only the scattering loss without cladding.

The refractive index of the Si_3N_4 used in the modal was measured with the Filmtek for all the wavelengths. Substrate radiation loss was almost zero until 1400nm and then increased exponentially. The exponential increase at longer wavelength corresponds to the increase in the mode field size at those wavelengths. The low refractive index top cladding also pushes the mode field down into the substrate (silicon) which results in a huge amount of optical loss. It is evident from the figure 3.22 that the overall loss curve behaves almost same as the scattering loss until 1400nm which suggests that only the scattering loss exists until that wavelength. The increase in loss at longer wavelengths can be overcome by using silica as top cladding which have a refractive index of 1.444 at 1550nm. Since scattering loss is the dominant loss component if substrate radiation loss is ammeliorated, it was computed for all the wavelengths with 5µm silica top cladding and is shown in figure 3.23.

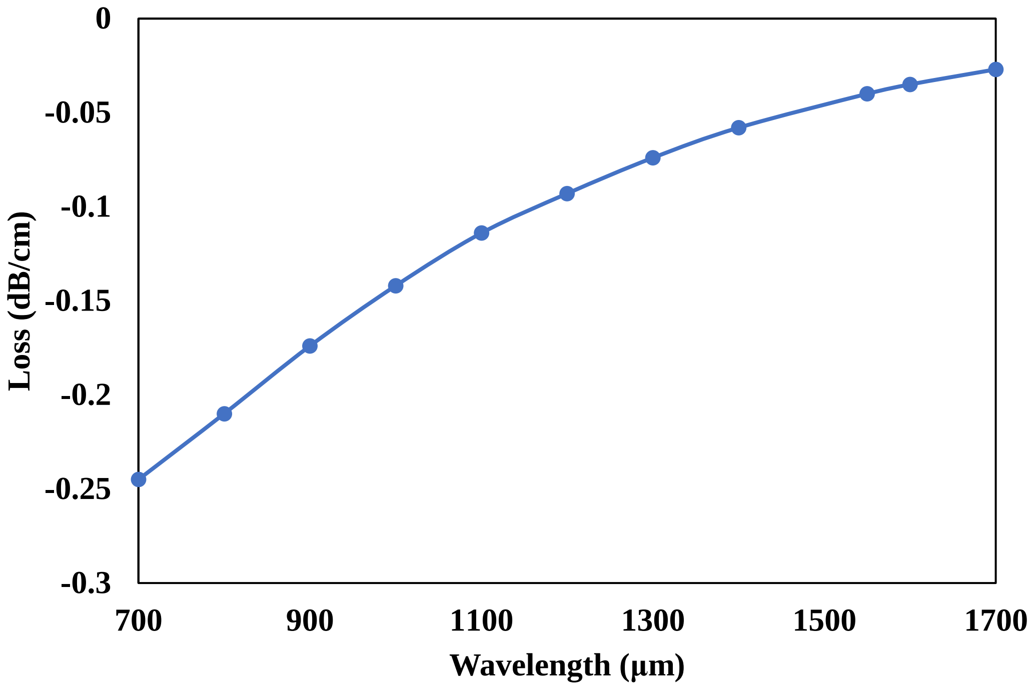

Figure 3.23: Scattering loss curve with silica cladding for 170 nm thick and 2.8 µm wide Si_3N_4 waveguide

Silica as top cladding improves the predicted scattering loss significantly and removes the substrate radiation loss issue as well. With silica, the mode field is evenly distributed into the bottom and top cladding. Therefore, it does not reach the silicon even at longer wavelengths. The reason behind the improved scattering loss is that the silica provides a lower refractive index contrast as compared to air which causes the reduction in the scattering loss throughout the spectrum.

Since the loss is scattering dominated, it can further be improved by using a thin waveguide. For that reason, the scattering loss was also computed for dimensions (t = 80nm & w = 2µm) optimized for single-mode single-polarisation and shown in figure 3.24. The minimum bend radius for negligible bending loss was found to be 2000µm. For minimum substrate radiation loss, the bottom cladding should be 7µm to 8µm thick.

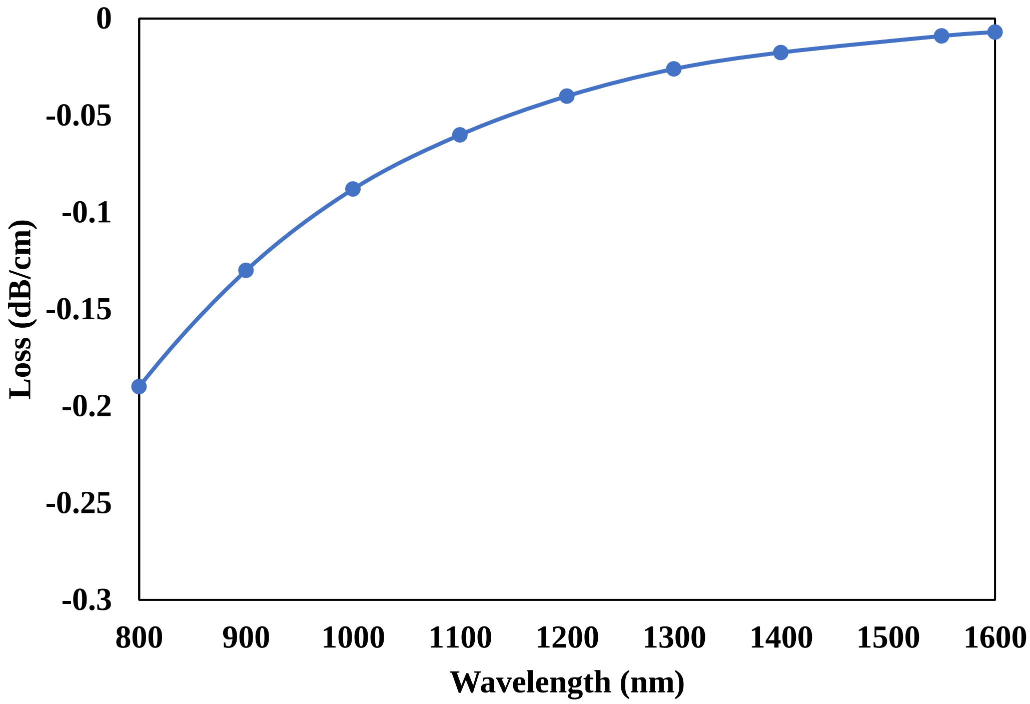

Figure 3.24: Scattering loss for a t = 80 nm & w = 2 µm Si_3N_4 waveguide with silica top cladding. In thin waveguides, most of the optical field is in the claddings and less field interacts with the sidewalls which causes the reduction in the scattering loss. By using the appropriate bending radius and bottom cladding, a loss of 0.009 dB/cm at 1550nm is predicted from thin Si_3N_4 waveguides with silica as cladding.

3.12.2 Experimental propagation loss results

170nm thick and 2.8µm wide Si_3N_4 waveguides were fabricated by the process detailed above in this chapter. After the etching, the chip was annealed at 1100 ^oC in argon for 6 hours. The ramp rate for heat up and cool down was chosen to be 5 ^oC/minute.

In each die on the mask, different length spirals were designed to measure the propagation loss through cutback method without cleaving the same dye twice to improve the reliability of the measurement. The comparison between experimentally measured and theoretical data of Si_3N_4 waveguides without cladding is shown in figure 3.25,

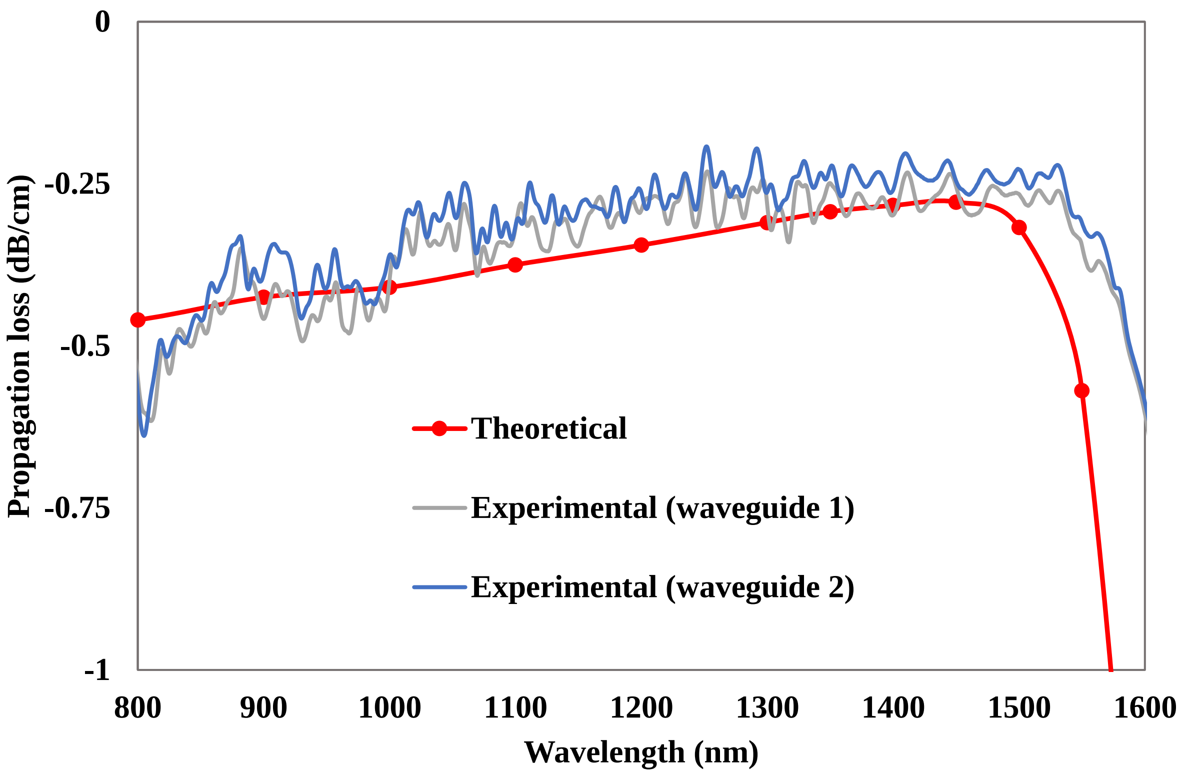

Figure 3.25: Illustrating the theoretical and experimental loss curves from thin Si_3N_4 waveguides.

Figure 3.24 shows that the experimentally obtained loss curve is close to the theoretical estimation. This shows that the process optimized for the fabrication of Si_3N_4 waveguide is providing the expected results. By using high aspect ratio waveguide geometry and silica cladding, extremely low loss, single-mode single-polarisation waveguides can be fabricated.

3.13 Conclusion

This chapter covered the theory behind optical waveguides, their fabrication process and characterization. Low loss Si_3N_4 waveguides were designed, fabricated, and measured. Different etching recipes were used to optimize the sidewall roughness. The measured results predicted that a propagation loss of 0.009 dB/cm is achievable by using the same fabrication process given the optimized waveguide dimensions and silica cladding. Due to the unavailability of the upper silica cladding at that time, ultra low loss thin Si_3N_4 waveguides (80 nm & 2μm) cannot be fabricated. Lastly, both PECVD silica and LPCVD Si_3N_4 require high temperature annealing to remove hydrogen content which makes them CMOS incompatible. Therefore, we moved from PECVD silica and LPCVD silicon nitride to IBS tantalum pentoxide and silica upon the availability of the IBS system.

Chapter 4 Fabrication of Tantalum Pentoxide (Ta_2O_5) waveguides and theoretical optimization of gyro components

4.1 Introduction

Tantalum pentoxide (Ta_2O_5), also known as tantala has emerged a potential material for integrated devices due to its unique optical and electrical properties. Ta_2O_5 is being used in the microelectronics industry as a high k gate [218] and is a suitable candidate for integration with silicon based photonic/electronic devices due to its CMOS back end of line (BEOL) compatibility i.e. low temperature processing capability. The refractive index of Tantala is only slightly higher than that of silcon nitride (the refractive index of tantala is 2.08 at 1550nm compared to 1.994 for Si_3N_4) and so it is also a good low loss waveguide candidate. Ta_2O_5 also has certain advantages over Si_3N_4. Firstly, it is a good host for doping rare earth ions such as Erbium in order to fabricate narrow linewidth on chip lasers. Secondly, in order to achieve minimum propagation loss in Si_3N_4 films or waveguides, annealing temperatures around 1100 ^{o}C are required to completely remove the hydrogen impurities. This massively exceeds the CMOS BEOL thermal budget of 400 ^{o}C or perhaps for a short time 500 ^{o}C. However, the maximum possible annealing temperature for tantala is 600 ^{o}C because it starts to crystalize beyond that. Further it can be deposited at low temperatures, even at room temperature by sputtering processes. Lastly the material can be deposited over large areas and with exquisite uniformity and thickness control as tantala was used to fabricate optical components for gravity wave sensing and huge amounts of process development was invested to this end. With the very thin layers used for ultra-low loss waveguide architectures, this is an important point.

In terms of waveguiding results, a low propagation loss of 3 dB/m has been achieved from Ta_2O_5 waveguides [112]. Tantala also has no free carrier and two-photon absorption issues in the IR range because of the large band gap (~5 eV at 1550 nm) [219].

The properties mentioned above make Ta_2O_5 a promising material for the development of integrated optoelectronic devices. Therefore, the process to fabricate good quality tantala waveguides with CMOS BEOL compatibility for true single chip gyros will be discussed in this chapter.

4.2 Deposition of Ta_2O_5 Films

This section covers the details of the deposition technique used for the deposition of Ta_2O_5 films. Physical Vapour Deposition (PVD) and Chemical Vapor Deposition (CVD) are preferred techniques for thin film fabrication. In PVD, thin films are grown by vaporizing/atomising solid or liquid targets and transporting the species to the substrates. They then condense in a highly non-equilibrium process to form a thin film. This can be done by several methods such as magnetron or ion beam sputtering (IBS), pulsed laser deposition (PLD) and thermal/electron beam evaporation. These techniques differ from each other primarily in the means for the material vaporization method, though the details of factors such as vapour transport/energy also differ. Therefore, the films produced by different deposition methods can have somewhat different properties. The highest quality optical coatings for mirrors and anti-reflection coatings were developed for laser interferometer gravitational-wave observatory (LIGO) applications and were fabricated by IBS [220]. Here optical absorption and thickness uniformity/precision were very important parameters. Therefore, this method was used to deposit Ta_2O_5 films. The schematic of the IBS chamber is shown in figure 4.1,

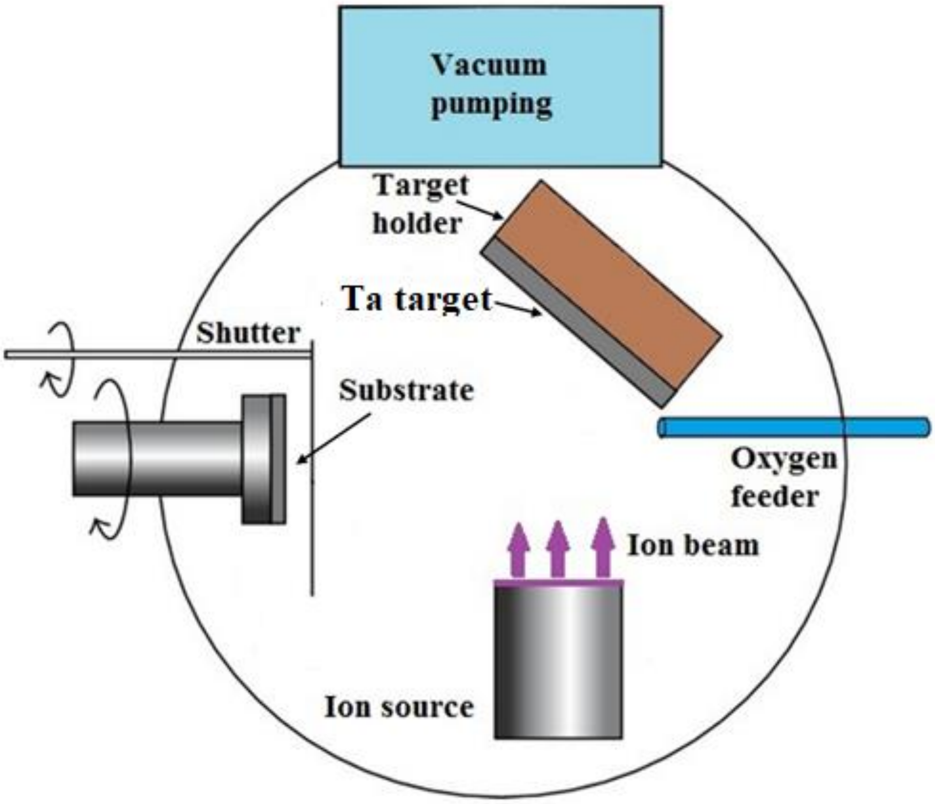

Figure 4.1: Schematic of the chamber of an ion beam sputtering system.

In the IBS deposition processes, the coating material is vaporized through direct irradiation with a beam of high energy species (typically Argon atoms). Despite the name IBS, in fact the bombarding beam in IBS is actually electrically neutral and atomic in nature. Atoms, molecules, or clusters are knocked out of the target material by the bombardment process. This process was discovered by Louderback and Wei in 1976 [221]. For Ta_2O_5 deposition, a pure tantalum (Ta) target was sputtered using an ion gun running on Argon. The sputtered Ta particles react with O_2 introduced into the chamber to form Ta_2O_5 before or whilst depositing on the substrate (s) [222]. The whole deposition process is done in a high vacuum environment at pressures usually around 1 x 10^{-4} Torr when all gas flows are on. The system is pumped by a large cryopump to avoid contamination.

This method has been proven to produce optical coatings with extremely low absorption in the few ppm range for propagation through the coatings. This method was the only one capable of meeting such stringent loss requirements which led to its use by both the Advanced Virgo and LIGO consortia to coat test masses etc [223].

The energy with which the sputtered particles reach the substrate is quite high which enables them to have higher surface mobility and this combined with the energetic bombardment results in a dense film with greater adhesion [224]. The kinetic energy (K.E) of the plume is around 10 ev which is almost 10 and 100 times greater than for magnetron sputtering and thermal evaporation, respectively. The distance between the ion gun and target is optimised such that only the target material is sputtered, otherwise the material around the target could also get sputtered and contaminate the film.

The independent control of the parameters in IBS is another advantage of this deposition method. Parameters such as sputtering rate, ion energy and angle of incidence of the ion beam can be varied/modified individually to fine tune the film quality and properties. IBS also has an advantage in the deposition of multilayer films. The neutrals which sputter the target material are not created at the target surface and kinetically propagated from the ion gun which is placed typically 30-50cm away from the target. This allows the targets to be mounted on a rotating turret in front of the incoming neutrals to select different materials and yet have the same beam sputter them to enhance uniformity between materials and produce multilayer coatings without breaking the vacuum [225].

A number of tantala films were deposited by IBS on 5µm thermal oxide (TOx) wafers. The parameters used for the coating process are tabulated in table 4.1.

Table 4.1: Encloses the parameters used to deposit T_2O_5 films.

Parameters	Values
Target material	Tantalum (Ta)
Base pressure (torr)	2 x10^{-7}
O_2 flow (sccm)	48
Ar flow (sccm)	11.20
Substrate rotation (rpm)	50
Substrate temperature (°C)	20
Neutralizer Ar flow (sccm)	5

The deposition rate with these parameters came out to be 6.3 nm/minute. IBS has the capability of depositing films with a uniformity of 0.5% and thickness accuracy of 1% across the 4-inch wafers. Several films with different thicknesses from 100nm to 500nm were deposited. The refractive index was measured with the FilmTek and found to be 2.08 before annealing and around 2.03 after annealing at 1550nm.

To measure the propagation loss of IBS SiO_2 and Ta_2O_5 films, trapezoidal waveguides were fabricated without direct pattering process (etching or lift-off) on core materials by our group and collaborators. The fabricated waveguide is shown in figure 4.2.

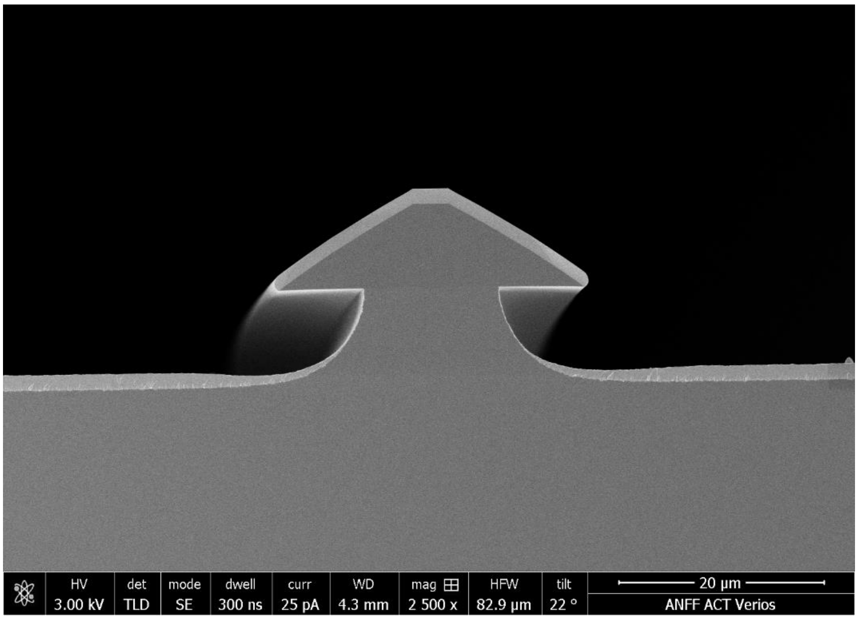

Figure 4.2: Showing the trapezoidal waveguide fabricated to measure the propagation loss of the IBS films.

A propagation loss of ~ 0.15 dB/cm and 0.05 dB/cm was measured from IBS Ta_2O_5 and SiO_2 respectively.

4.3 Optimization of Ta_2O_5 Waveguide Dimensions

In this section, single-mode, single-polarisation low loss tantala waveguides are investigated for the purpose of designing different gyro components. To realise low loss, single-mode and single-polarisation, the width and thickness of the waveguide were optimized by using R-Soft. As far as thickness is concerned, the ideal waveguide thickness should support only TE mode and at the same time does not allow the optical mode to leak into the silicon through 5µm TOx bottom cladding. 7µm and 10µm thick TOx wafers are significantly more expensive than 5µm, therefore, the thickness was optimised keeping both the mode polarisation state and TOx wafer cost in mind. Initially, the modes were computed by setting the waveguide width at 3µm for 5 different thicknesses and result is shown in figure 4.3. The thickness of the silica upper cladding was 6µm with a refractive index of 1.446 at 1550nm. Thick silica cladding was chosen to manage the substrate radiation loss as mode field of the thin waveguide is mostly in the claddings and if the upper cladding is thin, the air on top pushes the mode field deep into the bottom cladding which resulted in higher substrate radiation loss. The refractive index value was chosen to counter the same issue.

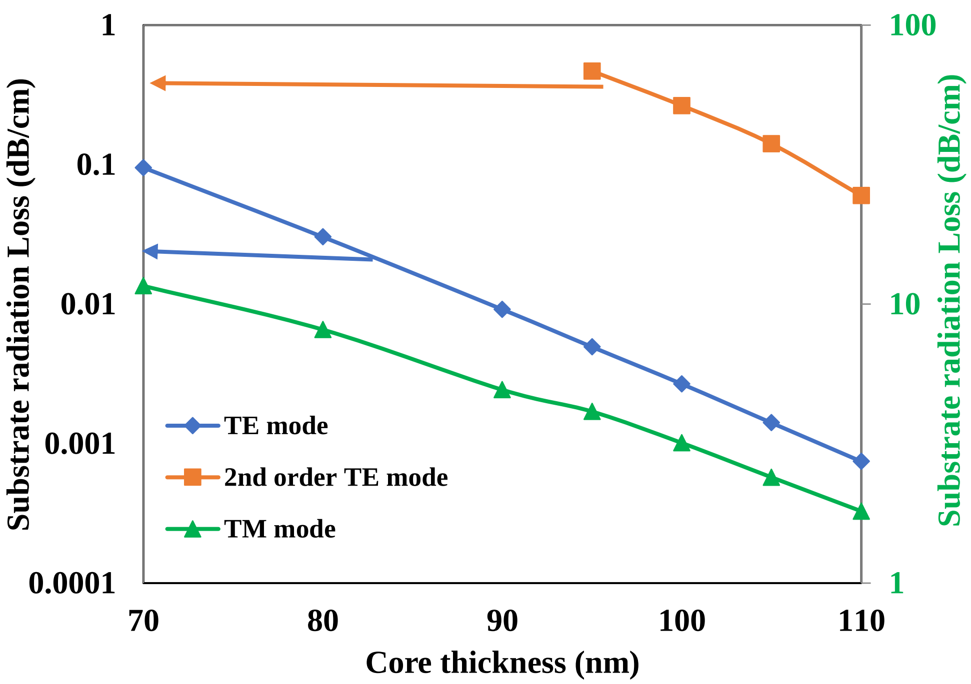

Figure 4.3: Substrate radiation loss, number of modes and polarisations excited in 3µm wide Ta_2O_5 waveguide against 5 different core thicknesses.

As can be seen in figure 4.3, the substrate radiation loss decreases for all the modes as the thickness increases from 70nm to 110nm. From 95nm onwards, the 2nd order TE mode is also excited, yet this is right about where the fundamental TE mode has sufficiently low substrate radiation losses. Therefore, to cut the higher order TE mode, the width of the waveguide was reduced to 2.5µm and findings are presented in figure 4.4.

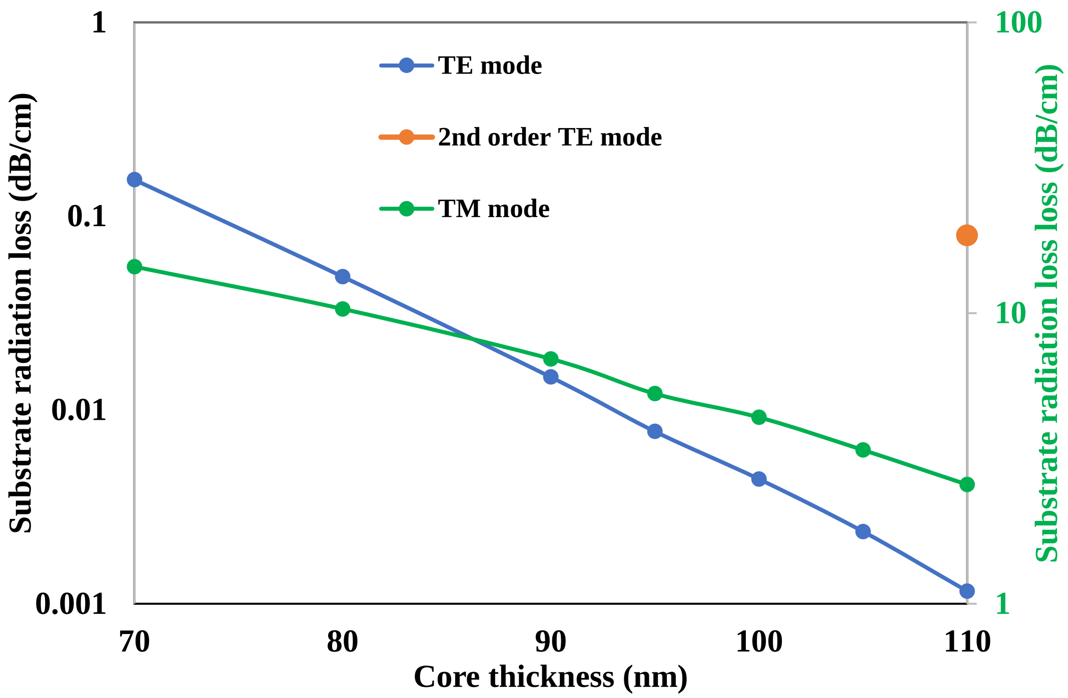

Figure 4.4: Substrate radiation loss vs core thicknesses for 2.5µm wide Ta_2O_5 waveguide.

By decreasing the width from 3µm to 2.5µm, the 2nd order TE mode was cut off for all thicknesses below 110nm. However, the substrate radiation loss went up for both the fundamental TE & TM modes. The fundamental TM mode exists for all the thicknesses modelled, but its loss is significantly higher than TE (> 4 dB/cm at 100 nm thickness) and would get killed by the waveguide bends. The bending loss of the TM mode for 15mm bend radius (used in optical gyro optimisation) is 42 dB per turn which if it is couple with the substrate radiation loss (4.38 dB/cm) means that the TM fundamental mode has a total ring single pass loss of 83 dB which is significantly high and TM mode will not be able to survive.

If one wants that the TM mode doesn't even excite at the first instance, it can be done by thinning the waveguide geometry but it would increase the substrate radiation loss even for the TE mode. A 60nm thick and 2.5µm wide Ta_2O_5 waveguide excite only TE mode but its substrate radiation loss is 0.4 dB/cm for 5µm thick bottom cladding. A thicker bottom cladding of 8µm decreases this loss to a reasonable number of 0.0071 dB/cm. These dimensions also offer a low bending loss of 0.06 dB/turn for 15mm bending radius. As pointed earlier, thicker bottom cladding is expensive. Therefore, computation was done by employing thin (5µm) bottom cladding and thicker (100nm) waveguide core.

A 100nm thick waveguide offers a substrate loss of 0.0044 dB/cm for TE mode which is low enough for gyro applications. Therefore, the waveguide dimensions chosen to simulate gyro components were width = 2.5µm & thickness = 100nm.

In the fabrication world, there is always a fabrication tolerance in the thickness and width of the waveguide which sometimes changes the outcome substantially. Canon (500 MPA) mask aligner, ICP etcher and Samco etcher were employed to fabricate the waveguides. Based on the previous experience, a width tolerance of ±200nm is expected from these tools. A thickness accuracy of 1% and uniformity of 0.5% has been achieved across 4-inch wafer by the IBS system but it required a lot of optimisation work and time. Therefore, the values for the thickness tolerance (±5nm) were chosen which can easily be achieved and 100% repeatable.

The fabrication tolerance for both width and thickness was simulated only for the TE mode and shown in figure 4.5.

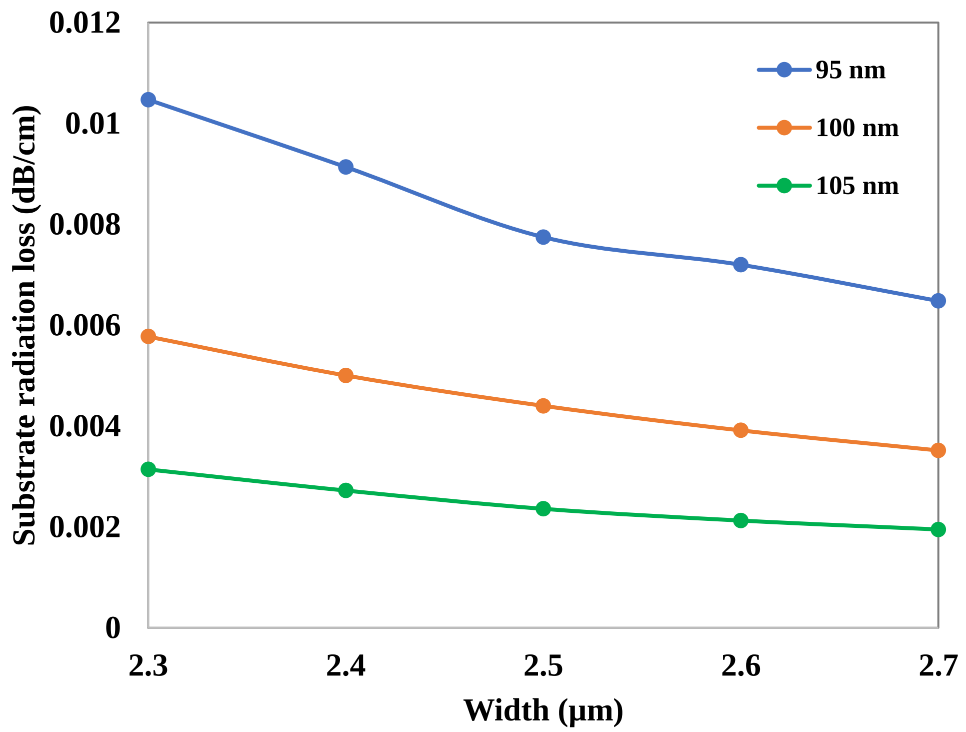

Figure 4.5: Exhibiting the fabrication tolerance analysis of the TE mode.

Figure 4.5 shows that the loss slightly changes with the change in both the thickness and width except for the case of 95nm where the loss goes up to 0.0104 dB/cm for 2.3µm width. Even at

2.5μm, it is almost double that of 100nm. With some extra efforts and time, a thickness of 100±1nm can be achieved across 4-inch wafer and a width of 2.5±0.1μm can be fabricated by the given tools. Therefore, a loss of 0.004±0.001 can be obtained.

The next task was to investigate the bending loss. A 30mm diameter ring resonator was initially used to compute the performance of the resonant gyro. However, this diameter is not suitable for optimizing the fabrication process and testing its performance as only 4 resonators along with other gyro components can fit onto a 4-inch/100mm wafer. Given the yields for experimental processes and the lack of availability to design for tolerancing with only four components, it was decided to design for 10mm diameter resonators for initial testing. This diameter allows 16 devices to fit onto the wafer. Bending loss along with fabrication tolerance was computed with a bending radius of 5mm and is shown in figure 4.6.

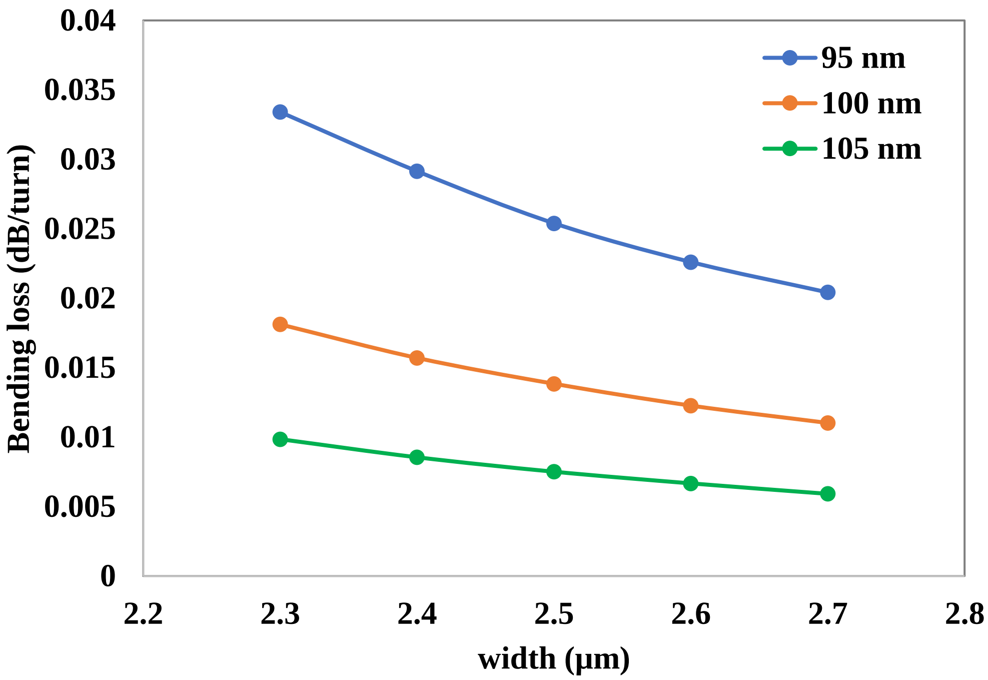

Figure 4.6: Showing the theoretical bending loss per turn for a 5mm bending radius ring along with the parameters within fabrication offset. Bending loss for TM mode was immensely higher than TE mode and therefore did not perform the tolerance analysis.

Figure 4.6 illustrates that the bending loss for the nominal waveguide dimensions was 0.013 dB/turn. For a 10mm diameter ring, the ring length is 3.14cm and so the effective additional propagation loss is 0.004 dB/cm which is acceptable. 95nm thick waveguides have almost triple this additional loss in the worst case which is becoming limiting in a 10mm ring, though this would be acceptable in a 30mm device. Bending loss for the fundamental TM mode for the nominal waveguide dimensions was 13.8 dB/turn at 5mm radius which is significantly higher than the TE mode and this coupled with the substrate radiation loss (4.38 dB/cm) means that the TM fundamental mode has a total ring single pass loss of 28.5 dB and so effectively does not propagate rendering the 10mm diameter ring single polarisation.

The above analysis concludes that the TM mode is quite lossy for both the cases (5mm and 15mm) and will not be able to propagate. However, single polarisation waveguides can also be realised by using 2.5μm wide and 60nm thick waveguide dimensions but thicker and expensive bottom cladding will be required.

4.4 3dB Coupler

Directional couplers are widely being employed for many photonics applications such as Wavelength-Division Multiplexers/Demultiplexers, power dividers, optical switches and Mach-Zehnder interferometer (MZI) [226, 227]. In a resonant ring gyro, low fraction couplers are needed for the ring coupling and 3dB couplers to generate the two counter-rotating carriers.

A directional coupler is composed of two straight waveguides and S-bends. The schematic of a typical directional coupler is presented in figure 4.7,

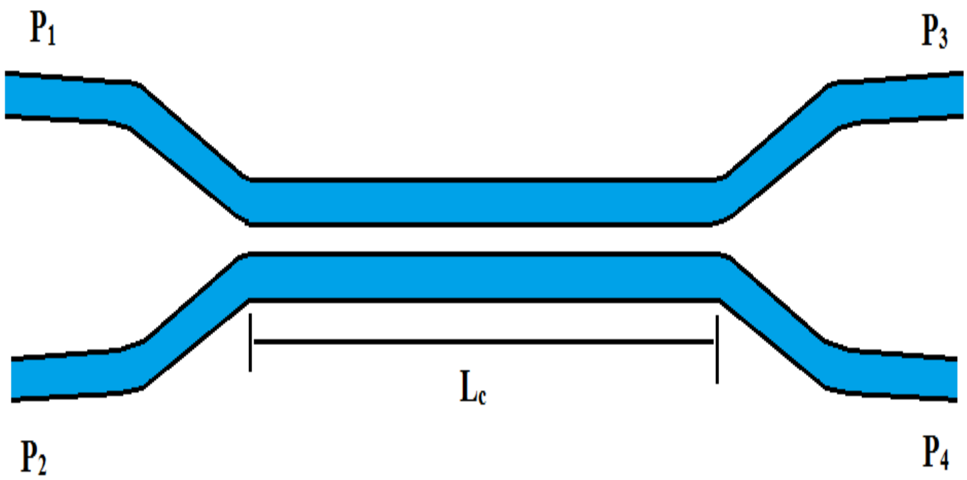

Figure 4.7: Exhibiting the schematic of a typical directional coupler.

The working principle of a directional coupler is based on the fact that even though the optical mode is confined and propagates along the core, a small amount of the field lies outside the core-cladding interface. Upon placing the two waveguides sufficiently close together, light couples from one waveguide to the other through an interaction involving their evanescent fields. It is important to note that the complete coupling of modes is possible only if the propagation constants of both the modes are equal. Waveguides with identical dimensions have equal propagation constants or phase velocities. In this case, for all modes having equal propagation constants, a complete transfer of power is possible from one channel to the other.

However, even when the two single-mode waveguides are placed in close proximity, they no longer behave as isolated single-mode waveguides. This phenomenon is easy to understand if two single-mode waveguides are brought together with zero separation. The wider waveguide thus formed is no longer single-mode and can support at least a pair of symmetric and antisymmetric modes (usually referred to as supermodes of the total structure) that have significantly different propagation constants. The interference of these modes at the end of the structure driven by the different propagation phases results in differing and wavelength sensitive excitations in the separated waveguides, and thus power splitting. Therefore, the wavelength dependent supermode effective indices need to be computed to calculate the coupling length for the light to completely cross coupled to the adjacent waveguide. For a given wavelength, the coupling length is calculated by using following equation [228]:

$$L_c = \frac{\lambda}{2(n_{effs} - n_{effa})} \tag{4.1}$$

L_c represents the coupling length required for the complete coupling/crossing of the light into the adjacent waveguide. n_{effs} and n_{effa} are effective index of symmetric and antisymmetric supermode, respectively.

The effective coupling length of the directional coupler is little bit different to the calculated coupling length from the supermode analysis due to additional coupling in the S-bends. Therefore, coupling through the S-bends should be computed along with the coupling length. In order to limit the device footprint and unwanted coupling, sharp S-bends may be employed.

Naming the input port as P_1 and output ports as P_3 and P_4 then the power at P_3 and P_4 can be derived from coupled mode theory [227] and is written as:

$$P_3 = \cos^2\left[\frac{\pi\Delta n(\lambda)}{\lambda}.L_c\right] * P_1 \tag{4.2}$$

$$P_4 = \sin^2\left[\frac{\pi\Delta n(\lambda)}{\lambda}.L_c\right] * P_1 \tag{4.3}$$

Where, λ is operating wavelength and L_c is the coupling length. For loss less couplers, the sum of the output powers is equal to the input power.

For a given wavelength, a desired splitting/coupling ratio between the waveguides can be achieved with an appropriate choice of coupling length. A 50:50 or 3dB coupler is often characterized by its imbalance, excess loss and the directivity. Equation (4.4) defines the imbalance [229]:

$$\text{Imbalance (dB)} = 10\log\frac{P_3}{P_4} = 10\log P_3 - 10\log P_4 \tag{4.4}$$

For an ideal 3dB coupler, the imbalance is zero. For $P_3 > P_4$ and $P_3 < P_4$, positive and negative imbalance occur respectively.

The excess loss is defined as the ratio of the total output power and the input power and represented by equation 4.6:

$$\text{Excess loss (dB)} = 10\log\frac{P_3 + P_4}{P_1} \tag{4.5}$$

Directivity is the measure of how much power is returning through backward coupling processes to the second input port (P_2) with respect to P_1. The second input port (P_2) is also known as the isolated port.

$$\text{Directivity (dB)} = 10\log\frac{P_2}{P_1} \tag{4.6}$$

Planar directional couplers have been realised from various materials including Ta_2O_5, silicon and SiO_2:TiO_2 [226, 230, 231]. The fabrication tolerance performance of Ta_2O_5 couplers based on the ultralow loss waveguide architecture is determined here to see if they should be integrated in this or an alternative hybrid integrated materials system in a single chip gyro implementation.

FemSIM and the MOST variable engine were employed to compute symmetric and anti-symmetric supermodes for different waveguide widths and edge to edge gaps between straight waveguides. The waveguide width was varied from 1.5µm to 3µm and gap was increased from 0µm to 7.5µm. In-house written LabVIEW code was used to calculate the (full power cross) coupling length for every width and gap from the MOST output data. The purpose of this exercise was to find out the minimum coupling length where the change in core width within the fabrication tolerances would minimally affect the coupling ratio. Data from this simulation is plotted in figure 4.8.

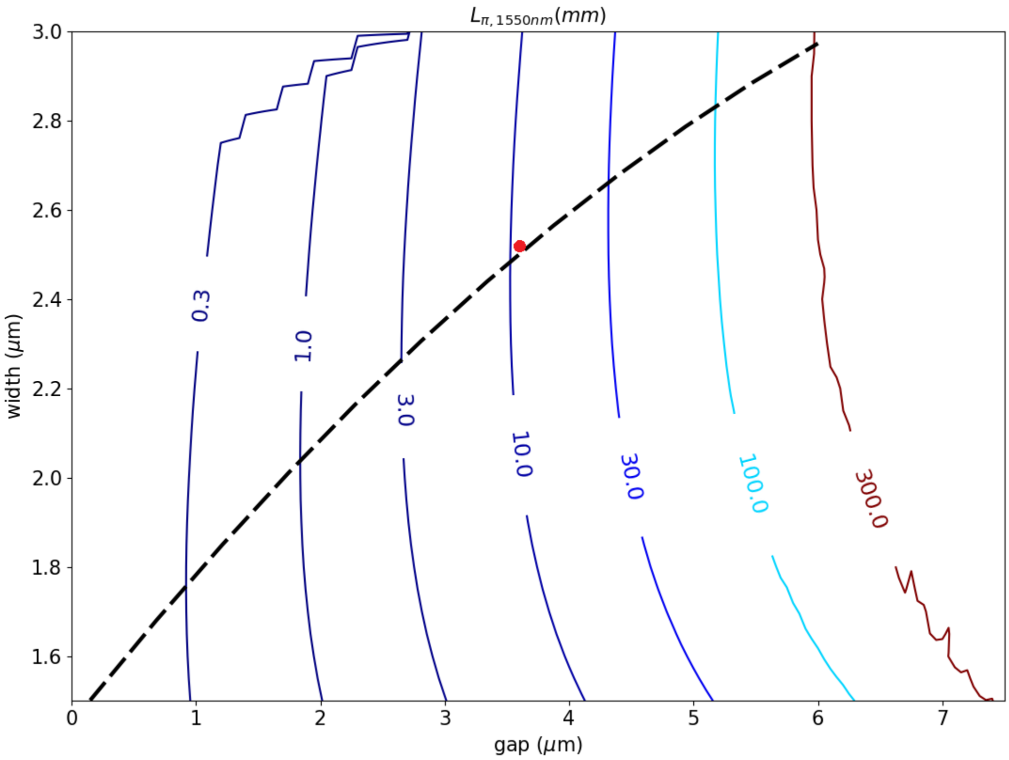

Figure 4.8: Contour plot of L_c coupling length against the waveguide width and edge to edge gap between the straight waveguides. The black line indicates the points where the width tolerance is maximum.

Figure 4.8 shows that for 2.5µm wide waveguide, the edge to edge gap of around 3.75µm (red dot on the figure) gives the maximum width tolerance. The L_c at 3.75µm gap is 13.5964mm. 3dB coupling is simply the half of this length which is 6.7982mm.

The FemSIM results for pure parallel waveguides were then verified by modelling the full device including S-bend inputs and outputs using BeamPROP. The S-bends had a large bending radius of 1143µm. The plotted data is shown in figure 4.9.

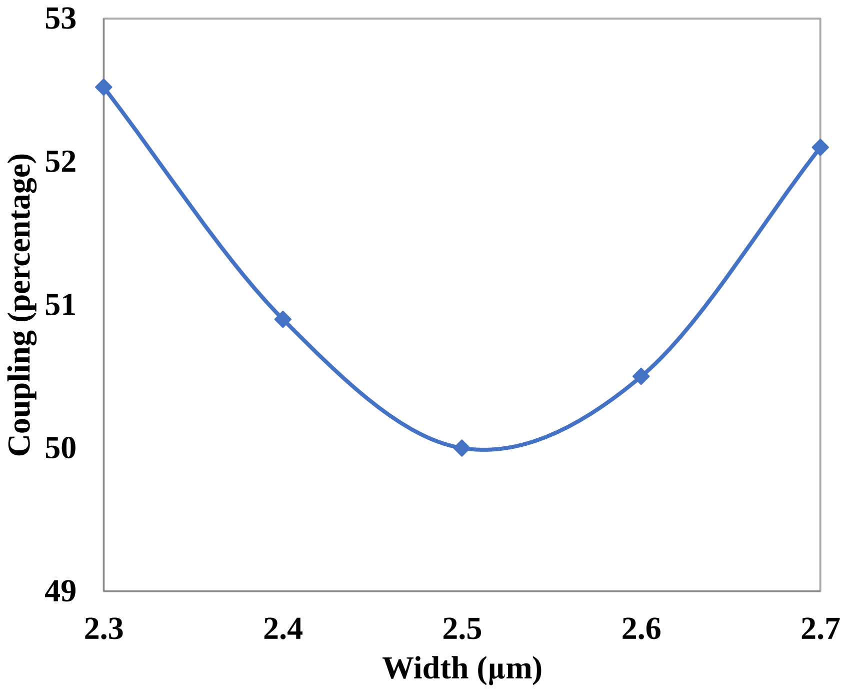

Figure 4.9: Illustrating the change in the cross coupling against the core width.

As can be seen in figure 4.9, 3 to 4 % change in the cross coupling was found in response to the maximum fabrication tolerance induced width variation. Thickness tolerance was also computed and is plotted in figure 4.10.

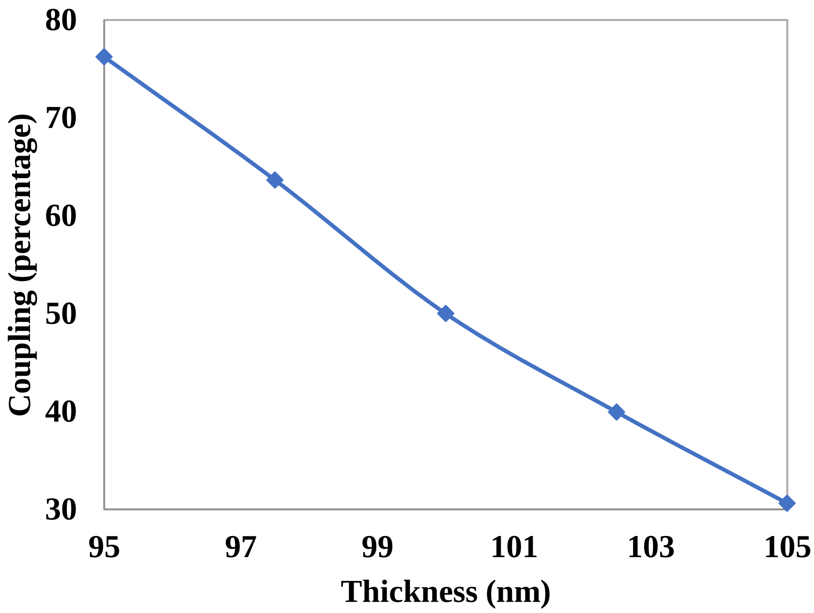

Figure 4.10: Showing the change in the cross coupling against the core thickness.

Thickness change has severe effects on cross coupling as compared to width. Only a 2.5 % change in the thickness would change the cross coupling more than 20 % which shows that the design is quite sensitive to minor fabrication offset. Because of the thin waveguide geometry, most of the field is outside of the core which makes the given design extremely sensitive to thickness variation. Although IBS system can deposit films with a thickness accuracy of 1% but it would still change the coupling percentage to more than 5%. If 10 mW of power is launched at the input of the 3dB coupler, with only 1% imbalance would induce an error of 49 °/s for the optimised waveguide dimensions. Kerr effect induced error was calculated in chapter 2 (see equation 2.19). The designed 3dB coupler will induce an imbalance of more than 5% for the best which suggests that this design is not suitable for gyroscopic applications.

4.5 Bus Waveguide Ring Resonator

Ring resonators are widely used in numerous integrated devices such as laser, sensors and optical components like delay lines and filters [232-234]. A resonator is useful only when it couples light to the outside world. Light coupling in and out of the resonator is done via a bus waveguide or add-drop waveguides. In the latter case, two waveguides are brought into close proximity with the ring to couple the light in and out of the ring separately. However, in bus waveguide ring resonators, only a single waveguide is used that forms an evanescent coupler between the ring and the waveguide for in and out coupling. The bus waveguide resonator will be discussed in this chapter. A schematic of a typical bus waveguide ring resonator architecture is shown in figure 4.11.

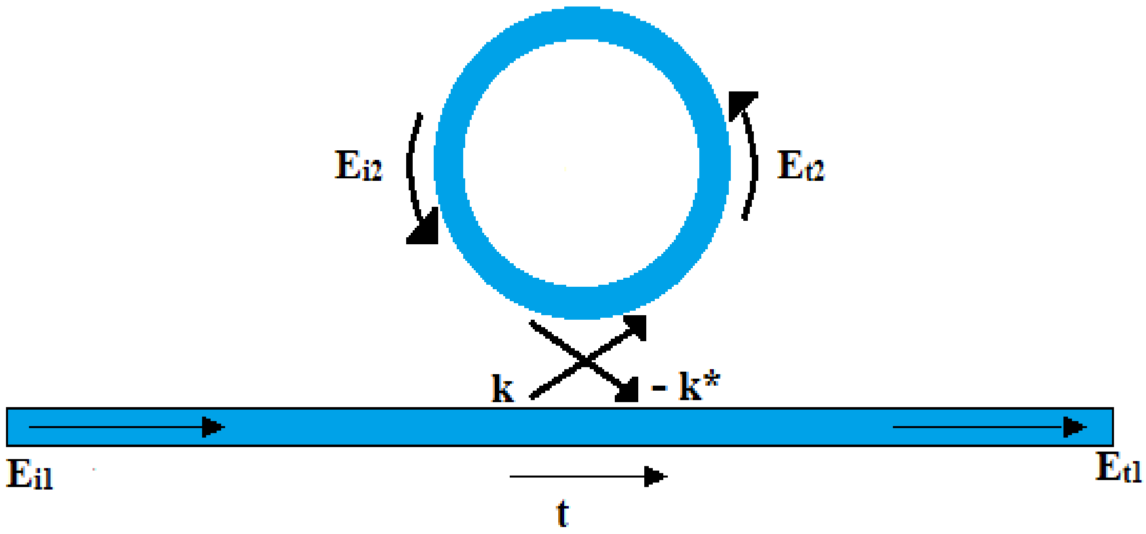

Figure 4.11: Showing the modal of a bus waveguide ring resonator.

The closest region between the ring and bus waveguide forms the coupling region, where a fraction of incident light is evanescently coupled from one component to the other and vice versa. The rest of the light is transmitted to the output port as $k^2 + t^2 = 1$. Here k and t are coupling and transmission coefficient, respectively. When the light circulating inside the ring builds up a phase shift of an integer multiple of 2π, constructive interference occurs, and the cavity becomes a resonator. Mathematically, the resonator is described by two elements: a feedback path and the coupling strength. As an alternative to using the infinite sum method employed for the Fabry–Perot and Gires–Tournois resonators, the spectral properties of a bus waveguide ring resonator can be derived by assuming steady state (continuous wave) operation and field matching. Both derivations are equally accurate, but the field matching method is simpler to derive.

The relation amongst the incident E_{i1}, circulating (E_{t2} & E_{i2}) and transmitted E_{t1} fields of a bus waveguide ring resonator are obtained by combining the relations for the coupler with that of the feedback path which is expressed by the following unitary matrix [235]:

$$\begin{pmatrix} E_{t1} \\ E_{t2} \end{pmatrix} = \begin{pmatrix} t & k \\ -k^{*} & t^{*} \end{pmatrix} \begin{pmatrix} E_{i1} \\ E_{i2} \end{pmatrix} \tag{4.7}$$

The feedback path (which is actually the length of the resonator) couples the output from port E_{t2} back into input port E_{i2} and is expressed as:

$$E_{i2} = e^{-\frac{\alpha_{ring}}{2}2\pi R}\, e^{iK2\pi R}\, E_{t2} \equiv a\,.\ e^{i\emptyset} E_{t2} \tag{4.8}$$

Where, $\emptyset = \beta L$ represents the single pass phase shift, β is the propagation constant of the propagating mode and L is the total length of the cavity. a in the above equation represents the single pass transmission amplitude which includes both the propagation loss of the resonator as well as the loss from the coupler.

Upon constructive interference, the circulating mode intensity builds significantly as compared to when injected. The intensity build up highly depends on the coherence of the light source. A coherent build up of intensity can lead to a dramatically enhanced nonlinear response. For non-coherent sources, the intensity of the circulating mode is same as the incident intensity.

The ratio of the circulating field to the incident fields can be obtained by solving the above two equations and is written as,

$$\frac{E_{i2}}{E_{i1}} = \frac{it\alpha e^{i\emptyset}}{1 - t\alpha e^{i\emptyset}} \tag{4.9}$$

The ratio of the intensity of the circulating mode to the intensity of the incident mode can be derived by simply taking the squared modulus of the equation,

$$\frac{I_{i2}}{I_{i1}} = \left|\frac{E_{i2}}{E_{i1}}\right|^2 = \frac{a^2 - 2tacos\emptyset + t^2}{1 - 2tacos\emptyset + (ta)^2} \tag{4.10}$$

The above equation refers to the situation that the light will be in resonance given the loss is negligible (a = 1) and $\emptyset = m * 2\pi$. m is an integer. Under these conditions, a resonator attains the maximally achievable ratio of circulating power. Even for a small value of cross coupling ($t^2 = 0.1$), the intensity of the light circulating in the resonator can be 40x higher than the light intensity at the input [236]. Along with the ring diameter, another important parameter in bus waveguide ring resonator is the gap between the ring and straight waveguide which determines the coupling ratio and ultimately coupling regime. Eight resonators with different coupling ratios were simulated by using a LabVIEW code as the loss of the Ta_2O_5 waveguide was not optimized/known at the time of simulation. Care was taken to have 25 % transmission (details are given in chapter 2 about the significance of 25 % transmission) for propagation losses of 0.1 dB/cm, 0.05 dB/cm and 0.01 dB/cm. Lastly, the gaps for these coupling ratios were obtained by using BeamPROP and tabulated in table 4.2,

Table 4.2: Minimum waveguide gap vs the coupling ratio for 25% transmission simulated for 8 bus waveguide ring resonators.

Waveguide loss (dB/cm)	Coupling ratio (percent)	Gap (μm)	Transmission (%)
	3.09	2.13	
0.1	2.45	2.21	25
	1.593	2.36	
0.05	1.235	2.45	25
	0.902	2.56	
	0.624	2.69	
	0.398	2.85	
0.01	0.191	3.11	~30

All the resulting gaps are comfortably within the range of feature sizes attainable by low cost (e.g. contact) lithography. To investigate the effect of fabrication tolerances, a coupler with a nominal coupling ratio of 0.191 was simulated with different widths and thicknesses within the fabrication tolerance and results are plotted in figure 4.12.

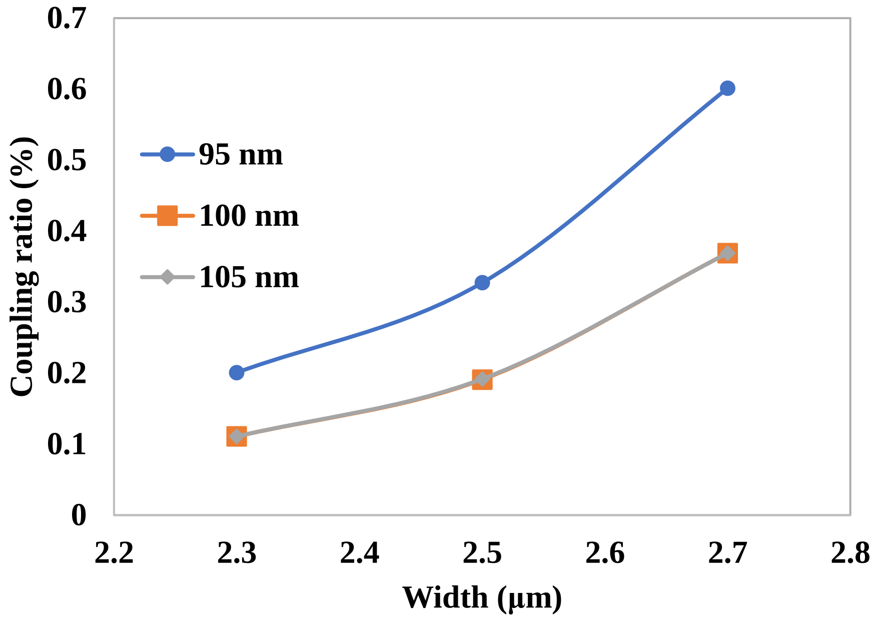

Figure 4.12: Variation in the coupling ratio vs core widths and thicknesses for 0.19% ring input coupler.

As can be seen in figure 4.12, the coupling ratio changes with both widths and thicknesses expect for 105nm where it follows almost the same trend as of 100nm. However, considering the thickness accuracy (1%) of the IBS system, the coupling ratio is quite stable around the optimised waveguide thickness (100nm) and would provide the similar performance numbers. On the other hand, let's consider the worst case scenario of going from 0.19% to 0.32% of coupling ratio due to the change in the thickness from 100nm to 95nm. The sensitivity of the gyro was calculated for both the coupling ratios by using equation (2.14) for the values of d = 10mm, t_0 = 1s, f_0 = 193 THz, η = 90 %, input power of the laser = 10 mW. The loss induced by the required additional optical components such as 3dB coupler (-3.1dB = -0.1dB excess loss + -3.0dB for splitting light into 50:50) and Phase modulator (-0.5dB), etc was also included. The resolution came out to be 9.17 ^{o}/h and 14.34 ^{o}/h for 0.19% and 0.32% of coupling ratio respectively. Even the 5% change in the waveguide thickness degraded the gyro sensitivity of only 5.17 ^{o}/h.

As for as width tolerance is concerned, the sensitivity was calculated by employing the same equation and values mentioned above for 100nm thick and 2.7µm wide waveguide and found out to be 17.20 ^{o}/h. The sensitivity is almost doubled as compared to calcuated from optimised waveguide dimensions but it is still in a reasonable range which suggests that the designed bus waveguide ring resonator is fabrication tolerant and can be employed for high performance gyro applications.

4.6 Waveguide Crossing Array

In order to realize an integrated loop gyro, the waveguide has to be looped in a way that the innermost waveguide will cross through all the waveguides (see figure 4.13) and as will be shown, it is not trivial in integrated technology to achieve very high performance in such devices. In this chapter, crossing loss in weakly confined ultra-low loss design tantala waveguides is studied in detail.

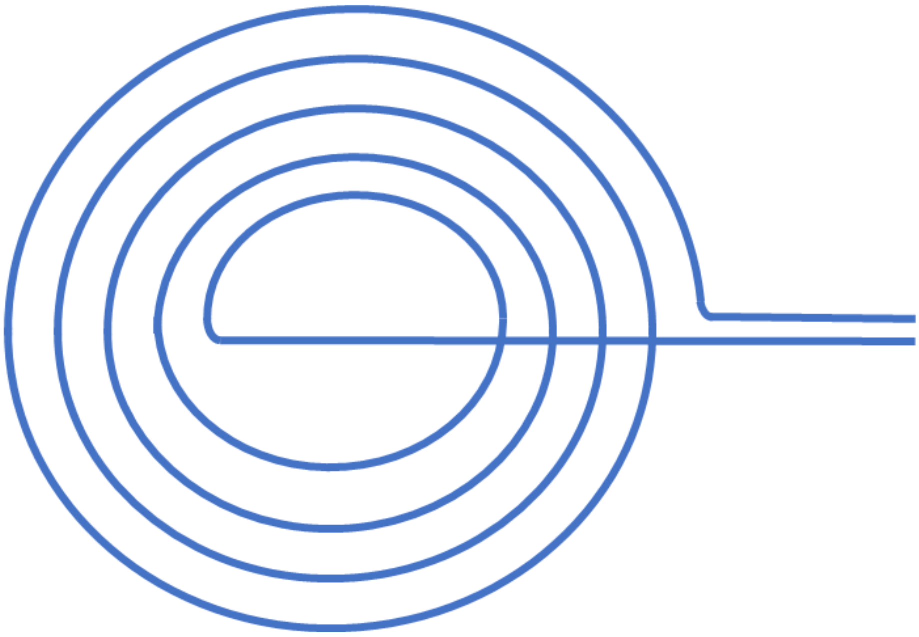

Figure 4.13: Waveguide gyro sensor loop in which inner waveguide is crossing through the loop waveguides.

Before addressing the optimisation of waveguide crossing loss, it is appropriate to address the loss mechanisms at work. Ideally, the light launched into one of the crossing waveguides should be fully transmitted without any loss and by association any reflection. However, a certain fraction of light is radiated away at the intersection due to diffraction and optical scattering. The crosstalk between the waveguides is very small when they are many wavelengths wide and is around 10 % when the width is on the order of the wavelength as it is in most high index contrast waveguides [237]. A loss of < 0.1 dB/crossing from high index contrast waveguides has been reported in the literature [238]. The intersection region was widened elliptically to broaden the effective aperture. The propagating mode has narrow angular spectrum in the widen region which resulted the reduction in the diffraction loss and cross talk. The long and short axes of the elliptical region were 7.2µm and 1.5µm respectively.

Most of the advance applications require even lower loss per crossing which can be achieved by employing multimode interference based crossings [239]. Once the desired loss from one crossing is obtained by widening the waveguides, the optimum gap between the crossings can be obtained by using the self-imaging concept for multimode waveguides. According to this concept, the field distribution in a multimode waveguide periodically changes along the propagation direction in a way that the excitation field is reproduced at discrete intervals. It has been proved that the loss of a waveguide crossing array is minimised if the multimode waveguides cross each other at the points where the width of the optical field is a minimum [240]. At those points, the width of the multimode waveguide is bigger than the width of the optical mode and almost zero power exists outside of the waveguide which resulted in a high transmission.

The length the multiple modes need to interfere, and form a single-fold image is known as the beat length. It is an important parameter and calculated by the following equation [241]:

$$L_{B,i} = \frac{2\pi}{(\beta_i - \beta_{i+2})} \qquad (4.11)$$

Where, $L_{B,i}$ represents the beat length of the mode (i=0,1). β_i and β_{i+2} represent the propagation constants of the respective modes.

The loss of the right angle crossing of two waveguides was optimised by changing the waveguide width and data is plotted in figure 4.14,

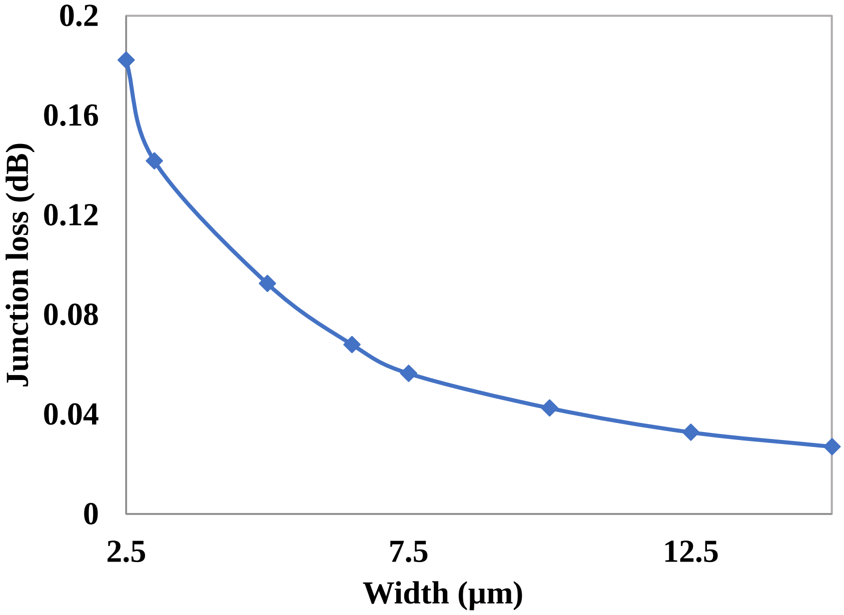

Figure 4.14: Exhibiting the junction loss of the two crossed waveguides vs width.

The loss decreases when the waveguide width at the crossing increases. The minimum loss can be achieved by having the widest waveguide, but then the tapers from the nominal waveguide width to this new width will have to be longer consuming device space. However, 2.5µm wide crossing cannot be chosen as the junction loss even for one crossing is quite high. Here the trade is to choose a width where the junction loss is reasonably low and not longer tapers are required in order to keep the footprint of the device as small as possible. Therefore, 6.5µm wide waveguide will be employed at the intersection where the loss is low enough and taper length would be reasonable.

For multiple crossings, the beat length was calculated by using equation (4.11), which came out to be 54µm for 6.5µm wide waveguides. The optimum taper length was found to be 40µm. The taper length vs total junction loss from 20 crossings was computed and shown in figure 4.15.

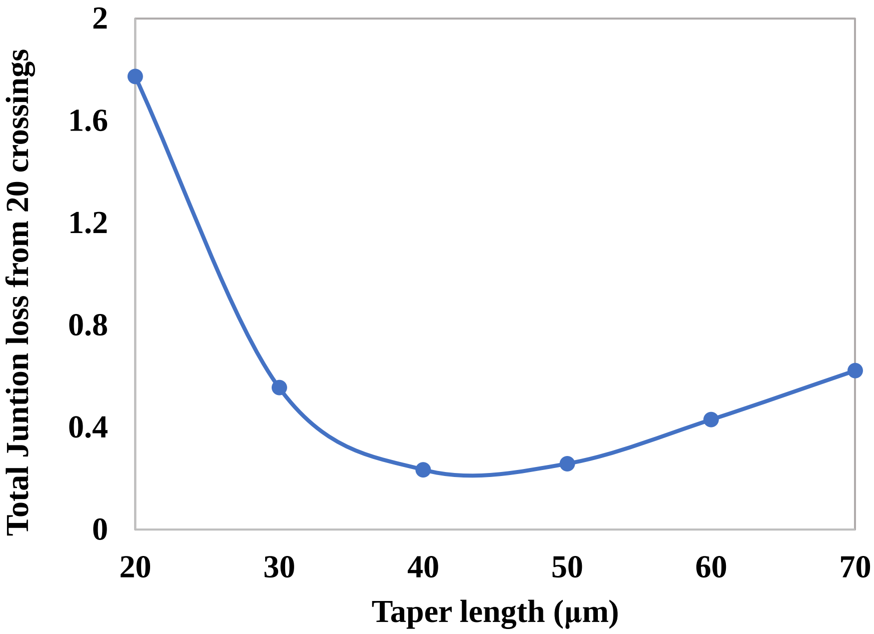

Figure 4.15: Illustrating the effect of taper length on the junction loss from 20 crossings.

Lastly, the junction loss for multiple crossing was modelled by having 54µm center to center gap between the two crossings and 40µm long input and output tapers.

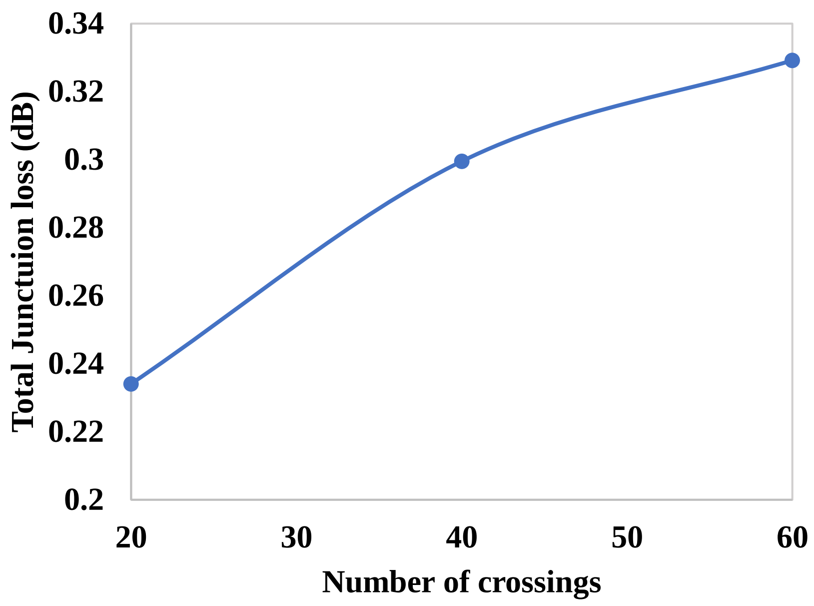

Figure 4.16: Total junction loss against the number of crossings when the beat length was 54 µm and tapers were 40µm long.

Figure 4.16 shows that the junction loss goes up almost linearly with number of crossings. After computed the waveguide width vs junction loss for one junction and calculated the beat length for the chosen width, the total junction loss vs number of crossing was simulated by running a BeamPROP simulation. More number of crossings (20, 40 and 60) were placed at an appropriate spacing and the loss from them was obtained.

The loss is not enormously high even for 60 crossings. For an integrated loop gyro, propagation loss dependent number of turns in a loop will decide the required number of crossings. The lower the propagation loss will be, the more the number of turns will be in the loop and ultimately crossings. Given the minimal crossings induced loss, a loop having large number of turns can be fabricated from thin Ta_2O_5 waveguides which then can be employed to realise high performance gyros.

4.7 Waveguide Dimensions Re-Optimization

As a result of measurements it was realized that to reliably fabricate ultralow-loss Ta_2O_5 devices, the waveguides should support only the fundamental TE mode for reasons related to mode coupling. Even though the TM and higher order TE modes of the previously optimised design were effectively not guided due to high substrate radiation and bend loss, the TE fundamental mode can be coupled to these other modes by sidewall roughness and bending of the waveguide creating an additional potential loss channel which needed to be addressed.

Therefore, the waveguide dimensions were re-optimized. Going thinner than 100nm induces high substrate radiation loss even for the TE fundamental mode and required thicker bottom cladding. The new dimensions were optimised with a 10μm thick silica bottom cladding. The upper cladding was chosen to be 2μm silica. Thicker upper cladding is in many ways a better conceptual choice but Belt et al. [112] reported that the quality of thicker sputtered silica films significantly degrades due to the incorporation of additional deleterious scattering centers.

Due to the shower head particle pattern issues with the PECVD silica (mentioned in chapter 3) and a number of ongoing and seemingly unresolvable issues around repeatability of the refractive index, a decision was made to use the newly available Veeco Spector IBS system to clad the devices. The IBS silica had a refractive index of 1.459 at 1550nm after annealing at 550 °C in air for 10 hours.

By keeping 10μm thick bottom cladding and 2μm thick top cladding, Ta_2O_5 waveguides with different widths and thicknesses were modelled and effective indices for TE and TM modes were recorded and plotted in figure 4.17,

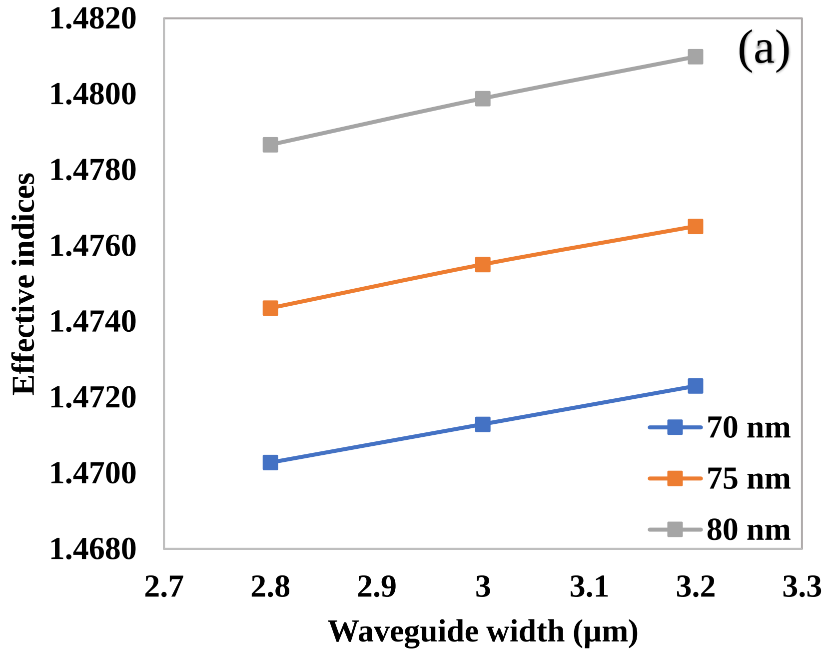

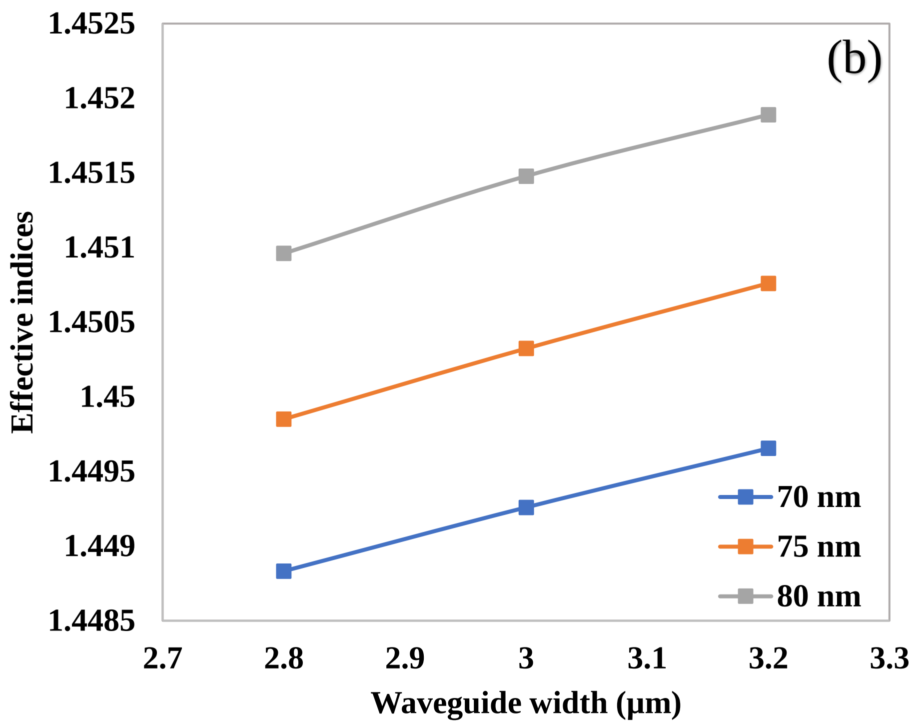

Figure 4.17: Effective index of (a) TE_0 mode and (b) TM_0 mode versus waveguide widths for three thicknesses 70nm, 75nm and 80nm.

As seen in figure 4.17, the effective index of the TM_0 mode for all the cases is lower than the refractive index of the upper silica cladding which suggested that the TM_0 mode would be cut off. Therefore a 3µm wide and 75nm thick design was chosen to fabricate single-mode, single-polarisation ultra-low loss waveguides. The substrate radiation and bending loss of the TE_0 mode was found to be negligible for the chosen dimensions.

4.8 Ta_2O_5 Waveguide Etching:

Due to the unavailability of the Oxford ICP etcher due to ongoing mechanical failures, Ta_2O_5 waveguides were etched in a Samco ICP etching system (RIE-400ip) available elsewhere in the university. Halogen containing gases (CHF_3 and SF_6) were used to etch Ta_2O_5 and O_2 was added into the gas mixture to produce non-vertical sidewalls, so the waveguides could be cladded by IBS silica without having any void between core and cladding in the waveguide corners.

Four different O_2 flows (5 sccm, 10 sccm, 15 sccm and 20 sccm) were tried and 20 sccm provided the desired non-vertical profile. Gas flows and etching parameters used for this process are listed in table 4.3:

Table 4.3: Gas flows and etching parameters used to etch Ta_2O_5 waveguides.

Parameters	Values
CHF_3	22 sccm
SF_6	5 sccm
Ar	10 sccm
O_2	20 sccm
ICP power	300 W
Pressure	5.25 mtorr
Table power	30 W
Temperature	20 °C

The etching rate for Ta_2O_5 was 40 nm/minute. Low etch rate and photoresist to material selectivity are mostly non-issues in the etching of such thin waveguides. A cross-sectional image of the etched waveguide is shown in figure 4.18,

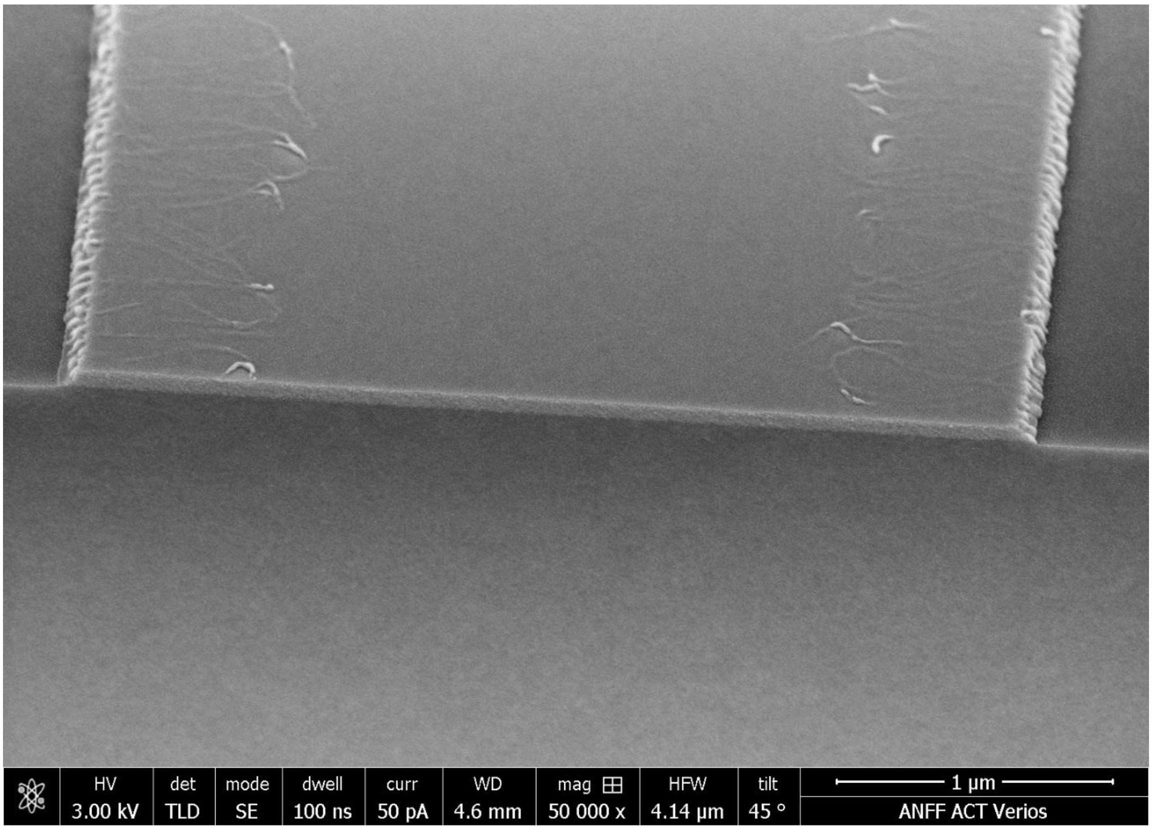

Figure 4.18: Illustrating the cross-sectional image of Ta_2O_5 waveguide etched with CHF_3, SF_6, Ar and O_2.

The waveguide is fully etched and mostly clean except for some residue left on top of the waveguide near the edges. It is believed that the residue is Ta_2O_5 deposited along the photoresist sidewalls during etching which collapses onto the waveguide upon resist removal. The residue needed to be removed to have clean waveguides. Therefore, the chip was placed under a mixture of O_2/CHF_3 (50 sccm/3 sccm) plasma in ICP for 10 minutes and result is shown in Fig. 4.19.

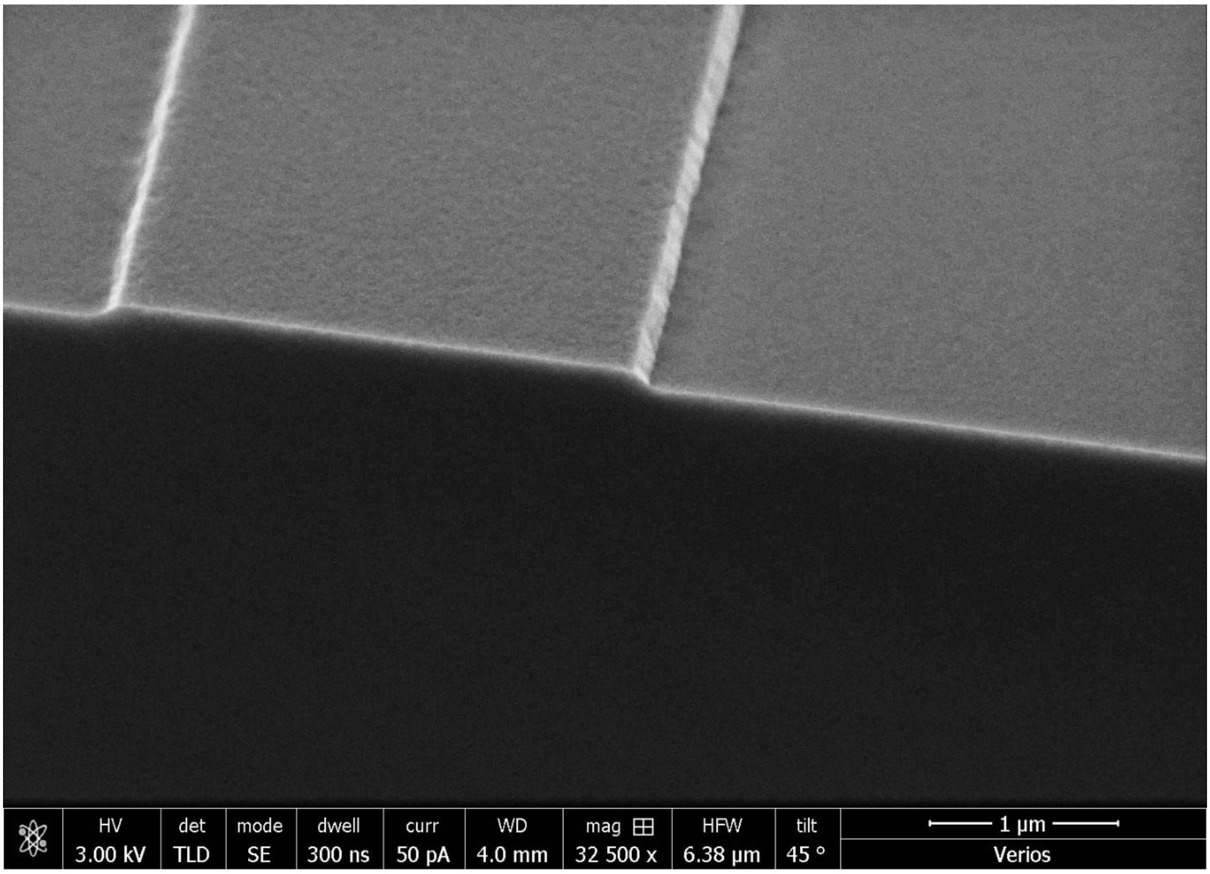

Figure 4.19: Showing the SEM images of Ta_2O_5 waveguide after 5 minutes of O_2 plasma treatment.

The residue is removed after the O_2/CHF_3 plasma treatment. However, the waveguide surface looks rougher due to the physical sputtering of the material which also resulted in the reduction of the waveguide thickness. Further experiments were conducted to try to optimise the Ta_2O_5 etching process. Unfortunately, the Samco etcher was not producing consistent results in terms of residue on top of the waveguide. Examples of the inconsistency in the processes are shown in figure 4.20 for devices etched in different sessions with exactly same conditions.

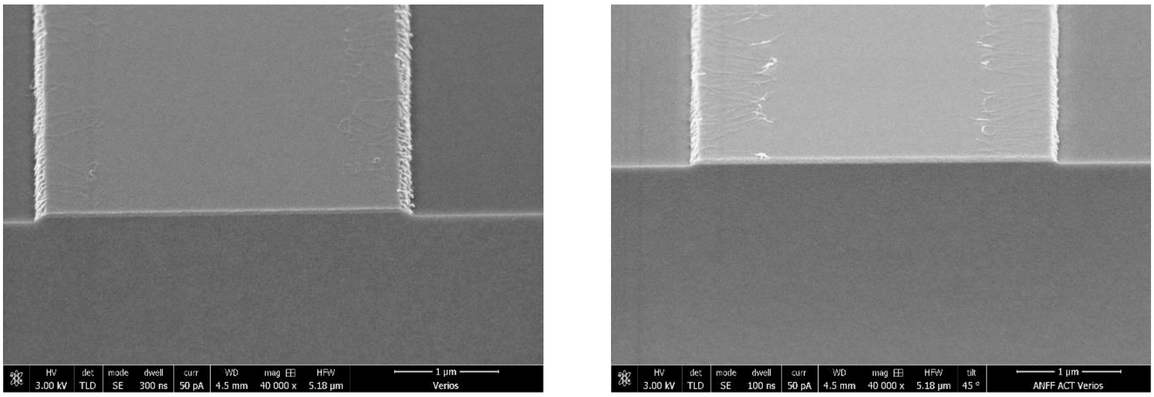

Figure 4.20: Exhibiting the difference in the residue sitting on top of the waveguides for two different chips processed with the same recipe.

The inconsistency in the process output is still under investigation. However, due to time limitations, it was decided to process the final wafer with the existing recipe and measure the loss. Figure 4.21 shows the SEM images of etched waveguides from the final wafer. After the photoresist removal, the residue was cleaned with the O_2 only plasma.

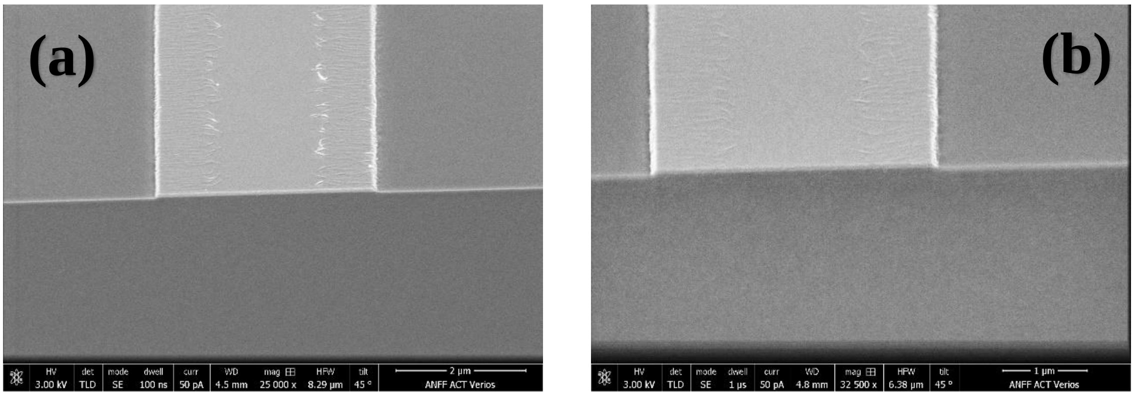

Figure 4.21: Showing the SEM images etched Ta_2O_5 waveguides, (a) after 8 minutes of only O_2 plasma treatment and (b) after 13 minutes of only O_2 plasma treatment.

As seen in figure 4.21, O_2 plasma treatment did reduce the residue but it is not fully removed. Longer O_2 plasma treatment could also roughen up the waveguide surface and reduce its thickness. Therefore, the wafer was cladded with IBS silica after 13 minutes of O_2 plasma treatment. After the cladding, the wafer was annealed at 550 ^{o}C in air for 10 hours to remove/reduce the hydrogen content in the waveguides. After measuring the loss, the wafer was annealed in humid air for 48 hours at 550 ^{o}C. However, the loss curve stayed the same as after the first annealing session.

4.9 Ta_2O_5 Waveguides Propagation Loss Measurement

The propagation loss of the Ta_2O_5 waveguides was measured through the spiral based cutback method. After cleaving the chip, spirals having different lengths were measured in order to be consistent with the end facet component of insertion loss. Figure 4.22 shows the propagation loss versus wavelength for the fabricated Ta_2O_5 waveguides. The loss curve was obtained by comparing the loss of 33.9cm long spiral to 11.4cm long spiral.

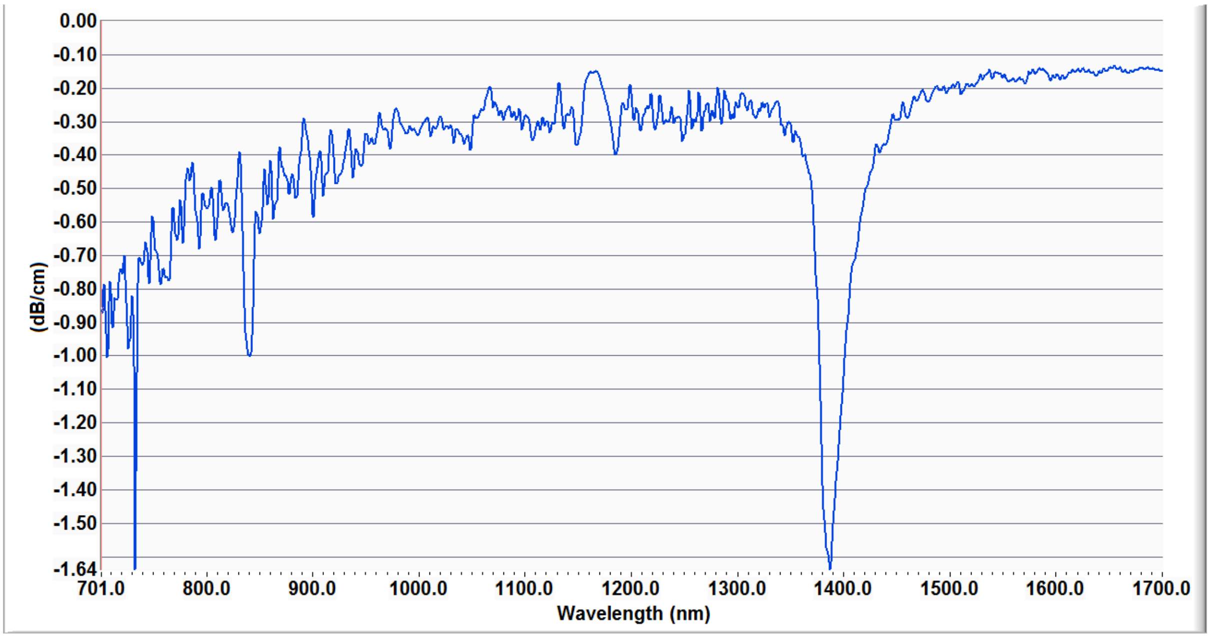

Figure 4.22: Illustrating the propagation loss of the fabricated Ta_2O_5 waveguides across 1000nm wavelength range.

As seen in figure 4.22, the propagation loss varies between 0.17 dB/cm and 0.14 dB/cm from 1530nm to 1700nm. The expected propagation loss was around 0.05 dB/cm at 1550nm which has been achieved from similar Ta_2O_5 waveguide dimensions by Belt et al. [112].

While measuring the propagation loss, it was observed through the camera that the straight waveguides induced/propagated the TM_0 mode as well which was lost around the bends due to the huge bending loss in the spirals for the TM_0 mode. The numerical model predicted that the TM_0 mode would cut-off because of its lower effective index than the refractive index of the top cladding. However, upon careful inspection of the model, it was found that both the TM_0 and 2nd order TE mode are propagating in the 2µm thin top cladding as strip loaded modes. The refractive index of the thin top cladding is slightly higher than the thick bottom cladding but the contrast was still sufficient to guide unwanted modes.

A lot of modelling work was performed to find out where the strip loaded TM_0 and 2nd order TE mode do not propagate. Waveguide dimensions and upper cladding refractive index were found to be the determining factors. With the existing refractive index (1.459 at 1550nm) of the IBS silica, even 2µm wide and 60nm thick Ta_2O_5 waveguide guides the TM_0 mode. Therefore, the upper cladding index was gradually reduced and at an index of 1.450, the TM_0

mode was cut-off. The mode field of the TM_0 mode is shown in figure 4.23,

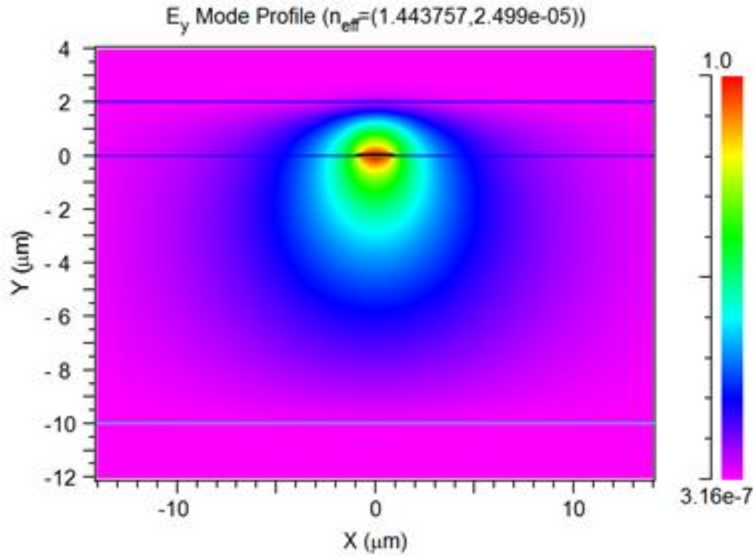

Figure 4.23: TM_0 mode field when the refractive index of the upper cladding was 1.450 at 1550nm and the core is 60nm thick by 2 microns wide.

As seen in figure 4.23, the effective index of the TM_0 mode is lower than both the cladding indices and mode is leaking into the substrate. However, 60nm thick waveguide imposes a larger minimum bending radius even for the TE_0 mode which is not suitable for compact applications. This thickness imposes a bending loss (dB/turn) of 0.09, 0.8 and 6.4 for a bending radius of 1500µm, 1000µm and 650µm respectively for TE_0 mode. Therefore, upper cladding refractive index was reduced from 1.450 to 1.444 to determine the threshold for matched claddings where the TM_0 mode cuts off. This allowed the thickness of the waveguide to increase to 70nm and width to 2.6µm for TE_0 only guidance. By using these dimensions, a bending loss of (dB/turn) of 0.0001 and 0.014 for a bending radius of 1000µm and 650µm can be achieved respectively. Therefore, it can be concluded that a smaller bending radius can be employed by using lower refractive index cladding.

The potential sources of the higher than expected propagation loss of the fabricated Ta_2O_5 waveguides are, coupling between the TE_0 and lossy TM_0 or 2nd order TE modes, scattering loss and material absorption loss. Coupling between the modes was checked both theoretically and experimentally. First, the waveguide modes (TE_0, TM_0 & 2nd order TE) were computed through FemSIM. Secondly, the TE_0 mode was launched into a 10cm long waveguide through BeamPROP and overlap between TE_0-TE_0, TE_0-TM_0 and TE_0-2nd order TE was computed and shown in figure 4.24. It is important to note that the waveguide had a 60-degree sidewall angle and sidewall roughness of 10nm in the simulation.

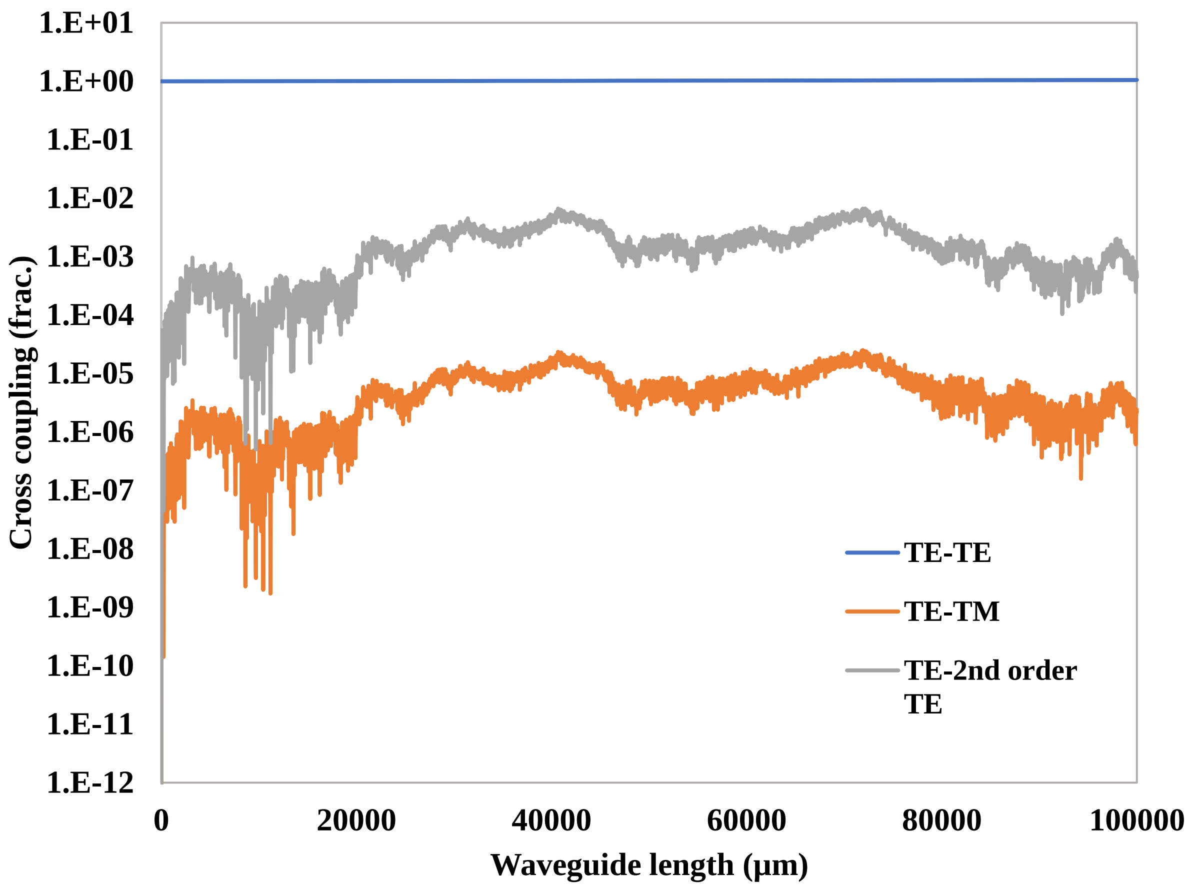

Figure 4.24: Exhibiting the overlap between the modes in the straight Ta_2O_5 waveguide.

As can be seen in figure 4.24, 0.1% of light is coupled into 2nd order TE mode in ~ 0.2 cm which corresponds to a propagation loss of 0.022 dB/cm. If this light is lost in the bend will then get re-excited and lost again. As can be seen in figure 3.21, the spirals have different length straight waveguides, so this loss will be different for different spirals which could result in slightly higher propagation loss. However, only 0.022 dB/cm is coupled in straight waveguides initially which does not explain the cause of high propagation loss.

The mode coupling was investigated experimentally as well for TE_0-TM_0 coupling. The polarisation of the input fibre was carefully adjusted to TE before being launched into a straight waveguide. Without touching the input fibre, the light was launched into a 6cm long straight waveguide (TM_0 propagation loss is low for the straight) and captured at the other end of the waveguide with a microscope objective and a highly sensitive InGaAs camera with a Wollaston prism to split the TE and TM polarisations vertically. This showed that the TE_0 polarisation present at the output to the sub percent level and a tiny bit of TM polarisation is also present which suggest that extremely small coupling occurs between the TE_0 and TM_0 modes during propagation at least in straight waveguides. The experimental result is shown in figure 4.25 for the fibre launch and waveguide output.

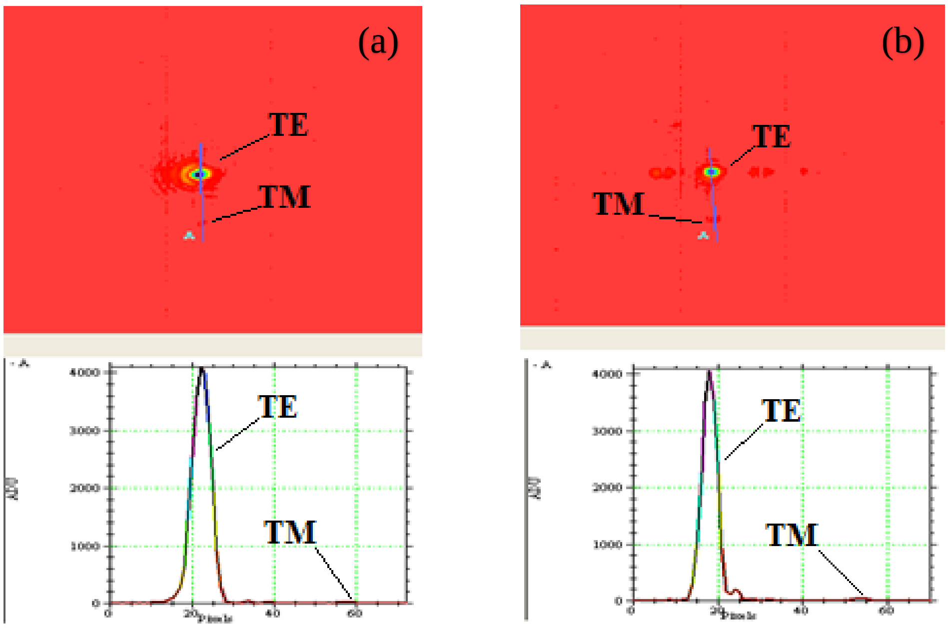

Figure 4.25: Showing the intensity of the TE and TM modes, (a) fibre only and (b) fibre and waveguide.

The intensity of both the modes was obtained by putting a cursor through the centre of the modes. As seen in figure 4.25, the intensity of the TM_0 mode is almost similar for both the cases (a) and (b) which is consistent with the theoretical result that there is an extremely weak coupling between the modes. Further, the output for the TE polarisation looks very Gaussian like with no clear evidence of a higher order mode propagating. This analysis could only be performed for the straight waveguides as both TM_0 and 2nd order TE mode have high bend loss and so it is not easy to measure if they are coupled to the fundamental TE by the bend structure which is certainly possible due to the orthogonality violation imposed by a bend. Having established that coupling does not occur at meaningful levels in the straights, the TM polarisation coupling can be further investigated by comparing the straights to the bends.

The source of the propagation loss was therefore further investigated by measuring the waveguides with nominally unpolarised light from an Erbium doped fibre amplifier. The insertion loss of the four different waveguide lengths (3 spirals with the same structure and one straight) was plotted at three different wavelengths of 1480nm, 1550nm and 1600nm. The graph is presented in figure 4.26.

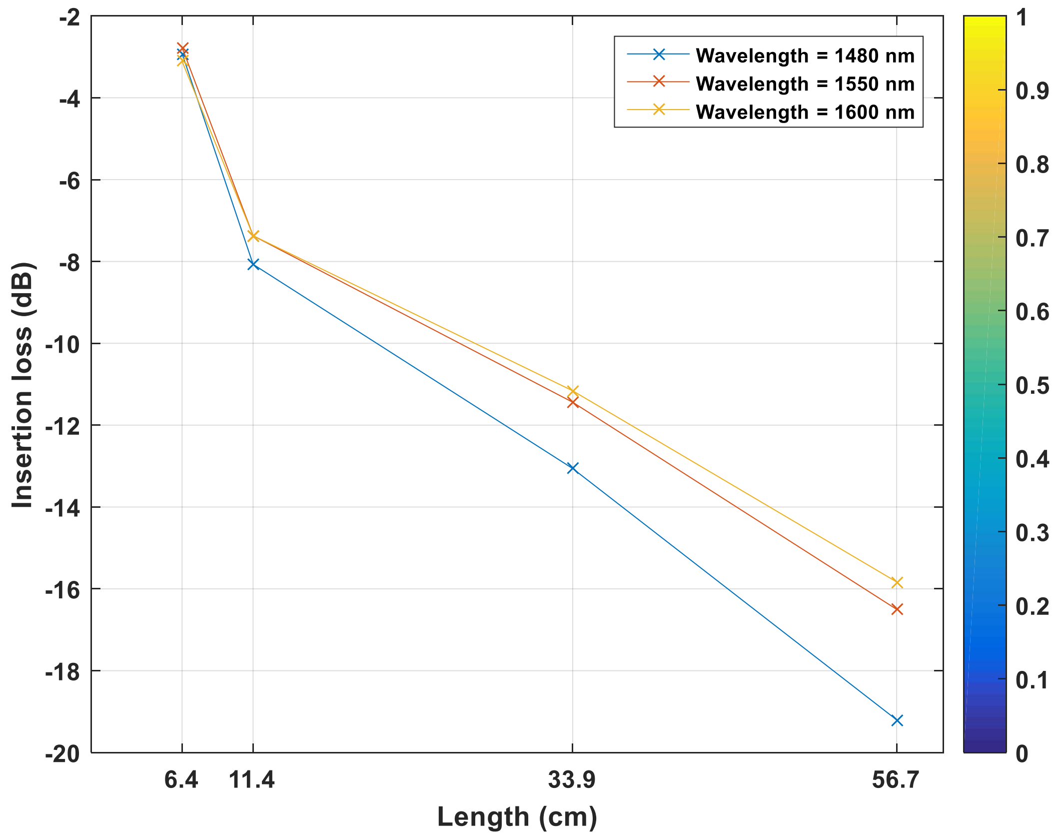

Figure 4.26: Insertion loss of the four waveguides measured with nominally unpolarised ASE from fibre amplifier. Except 6.4cm long waveguide, all other waveguides were in the form of spirals with the minimum bending radius of 650µm.

Figure 4.26 clearly shows that the insertion loss of the straight waveguide (6.4cm) is significantly lower as compared to the spirals for all three wavelengths. For the case of spirals only, the gradient of the 1550nm wavelength shows a propagation loss of around 0.19 dB/cm which is slightly higher than what is reported in figure 4.22. Extrapolating the 1550nm spiral loss curve suggested an insertion loss of -6.42 dB at 6.4cm compared to the observed loss of -2.8 dB which is -3.62 dB lower. Given that all TM polarised light in the unpolarised launch is lost in the bends, the expected loss difference would be 3dB plus the total bend and junction losses for the spiral. All the spirals have 43 junctions with the bending radius ranging from 650µm to 2400µm. The total junction loss from a spiral was computed through FemSIM and found to be 0.318 dB. Thus a loss of 0.3 dB still exists even after offsetting the junction loss and TM polarisation power from -3.62 dB. Even taking this additional loss which then equates to 0.047 dB/cm, this is not sufficient to explain the higher than expected propagation losses, indicating that coupling to TM_0 even in the bends is not the problem. There was no feasible means to investigate the TE_1 coupling in the bends.

As a further means of studying the propagation loss, the waveguides were tested using Optical Low-Coherence Reflectometry (OLCR) measurement. The reasoning behind this measurement was to determine if the propagation loss was uniform with distance (i.e. is there unexpected loss at the bends or at any scattering centres, etc). In this method, a broadband low-coherent light is launched into the waveguide through a fibre. At the front facet of the waveguide, a part of the light is reflected back by means of Fresnel reflection and coupled into the fibre resulting the formation of first reflection signal. The other part of the light which was transmitted into the waveguide travels a single trip and reflected back from the back facet of the waveguide. upon reaching the front facet, a portion of the light is coupled into the fibre resulting the formation of second reflection signal. In parallel to that, a movable reference mirror is continuously being scanned. The reflected beams from the waveguide and reference mirror are then combined and transmitted to the detection system. Due to incoherent light source, interference occurs only when the path difference between the two beams is zero. In this way, the spatial distribution of the multiple reflection signals can be resolved by the reflectometer. From the magnitudes of the multiple reflection signals, the propagation loss of the waveguide is extracted [242, 243]. This method has the capability of achieving a spatial resolution in the micrometer range. Figure 4.27 shows a representative OLCR trace of a 33.9cm long waveguide.

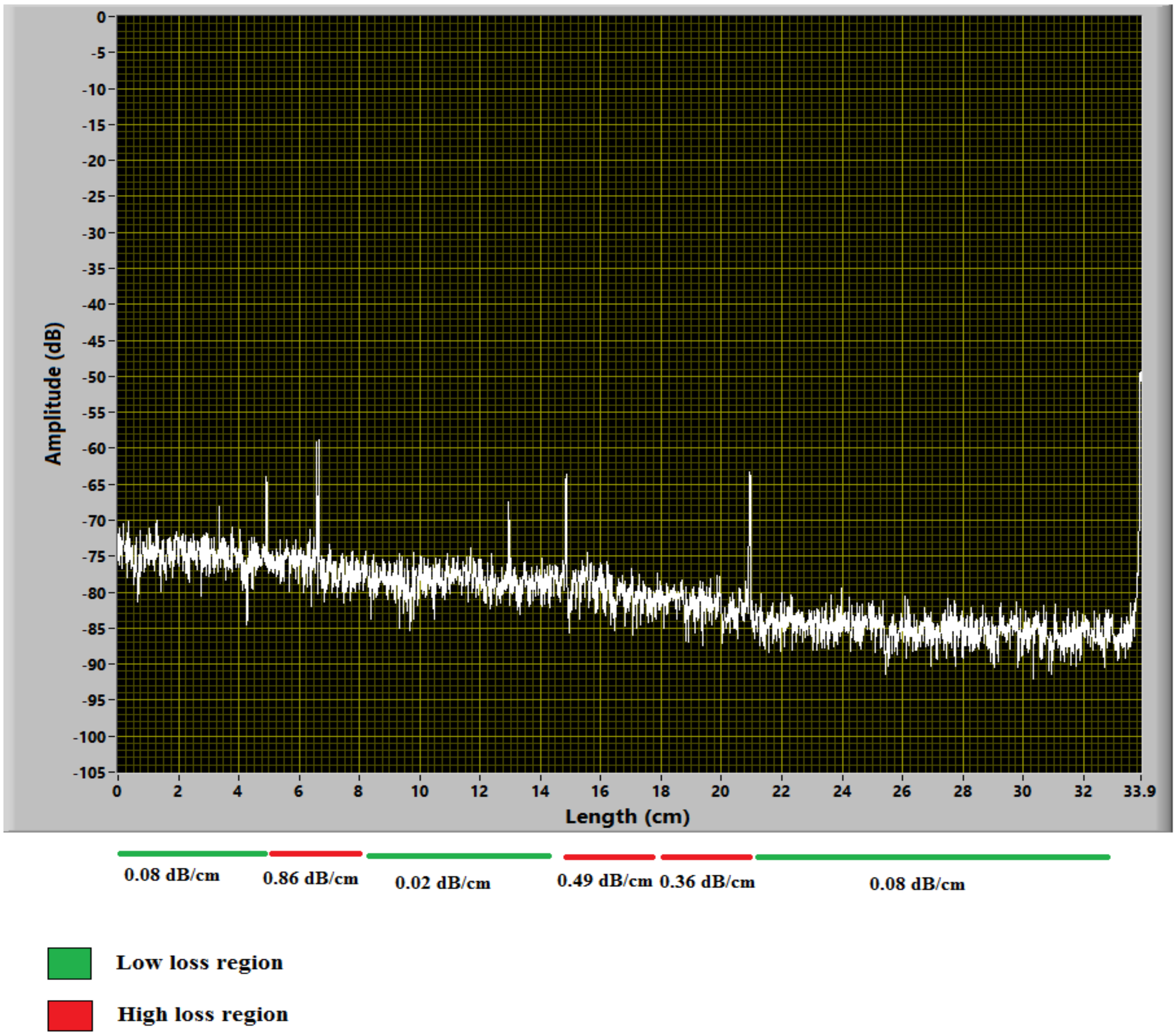

Figure 4.27: OLCR trace of 33.9cm long waveguide

The first conclusion from all the traces obtained was that there was no systematic loss source present that correlated with the bend positions, thereby ruling out the TE_1 coupling as a major contributor. Secondly, the traces in general showed occasional local point losses and in some cases staircase like slope indicating the presence of significant scratch like defects. With the help of a custom LabVIEW code, the propagation loss was computed locally and indicated with green and red bars in Figure 4.25 which correspond to low and high loss regions, respectively. Notably a 6cm long region has an observed propagation loss of 0.02 dB/cm, reasonably close to the predicted loss. For the illustrated 33.9cm long waveguide, integrated overall propagation loss was computed from the indicated local losses which returned an average propagation loss of 0.17 dB/cm, a very good match to the measured results from figures 4.22 and 4.26 thereby validating the accuracy of the OLCR measurement. Therefore, it can be concluded that localised high loss regions arising from the etching inhomogeneities observed likely increase the overall propagation loss of the waveguides, but that fundamentally they are capable of operating in the ultra low loss mode desired.

4.10 Conclusion

This chapter starts with the introduction of the Ta_2O_5 and its significance in the field of integrated photonics. Ta_2O_5 films were deposited by employing IBS system. Waveguide dimensions were optimised, and a number of gyro components were designed which include 3dB coupler, bus waveguide ring resonator and low loss crossing arrays. The designed 3dB coupler is found to be quite sensitive to minor fabrication offset which makes it unsuitable for gyroscopic applications. The designed bus waveguide ring resonator is fabrication tolerant and can be employed for high performance applications. The loss of the crossing arrays is found to be quite nominal means the designed crossing arrays can be employed to fabricate a long waveguide loop which will ultimately result in a better sensitivity.

Furthermore, Ta_2O_5 waveguides were fabricated, and a propagation loss of 0.17 dB/cm was measured at 1550nm. A detailed theoretical and experimental analysis was performed to investigate the possible cause of the higher propagation loss. OLCR measurement showed occasional local point losses and in some cases staircase like slope indicating the presence of significant scratch like defects. However, a 6cm long region has an observed propagation loss of 0.02 dB/cm, reasonably close to the predicted loss. Therefore, it can be concluded that by addressing inhomogeneities related to etching, ultra-low loss waveguides can be achieved.

Chapter 5 Design optimisation and performance prediction for an integratable thermo-optic phase modulator

5.1 Introduction

Modulation and active trimming are fundamental operations needed in many integrated optical circuits. Optical Modulation refers to a change induced in the optical field e.g. phase, frequency, polarisation, amplitude or quantum state. Optical modulators are fundamental components of high-speed optical transceivers (a combination of optical transmitter and receiver) and play an important part in high capacity optical networks because they allow high speed and high quality optical signal generation.

Optical modulators are also used in other applications such as optical switching, sensing and neural networks [244-246]. Optical phase modulators are a fundamental part of angular velocity sensors (gyroscope). In fibre loop or waveguide loop gyros, the output intensity signal is essentially the interference between the counter propagating beams with different phases induced by the Sagnac effect. The natural response of the interference signal is cosine shaped (equation and details are given in chapter 2). Therefore, phase biasing is required to overcome the inherent zero sensitivity at the peak of the response and avoid ambiguous detection [247]. A phase modulator is placed in one input arm of the gyro to produce required biasing.

In resonant gyros, the phase modulation technique is widely used in order to accurately detect the extremely small shift in the resonant frequencies induced by the Sagnac effect [248]. The well-known Pound Drever hall method is employed for laser frequency locking and often realised using phase modulation. Both the modulation frequency and index affect the slope of the demodulation curve which determines the signal-to-noise ratio of the sensor. It has also been reported in the literature that phase modulators with a bandwidth of few MHz are good enough to optimize the performance of the resonant gyros [151]. Optical modulators are also employed for tunning/trimming application. In integrated photonics, it is difficult to achieve the desired performance from a fabricated device (e.g. splitting ratio of a 3dB coupler) due to fabrication imperfections and trimming is required to address this issue. Kiyat et al. [249] reported a resonator based optical switch on a SOI rib waveguide having dimensions of 1μm^2. The switch requires only 17 mW of electrical power to scan the resonance wavelength to over full free spectral range. The response time of the device was found to be 210 kHz.

In integrated photonics, modulation is most usually achieved by changing the complex effective modal refractive index of a waveguide. The refractive index of a material depends on several effects, of which the most interesting for phase modulation are the intensity of the interacting light, applied electric field strength, number of charge carriers and temperature. The change in the refractive index of a material by the above mentioned effects is represented as [250]:

$$\Delta n^{/} = \Delta n + \Delta ik \tag{5.1}$$

Where, Δn and Δik represent the change in the real refractive index and optical extinction coefficient, respectively.

For practical low loss materials and effects, direct optically driven phase modulation is too weak to be effective as it relies upon the Kerr effect.

The refractive index of a material can also be modified under the application of an electric field and this is considered a preferred way of optical modulation because it implies fast response time and low power consumption. The modification in the refractive index with respect to an applied electric field is described by the following equation:

$$\Delta n^{/} = PE + KE^2 \tag{5.2}$$

Where, P and K are wavelength dependent constants and E represents the electric field. The first and second order change of the refractive indices are recognized as the Pockels and Kerr effect, respectively. The Pockels effect produces birefringence in materials that lack inversion symmetry and commonly known as non-centrosymmetric materials (e.g. gallium arsenide and lithium niobate). However, it is not accessible in materials that exhibits inversion symmetry (i.e. centrosymmetric materials) as the reversal of sign in the total electric field must cause a reversal of sign in the total polarisation density component [251]. Therefore, Pockels effects is possible only in non-centrosymmetric materials.

The Kerr effect has no requirement on crystalline structure for its operation and so induces a refractive index change in all materials. In this effect, an optical beam experiences polarisation dependent phase change while travelling through a medium in the presence of an electric field which is proportional to the square of the applied electric field. In comparison with the Pockels effect, the Kerr effect is weak because the change in refractive index is proportional to the square of the electric field rather than the linear [252].

Another electric field effect that is commonly used for optical modulation is known as the

Franz–Keldysh effect. Here the refractive index of a semiconductor at a wavelength near the band edge is affected through the Kramers-Kronig relationship by changing the absorption near the bandgap under the application of an electric field. This effect is only suitable/applicable for direct bandgap semiconductors (e.g. GaAs) because the absorption coefficient changes quickly near the band edge for such semiconductors. The absorption coefficient near the band edge in indirect semiconductor is weak due to phonon involvement in absorption in the indirect transitions. Therefore, this effect is unsuitable for indirect semiconductors such as silicon [253].

Alternative methods are employed to induce optical modulation in centrosymmetric materials or indirect semiconductors. For semiconductors, the commonly used method is the free carrier plasma dispersion effect. This describes both the real and imaginary refractive index change in response to a change in the free carrier concentration of a material. The relation between the change in the absorption coefficient (Δα) and refractive index (Δn) to the change in the density of the free charge carriers (electrons and holes) is described by the Drude-Lorenz equations which is written as:

$$\Delta\alpha = \left(\frac{e^3\lambda_0^2}{4\pi^2 c^3 \varepsilon_0 n}\right).\left(\frac{\Delta N_e}{\mu_e (m_{ce}^*)^2} + \frac{\Delta N_h}{\mu_h \left(m_{ch}^*\right)^2}\right) \tag{5.3}$$

$$\Delta n = \left(\frac{-e^2\lambda_0^2}{8\pi^2 c^2 \varepsilon_0 n}\right).\left(\frac{\Delta N_e}{m_{ce}^*} + \frac{\Delta N_h}{m_{ch}^*}\right) \tag{5.4}$$

Where, ΔN_e and ΔN_h is the change in the electron and hole density respectively, c is the speed of light in vacuum, λ is the wavelength, e is the electronic charge, ε_0 is the vacuum permittivity, m_{ce}^* and m_{ch}^* represent the effective masses of electrons and holes respectively and μ_e and μ_h represent the electron and hole mobility.

Bennett and Soref [254] quantified Δn and Δα more accurately from the experimentally measured absorption curve and came up with empirical expressions which are now used universally. The expressions for 1.55μm are:

$$\Delta n = \Delta n_e + \Delta n_h = -8.8 * 10^{-18}.\Delta N_e - 8.5 * 10^{-18}.(\Delta N_h)^{0.8} \tag{5.5}$$

$$\Delta\alpha = \Delta\alpha_e + \Delta\alpha_h = 8.5 * 10^{-18}.\Delta N_e + 6 * 10^{-18}.\Delta N_h \tag{5.6}$$

Where, Δn_e represents the change in the refractive index as a result of change in the density of electrons and similarly Δn_h is the change in refractive index due to the change in the density of holes. $\Delta\alpha_e$ and $\Delta\alpha_h$ represent the change in absorption coefficient resulting from the change in density of electrons and holes, respectively.

The concentration of electrons and holes can easily be modified/changed by passing a current through semiconductors. The performance of such modulators is essentially based on how quickly the free carriers are injected or removed from the area where the optical beam is propagating. The plasma dispersion effect is known to provide fast modulation of up to or above 10 GHz.

Furthermore, the free charge carriers needed for the modification of the refractive index also absorb light which results in the attenuation of the optical power [255]. Therefore, the modulators based on this effect are unsuitable for number of emerging applications due to the intrinsic losses result from the free carrier absorption and large passive insertion losses [256]. The formation of a doping zone to enable carrier injection also adds significant complexity in the fabrication process.

Polymers based electro-optic modulators have been emerged as an ideal option for applications require fast modulation. Electro-optic polymers are a new class of materials that are designed to have high thermo-optic coefficient, compatible with other materials and provide fast response. Lee et al. [257] achieved a modulation bandwidth of upto 200 GHz from a polymer modulator which is quite high as compared to its alternatives.

On the other hand, there are certain drawbacks associated with polymer modulators which include stability (thermal and long term electro-optic coefficient) and loss, and require considerable research efforts to be solved. Optical absorption and scattering of chromophores are found to be source of high loss in electro-optic polymers [258]. A loss as low as 1.5 dB/cm at 1550nm has been reported from electro-optic polymer by Garner et al. [259]. These drawbacks restrict its employability in applications require low loss and operate in harsh environments.

The thermo-optic effect is relatively simple to implement and has been successfully employed for modulation at up to few MHz without having a free carrier absorption and stability issues. In the thermo-optic effect, the phase of an optical beam is modulated by putting a heater close to a waveguide that modifies its refractive index. The reason behind their slow time response or low modulation rate is large thermal spreading and thermal capacitance. The heater can be placed on top of the waveguide or on either side of the waveguide. However, heater on top of the waveguide geometry would require the deposition of an insulating layer between the heater and waveguide in order to isolate the optical mode from the heater. The extra step (deposition of an insulating layer) in the fabrication process can be avoided by placing heater on side of the waveguide. For polymer cladded waveguides, the real issue is the surface temperature of the polymer when the heater is on top. This argument is backed up with the simulation results later in this chapter.

A number of thermo-optic modulators have been designed and fabricated [256, 260, 261]. The energy efficiency of such modulators mainly depends on the efficiency of the heat transfer and its confinement to the waveguide region. In other words, heat isolation around and/or underneath the waveguide region determines the power consumption of thermo optic modulators. The creation of an air trench is a common approach to increase the heat isolation. The air trench reduces the heat leakage into the silicon substrate which then results in a significant reduction in the power consumption. However, doing so adds an extra step in the fabrication process and also causes the reduction in the reliability due to the piled mechanical fatigue from the thermal stress [262].

Another method to improve the efficiency is the fabrication of multipass waveguide routing under the heater in order to increase the optical interaction length with the heated region. However, care must be taken while designing such modulators because optical coupling can occur between adjacent waveguides. If the adjacent waveguides have similar dimensions and are close enough, the light coupling between them is resonant and all the light can be transferred over a coupling length short enough to be of concern. The waveguide spacing issue limits the number of waveguides under the heating region and therefore ultimately the power efficiency. This problem can be solved by having waveguides with different widths because light coupling between different dimension waveguides does not achieve phase matching and results in minimal power coupling.

Generally speaking, the time response of thermo-optic devices is inversely proportional to the switching power. Therefore, a trade off among the time response, switching power and optical loss is considered while designing such devices. Chung et al. [260] recently reported a silicon thermo-optic modulator with a total footprint of 0.0023 mm^2 and consumes only 2.56 mW for 180^o phase shift. The device also has low (for silicon) optical loss of 1.23 dB. Jacques et al. [263] reported a SOI based modulator with a switching power of 21.4 mW for л phase shift and time constant of only 5.6 µs. Considering the advantages of thermo-optic devices, a phase modulator based on this effect is designed for this project.

Thermo-optic modulators are used in a broad range of applications and are not limited to a single type of material or design [256, 261] though they are most commonly employed where a Pockels effect is unavailable, i.e. in amorphous materials or centrosymmetric semiconductors. Thin Ta_2O_5 waveguides cannot be employed for thermo-optic modulation as most of the mode field is in the cladding and heat could not push it much into the core. This ultimately resulted in a small change in the effective index. Same reason goes with high index contrast waveguides where the field is tightly confined in the core and there is not enough room to change the effective index.

Germanium doped silica ($Ge:SiO_2$) waveguides with silica or polymer cladding on top are widely used in photonic applications [264-266] due to their low propagation loss in the visible and infrared range, their highly efficient coupling to optical fibre, and high photosensitivity to ultra-violet (UV) light [267] enabling photo tuning of devices or the inscription of Bragg gratings. The refractive index of 3% index contrast $Ge:SiO_2$ is 1.486 at 1550nm [268].

The change in the effective index was computed for both Ta_2O_5 and $Ge:SiO_2$ waveguides by using the exact same conditions in terms of cladding index, temperature change and edge to edge gap between the waveguide core and heaters. The thickness of the core was the only difference between the two geometries where 3µm thick $Ge:SiO_2$ waveguide core was thinned to 80nm thick Ta_2O_5 core. The change in the effective index was found to be 0.001135 and 0.000072 for $Ge:SiO_2$ and Ta_2O_5 waveguides respectively. Due to the significant difference in change in the effective index induced by two different geometries, $Ge:SiO_2$ was used to design thermo-optic phase shifter.

5.2 Theoretical Optimisation

Thermo-optic modulators must be designed to efficiently and compactly modulate the phase of the light without inducing high optical losses. $Ge:SiO_2$ is found to be an option which match all the requirements. Single-mode $Ge:SiO_2$ waveguide was computed by using RSoft FemSIM [165]. The optimised width of the single-mode $Ge:SiO_2$ waveguide was found to be 3µm for 3µm thick $Ge:SiO_2$ waveguide and these dimensions will be used in for the remainder of this work as the design for the phase modulators. Initial modelling as carried out using Silica index matched Acrylate polymers have a thermo-optic coefficient of $-1x10^{-4}/^{o}C$ [269] which is an order magnitude higher than silica at $1x10^{-5}/^{o}C$ [270]. Polymers with refractive indices ranging from 1.430–1.480 at 1550nm are commercially available and hence a good selection for an over cladding material here [271]. Polymers for modern planar photonic devices are found to be an attractive candidate due to the combination of their exceptional optical properties such as, tuneable refractive indices, low optical losses, reasonable temperature stability and large thermo-optic coefficient. They are easy to fabricate and commercially available (low cost) [272]. Unfortunately, only a few polymers are suitable from a large pool of commercially developed polymers. A list of suitable polymers is tabulated in table 5.1 that are suitable for optical applications [273].

Table 5-1: comparing the important properties of polymers for thermo-optic applications [273-278].

Polymer type	Propagation loss in dB/cm at 1550 nm	Thermo-optic coefficient (10^{-4} °C^{-1})	Thermal conductivity (W/m.°C)
Cyclic olefin copolymer	0.7	-1	0.16
ZPU	0.35	-1	0.2
Cyclotene	1.5	-0.15	0.29
PMMA		-0.85	0.18
EpoCore	2.2	-0.7	
Deuterated Polysiloxane	<0.5	-3	~0.22

Propagation loss and thermo-optic coefficient are important properties for the planar implementation of thermo-optic phase modulators. Among all the polymers tabulated above, ZPU exhibits the lowest propagation loss and has a reasonable thermo-optic coefficient. In comparison with the ZPU, polysiloxane has quite a large thermo-optic coefficient. However, it induces a propagation loss of slightly less than 0.5 dB/cm which is higher than ZPU. Whereas thermal conductivity of both the materials is almost similar. Lower propagation loss, reasonable thermo-optic coefficient, and availability make ZPU a preferred candidate for testing thermo-optic phase modulators.

The amount of phase shift induced depends on the thermo-optic coefficient of every material, the temperature achieved in each material, and the temperature and optical intensity distribution between the materials. The phase shift is defined as [260, 279]:

$$\Delta\Phi = 2\pi L \Delta n/\lambda \quad (5.7)$$

Where, $\Delta\Phi$ is the phase shift, L is the heated length, Δn is the change in the effective index of the waveguide and λ is the operating wavelength.

A phase shifter can be designed with different optimisation goals: lowest loss, smallest power consumption, highest speed, shortest length or a compromise between these parameters. For this work, a phase modulator is desired with insertion loss ≤ 0.5 dB and total length ≤ 2mm respectively. Modulation speed should be as high as possible subject to the prior constraints.

The reason behind the chosen loss and length is to fabricate a phase modulator which provides sufficient modulation and can easily be integrated on the chip along with other gyro components. The globally accepted figure of merit for thermo-optic phase modulators is the product of electrical power required for a л phase shift and time constant for heat diffusion (rise or fall) $P_\pi.\tau$ which should be as small as possible.

Thermo-optic phase modulators can be realised in number of ways. Heaters can either be placed on top of the waveguide or with some lateral separation. It has also been reported that moderately low loss heaters can be embedded directly into a silicon waveguide by doping that part of the waveguide [280]. However, doing so increases the optical loss of the device which is unsuitable especially for cascaded switches such as in switch networks. This approach is advantageous where a single modulator is required but doping the part of waveguide adds further complexity in the fabrication and is not applicable to non-semiconductor materials.

As stated above, heaters on top of the waveguide geometry requires an insulating layer between the heater and waveguide to isolate the optical mode from the metal heater. This approach also has reliability issues due to the accumulated mechanical fatigue from the thermal stress [262]. For polymer cladded waveguides, putting heaters on top of the polymer reduces the amount of heat reaching the waveguide core significantly. Energy 2D software was used to find out how much temperature of the heaters (placed on top of the polymer) needs to be raised to get the same amount of heat on the core surface as compared to when they are sitting on the side waveguides. The thickness and thermal conductivity of the polymer chosen in the simulation were 12μm and 0.2 W/m.^{o}C respectively. The results of the computation are shown in figure 5.1.

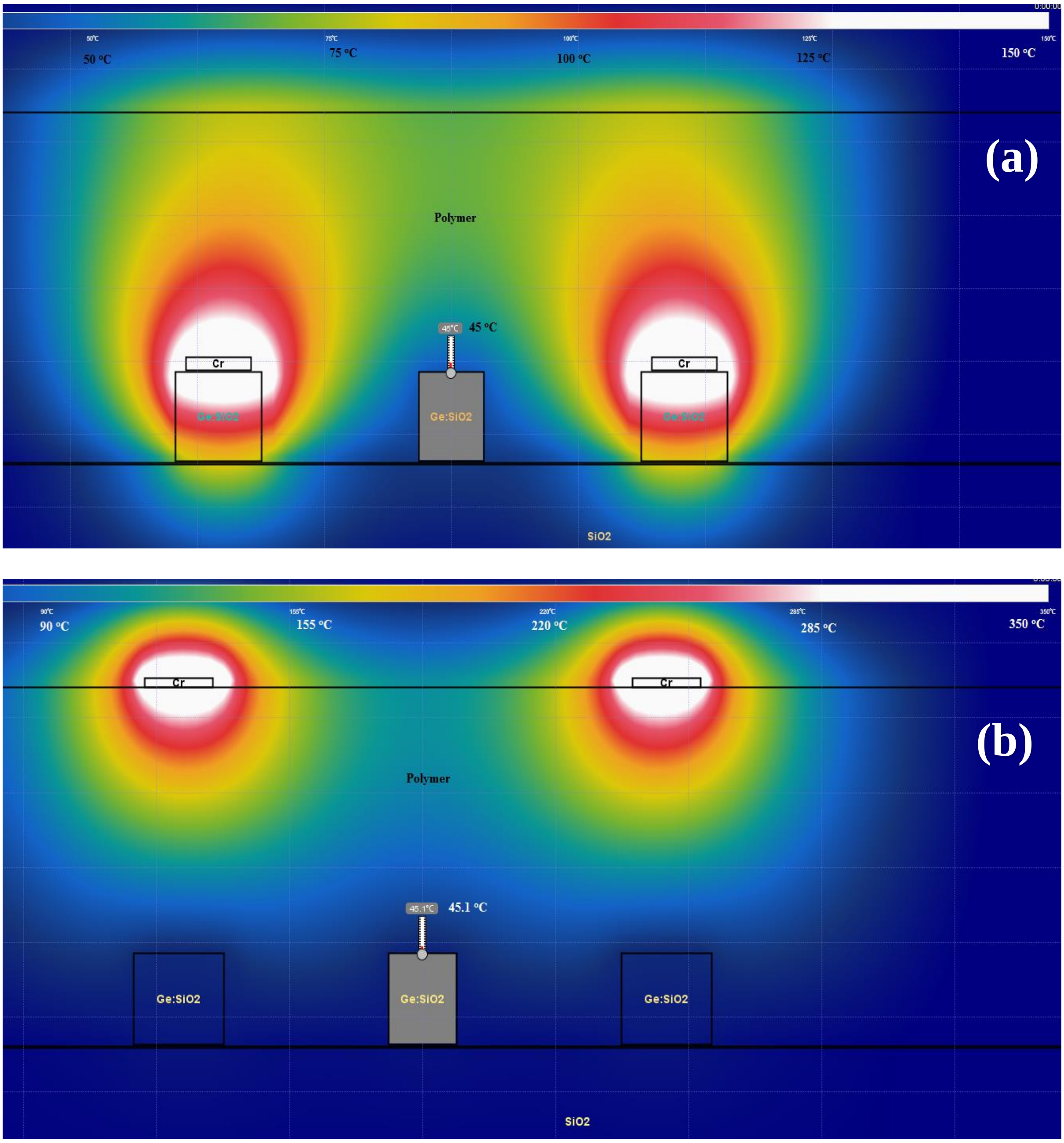

Figure 5.1: Illustrating the temperature of the heaters required to get the same amount of heat on the core surface, (a) when they are sitting on the side waveguides and (b) when they are on top of the polymer.

As can be seen in figure 5.1, heater's temperature needs to be increased from 150 ^{o}C to 350 ^{o}C to get the same amount of heat on the core surface when they are placed on top of the polymer. One wider (6µm) heater exactly on top of the core also requires more than 230 ^{o}C to get 45 ^{o}C on the core surface. Most of the polymers do not withstand such a high temperature, therefore side heater's design was adopted for this work.

As mentioned previously, adjacent structures that have waveguide like index distributions cannot be made phase synchronous in order to avoid optical coupling. As the simplest method to make raised side heaters is to leave some core material present for the heater pedestals, this effect was analysed by putting 3μm wide heaters on 3μm wide side pedestals when the main waveguide was 3μm wide. The heaters were turned optically inactive implying they are physically not present. The edge to edge gap between the heaters sitting on side waveguides (pedestal's) and the main waveguide was chosen to be 8μm. The optimum gap between them is discussed later in this chapter. FemSIM results showed a very strong optical coupling in the side waveguides as seen in figure 5.2,

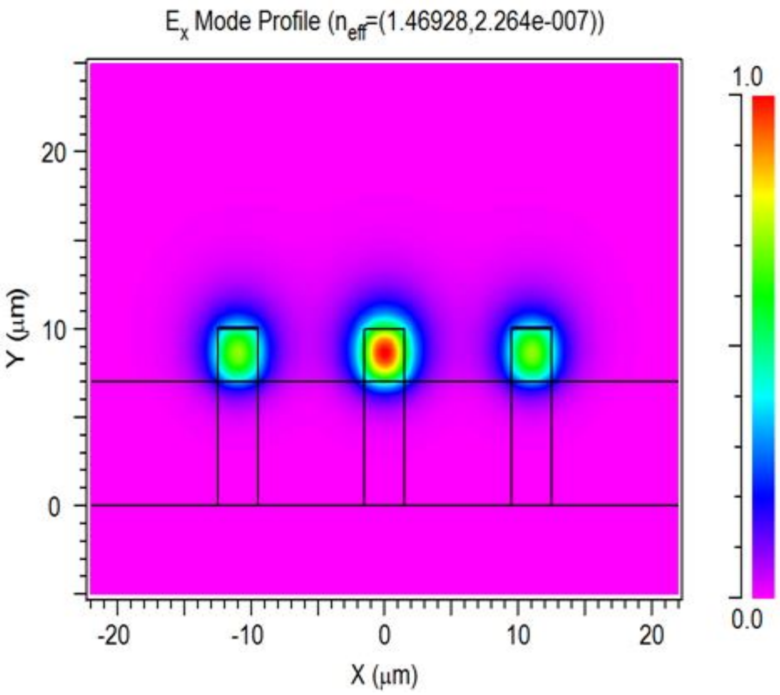

Figure 5.2: Showing a strong optical coupling when the dimensions and index profile of the heater pedestals are exactly the same as the waveguide core. The upper cladding refractive index used for this simulation was 1.465.

Even a bigger edge to edge gap between the waveguides doesn't change this effect. However, a slight change as small as 0.1μm in the width of the pedestal eliminates this issue as can be seen in figure 5.3.

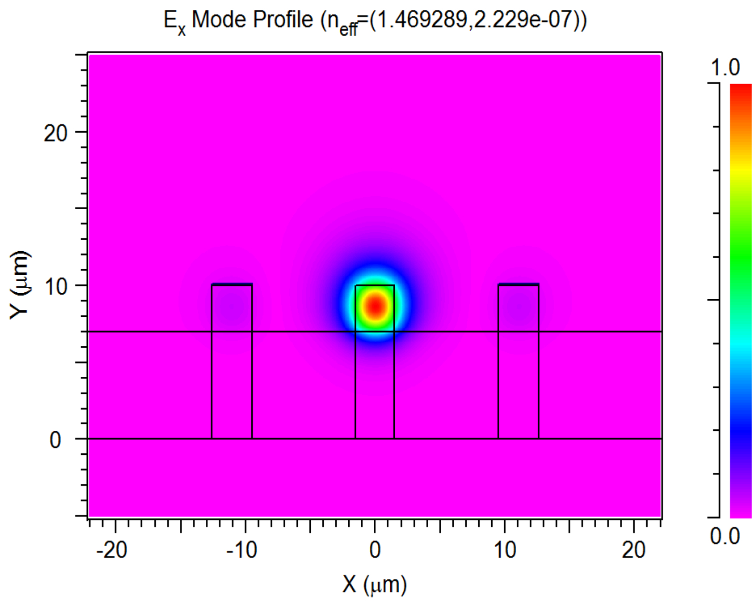

Figure 5.3: Illustrating a negligible optical coupling when the width of the heaters is only 0.1µm bigger than the waveguide core. The upper cladding refractive index used for this simulation was 1.465.

As seen in figure 5.3, the optical coupling in the pedestal's becomes negligible after a slight increment of 0.1µm in the pedestal's width. Doing so would improve the loss of the device as minimal amount of light will be coupled into the pedestal's and interact with the metal heaters.

Using FemSIM, two designs (heater's on pedestal's and heater's on bottom cladding) were simulated to investigate which gives the larger change in the effective index. The ZPU with a refractive index of 1.465 at 1550 nm was used as top cladding for the optimum design illustration purposes. For both the designs, the 4µm wide heaters were placed on 4µm wide pedestals which were 8µm away (edge to edge gap) from the main waveguide just to compare the change in effective indices. Optical coupling becomes non-issue with only 0.1µm increment in the pedestals width but 3.1µm wide heater's do not change effective index as much as 4µm wide do. The index change was found to be 0.001091 and 0.001135 when the heaters were placed at the bottom cladding and on top of the pedestals, respectively. This comparison gives a slightly large Δn when heaters were placed on the side waveguides and secondly the deposition of heaters on the side waveguides is relatively uncomplicated as compared to the bottom cladding. A schematic of the designed phase shifter is illustrated in figure 5.4,

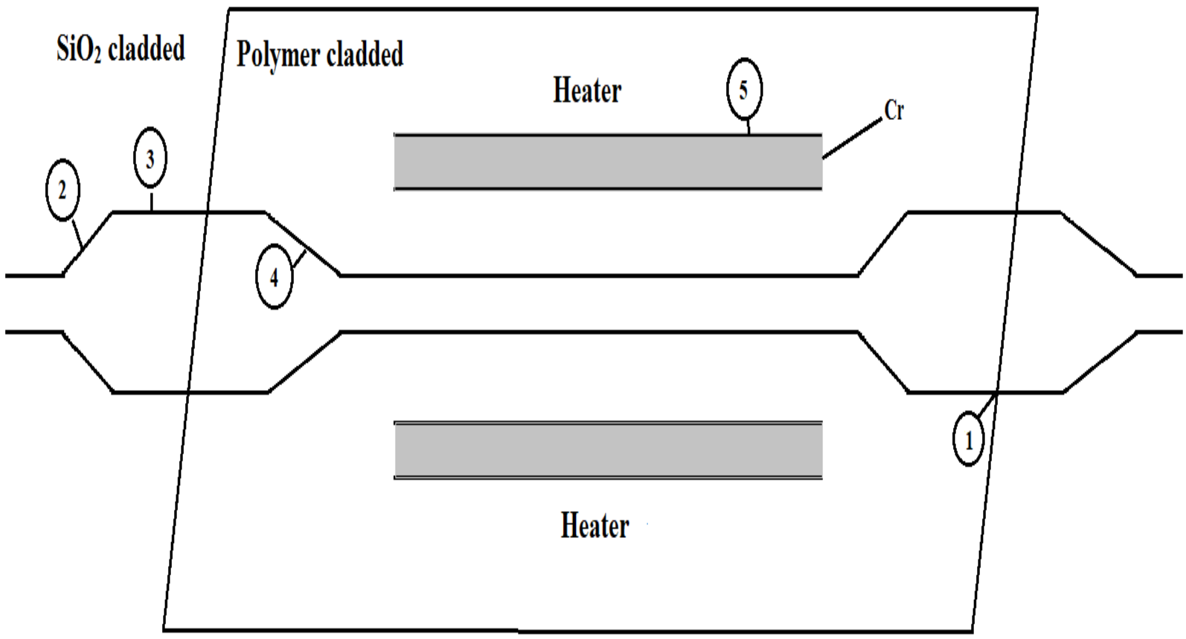

Figure 5.4: Showing the block diagram of the designed thermo-optic phase modulator. The device has 5 potential loss sources which are numbered in the figure and need to be optimized. The losses are exactly the same for the input and output of the device, that's why bundle them in one category.

As pointed in figure 5.4, there are 10 optical loss elements that fall into 5 groups which need to be optimized while designing a phase shifter in order to be within set limitations/loss budget mentioned above. These points include (1) two junctions, (2) four outer horizontal tapers, (3) two widened waveguides, (4) four inner horizontal tapers and (5) two heaters. Junction loss as well as absorption loss due to heaters are expected to be the major loss sources which need to be carefully optimised. Low loss horizontal tapers and widened waveguides have been reported and expected to be a small part of the overall loss of the device but still optimisation would be required. The junction loss (1) arises due to the difference in the refractive index of the polymer and silica. This difference leads to a change in the effective index and mode profile at the junction which can be reduced by widening the waveguide at junction. Efficient coupling between the two waveguides having different widths can be done via optimised waveguide tapering (2), (4). Widened waveguide width and length is chosen according to the loss and length set for the device. The coupling efficiency between the waveguides is controlled through the taper length and shape which is also analysed in this chapter. The metal heaters absorb light if placed too close to the waveguide. Therefore, the gap between the heaters and waveguide needs to be optimised where the optical loss and change in the effective index is acceptable.

5.2.1 Junction loss optimization

First of all, loss at the junction was computed for polymer cladding indices of 1.444–1.470

when the waveguide width was 3µm throughout the device and shown in figure 5.5.

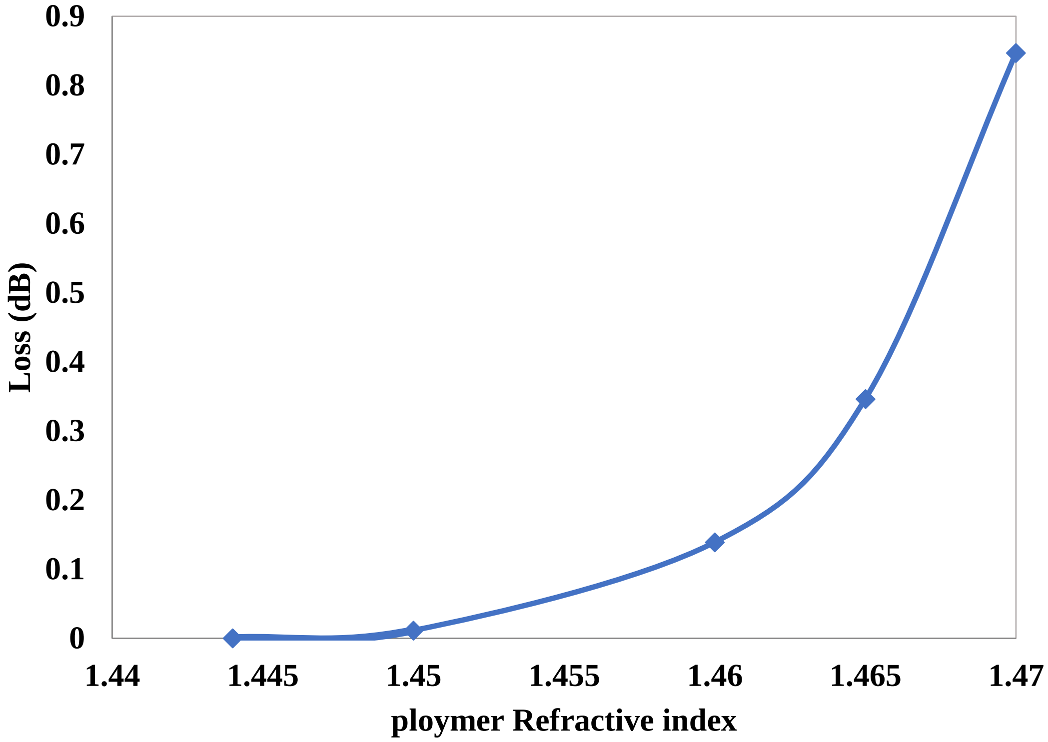

Figure 5.5: Showing the overlap loss at the junction for 5 different ZPU cladding indices.

FemSIM results showed quite a high junction loss for all the polymer claddings with higher refractive indices than silica. This arises from two factors, the modal overlap loss and the additional polymer absorption loss as more light starts propagating in the polymer. As the polymer (cladding) refractive index increases from 1.444–1.470, the reduced index contrast between the core and cladding decreases the confinement which results in a higher mode field interaction with the cladding material and a larger mode field. The loss (at 1550nm) of the silica (0.25×10^{-5} dB/cm) [281] is much lower than the polymer (around 0.35 dB/cm) [282], therefore higher mode field interaction with the polymer cladding induces a higher optical loss.

For an efficient mode coupling between the waveguides, they can be tapered horizontally or vertically. Horizontal tapers are fabricated via standard planar processing, whereas vertical tapering needs 3D processing which an additional processing burden [283]. Therefore, horizontal tapering is preferred in integrated optics and employed for this work.

To investigate the tapering effect on the loss, the junction was horizontally tapered at 6 different widths and junction loss is seen in figure 5.6. Initially 40µm (input) and 60µm (output) long linear tapers were employed to carry out these simulations. After the junction loss optimisation, taper's profile and length is also optimised.

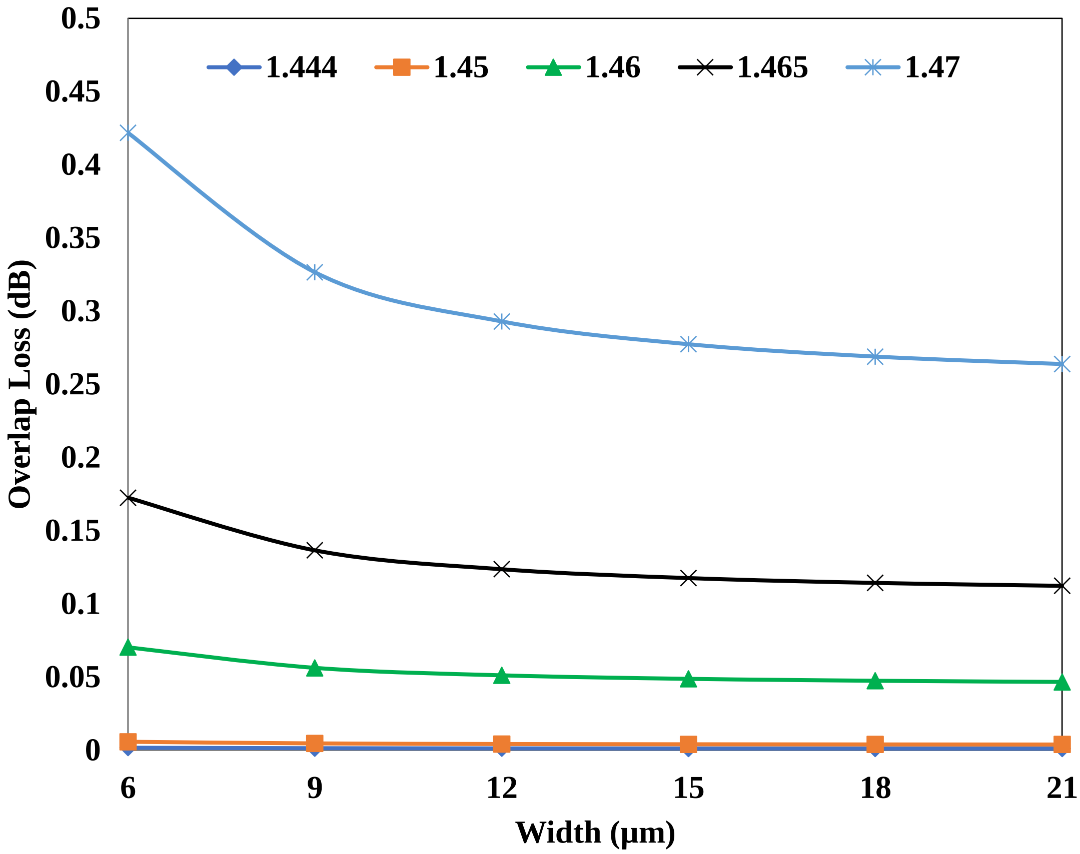

Figure 5.6: Depicting the overlap loss at the tapered junction for five different cladding indices.

It is evident from figure 5.6 that tapering the waveguide at the junction significantly resolves the overlap loss issue as compared to without tapering (see figure 5.5). A notable reduction in the loss can be achieved by only tapering the junction to 6µm which keeps going down with the further increment in the width for all cladding indices except for 1.444 where the loss is already zero. It is important to note that this loss corresponds to one junction of the device implying total junction loss will be doubled. From figure 5.6, It can be clearly seen that cladding indices of 1.470 and 1.465 cannot be used as both the claddings induce significantly high junction loss even after tapering the junction for any given width. Therefore, the cladding index must be less than 1.463.

For the purposes of design optimisation on the compact thermo-optic phase shifter, the width of the widened waveguide chosen for all following simulations was 6µm as it lowers the loss down by almost 50% as compared to the waveguide without tapering. The junction loss with and without tapering can be compared from the figures 5.5 and 5.6. Wider waveguides (9µm and more) could also have been chosen to achieve even lower junction loss but they do not reduce a significant amount of junction loss as compared to 6µm widened waveguide for the cladding indices of 1.444, 1.450 and 1.460. Also, wider waveguides require longer tapers for low loss operation. Considering all the factors in mind, it was decided to use 6μm wide waveguides at the junction.

Having established a good design choice for the widened waveguide at the junction between the polymer and silica claddings, the effect of varying the length of the 6μm widened waveguide was investigated using BeamPROP for cladding indices of 1.444, 1.450 and 1.460. The light was coupled into 3μm wide waveguide cladded with silica. The waveguide then tapered to 6μm wide waveguide with the help of 40μm long linear taper. Half-length of the widened waveguide and 60μm long output taper were cladded with the ZPU polymer (structure can be seen in figure 5.4). The length of the widened waveguide was varied and the transmission of the light through the structure was recorded. Figure 5.7 shows the variation of the loss with the length of the 6μm wide widened waveguide.

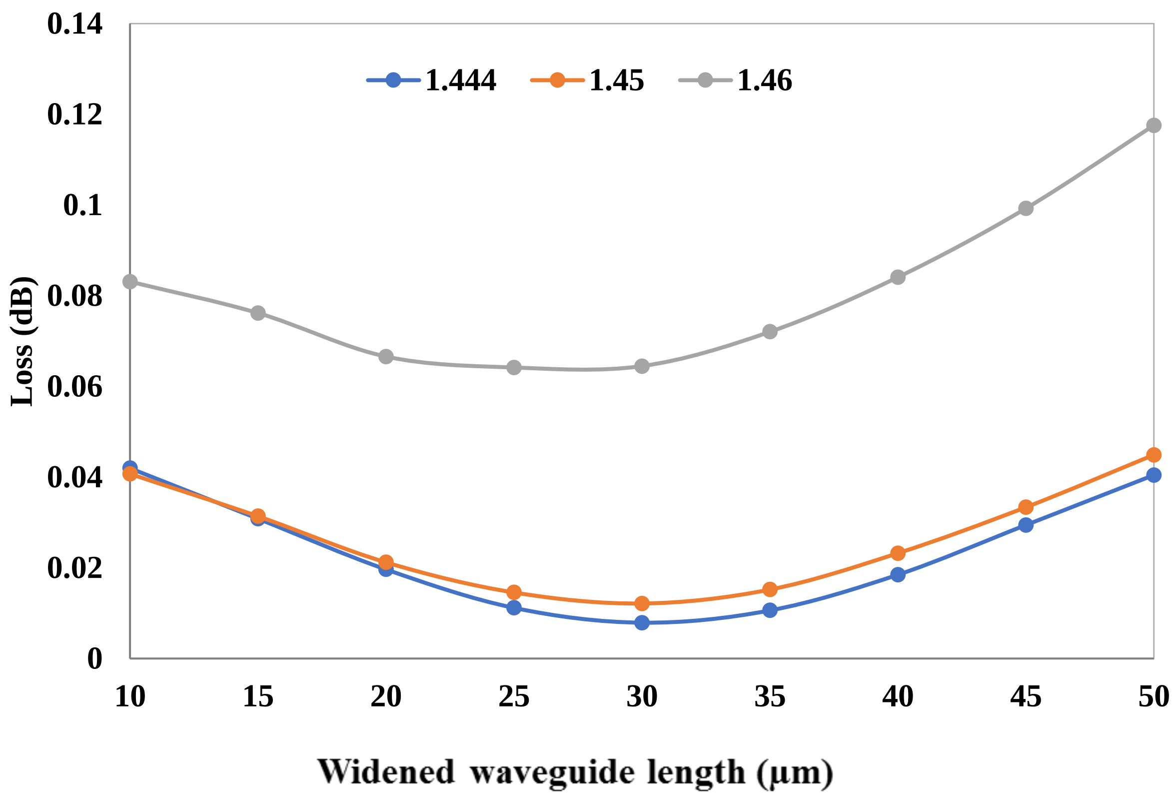

Figure 5.7: Loss variation with widened waveguide length between tapers for cladding indices of 1.444, 1.450 and 1.460.

The minimum loss occurred when the widened waveguide was 30 μm, 30 μm and 25 μm long respectively for overclad indices of 1.460, 1.450 and 1.444. Again, this loss is for a single junction and needs to be doubled for the whole device. The total loss from both the junctions for 1.444, 1.450 and 1.460 found to be 0.0195 dB, 0.036 dB and 0.128 dB respectively. Whilst small the loss is a non-negligible component of the loss budget if it is not optimised.

After the widened waveguide length optimisation, a wavelength scan was performed to investigate if there is any interference induced when the waveguide widened from 3µm to 6µm. For the cladding index of 1.460, the result of the wavelength scan across the junction is shown in figure 5.8.

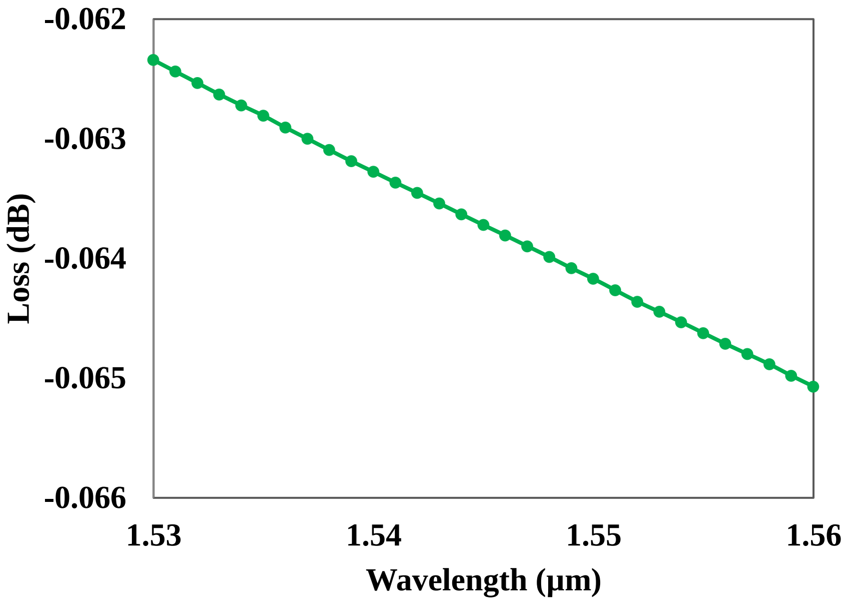

Figure 5.8: Showing no phase interference across the junction when waveguide tapered from 3µm to 6µm.

The wavelength from 1.53µm to 1.56µm was scanned across the junction and found no interference as the optical loss decreases linearly with increasing wavelength. No interference was found for other cladding indices as well.

Three different taper profiles (linear, exponential and quadratic) were studied to determine which profile induces the minimum loss from 3µm wide input waveguide to 6µm widened waveguide as well as 6µm widened waveguide to 3µm wide output waveguide. The widened waveguide was 25µm long. This simulation was done to find out the best taper profile, therefore input and output tapers were randomly chosen to be 100µm long. Table 5.2 shows the loss from different taper profiles for cladding index of 1.460.

Table 5-2: Showing loss for all taper profiles when widened waveguide width is 6 µm and length is 25 µm.

Cladding indices	Linear	Exponential	Quadratic
1.460	-0.084 (dB)	-0.083 (dB)	-0.084 (dB)

As seen in table 5.2, exponential taper is giving the lowest loss but not significantly better than linear and quadratic tapers. Therefore, any taper profile can be used to optimise the input and output taper lengths. Furthermore, Linear taper profile was then used for length optimisation.

Using BeamPROP, the taper length was optimised by simulating 10 different input and output taper lengths and results are shown in figure 5.9 (a & b) for cladding index of 1.450 and 1.460.

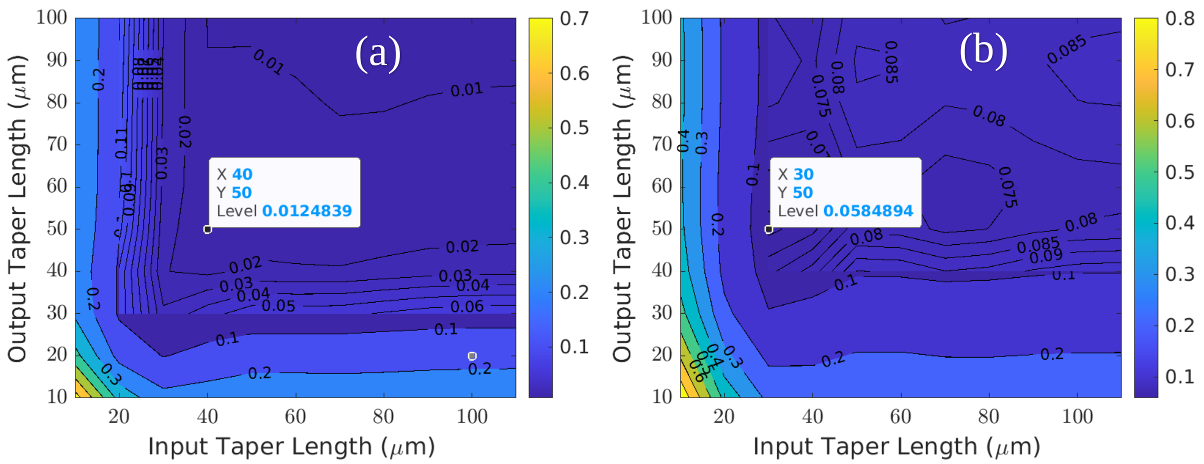

Figure 5.9: Showing the input/output taper length vs loss for cladding index of (a) 1.450 and (b) 1.460.

Despite putting serious efforts, this is the best resolution contour plots we could obtain from MATLAB. Input and output tapers are cladded with different materials (silica and ZPU); therefore, they have different lengths to get the minimum loss. The chosen input and output taper lengths for n_{clad}=1.444 are 40µm & 40µm, for n_{clad}=1.450 are 40µm & 50µm and for n_{clad}=1.460 are 30µm & 50µm. The chosen taper lengths do not correspond to minimum loss except for cladding index of 1.460. Slightly shorter tapers were employed to elongate the heating region of the device with the minimal sacrifice of the loss. This trade off was done to increase the phase shift within the set loss and length budget. For 1.460, the chosen taper lengths induce minimum loss which is not too small. Therefore, the trade off between loss and length cannot be made for this case. The loss induced by these tapers is 0.00912 dB, 0.01248 dB and 0.06 dB for 1.444, 1.450 and 1.460 respectively. Total loss and length consumed by junctions and tapers are summarized in table 5.3:

Table 5-3: summarizing the loss and length consumed by tapers and junctions and left in the budget.

Cladding Index	Loss consumed by junctions and tapers	Length consumed by junctions and tapers	Loss left in the budget	Length left in the budget
1.444	0.0375 dB	220 μm	0.4325 dB	1780 μm
1.450	0.061 dB	240 μm	0.409 dB	1760 μm
1.460	0.388 dB	210 μm	0.082 dB	1790 μm

As can be seen in table 5.3, the amount of length left in the budget is slightly different (within ± 30μm) for all the cladding indices. However, the loss left in the budget decreases sharply as cladding indices goes from 1.444–1.460 respectively. This sharp decrease in the loss left in the budget is mainly due to the junction loss variation with the cladding indices (See figure 5.5 or 5.6). For 1.444 and 1.450, a bit of length can be traded for some loss to place the heaters closer to the core for higher phase shift. Doing so, a slight change in the phase shift is expected as due to relatively high index contrast, less Δn will be induced even with the presence of more heat around the waveguide core. Lastly, there is no room for trade off for cladding index of 1.460 and any change in the length or loss would disturb the budget.

5.2.2 Absorption loss optimization

The last task was to optimize the gap between the heaters and waveguide. A thin layer (100nm) of Cr on the pedestals was assumed to be the heating material. High electrical resistivity and melting point make Cr a suitable option for resistive heating. Phase shift varies with how close the heaters are placed with respect to the main waveguide and this gap depends on the absorption loss due to Chromium (Cr) sitting on top of the pedestals (see figure 5.4).

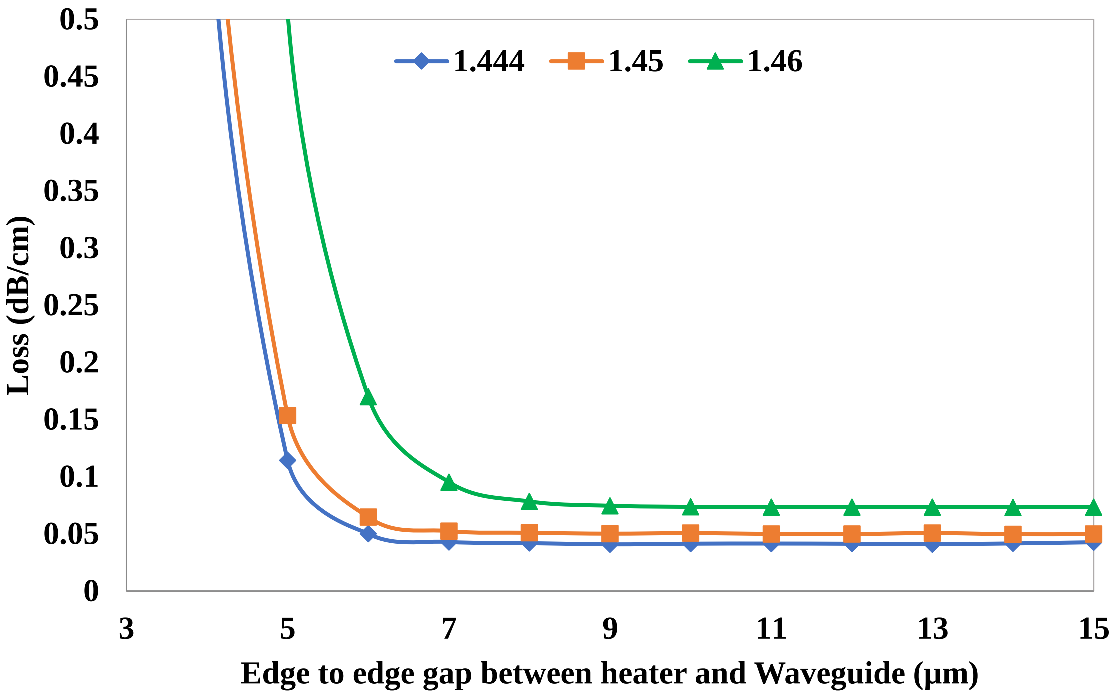

Figure 5.10: Depicting absorption loss varies with edge to edge gaps between heaters and waveguide.

Through FemSIM, absorption loss was simulated for 14 different gaps with all the cladding indices using 4µm wide heaters and pedestals around the main waveguide. For cladding indices of 1.450 and 1.460 where the index contrast in relatively lower as compared to the cladding index of 1.444, larger separation between the core and absorbing material which is Cr heater is this case is required to completely remove the absorption loss. After a certain gap which depends on the cladding index (e.g. 7µm for cladding indices of 1.444 & 1.450), the absorption loss due to the heaters goes down to zero. The remaining loss corresponds to the ZPU cladding absorption loss and cannot be avoided. For a given cladding index, heaters can be placed according to the loss and length left in the budget by using the data plotted in figure 5.10. For higher phase shift, heaters can be placed closer to the core, but it would induce more loss and ultimately consume more power. Therefore, a balance is required between the phase shift and power consumption.

5.2.3 Phase shift calculation

Knowing the loss and length left in the budget from table 5.3, edge to edge gap between the heaters and waveguide core can be obtained from the figure 5.10 for all the cladding indices. Table 5.4 shows the gap where heaters can be placed according to loss and length left in the budget,

Table 5-4: Revealing the gap between heaters and waveguide according to budget.

Cladding index	Gap
1.444	3.3 µm
1.450	3.4 µm
1.460	5.1 µm

By assigning the heater length according to the length left in the budget and gaps mentioned/found in table 5.3 and 5.4 respectively, Δn was computed by using Multiphysics utility in RSoft when the temperature changes from 20 ^{o}C to 150 ^{o}C. Due to low melting point (200 ^{o}C) of the polymer, the maximum temperature used in the simulation was chosen to 150 ^{o}C. Using equation (5.7), the phase shift was calculated for all the cladding indices. Figure 5.11 shows the phase shift variation with the cladding index.

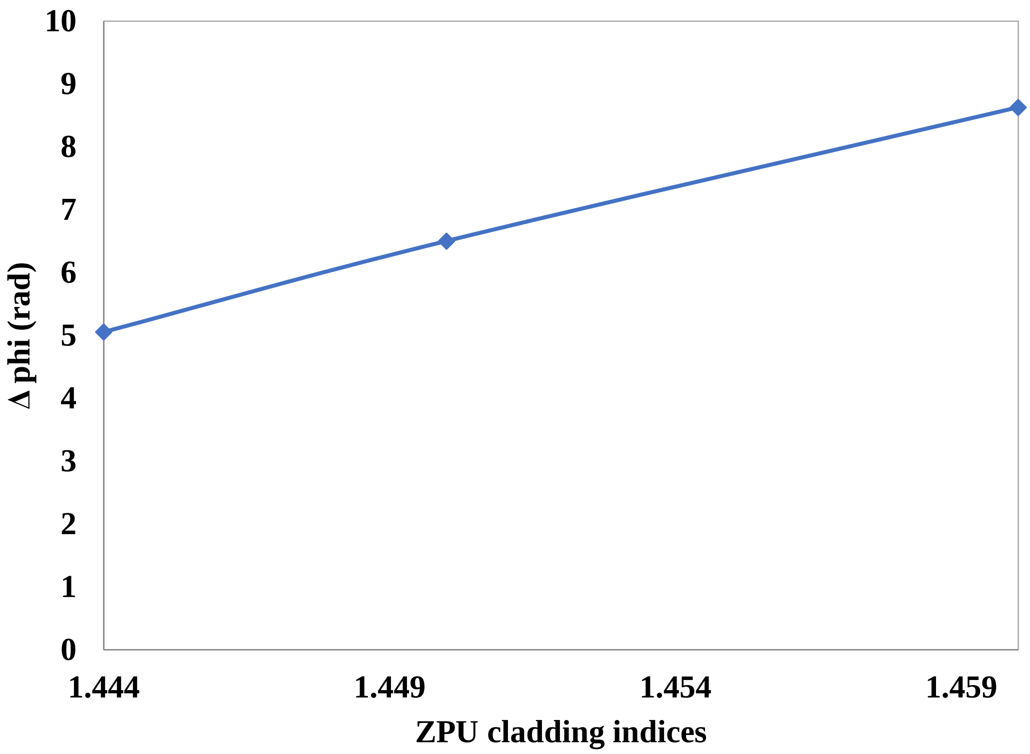

Figure 5.11: Phase shift vs cladding index for optimised design

Under the limits set initially on the optical loss and length of the phase shifters, cladding refractive indices of 1.444, 1.450 and 1.460 result in phase shifts of 5.02 rads, 6.50 rads and 8.63 rads. The phase shift increases with the cladding index because the index contrast between core and cladding is lower at higher cladding indices meaning more mode field is in the cladding and can be pushed back into the core as compared to the lower cladding indices. Consequently, more change in effective index and phase shift is induced through thermo-optic effect at higher cladding indices. Phase shift at 1.460 is 1.7 times higher than 1.444. Given the loss and length budget, 1.460 is the most suitable cladding index in terms of inducing the highest phase shift.

As detailed in chapter 2, a phase shift of π/2 is required to operate the interferometric gyro in the maximum sensitivity region which can be achieved even from 1.444 cladding index. This suggests that the excess phase shift can be traded to shorten the device or reduce the power consumption by putting the heaters away from the waveguide core. E.g. using the same design and loss budget, a phase shift of π/2 can be achieved from only 0.8mm long modulator for the cladding index of 1.444 and length would be even shorter for 1.460 as it provides higher phase shift.

To improve the design for even more shorter an less power consuming modulator, the effect of extending the heater pedestals (not the heater) towards the main waveguide was analysed as the thermal conductivity of the Ge:SiO_2 is higher than ZPU. This would cause more heat reaching at the waveguide and consequently bigger change in the real effective index. Figure 5.12 is showing the change in Δn vs extension of the side waveguides.

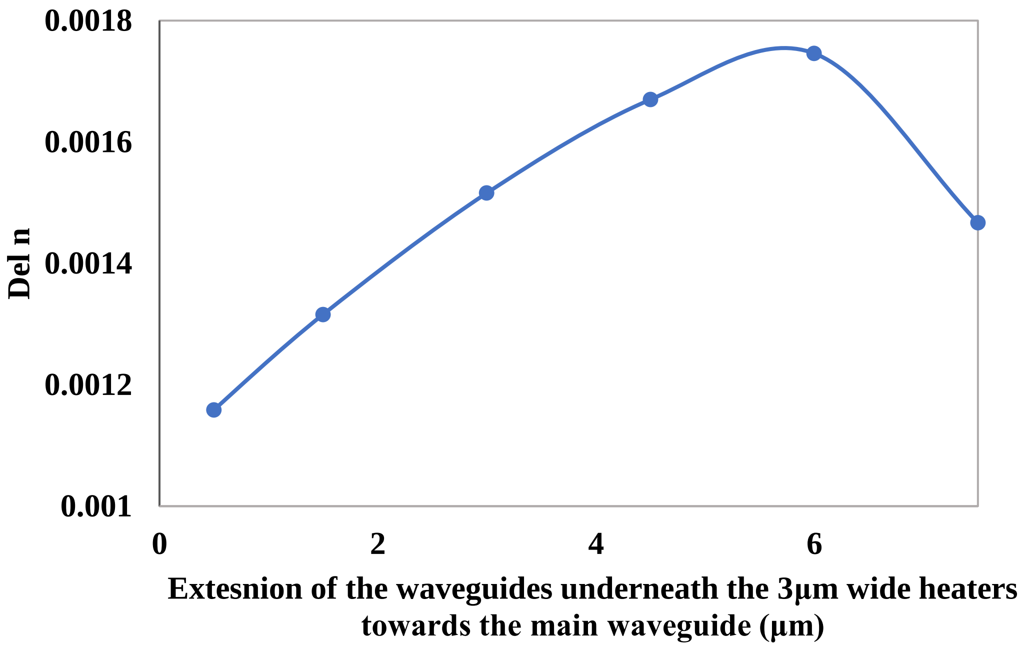

Figure 5.12: Illustrating the change in Δn with respect to the change in the width of side waveguides extending towards the main waveguide. The edge to edge gap between the heaters and main waveguide was maintained to be 8µm.

In the given case, the maximum extension of the pedestals cannot be more than 8μm because the edge to edge gap between the heaters and main waveguide was 8μm. For 3μm heaters, the initial width of the pedestals was chosen to be 4μm. It is evident from the figure 5.12 that the more the extension of pedestal is the bigger the value of Δn which is consistent with more heat reaching at the waveguide. However, when the pedestals extension is more than 6μm, the lack of polymer with its higher thermo-optic coefficient starts to bring down the Δn. Therefore, the optimum extension of the pedestals is 6μm for the given case. This approach can be employed to improve heat transfer which will ultimately improve the phase shift.

5.2.4 Frequency Response calculation

The frequency response of the phase modulator was also simulated. The phase shifter geometry chosen to analyse the frequency response was 3μm wide heaters sitting on the pedestals that have 3μm extensions toward the main waveguide. The edge to edge gap between the heater's and the waveguide core was 8μm. The polymer cladding used for the simulation was ZPU with a thickness and refractive index of 12μm and 1.460, respectively. The "Energy 2d" software was used to compute the temperature distribution vs time for heating up and cooling down. The thermal parameters used in the simulation are tabulated in table 5.5:

Table 5-5: Showing the materials and their thermal properties used to capture images for temperature distribution vs time.

Materials	Thermal conductivity (W/m.^{o}C)	Specific heat capacity (J/Kg. ^{o}C)	Density (Kg/m^3)
Si (substrate)	150	700	2300
SiO_2 (bottom cladding)	1.4	700	2200
Ge:SiO_2 (core)	1.4	700	2200
Cr (heater)	93.6	460	7000
ZPU (upper cladding)	0.2	1500	1000

The example of the images taken at different times for the case of heating up are shown in figure 5.13.

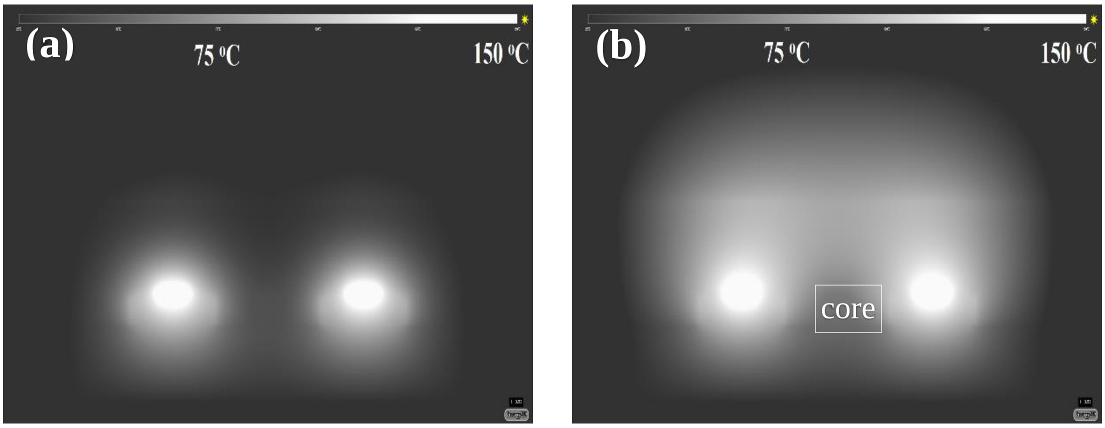

Figure 5.13: Illustrating the sample of images taken through Energy 2D for the case of heating up, (a) after 50μs and (b) after 1200μs.

For the case of cooling down, the images were taken at the exact same time intervals as for the case of heating up. The images were then imported into custom LabVIEW to obtain the temperature and so refractive index at every point of the image. The resulting data file was then imported into RSoft to compute the effective indices. A graph of effective index versus time was plotted for heating up and cooling down as seen in figure 5.14.

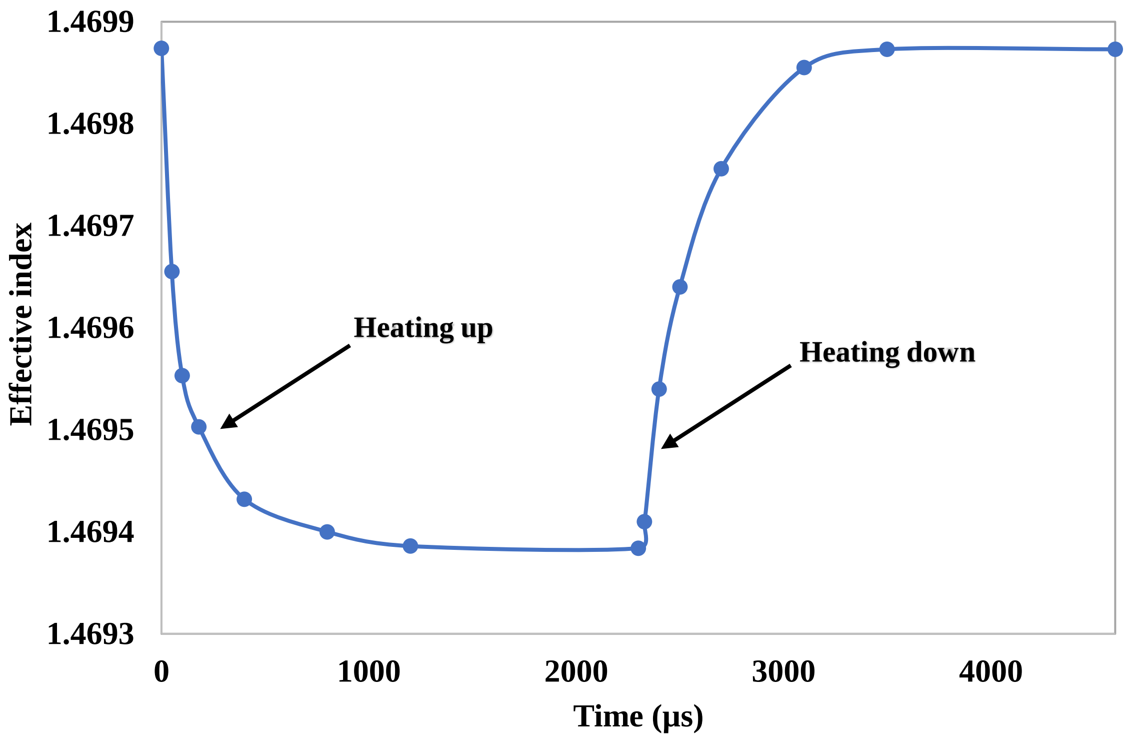

Figure 5.14: Illustrating the change in the effective index against the same time intervals for both heating up and down.

Figure 5.14 shows that the effective index goes down when the heaters are activated. As previously mentioned, the index contrast between the core and cladding increases with the heat which ultimately results in the reduction of effective index and vice versa. Non-linear curve fitting was performed to obtain equations that were used to generate an interpolated uniformly gridded version of figure 5.14 with 4000 data points.

Another LabVIEW code was written to perform Fourier transform of a perfect square wave and the curve obtained through the Energy 2d and R-Soft. The amplitudes of the fundamental frequency components and its harmonics were compared to plot the frequency response of the phase modulator and are seen in figure 5.15.

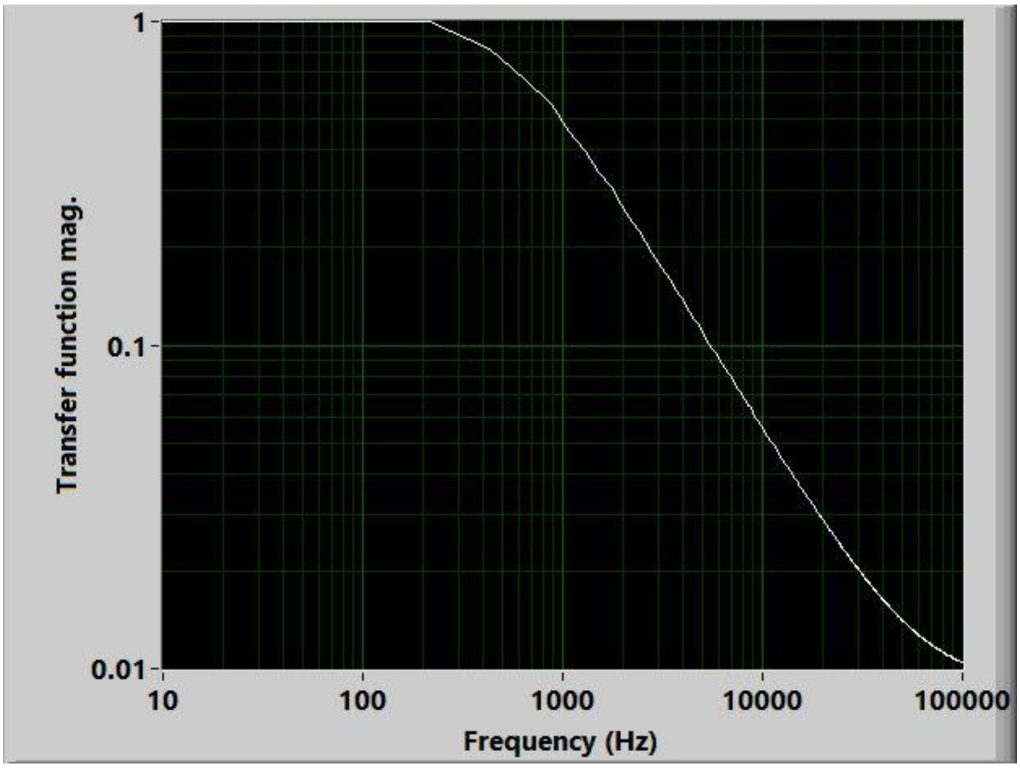

Figure 5.15: Showing theoretical frequency response of a thermo-optic phase modulator.

As seen in figure 5.15, the 3dB bandwidth of the phase shifter is 1 kHz. This compares with the desirable bandwidth of ~1000 kHz for backscatter impairment suppression, ~5000 kHz for frequency locking, and 200 kHz for trimming applications. This analysis suggest that the response time of the designed modulator needs to be improved. It can be done by using high thermal conductivity polymer as a top cladding. Energy 2D showed around 100 times improvement in the heating up and cooling down rate by increasing the thermal conductivity from 0.2 to 1.5 W/m.^{o}C.

5.3 Conclusion

A compact and integratable thermo-optic phase shifter is designed in this chapter. The sources of the optical loss which include absorption loss due to heaters, loss from the horizontal tapers, widened waveguides and junctions were optimised. The designed device induced an optical loss of less than 0.47 dB, not more than 2mm long and induced a large phase shift of 8.63 radians for cladding index of 1.460. The design can be modified to realise even a shorter and less power consuming device which would also match the phase shift requirements of an optical gyro. A polymer having high thermal conductivity would be needed to improve the response time of the designed phase modulator.

Chapter 6 Conclusions and recommendations

6.1 Conclusions

This work mainly focused on the theoretical optimization of an optical gyroscope which is suitable for planar integration and provide moderate performance. To the best of author's knowledge this kind of optimization has been done for the first time. Different gyro components which include thermo-optic phase modulator, sensing cavity and 3dB coupler were also simulated. This thesis also included/covered the fabrication of Si_3N_4 and Ta_2O_5 waveguides which can be used to realise fundamental optical gyro components mentioned above. Low hydrogen content Si_3N_4 films were deposited by using low pressure chemical vapor deposition (LPCVD) technique. Whereas Ta_2O_5 films were grown by using ion beam sputtering (IBS). Both the films were printed through standard optical lithography technique and waveguides were etched through reactive ion plasma etching followed by chemically removal of Photoresist. A propagation loss of around 0.25 dB/cm has been achieved at 1550nm from air cladded Si_3N_4 waveguide. By using the same etching recipe (line edge roughness), theoretical loss model predicted a propagation loss of 0.009 dB/cm at 1550nm from optimized waveguide dimensions and silica as top cladding. Whereas a propagation loss of 0.17 dB/cm has been achieved from Ta_2O_5 waveguides. A thermo-optic phase modulator with an insertion loss of less than 5dB and total length of less than 2mm was also modelled and reported in this thesis.

This work has investigated number of gyros based on different operating principles and come up with an optimized type and structure for miniaturized applications. Optical gyros based on the Sagnac effect found to be the most reasonable option. In active optical gyros, gaseous RLGs were found to be limited by the lock-in effect and mechanical dithering is needed to use them which makes the whole system bigger, heavier and more power consuming. Semiconductor ring laser gyros (SRLGs) were found to be even more severely limited by the lock-in effect due to numerous non-linearities present in the solid-state gain medium. However, passive optical gyros found to be a viable option for integrated gyros as their sensitivity was not limited by the lock-in effect and hybridization of different optical components on the same platform make it a more robust and reliable device. The performance comparison of different types and structures of passive integrated optical gyro (PIOG) was studied in a great detail. The performance of interferometric integrated optical gyroscope (IIOG) and resonant integrated optical gyroscope (RIOG) was simulated by using LabVIEW based simulators followed by numerical calculations. For propagation losses of 0.1 dB/cm and 0.01 dB/cm, a resolution of 41.89 ^{o}/h and 5.25 ^{o}/h was found respectively for IIOG. However, for bus waveguide ring resonator, the resolution came out to be 13.41 ^{o}/h and 1.34 ^{o}/h for propagation losses of 0.1 dB/cm and 0.01 dB/cm, respectively. For the case of add-drop ring resonator, the resolution found to be 27.24 ^{o}/h and 2.61 ^{o}/h for propagation losses of 0.1 dB/cm and 0.01 dB/cm, respectively. Although the bus waveguide ring resonator gyro offers better ultimate sensitivity, this is achieved in the highly under coupled state approaching zero coupling as is evident in figure 2.11 where the resonance dip is becoming very small. A small parasitic reflection in the system or other disturbance could lead to frequency lock on the resonance being lost. The add-drop ring resonator achieves maximum sensitivity at 25% transmission and is therefore much more robust and further circulators can be avoided with this design. The performance degradation compared to the very best a bus based ring might be able to achieve is at most a factor of two, the far greater ease that this can be accomplished with making the add-drop ring a better choice for planar integrated gyros.

A significant portion of this thesis comprised the fabrication of low loss Si_3N_4 and Ta_2O_5 waveguides. Si_3N_4 films were deposited through thermal decomposition of reactants (ammonia and dichlorosilane) on the substrate surface in a furnace. Afterwards, a lot of etching work was done to optimize the sidewall roughness of the waveguide which is a dominant loss factor in high index contrast waveguides. A plasma generated by the gas mixture of CHF_3/O_2 in the ICP was found to be the optimum option to achieve smooth sidewalls. A sidewall roughness of 6nm was achieved which can further be improved by modifying the etching process. However, the achieved sidewall roughness was good enough to fabricate low loss waveguides due to their thin geometry. The outcome of this study was a demonstration of low loss Si_3N_4 waveguides which can be used to realise sensing cavity for optical gyroscope.

Waveguides from IBS deposited Ta_2O_5 were also fabricated to realise gyro components. The room temperature deposition of IBS Ta_2O_5 favours hybrid integration. Therefore, several fundamental gyro components were simulated by using Ta_2O_5. The films were deposited through ion beam sputtering of pure tantalum target in O_2 and Ar environment. Furthermore, Different etching systems and gas mixtures were used to optimise etching recipe. A propagation loss of 0.17 dB/cm has been achieved. A detailed investigation on high propagation loss concluded that point defects within the waveguide cause occasional high losses which is correlated to the etching inhomogeneities. However, a 6cm long region has an observed propagation loss of 0.02 dB/cm, reasonably close to the expected loss.

Lastly, thermo-optic phase modulator as one of the major optical gyro component was also simulated by using Ge:SiO_2 waveguides because thin Si_3N_4 and Ta_2O_5 waveguides did not provide enough change in effective index with respect to temperature. A polymer called ZPU was used as top cladding because of its higher thermo-optic coefficient than silica. Considering the length and optical loss numbers set for phase modulator, the amount of phase shift induced by the device depends on the cladding refractive index and 1.460 provides the highest phase shift of 8.63 radians which is 1.7 times higher than 1.444. The thermal response of the designed thermo-optic phase shifter is found to be 1 kHz which needs to be improved to be employed in gyro applications. Higher thermal conductivity of the top cladding would improve the response significantly.

6.2 Recommendations for Future Work

- The resolution of an optical gyroscope has strong dependence on propagation loss of the sensing cavity. Despite of predicting ultra-low loss from thin Si_3N_4 waveguides having 6nm rough sidewalls, the loss can further be improved (consequently the resolution) by investing a significant amount of time on optimizing the etching recipe. It has already been demonstrated that the Si_3N_4 waveguides can be etched with a sidewall's roughness of only 3.14nm [110] almost half of what is reported in this work.
- This work provides the design and technology for an optical gyro which is suitable for miniaturized high-tech applications. With a minor modification in the design, the submitted work can be used to fabricate a high performing integrated gyro. E.g. the designed 3dB coupler from thin Ta_2O_5 waveguide is quite sensitive to thickness tolerance, therefore it can be designed with thick (3µm) Ge:SiO_2 waveguide which found to be less affected by the thickness tolerance. In this way a vertical taper can be removed from the design which consequently will reduce the complexity in the fabrication process.
- Overall propagation loss of the Ta_2O_5 waveguides can be improved by investing more time on the etching recipe and removal of the unwanted material from the surface.
- The designed thermo-optic phase modulator is quite efficient in terms of size and optical loss, but its thermal time response is very slow for the given application and requires modification in the design. Several designs have been reported in the literature

for that purpose and work can be done on them. Also, by using a polymer with higher thermal conductivity, the thermal time response can be improved substantially.

References

[1] J. Gambino, MEMS Rate Sensors for Space, (2000).

[2] L. Barreda Pupo, Characterization of errors and noises in MEMS inertial sensors using Allan variance method, Universitat Politècnica de Catalunya, (2016).

[3] IndustryARC, https://www.industryarc.com/Report/15628/gyroscope-market.html,

[4] Mordor Intelligence, https://www.mordorintelligence.com/industry-reports/global-gyroscopes-market-industry#:~:text=Market%20Overview,period%20(2021%2D2026,

[5] F. Dell'Olio, T. Tatoli, C. Ciminelli and M. Armenise, Recent advances in miniaturized optical gyroscopes, J. Eur. Opt. Soc-Rapid **9,** (2014).

[6] A. Shamir, (2006), An overview of Optical Gyroscopes Theory, Practical Aspects, Applications and Future Trends, Technical paper: Adi Shammir.

[7] R. J. P. Menéndez, (2019), IFOG and IORG Gyros: A Study of Comparative Performance, IntechOpen.

[8] NASA, https://mars.nasa.gov/mars2020/,

[9] B. Wu, Y. Yu, J. Xiong and X. Zhang, Silicon Integrated Interferometric Optical Gyroscope, Sci. Rep. **8,** 8766 (2018).

[10] M. Larsen and M. Bulatowicz, Nuclear magnetic resonance gyroscope: For DARPA's micro-technology for positioning, navigation and timing program, 2012 IEEE International Frequency Control Symposium Proceedings, 1-5 (2012).

[11] R. Usubamatov, A mathematical model for motions of gyroscope suspended from flexible cord, Cogent Engineering **3,** 1245901 (2016).

[12] D. Xia, C. Yu and L. Kong, The development of micromachined gyroscope structure and circuitry technology, Sens. **14,** 1394-1473 (2014).

[13] E. Stein, (2013), The History of Theoretical, Material and Computational Mechanics-Mathematics Meets Mechanics and Engineering, Springer Science & Business Media.

[14] H. Everett, Sensors for Mobile Robots: Theory and Application. Wellesley, MA: A, K. Peters, Ltd (1995).

[15] J. Sommeria, Foucault and the rotation of the Earth, Comptes Rendus Physique **18,** 520-525 (2017).

[16] F. Hamza-Lup, Kinesthetic Learning--Haptic User Interfaces for Gyroscopic Precession Simulation, arXiv preprint arXiv:1908.09082 (2019).

[17] V. Passaro, A. Cuccovillo, L. Vaiani, M. D. Carlo and C. E. Campanella, Gyroscope Technology and Applications: A Review in the Industrial Perspective, Sens. **17,** 2284 (2017).

[18] N. El-Sheimy and A. Youssef, Inertial sensors technologies for navigation applications: state of the art and future trends, Satellite Navigation **1,** 2 (2020).

[19] S. Nagabhushana and L. Sudha, (2010), Aircraft instrumentation and systems, IK International Pvt Ltd.

[20] G. J. Martin, Gyroscopes may cease spinning: Optical gyroscopes without moving parts are more reliable and more rugged than conventional mechanical systems, IEEE Spectrum **23,** 48-53 (1986).

[21] A. Persson, The Coriolis Effect, History of Meteorology **2,** 1-24 (2005).

[22] D. K. Shaeffer, MEMS inertial sensors: A tutorial overview, IEEE Communications Magazine **51,** 100-109 (2013).

[23] C. He, Q. Zhao, Q. Huang, D. Liu, Z. Yang, D. Zhang and G. Yan, A MEMS vibratory gyroscope with real-time mode-matching and robust control for the sense mode, IEEE Sensors Journal **15,** 2069-2077 (2014).

[24] J. Xie, Y. Hao and W. Yuan, Energy Loss in a MEMS Disk Resonator Gyroscope, Micromachines **10,** 493 (2019).

[25] R. N. Candler, H. Li, M. Lutz, W.-T. Park, A. Partridge, G. Yama and T. W. Kenny, Investigation of energy loss mechanisms in micromechanical resonators, TRANSDUCERS'03. 12th International Conference on Solid-State Sensors, Actuators and Microsystems. Digest of Technical Papers (Cat. No. 03TH8664), 332-335 (2003).

[26] R. Wang, B. Bai, H. Feng, Z. Ren, H. Cao, C. Xue, B. Zhang and J. Liu, Design and fabrication of micro hemispheric shell resonator with annular electrodes, Sens. **16,** 1991 (2016).

[27] N. V. Lavrik and P. G. Datskos, Optically read Coriolis vibratory gyroscope based on a silicon tuning fork, Microsystems & nanoengineering **5,** 1-11 (2019).

[28] S. Park and S. S. Pannu, (2016), Cylindrical resonator gyroscope, Google Patents.

[29] D. H. Titterton and J. L. Weston, Strapdown Inertial Navigation Technology. 2nd, London: Institution of Electrical Engineers (2004).

[30] Q. Li, D. Xiao, X. Zhou, Y. Xu, M. Zhuo, Z. Hou, K. He, Y. Zhang and X. Wu, 0.04 degree-per-hour MEMS disk resonator gyroscope with high-quality factor (510 k) and long decaying time constant (74.9 s), Microsystems & nanoengineering **4,** 1-11 (2018).

[31] J. Söderkvist, Micromachined gyroscopes, Sensors and Actuators A: Physical **43,** 65-71 (1994).

[32] V. M. Sundararajan, Principles of biomedical engineering, Artech House 481 (2010).

[33] J. Dolinšek, M. Vilfan and S. Žumer, (2006), Novel NMR and EPR techniques, Springer.

[34] K. Liu, W. Zhang, W. Chen, K. Li, F. Dai, F. Cui, X. Wu, G. Ma and Q. Xiao, The development of micro-gyroscope technology, Journal of Micromechanics and Microengineering **19,** 113001 (2009).

[35] D. Meyer and M. Larsen, Nuclear magnetic resonance gyro for inertial navigation, Gyroscopy and Navigation **5,** 75-82 (2014).

[36] T. Kornack, R. Ghosh and M. V. Romalis, Nuclear spin gyroscope based on an atomic comagnetometer, Phys. Rev. Lett. **95,** 230801 (2005).

[37] D. Tazartes, An historical perspective on inertial navigation systems, 2014 International Symposium on Inertial Sensors and Systems (ISISS), 1-5 (2014).

[38] B. Canuel, A. Gauguet, F. Leduc, D. Holleville, N. Dimarcq, A. Clairon and A. Landragin, Characterization of a cold atom gyroscope, 2005 Quantum Electronics and Laser Science Conference, 476-477 (2005).

[39] J. Kitching, S. Knappe and E. A. Donley, Atomic sensors–a review, IEEE Sensors Journal **11,** 1749-1758 (2011).

[40] J. Fang and J. Qin, Advances in atomic gyroscopes: A view from inertial navigation applications, Sens. **12,** 6331-6346 (2012).

[41] L. Zhang, W. Gao, Q. Li, R. Li, Z. Yao and S. Lu, A novel monitoring navigation method for cold atom interference gyroscope, Sens. **19,** 222 (2019).

[42] P. Kapitza, Viscosity of liquid helium below the λ-point, Nature **141,** 74-74 (1938).

[43] R. E. Packard and S. Vitale, Principles of superfluid-helium gyroscopes, Physical Review B **46,** 3540 (1992).

[44] G. B. Hess, Superfluid gyroscope, Nature **359,** 192 (1992).

[45] P. W. Anderson, Considerations on the flow of superfluid helium, Reviews of Modern Physics **38,** 298 (1966).

[46] E. Hoskinson, Y. Sato and R. Packard, Superfluid He 4 interferometer operating near 2 K, Physical Review B **74,** 100509 (2006).

[47] G. Sagnac, L'éther lumineux démontré par l'effet du vent relatif d'éther dans un interféromètre en rotation uniforme, CR Acad. Sci. **157,** 708-710 (1913).

[48] B. Regimanu, K. C. Das and K. S. Rao, Development of Multistage Digital Filters for Dither Signal Removal in Ring Laser Gyro, Frequenz **73,** 123-130 (2019).

[49] M. Faucheux, D. Fayoux and J. Roland, The ring laser gyro, Journal of optics **19,** 101 (1988).

[50] N. Liang, G. Lijun, K. Mei and C. Tuoyuan, Waveguide-type optical passive ring resonator gyro using frequency modulation spectroscopy technique, Journal of Semiconductors **35,** 124008 (2014).
[51] H. C. LEFÈRE, Fundamentals of the interferometric fiber-optic gyroscope, Optical review **4,** 20-27 (1997).
[52] W. Chow, J. Gea-Banacloche, L. Pedrotti, V. Sanders, W. Schleich and M. Scully, The ring laser gyro, Reviews of Modern Physics **57,** 61 (1985).
[53] J. Hecht, (2011), Understanding lasers: an entry-level guide, John Wiley & Sons.
[54] M. Salit, K. Salit and P. Bauhahn, Prospects for enhancement of ring laser gyroscopes using gaseous media, Opt. Exp. **19,** 25311-25318 (2011).
[55] H.-J. Cho, J.-C. Lee and S.-H. Lee, Design and Development of an Ultralow Optical Loss Mirror Coating for Zerodur Substrate, Journal of the Optical Society of Korea **16,** 80-84 (2012).
[56] J. Covino and J. M. Bennett, Laser-Gyro materials studies, NAVAL WEAPONS CENTER CHINA LAKE CA (1986).
[57] C. Ciminelli, F. Dell'Olio, C. E. Campanella and M. N. Armenise, Photonic technologies for angular velocity sensing, Adv. Opt. Photonics **2,** 370-404 (2010).
[58] M. N. Armenise, C. Ciminelli, F. Dell'Olio and V. M. Passaro, (2010), Advances in gyroscope technologies, Springer Science & Business Media.
[59] P. Ayswarya, S. Pournami and R. Nambiar, A survey on ring laser gyroscope technology, Int. J. Comput. Appl. **116,** (2015).
[60] M. Naftaly, Mode locking in the ring laser gyroscope: Reduced threshold for two cavity modes, Brunel University School of Engineering and Design, (1990).
[61] D. C. Lee, G. Moon and J. C. Lee, Mechanical dither design for ring laser gyroscope, Ksme Int. J. **16,** 485-491 (2002).
[62] A. Khandelwal, A. Syed and J. Nayak, Limits imposed by nonlinear coupling on rotation sensitivity of a semiconductor ring laser gyroscope, Appl. Opt. **55,** 5187-5191 (2016).
[63] A. Khandelwal, A. Syed and J. Nayak, Performance evaluation of integrated semiconductor ring laser gyroscope, J. Lightwave Technol. **35,** 3555-3561 (2017).
[64] P. J. Laybourn, M. Sorel, G. Giuliani and S. Donati, Integrated semiconductor laser rotation sensors, Proc. SPIE, 322-331 (1999).
[65] H. Cao, C. Liu, H. Ling, H. Deng, M. Benavidez, V. A. Smagley, R. B. Caldwell, G. M. Peake, G. A. Smolyakov and P. G. Eliseev, Frequency beating between monolithically integrated semiconductor ring lasers, Appl. Phys. Lett. **86,** 041101 (2005).

[66] J. Qian, J. Su, X. Wang and B. Zhu, Er-doped fiber ring laser gyroscopes operating in continuous waves, Chin. Opt. Lett. **5,** 229-231 (2007).
[67] W. Wang, J. Wang and J. Xia, Er-doped fiber ring laser gyroscope with reciprocal polarisation maintaining cavity, Opt. Eng. **51,** 104401 (2012).
[68] B. Culshaw and I. Giles, Fibre optic gyroscopes, J. Phys. E: Sci. Instrum. **16,** 5 (1983).
[69] J.-N. Juang and R. Radharamanan, Evaluation of ring laser and fiber optic gyroscope technology, School Of Engineering, Mercer University, Macon, GA **31207,** (2009).
[70] S. Merlo, M. Norgia and S. Donati, Fiber gyroscope principles, Handbook of Fibre Optic Sensing Technology 1-23 (2000).
[71] H. Ma, Y. Yan, L. Wang, X. Chang and Z. Jin, Laser frequency noise induced error in resonant fiber optic gyro due to an intermodulation effect, Opt. Exp. **23,** 25474-25486 (2015).
[72] H. Ma, Z. Chen, Z. Yang, X. Yu and Z. Jin, Polarisation-induced noise in resonator fiber optic gyro, Appl. Opt. **51,** 6708-6717 (2012).
[73] K. Takada, Calculation of Rayleigh backscattering noise in fiber-optic gyroscopes, JOSA A **2,** 872-877 (1985).
[74] D. M. Shupe, Thermally induced nonreciprocity in the fiber-optic interferometer, Appl. Opt. **19,** 654-655 (1980).
[75] P. B. Ruffin, Review of fiber optics technology for military applications, Novel Materials and Crystal Growth Techniques for Nonlinear Optical Devices: A Critical Review, 1029902 (2000).
[76] A. Ohno, S. Motohara, R. Usui, Y. Itoh and K. Okada, Development of fiber optic gyroscope with environmental ruggedness, Fiber Optic Gyros: 15th Anniversary Conf, 82-89 (1992).
[77] J. Nayak, Fiber-optic gyroscopes: from design to production Invited, Appl. Opt. **50,** E152-E161 (2011).
[78] H. C. Lefevre, (2014), The fiber-optic gyroscope, Artech house.
[79] A. Cordova, D. J. Bilinski, S. N. Fersht, G. M. Surabian, J. D. Wilde and P. A. Hinman, (1994), Sensor coil for low bias fiber optic gyroscope, Google Patents.
[80] S. Ezekiel and S. Balsamo, Passive ring resonator laser gyroscope, Appl. Phys. Lett. **30,** 478-480 (1977).
[81] Y.-y. Liu, X.-w. Cui, J.-b. Zang, Z.-d. Zhang, Y.-h. Wang, Y.-n. Li, J. Liu and C.-y. Xue, Systematically analysis of resonant fiber optic gyroscope, Optik **126,** 3420-3423 (2015).
[82] H. Ma, W. Wang, Y. Ren and Z. Jin, Low-noise low-delay digital signal processor for resonant micro optic gyro, IEEE Photonics Technol. Lett. **25,** 198-201 (2013).

[83] H. Wen, (2019), Toward Inertial-Navigation-on-Chip: The Physics and Performance Scaling of Multi-Degree-of-Freedom Resonant MEMS Gyroscopes, Springer Nature.
[84] C. L. Garrido Alzar, Compact chip-scale guided cold atom gyrometers for inertial navigation: Enabling technologies and design study, AVS Quantum Science **1,** 014702 (2019).
[85] Y.-H. Lai, M.-G. Suh, Y.-K. Lu, B. Shen, Q.-F. Yang, H. Wang, J. Li, S. H. Lee, K. Y. Yang and K. Vahala, Earth rotation measured by a chip-scale ring laser gyroscope, Nature Photonics 1-5 (2020).
[86] J. Li, M.-G. Suh and K. Vahala, Microresonator brillouin gyroscope, Optica **4,** 346-348 (2017).
[87] X. Ji, F. A. Barbosa, S. P. Roberts, A. Dutt, J. Cardenas, Y. Okawachi, A. Bryant, A. L. Gaeta and M. Lipson, Ultra-low-loss on-chip resonators with sub-milliwatt parametric oscillation threshold, Optica **4,** 619-624 (2017).
[88] S. Gundavarapu, M. Belt, T. A. Huffman, M. A. Tran, T. Komljenovic, J. E. Bowers and D. J. Blumenthal, Interferometric Optical Gyroscope Based on an Integrated Si 3 N 4 Low-Loss Waveguide Coil, J. Lightwave Technol. **36,** 1185-1191 (2018).
[89] H. Mao, H. Ma and Z. Jin, Polarisation maintaining silica waveguide resonator optic gyro using double phase modulation technique, Opt. Exp. **19,** 4632-4643 (2011).
[90] A. Vershovskii, Y. A. Litmanovich, A. Pazgalev and V. Peshekhonov, Nuclear Magnetic Resonance Gyro: Ultimate Parameters, Gyroscopy and Navigation **9,** 162-176 (2018).
[91] K. Pister, On the limits and applications of MEMS sensor networks, Defense Science Study Group report (2001).
[92] R. G. Hunsperger, (1995), Integrated optics, Springer.
[93] J. F. Ready, (1997), Industrial applications of lasers, Elsevier.
[94] G. Lifante, (2003), Integrated photonics: fundamentals, John Wiley & Sons.
[95] C. Ciminelli, F. Dell'Olio and M. Armenise, Resonant optical gyro: Monolithic vs. hybrid integration, 2013 15th International Conference on Transparent Optical Networks (ICTON), 1-4 (2013).
[96] S. Madden, Z. Jin, D. Choi, S. Debbarma, D. Bulla and B. Luther-Davies, Low loss coupling to sub-micron thick rib and nanowire waveguides by vertical tapering, Opt. Exp. **21,** 3582-3594 (2013).
[97] J. Mu, T. Alexoudi, Y.-S. Yong, S. A. Vázquez-Córdova, M. Dijkstra, K. Wörhoff, J. Duis and S. M. García-Blanco, Low-loss highly tolerant flip-chip couplers for hybrid integration of Si 3 N 4 and polymer waveguides, IEEE Photonics Technol. Lett. **28,** 2748-2751 (2016).

[98] K. Wörhoff, R. G. Heideman, A. Leinse and M. Hoekman, TriPleX: a versatile dielectric photonic platform, Advanced Optical Technologies **4,** 189-207 (2015).

[99] S. Tang, InP-based semiconductor lasers with novel sampled Bragg gratings and applications, University of Glasgow, (2019).

[100] R. Nagarajan, M. Kato, D. Lambert, P. Evans, S. Corzine, V. Lal, J. Rahn, A. Nilsson, M. Fisher and M. Kuntz, Terabit/s class InP photonic integrated circuits, Semiconductor Science and Technology **27,** 094003 (2012).

[101] Y. Zhu and L. Zhu, Narrow-linewidth, tunable external cavity dual-band diode lasers through InP/GaAs-Si 3 N 4 hybrid integration, Opt. Exp. **27,** 2354-2362 (2019).

[102] K.-J. Boller, A. van Rees, Y. Fan, J. Mak, R. E. Lammerink, C. A. Franken, P. J. van der Slot, D. A. Marpaung, C. Fallnich and J. P. Epping, Hybrid integrated semiconductor lasers with silicon nitride feedback circuits, Photonics, 4 (2020).

[103] Y. Zhu, S. Zeng, Y. Zhao and L. Zhu, Hybrid integration of active semiconductor devices with passive micro/nano optical structures for emerging applications, Nanoengineering: Fabrication, Properties, Optics, Thin Films, and Devices XVI, 1108908 (2019).

[104] M. Piels, J. F. Bauters, M. L. Davenport, M. J. Heck and J. E. Bowers, Low-loss silicon nitride AWG demultiplexer heterogeneously integrated with hybrid III–V/silicon photodetectors, J. Lightwave Technol. **32,** 817-823 (2013).

[105] Y. Baumgartner, C. Caër, M. Seifried, G. Villares, D. Caimi, T. Morf, J. Faist, B. J. Offrein and L. Czornomaz, CMOS-compatible hybrid III-V/Si photodiodes using a lateral current collection scheme, 2018 European Conference on Optical Communication (ECOC), 1-3 (2018).

[106] C. Ciminelli, F. Dell'Olio, M. N. Armenise, F. M. Soares and W. Passenberg, High performance InP ring resonator for new generation monolithically integrated optical gyroscopes, Opt. Exp. **21,** 556-564 (2013).

[107] O. Kononchuk and B.-Y. Nguyen, (2014), Silicon-on-insulator (soi) technology: Manufacture and applications, Elsevier.

[108] R. Baets, A. Z. Subramanian, S. Clemmen, B. Kuyken, P. Bienstman, N. Le Thomas, G. Roelkens, D. Van Thourhout, P. Helin and S. Severi, Silicon Photonics: silicon nitride versus silicon-on-insulator, Optical Fiber Communication Conference, Th3J. 1 (2016).

[109] U. Fischer, T. Zinke, J.-R. Kropp, F. Arndt and K. Petermann, 0.1 dB/cm waveguide losses in single-mode SOI rib waveguides, IEEE Photonics Technol. Lett. **8,** 647-648 (1996).

[110] J. F. Bauters, M. J. Heck, D. John, D. Dai, M.-C. Tien, J. S. Barton, A. Leinse, R. G. Heideman, D. J. Blumenthal and J. E. Bowers, Ultra-low-loss high-aspect-ratio Si 3 N 4 waveguides, Opt. Exp. **19,** 3163-3174 (2011).

[111] J. F. Bauters, M. J. Heck, D. D. John, J. S. Barton, C. M. Bruinink, A. Leinse, R. G. Heideman, D. J. Blumenthal and J. E. Bowers, Planar waveguides with less than 0.1 dB/m propagation loss fabricated with wafer bonding, Opt. Exp. **19,** 24090-24101 (2011).

[112] M. Belt, M. L. Davenport, J. E. Bowers and D. J. Blumenthal, Ultra-low-loss Ta 2 O 5-core/SiO 2-clad planar waveguides on Si substrates, Optica **4,** 532-536 (2017).

[113] P. Dumais, C. Callender, C. Blanchetière and C. Ledderhof, High-contrast germanium-doped silica-on-silicon waveguides, Photonics North 2012, 84120M (2012).

[114] R. Bellman, G. Bourdon, G. Alibert, A. Beguin, E. Guiot, L. Simpson, P. Lehuede, L. Guiziou and E. LeGuen, Ultralow loss high delta silica germania planar waveguides, Journal of The Electrochemical Society **151,** G541 (2004).

[115] M. A. Tran, D. Huang and J. E. Bowers, Tutorial on narrow linewidth tunable semiconductor lasers using Si/III-V heterogeneous integration, APL photonics **4,** 111101 (2019).

[116] S. Srinivasan, R. Moreira, D. Blumenthal and J. E. Bowers, Design of integrated hybrid silicon waveguide optical gyroscope, Opt. Exp. **22,** 24988-24993 (2014).

[117] K. T. Grattan and B. T. Meggitt, (1995), Optical fiber sensor technology, Springer.

[118] R. Bergh, H. Lefevre and H. Shaw, An overview of fiber-optic gyroscopes, J. Lightwave Technol. **2,** 91-107 (1984).

[119] W. K. Burns, P. F. Liao and P. Kelley, (2012), Optical fiber rotation sensing, Academic Press.

[120] J. Davis and S. Ezekiel, Techniques for shot-noise-limited inertial rotation measurement using a multiturn fiber Sagnac interferometer, Laser inertial rotation sensors, 131-137 (1978).

[121] S. Gundavarapu, T. Huffman, R. Moreira, M. Belt, J. E. Bowers and D. J. Blumenthal, Integrated ultra-low-loss silicon nitride waveguide coil for optical gyroscopes, Optical Fiber Communication Conference, W4E. 5 (2016).

[122] E. D. Black, An introduction to Pound–Drever–Hall laser frequency stabilization, Am. J. Phys. **69,** 79-87 (2001).

[123] H. L. Ma, X. L. Zhang, Z. H. Jin and C. Ding, Waveguide-type optical passive ring resonator gyro using phase modulation spectroscopy technique, Opt. Eng. **45,** (2006).

[124] C. Ciminelli, F. Peluso and M. N. Armenise, A new integrated optical angular velocity sensor, Integrated Optics: Devices, Materials, and Technologies IX, 93-101 (2005).

[125] G. A. Sanders, M. Prentiss and S. Ezekiel, Passive ring resonator method for sensitive inertial rotation measurements in geophysics and relativity, Opt. Lett. **6,** 569-571 (1981).
[126] D. M. Shupe, FIBER RESONATOR GYROSCOPE - SENSITIVITY AND THERMAL NONRECIPROCITY, Appl. Opt. **20,** 286-289 (1981).
[127] R. E. Meyer, S. Ezekiel, D. W. Stowe and V. J. Tekippe, PASSIVE FIBER-OPTIC RING RESONATOR FOR ROTATION SENSING, Opt. Lett. **8,** 644-646 (1983).
[128] D. Ying, M. Demokan, X. Zhang and W. Jin, Sensitivity analysis of a fiber ring resonator based on an air-core photonic-bandgap fiber, Optical Fiber Technology **16,** 217-221 (2010).
[129] F. Dell'Olio, C. Ciminelli, M. N. Armenise, F. M. Soares and W. Rehbein, Design, fabrication, and preliminary test results of a new InGaAsP/InP high-Q ring resonator for gyro applications, 2012 International Conference on Indium Phosphide and Related Materials, 124-127 (2012).
[130] K. Qian, J. Tang, H. Guo, W. Liu, J. Liu, C. Xue, Y. Zheng and C. Zhang, Under-Coupling Whispering Gallery Mode Resonator Applied to Resonant Micro-Optic Gyroscope, Sens. **17,** 100 (2017).
[131] T. Kominato, Y. Hida, M. Itoh, H. Takahashi, S. Sohma, T. Kitoh and Y. Hibino, Extremely low-loss (0.3 dB/m) and long silica-based waveguides with large width and clothoid curve connection, Proceedings of ECOC, 5-9 (2004).
[132] G. Feugnet, A. Ravaille, S. Schwartz and F. Bretenaker, Analysis of the design of a passive resonant miniature optical gyroscope based on integrated optics technologies, Opt. Eng. **56,** (2017).
[133] R. Zhang, C. Wang, H. Wang, X. Li, J. Li and M. Kong, Improving Locking Accuracy of Resonant Optical Gyroscope by Laser and Acoustooptic Frequency Shifter Jointed Pound-Drever-Hall Technique, Fiber Integr. Opt. 1-11 (2019).
[134] G. A. Vawter, W. J. Zubrzycki, J. Guo and C. T. Sullivan, (2006), Integrated resonant micro-optical gyroscope and method of fabrication, Google Patents.
[135] G. Qian, J. Tang, X. Y. Zhang, R. Z. Li, Y. Lu and T. Zhang, Low-Loss Polymer-Based Ring Resonator for Resonant Integrated Optical Gyroscopes, J. Nanomater. (2014).
[136] C. Vannahme, H. Suche, S. Reza, R. Ricken, V. Quiring and W. Sohler, Integrated optical Ti: LiNbO3 ring resonator for rotation rate sensing, Proc. 13th ECIO **2007,** (2007).
[137] K. Iwatsuki, M. Saruwatari, M. Kawachi and H. Yamazaki, Waveguide-type optical passive ring-resonator gyro using time-division detection scheme, Electron. Lett. **25,** 688-689 (1989).

[138] K. Suzuki, K. Takiguchi and K. Hotate, Monolithically integrated resonator microoptic gyro on silica planar lightwave circuit, J. Lightwave Technol. **18,** 66-72 (2000).

[139] B. Morrison, Stimulated Brillouin Scattering in Integrated Circuits: Platforms and Applications, (2017).

[140] S. P. Smith, F. Zarinetchi and S. Ezekiel, (1992), FIBER LASER GYROS BASED ON STIMULATED BRILLOUIN-SCATTERING,

[141] D. Garcus, T. Gogolla, K. Krebber and F. Schliep, Brillouin optical-fiber frequency-domain analysis for distributed temperature and strain measurements, J. Lightwave Technol. **15,** 654-662 (1997).

[142] K. Iwatsuki, K. Hotate and M. Higashiguchi, EFFECT OF RAYLEIGH BACKSCATTERING IN AN OPTICAL PASSIVE RING-RESONATOR GYRO, Appl. Opt. **23,** 3916-3924 (1984).

[143] W. Burns and R. Moeller, Rayleigh backscattering in a fiber gyroscope with limited coherence sources, J. Lightwave Technol. **1,** 381-386 (1983).

[144] H. Yu, C. Zhang, L. Feng, L. Hong and M. Lei, Limitation of rotation sensing in IORG by Rayleigh backscattering noise, Europhys. Lett. **95,** 64001 (2011).

[145] C. Cutler, S. Newton and H. J. Shaw, Limitation of rotation sensing by scattering, Opt. Lett. **5,** 488-490 (1980).

[146] T. J. Kaiser, D. Cardarelli and J. G. Walsh, Experimental developments in the RFOG, Fiber optic and laser sensors VIII, 121-127 (1991).

[147] H. Ma, Z. He and K. Hotate, Reduction of backscattering induced noise by carrier suppression in waveguide-type optical ring resonator gyro, J. Lightwave Technol. **29,** 85-90 (2011).

[148] F. Dell'Olio, A. Di Nisio, F. Indiveri, P. Lino, C. Ciminelli and M. Armenise, Backscattering noise control in the readout circuit of innovative optoelectronic resonant gyroscopes, 2014 Fotonica AEIT Italian Conference on Photonics Technologies, 1-3 (2014).

[149] Y. Zhi, L. Feng, J. Wang and Y. Tang, Reduction of backscattering noise in a resonator integrated optic gyro by double triangular phase modulation, Appl. Opt. **54,** 114-122 (2015).

[150] F. Hakimi and J. Moores, RIN-reduced light source for ultra-low noise interferometric fibre optic gyroscopes, Electron. Lett. **49,** 205-207 (2013).

[151] H. Ma, X. Li, G. Zhang and Z. Jin, Reduction of optical Kerr-effect induced error in a resonant micro-optic gyro by light-intensity feedback technique, Appl. Opt. **53,** 3465-3472 (2014).

[152] K. Iwatsuki, K. Hotate and M. Higashiguchi, Kerr effect in an optical passive ring-resonator gyro, J. Lightwave Technol. **4,** 645-651 (1986).

[153] R. A. Bergh, H. C. Lefevre and H. J. Shaw, Compensation of the optical Kerr effect in fiber-optic gyroscopes, Opt. Lett. **7,** 282-284 (1982).

[154] M. Lei, L. Feng, Y. Zhi and H. Liu, Effect of intensity variation of laser in resonator integrated optic gyro, Appl. Opt. **52,** 4576-4581 (2013).

[155] D. Ying, M. Demokan, X. Zhang and W. Jin, Analysis of Kerr effect in resonator fiber optic gyros with triangular wave phase modulation, Appl. Opt. **49,** 529-535 (2010).

[156] L. F. Stokes, (1984), Single-mod Optical-fiber Resonator and Applications to Sensing, University Microfilms Internnational.

[157] X. Wang, Z. He and K. Hotate, Reduction of polarisation-fluctuation induced drift in resonator fiber optic gyro by a resonator with twin 90 polarisation-axis rotated splices, Opt. Exp. **18,** 1677-1683 (2010).

[158] K. Iwatsuki, K. Hotate and M. Higashiguchi, EIGENSTATE OF POLARISATION IN A FIBER RING RESONATOR AND ITS EFFECT IN AN OPTICAL PASSIVE RING-RESONATOR GYRO, Appl. Opt. **25,** 2606-2612 (1986).

[159] K. Takiguchi and K. Hotate, BIAS OF AN OPTICAL PASSIVE RING-RESONATOR GYRO CAUSED BY THE MISALIGNMENT OF THE POLARISATION AXIS IN THE POLARISATION-MAINTAINING FIBER RESONATOR, J. Lightwave Technol. **10,** 514-522 (1992).

[160] H. L. Ma, X. H. Yu and Z. H. Jin, Reduction of polarisation-fluctuation induced drift in resonator fiber optic gyro by a resonator integrating in-line polarizers, Opt. Lett. **37,** 3342-3344 (2012).

[161] L. K. Strandjord and G. A. Sanders, Resonator fiber optic gyro employing a polarisation-rotating resonator, Fiber Optic Gyros: 15th Anniversary Conf, 163-173 (1992).

[162] H. Ma, Y. Yan, Y. Chen and Z. Jin, Improving long-term stability of a resonant micro-optic gyro by reducing polarisation fluctuation, IEEE Photonics J. **4,** 2372-2381 (2012).

[163] F. J. Duarte, (2017), Tunable laser optics, CRC Press.

[164] K. Okamoto, Recent progress of integrated optics planar lightwave circuits, Optical and Quantum Electronics **31,** 107-129 (1999).

[165] Inc. Synopsys. RSoft CAD Environment Product Overview, https://www.synopsys.com/photonic-solutions/rsoft-photonic-device-tools/cad-environment.html, (2020).

[166] A. Melikyan, (2018), Active and Passive Plasmonic Devices for Optical Communications, KIT Scientific Publishing.
[167] R. Scarmozzino, A. Gopinath, R. Pregla and S. Helfert, Numerical techniques for modeling guided-wave photonic devices, IEEE Journal of Selected Topics in Quantum Electronics **6,** 150-162 (2000).
[168] K. Y. You, (2018), Emerging Waveguide Technology, InTech.
[169] D. B. Bonneville, M. A. Méndez-Rosales, H. C. Frankis, L. M. Gonçalves, R. N. Kleiman and J. D. Bradley, Flexible and low-cost fabrication of optical waveguides by UV laser resist-mask writing, Optical Materials Express **9,** 1728-1737 (2019).
[170] D. T. Spencer, J. F. Bauters, M. J. Heck and J. E. Bowers, Integrated waveguide coupled Si 3 N 4 resonators in the ultrahigh-Q regime, Optica **1,** 153-157 (2014).
[171] Y. A. Vlasov and S. J. McNab, Losses in single-mode silicon-on-insulator strip waveguides and bends, Opt. Exp. **12,** 1622-1631 (2004).
[172] F. T. Dullo, J.-C. Tinguely, S. A. Solbø and O. G. Hellesø, Single-Mode Limit and Bending Losses for Shallow Rib $\hbox {Si} _ {3}\hbox {N} _ {4}} $ Waveguides, IEEE Photonics J. **7,** 1-11 (2015).
[173] L. Chrostowski and M. Hochberg, (2015), Silicon photonics design: from devices to systems, Cambridge University Press.
[174] D. Marcuse, Curvature loss formula for optical fibers, JOSA **66,** 216-220 (1976).
[175] R. Baets and P. Lagasse, Loss calculation and design of arbitrarily curved integrated-optic waveguides, JOSA **73,** 177-182 (1983).
[176] T. Chen, H. Lee, J. Li and K. J. Vahala, A general design algorithm for low optical loss adiabatic connections in waveguides, Opt. Exp. **20,** 22819-22829 (2012).
[177] T. D. Bucio, A. Z. Khokhar, C. Lacava, S. Stankovic, G. Z. Mashanovich, P. Petropoulos and F. Y. Gardes, Material and optical properties of low-temperature NH3-free PECVD SiN x layers for photonic applications, Journal of Physics D: Applied Physics **50,** 025106 (2016).
[178] F. Ay and A. Aydinli, Comparative investigation of hydrogen bonding in silicon based PECVD grown dielectrics for optical waveguides, Optical materials **26,** 33-46 (2004).
[179] S. Mao, Y. Xu, X. Sun, S. Tao, M. Yu, G. Lo and D. Kwong, Low hydrogen component SiN films by PECVD for low propagation loss waveguide, 2008 IEEE PhotonicsGlobal@ Singapore, 1-4 (2008).
[180] D. Wright, E. Marstein and A. Holt, Effect of annealing on PECVD silicon nitride films 22nd European Photovoltaic Solar Energy Conf, Milan, Italy, 3-7 September 2007 (2007).

[181] T. Lazerand and D. Lishan, Silicon Nitride for MEMS Applications: LPCVD and PECVD Process Comparison, White paper, January (2014).

[182] C. Yang and J. Pham, Characteristic study of silicon nitride films deposited by LPCVD and PECVD, Silicon **10,** 2561-2567 (2018).

[183] SCI, https://sci-soft.com/product/filmtek-4000/,

[184] H. Fujiwara and R. W. Collins, (2019), Spectroscopic Ellipsometry for Photovoltaics: Volume 1: Fundamental Principles and Solar Cell Characterization, Springer.

[185] A. S. K. Tong, Tantalum pentoxide integrated photonic devices, University of Southampton, (2019).

[186] C.-K. Chung, (2013), Plasma Etching, Springer US.

[187] N. Layadi, J. I. Colonell and J. T.-C. Lee, An introduction to plasma etching for VLSI circuit technology, Bell Labs technical journal **4,** 155-171 (1999).

[188] N. Hosokawa, R. Matsuzaki and T. Asamaki, RF sputter-etching by fluoro-chloro-hydrocarbon gases, Jpn. J. Appl. Phys. **13,** 435 (1974).

[189] C. Wilkinson and M. Rahman, Dry etching and sputtering, Philosophical Transactions of the Royal Society of London. Series A: Mathematical, Physical and Engineering Sciences **362,** 125-138 (2004).

[190] J. W. Haus, (2016), Fundamentals and applications of nanophotonics, Woodhead Publishing.

[191] D. K. Sparacin, S. J. Spector and L. C. Kimerling, Silicon waveguide sidewall smoothing by wet chemical oxidation, J. Lightwave Technol. **23,** 2455 (2005).

[192] F. Payne and J. Lacey, A theoretical analysis of scattering loss from planar optical waveguides, Optical and Quantum Electronics **26,** 977-986 (1994).

[193] S. Tinck and A. Bogaerts, Computational study of the CF4/CHF3/H2/Cl2/O2/HBr gas phase plasma chemistry, Journal of Physics D: Applied Physics **49,** 195203 (2016).

[194] G. Z. Yin, X.-y. Qian, P. L. Leahey, J. D. Mohn, W. Chow, A. Y. Chen, Z.-W. Sun and B. K. Hatcher, (2002), Treatment of etching chambers using activated cleaning gas, Google Patents.

[195] C. Gatzert, A. Blakers, P. N. Deenapanray, D. Macdonald and F. Auret, Investigation of reactive ion etching of dielectrics and Si in CHF 3⁄ O 2 or CHF 3⁄ Ar for photovoltaic applications, Journal of Vacuum Science & Technology A: Vacuum, Surfaces, and Films **24,** 1857-1865 (2006).

[196] C. Reyes-Betanzo, S. Moshkalyov, M. Pavanello, A. Ramos and J. Swart, Plasma etching of Si3N4 with high selectivity over Si and SiO2, Proceedings of SBMicro2001-XVI International Conference on Microelectronics and Packaging, 70-75 (2001).

[197] E. Baquedano, R. V. Martinez, J. M. Llorens and P. A. Postigo, Fabrication of silicon nanobelts and nanopillars by soft lithography for hydrophobic and hydrophilic photonic surfaces, Nanomaterials **7,** 109 (2017).

[198] S. M. Williams, W. Liu and D. Mui, (2003), Nitride open etch process based on trifluoromethane and sulfur hexafluoride, Google Patents.

[199] S. Grigoropoulos, E. Gogolides, A. Tserepi and A. Nassiopoulos, Highly anisotropic silicon reactive ion etching for nanofabrication using mixtures of SF 6/CHF 3 gases, Journal of Vacuum Science & Technology B: Microelectronics and Nanometer Structures Processing, Measurement, and Phenomena **15,** 640-645 (1997).

[200] G. Cunge and J. Booth, CF 2 production and loss mechanisms in fluorocarbon discharges: Fluorine-poor conditions and polymerization, J. Appl. Phys. **85,** 3952-3959 (1999).

[201] T. Shao, L. Sun, W. Li, X. Zhou, F. Wang, J. Huang, X. Ye, L. Yang and W. Zheng, Understanding the role of fluorine-containing plasma on optical properties of fused silica optics during the combined process of RIE and DCE, Opt. Exp. **27,** 23307-23320 (2019).

[202] M. Taimoor, A. Alatawi, S. Reuter, H. Hillmer and T. Kusserow, Single-step inductively coupled plasma etching of sputtered Nb2O5/SiO2 multilayer stacks using chromium etch mask, Journal of Vacuum Science & Technology A: Vacuum, Surfaces, and Films **35,** 041302 (2017).

[203] J. Wu, X. Ye, L. Sun, J. Huang, J. Wen, F. Geng, Y. Zeng, Q. Li, Z. Yi and X. Jiang, Growth mechanism of one-step self-masking reactive-ion-etching (RIE) broadband antireflective and superhydrophilic structures induced by metal nanodots on fused silica, Opt. Exp. **26,** 1361-1374 (2018).

[204] T. Wong and S. Ingram, Fabrication of sub-20 nm trenches in silicon nitride using CHF3/O2 reactive ion etching and oblique metallization, Journal of Vacuum Science & Technology B: Microelectronics and Nanometer Structures Processing, Measurement, and Phenomena **10,** 2393-2397 (1992).

[205] A. J. Maker and A. M. Armani, Low-loss silica-on-silicon waveguides, Opt. Lett. **36,** 3729-3731 (2011).

[206] M. Zarchi, S. Ahangarani and M. Z. Sanjari, Properties of silicon dioxide film deposited by PECVD at low temperature/pressure, Metallurgical and Materials Engineering **20,** 89-96 (2014).

[207] M. Ceiler, P. Kohl and S. Bidstrup, Plasma-Enhanced Chemical Vapor Deposition of Silicon Dioxide Deposited at Low Temperatures, Journal of the Electrochemical Society **142,** 2067-2071 (1995).

[208] M. Dainese, Plasma assisted technology for Si-based photonic integrated circuits, KTH, (2005).

[209] B. Shokri, M. A. Firouzjah and S. Hosseini, FTIR analysis of silicon dioxide thin film deposited by metal organic-based PECVD, Proceedings of 19th international symposium on plasma chemistry society, Bochum, Germany, (2009).

[210] A. Coyopol, T. Díaz-Becerril, G. García-Salgado, E. Rosendo, H. Juárez, R. López, E. De La Rosa, M. Pacio and R. Galeazzi, Morphological and optical properties of porous silicon annealed in atomic hydrogen, Superficies y vacío **25,** 226-230 (2012).

[211] S. M. Han and E. S. Aydil, Detection of combinative infrared absorption bands in thin silicon dioxide films, Appl. Phys. Lett. **70,** 3269-3271 (1997).

[212] C.-H. Huang, H. Bai, S.-L. Liu, Y.-L. Huang and Y.-H. Tseng, Synthesis of neutral SiO2/TiO2 hydrosol and its photocatalytic degradation of nitric oxide gas, Micro & Nano Letters **6,** 646-649 (2011).

[213] W. Li, Y. Xu, Y. Zhou, W. Ma, S. Wang and Y. Dai, Silica nanoparticles functionalized via click chemistry and ATRP for enrichment of Pb (II) ion, Nanoscale research letters **7,** 485 (2012).

[214] M. Hussein, K. Wörhoff, G. Sengo and A. Driessen, Optimization of plasma-enhanced chemical vapor deposition silicon oxynitride layers for integrated optics applications, Thin Solid Films **515,** 3779-3786 (2007).

[215] Z. Wang, B. Mikkelsen, B. Pedersen, K. E. Stubkjaer and D. S. Olesen, Coupling between angled-facet amplifiers and tapered lens-ended fibers, J. Lightwave Technol. **9,** 49-55 (1991).

[216] D. Stocker, E. Schubert, W. Grieshaber, K. Boutros and J. M. Redwing, Facet roughness analysis for InGaN/GaN lasers with cleaved facets, Appl. Phys. Lett. **73,** 1925-1927 (1998).

[217] K. K. Lee, D. R. Lim, H.-C. Luan, A. Agarwal, J. Foresi and L. C. Kimerling, Effect of size and roughness on light transmission in a Si/SiO 2 waveguide: Experiments and model, Appl. Phys. Lett. **77,** 1617-1619 (2000).

[218] A. Persano, F. Quaranta, A. Cola, A. Taurino, G. De Angelis, R. Marcelli and P. Siciliano, Ta2O5 thin films for capacitive RF MEMS switches, Journal of Sensors **2010,** (2010).

[219] A.-K. Chu, Y.-Y. Lu and Y.-Y. Lin, Fabrication and analysis of tantalum pentoxide optical waveguide resonator of high thermal stability, Opt. Exp. **27,** 6629-6639 (2019).
[220] L. Pinard, C. Michel, B. Sassolas, L. Balzarini, J. Degallaix, V. Dolique, R. Flaminio, D. Forest, M. Granata and B. Lagrange, Mirrors used in the LIGO interferometers for first detection of gravitational waves, Appl. Opt. **56,** C11-C15 (2017).
[221] D. T. Wei and A. W. Louderback, (1979), Method for fabricating multi-layer optical films, Google Patents.
[222] W. Kulisch, D. Gilliland, G. Ceccone, H. Rauscher, L. Sirghi, P. Colpo and F. Rossi, Ion beam deposition of tantalum pentoxide thin film at room temperature, Journal of Vacuum Science & Technology A: Vacuum, Surfaces, and Films **26,** 991-995 (2008).
[223] N. Robertson, K. Strain and J. Hough, Measurements of losses in high reflectance mirrors coated for λ= 514.5 nm, Optics communications **69,** 345-348 (1989).
[224] L. Yang, E. Randel, G. Vajente, A. Ananyeva, E. Gustafson, A. Markosyan, R. Bassiri, M. Fejer and C. Menoni, Modifications of ion beam sputtered tantala thin films by secondary argon and oxygen bombardment, Appl. Opt. **59,** A150-A154 (2020).
[225] R. Robie, Characterisation of the mechanical properties of thin-film mirror coating materials for use in future interferometric gravitational wave detectors, University of Glasgow, (2018).
[226] H. Yamada, T. Chu, S. Ishida and Y. Arakawa, Optical directional coupler based on Si-wire waveguides, IEEE Photonics Technol. Lett. **17,** 585-587 (2005).
[227] R. K. Gupta, S. Chandran and B. K. Das, Wavelength-independent directional couplers for integrated silicon photonics, J. Lightwave Technol. **35,** 4916-4923 (2017).
[228] C. Lai, Y. Zhong, T. Han, W. Chong, D. Choi, H. Goldsmith, P. Ma, H. Ahmad and S. Madden, Fabrication tolerant planar directional couplers, AOS Australian Conference on Optical Fibre Technology (ACOFT) and Australian Conference on Optics, Lasers, and Spectroscopy (ACOLS) 2019, 1120033 (2019).
[229] L. Leick, J. H. Povlsen and E. Nicolaisen, (2002), Silica-on-silicon optical couplers and coupler based optical filters,
[230] L. Splitthoff, M. A. Wolff, T. Grottke and C. Schuck, Tantalum pentoxide nanophotonic circuits for integrated quantum technology, Opt. Exp. **28,** 11921-11932 (2020).
[231] C. Tyszkiewicz, P. Karasiński and R. Rogoziński, Directional couplers fabricated via a sol–gel route and conventional optical lithography, Optical and Quantum Electronics **48,** 19 (2016).

[232] I. M. White, S. I. Shapova, H. Zhu, J. D. Suter, S. Lacey, P. Zhang, H. Oveys, L. Brewington, J. Gohring and X. Fan, Applications of the liquid core optical ring resonator platform, Sensors for Harsh Environments III, 675707 (2007).

[233] L. Feng, Q. Wang and J. Yang, Design and Fabrication of Silicon Nitride Waveguide Ring Resonator Used for Resonator Integrated Optic Gyro, Micro-nano Technology Xvii-xviii-Proceedings Of The 17th-18th Annual Conference And 6th-7th International Conference Of The Chinese Society Of Micro/nano Technology, 80 (2017).

[234] D. G. Rabus, Z. Bian and A. Shakouri, Ring resonator lasers using passive waveguides and integrated semiconductor optical amplifiers, IEEE Journal of Selected Topics in Quantum Electronics **13,** 1249-1256 (2007).

[235] S. Daud, S. M. Idrus and J. Ali, (2015), Simulation of Optical Soliton Control in Micro- and Nanoring Resonator Systems, Springer.

[236] J. Heebner, R. Grover, T. Ibrahim and T. A. Ibrahim, (2008), Optical microresonators: theory, fabrication, and applications, Springer Science & Business Media.

[237] C. Manolatou and H. A. Haus, (2002), High density integrated optics, Springer.

[238] T. Fukazawa, T. Hirano, F. Ohno and T. Baba, Low loss intersection of Si photonic wire waveguides, Jpn. J. Appl. Phys. **43,** 646 (2004).

[239] M. A. Popovic, E. P. Ippen and F. X. Kartner, Low-loss Bloch waves in open structures and highly compact, efficient Si waveguide-crossing arrays, LEOS 2007-IEEE Lasers and Electro-Optics Society Annual Meeting Conference Proceedings, 56-57 (2007).

[240] Y. Zhang, A. Hosseini, X. Xu, D. Kwong and R. T. Chen, Ultralow-loss silicon waveguide crossing using Bloch modes in index-engineered cascaded multimode-interference couplers, Opt. Lett. **38,** 3608-3611 (2013).

[241] B. Wu, Y. Yu and X. Zhang, Multimode waveguide crossing with ultralow loss and low imbalance, Opt. Exp. **28,** 14705-14711 (2020).

[242] S. Chen, Q. Yan, Q. Xu, Z. Fan and J. Liu, Optical waveguide propagation loss measurement using multiple reflections method, Optics communications **256,** 68-72 (2005).

[243] Y. Yuan, D. Lu, J. Yang, J. Wang, H. Li, Z. Yu, H. Zhang, F. Peng, Z. Liu and L. Yuan, Range extension of the optical delay line in white light interferometry, Appl. Opt. **56,** 4598-4605 (2017).

[244] G. Coppola, L. Sirleto, I. Rendina and M. Iodice, Advance in thermo-optical switches: principles, materials, design, and device structure, Opt. Eng. **50,** 071112 (2011).

[245] J. Milvich, D. Kohler, W. Freude and C. Koos, Surface sensing with integrated optical waveguides: a design guideline, Opt. Exp. **26,** 19885-19906 (2018).

[246] A. N. Tait, T. F. De Lima, E. Zhou, A. X. Wu, M. A. Nahmias, B. J. Shastri and P. R. Prucnal, Neuromorphic photonic networks using silicon photonic weight banks, Sci. Rep. **7,** 7430 (2017).

[247] M. Skalský, Z. Havránek and J. Fialka, Efficient Modulation and Processing Method for Closed-Loop Fiber Optic Gyroscope with Piezoelectric Modulator, Sens. **19,** 1710 (2019).

[248] X. Jin, Y. Lin, Y. Lu, H. Ma and Z. Jin, Short fiber resonant optic gyroscope using the high-frequency Pound–Drever–Hall technique, Appl. Opt. **57,** 5789-5793 (2018).

[249] I. Kiyat, A. Aydinli and N. Dagli, Low-power thermooptical tuning of SOI resonator switch, IEEE Photonics Technol. Lett. **18,** 364-366 (2006).

[250] M. L. Calvo and V. Lakshminarayanan, (2007), Optical waveguides: from theory to applied technologies, CRC Press.

[251] A. Üstündağ, Kerr electro-optic tomography for determination of nonuniform electric field distributions in dielectrics, Massachusetts Institute of Technology, (1999).

[252] H. Yu, L. Chen, K. Li and X. Deng, Electro-optic polymer waveguide modulator based on the Pockels and Kerr effects, Opt. Eng. **52,** 044601 (2013).

[253] L. C. Kimerling, K. Wada, D. D. Cannon and K. K. Lee, (2007), Light modulation using the Franz-Keldysh effect, Google Patents.

[254] B. Bennett and R. Soref, Electrorefraction and electroabsorption in InP, GaAs, GaSb, InAs, and InSb, IEEE J. Quantum Electron. **23,** 2159-2166 (1987).

[255] H. Pinhas, L. Bidani, O. Baharav, M. Sinvani, M. Danino and Z. Zalevsky, All optical modulator based on silicon resonator, Infrared Sensors, Devices, and Applications V, 96090L (2015).

[256] N. C. Harris, Y. Ma, J. Mower, T. Baehr-Jones, D. Englund, M. Hochberg and C. Galland, Efficient, compact and low loss thermo-optic phase shifter in silicon, Opt. Exp. **22,** 10487-10493 (2014).

[257] M. Lee, H. E. Katz, C. Erben, D. M. Gill, P. Gopalan, J. D. Heber and D. J. McGee, Broadband modulation of light by using an electro-optic polymer, Science **298,** 1401-1403 (2002).

[258] Z. Liu and D. Zhu, A low-loss electro-optic waveguide polymer modulator and its optimization design, Optical and quantum electronics **37,** 949-963 (2005).

[259] S. M. Garner, S.-S. Lee, V. Chuyanov, A. Chen, A. Yacoubian, W. H. Steier and L. R. Dalton, Three-dimensional integrated optics using polymers, IEEE J. Quantum Electron. **35,** 1146-1155 (1999).

[260] S. Chung, M. Nakai and H. Hashemi, Low-power thermo-optic silicon modulator for large-scale photonic integrated systems, Opt. Exp. **27,** 13430-13459 (2019).

[261] A. Malik, S. Dwivedi, L. Van Landschoot, M. Muneeb, Y. Shimura, G. Lepage, J. Van Campenhout, W. Vanherle, T. Van Opstal and R. Loo, Ge-on-Si and Ge-on-SOI thermo-optic phase shifters for the mid-infrared, Opt. Exp. **22,** 28479-28488 (2014).

[262] S.-K. Ryu, J. Im, P. S. Ho and R. Huang, A kinetic decomposition process for air-gap interconnects and induced deformation instability of a low-k dielectric cap layer, Journal of Mechanical Science and Technology **28,** 255-261 (2014).

[263] M. Jacques, A. Samani, E. El-Fiky, D. Patel, Z. Xing and D. V. Plant, Optimization of thermo-optic phase-shifter design and mitigation of thermal crosstalk on the SOI platform, Opt. Exp. **27,** 10456-10471 (2019).

[264] B. Poumellec, P. Guenot, I. Riant, P. Sansonetti, P. Niay, P. Bernage and J. Bayon, UV induced densification during Bragg grating inscription in Ge: SiO2 preforms, Optical materials **4,** 441-449 (1995).

[265] K. Okada, H. Kasa, K. Kintaka and K. Hirao, Resonance modes in si micro-cubic cavity coupled with Ge: SiO2 waveguide, Jpn. J. Appl. Phys. **45,** 6663 (2006).

[266] J. Nishii, K. Kintaka, Y. Kawamoto and M. Takahashi, Optical waveguide filter fabricated by excimer laser irradiation, RIKEN REVIEW 38-41 (2003).

[267] W. Li, D. Bulla, C. Charles, R. Boswell, J. Love and B. Luther-Davies, Ge-doped SiO2 thin films produced by helicon activated reactive evaporation, Thin Solid Films **419,** 82-87 (2002).

[268] C. Wang, M. Wang and J. Wu, Heavily germanium-doped silica fiber with a flat normal dispersion profile, IEEE Photonics J. **7,** 1-10 (2015).

[269] A. S. M. Supa'at, Design and Fabrication of a Polymer Based Directional Coupler Thermooptic Switch, Universiti Teknologi Malaysia: PhD Thesis (2004).

[270] B. A. Rose, A. J. Maker and A. M. Armani, Characterization of thermo-optic coefficient and material loss of high refractive index silica sol-gel films in the visible and near-IR, Optical Materials Express **2,** 671-681 (2012).

[271] M. Dudek and M. Kujawińska, Polymer optical bridges for efficient splicing of optical fibers, Photonic Fiber and Crystal Devices: Advances in Materials and Innovations in Device Applications XII, 107550B (2018).

[272] V. Prajzler, P. Nekvindova, P. Hyps, O. Lyutakov and V. z. Jerˇabek, Flexible polymer planar optical waveguides, Radioengineering **23,** 776-782 (2014).

[273] V. Prajzler, P. Hyps, R. Mastera and P. Nekvindova, Properties of siloxane based optical waveguides deposited on transparent paper and foil, Radioengineering **25,** 230-235 (2016).

[274] M. R. Saleem, S. Honkanen and J. Turunen, Thermo-optic coefficient of Ormocomp and comparison of polymer materials in athermal replicated subwavelength resonant waveguide gratings, Optics Communications **288,** 56-65 (2013).

[275] M. F. Hossain, H. P. Chan and M. A. Uddin, Study of optical anisotropies in benzocyclobutene thin films for the efficient design of optical waveguide devices, Opt. Exp. **18,** 8896-8905 (2010).

[276] J. Missinne, A. Vasiliev, A. Elmogi, N. T. Beneitez, E. Bosman, B. Van Hoe and G. Van Steenberge, Bragg grating sensors in laser-written single-mode polymer waveguides, Procedia engineering **120,** 878-881 (2015).

[277] G. Khanarian, Optical properties of cyclic olefin copolymers, Opt. Eng. **40,** 1024-1030 (2001).

[278] T. Han, S. Madden, M. Zhang, R. Charters and B. Luther-Davies, Low loss high index contrast nanoimprinted polysiloxane waveguides, Opt. Exp. **17,** 2623-2630 (2009).

[279] T. Fujigaki, S. Takagi and M. Takenaka, High-efficiency Ge thermo-optic phase shifter on Ge-on-insulator platform, Opt. Exp. **27,** 6451-6458 (2019).

[280] M. R. Watts, J. Sun, C. DeRose, D. C. Trotter, R. W. Young and G. N. Nielson, Adiabatic thermo-optic Mach–Zehnder switch, Opt. Lett. **38,** 733-735 (2013).

[281] R. Ramaswami, K. Sivarajan and G. Sasaki, (2009), Optical networks: a practical perspective, Morgan Kaufmann.

[282] ChemOptics, http://www.chemoptics.co.kr/eng/sub/product_view.php?cat_no=33&idx=16&sw=&sk=&offset=, (2020).

[283] E. Iannone, (2018), Labs on chip: Principles, design and technology, CRC Press.